Controls on the evolution of strength and failure style in shallow rock slope failures

SASKIA JOAN DE-VILDER

Controls on the evolution of strength and failure style in shallow rock slope failures

Saskia Joan de Vilder

Department of Geography

Durham University

Thesis submitted in partial fulfilment of the requirements for the University of Durham for the degree of Doctor of Philosophy

April 2018

Durham University

Abstract

Rock fall failure comprises fracturing through zones of intact rock, known as rock bridges, and kinematic release along discontinuity surfaces. Understanding controls on magnitude – frequency relationships of rockfalls, and their associated failure characteristics aids susceptibility analysis and interpretation of pre-failure deformation. For failure to occur, these rock bridges must have been weakened, with this damage accumulation driven by a suite of weathering processes. This thesis aims to explore the spatial and temporal controls on weathering induced strength degradation and its subsequent influence on the mechanics of rockfall detachment. Within this, it examines the role of gravitational ambient stress, as dictated by slope topography and rock mass structure, which recent research suggests influences the efficiency of weathering processes.

The project integrates field observations, analogue experiments and numerical modelling over varying spatial scales. Terrestrial laser scanning and gigapixel photography are combined to forensically map rock bridge attributes within rockfall detachment surfaces. The role of slope geometry and rock mass structure in concentrating stress is assessed via conceptual finite element models. Finally, samples are subjected to stress conditions induced by the slope structure and environmental conditions in a series of weathering analogue experiments. Together, these results indicate that weathering significantly reduces intact rock strength with areas of stress concentration purely a mechanical control on rockfall release rather than a temporal control on weakening. Weaker rock is characterised by substantial post-peak strength, which requires multiple stages of brittle fracture before ultimate failure occurs. This in turn influences the stages of failure required through rock bridges before final failure, with this number of rock bridges dependent on rockfall size. Mechanically, failure mode is dependent on rock bridge proportion, distribution and location for individual rockfalls. A conceptual model describes magnitude-frequency characteristics and the observable pattern of pre-failure deformation expected for different stages of weathering

Table of Contents

List of Tables

List of Illustrations

List of Equations

Declaration

I confirm that no part of the material presented in this thesis has previously been submitted for a degree in this or any other university. In all cases the work of others, where relevant, has been fully acknowledged.

Saskia de Vilder

Acknowledgements

There are many people to whom I'm grateful for all their help and encouragement in undertaking this PhD.

Firstly, thank you to my supervisors, Nick Rosser and Matt Brain, for all the advice, guidance and encouragement provided through this process, and for setting the bar high. Nick has always been a great sounding board for technical and general questions and helped to remind me of the broader picture for the project. Matt has been a great guide through the world and intricacies of rock mechanics and helped me view this project through that lens. Thanks to Emma Vann Jones for her role as an advisor on the project and for always being so encouraging.

The field and lab components of this project would not have been possible without the help of the technicians in the department. Thanks to Sam Waugh for being a great help with all kinds of fieldwork and always making going out to the coast fun, whatever the weather. Thanks to Dave Hogdson for his technical advice and help in the design and installation of the pump system, as well as the construction of the concrete weights used within the weathering experiments. Thanks to Neil Tunstall and Chris Longley for all their help with lab work, in particular the frustrating work of core preparation and RSV plus running many many UCS tests. The technicians in the Physics mechanical workshop also provided helpful design advice towards the construction of one of the more bizarre things installed out at the Boulby coast.

This project has been possible thanks to the funding provided by ICL Fertilizers (UK) Ltd, and their support of the wider monitoring project over the years. Within ICL Ltd, Peter Jones' help with the installation and monitoring of the weathering frame is greatly appreciated, along with discussions had with Angus Nicholson of Wilf Noble Ltd surrounding the practicalities of constructing the frame.

Many thanks to all the others who have come and helped on often cold and wet fieldwork, including Simon Varley, Zuzanna Swirad, Heather Bell, Rich Boothroyd, Jess Benjamin and Rob Tomkies.

This PhD and my time in Durham has been rewarding, fulfilling and fun, in no small part due to an amazing bunch of friends with which I've been able to share this journey. A big thanks to; the Geography cohort for providing daily light-heated relief and many good memories; fellow Chad's friends for being there right from the beginning; the Durham Ladies netball crew for all the fun; and the wonderful community of St George's for all their support. Finally, I'm so thankful and grateful for the constant support, confidence and love of my family.

1 Introduction

1.1 Context and justification of the thesis

Rockfalls, defined as the detachment and subsequent fall, roll and bounce of rock blocks from a slope (Varnes, 1978), represent a serious hazard to people, property and infrastructure in steep terrain (e.g. Guzzetti et al., 2003; Hungr et al., 1999). They form a principal mechanism of erosion in steep and mountainous terrain (Matsuoka and Sakai, 1999; Moore et al., 2009; Whalley, 1984), with their frequency – magnitude characteristics influencing erosion rates (Barlow et al., 2012). Understanding the size and timing of rockfalls across a slope enables broad susceptibility analysis (Fell et al., 2008), as well as the knowledge of where and when an individual rockfall could occur. High frequency monitoring of slopes has revealed that areas of incipient failure can be delimited via millimetre to centimetre surface deformation monitoring (e.g. Abellán et al., 2009; Crosta and Agliardi, 2003), precursory rockfalls (Kromer et al., 2015; Rosser et al., 2007; Royán et al., 2014), and micro-seismicity (e.g. Amitrano, 2005; Senfaute et al., 2009). The advent of 4-D monitoring and associated analysis of the, often large, pre-failure deformation data for the development of early-warning systems (Eitel et al., 2016) necessitates an accurate understanding and, therefore, correct interpretation of the underlying mechanics of rockfall detachment (Kromer et al., 2017; Petley et al., 2005; Rowe et al., 2017).

Detachment is a function of kinematic release along discontinuity surfaces and fracturing through intact zones of rock, defined as rock bridges, which separate non-continuous discontinuities (Jennings, 1970), in a process known as step-path failure (Brideau et al., 2009; Eberhardt et al., 2004a; Scavia, 1995). Rockfalls in many settings occur via progressive failure, whereby a perturbation to the stress in the slope occurs (e.g. storm, rockfall, earthquake), resulting in stress redistribution throughout the surrounding rock mass (Eberhardt et al., 2004a; Rosser et al., 2007). This redistribution can result in fracture propagation over time, which cascades to the failure of the surrounding rock

mass (Eberhardt et al., 2004a; Rosser et al., 2007), including upward propagation of further failures above (Rosser et al., 2013).

However, rockfall failure has been observed to occur at stresses lower than those required to fracture intact rock (Lim et al., 2010; Rosser et al., 2007; Wieczorek et al., 1992). Additionally, most previous slope failure studies are concerned with modelling relatively large-scale, full slope collapse (e.g. Grøneng et al., 2009; Lévy et al., 2010; Senfaute et al., 2009), whereby failure occurs only where gravitational stresses are sufficient to instigate collapse based upon slope geometry alone. Monitoring data from actively failing rock slopes (e.g. Dewez et al., 2013; Lim et al., 2010; Stock et al., 2012) shows that the majority of rockfalls are commonly shallow in depth (< 2 m). In such circumstances, the rockfall volume, and hence mass, are insufficient to generate the magnitude of stress required to fracture intact rock, based upon classical failure mechanics. Smaller and hence more frequent rockfalls have been shown to be significant, not only in terms of number of events but also their contribution to net erosion of a slope (e.g. Lim et al., 2010; Moore et al., 2009; Rosser et al., 2013).

To allow rockfalls to be triggered by relatively low magnitude events, the strength of the rock mass must have been reduced prior to triggering (Gunzburger et al., 2005). This strength reduction, referred to by some as damage, can occur via weathering, which acts to weaken a rock slope over time, predisposing it to failure and in some cases even triggering failure itself (Viles, 2013). Within this thesis, weathering is defined broadly as the in-situ breakdown of rock at or near the Earth's surface, which acts both along discontinuities and within intact rock (Yatsu, 1988). Weathering is an often ambiguous term due to the multitude of physical, chemical and biological geomorphic processes it encompasses, and the varying scales over which these processes act and are considered (Hall et al., 2012; Viles, 2013). The physical break-down of rock, and hence the reduction of intact strength, via micro-crack growth necessary for failure, is the result of the many competing and often non-linear weathering processes. As such, weathering

in this thesis is viewed as the net effect of any geomorphic process that generates and results in the growth of micro- and macro-cracks (Eppes and Keanini, 2017).

Recent research has suggested that stress concentrations in a slope may determine areas of either enhanced (Brain et al., 2014) or dampened weathering (Bruthans et al., 2014; Zhang et al., 2012). The gravitationally induced ambient stress within and upon a slope is concentrated by the topography in conjunction with the nature and distribution of rock bridges, which is suggested to determine areas of greater spatial susceptibility to weakening, and therefore failure as rockfall.

Within the broader field of rock weathering, studies of its influence have either focussed on long-term changes in the nature of failure as rock transitions from slightly weathered to highly weathered (e.g. Durgin, 1977), or as surficial characteristics such as slaking or frittering (Moses et al., 2014 and references therein). Conversely, the mechanics of failure are often reduced to simple styles of kinematic release, with little consideration of time and hence sequences of events such as incremental rock bridge fracture (e.g. Goodman and Shi, 1985; Wyllie and Mah, 2004). Gravitational stresses are seen as a driver of bedrock fracture at depth (Miller and Dunne, 1996; Molnar, 2004; St Clair et al., 2015) or sheeting joint propagation and associated rock failure (Martel, 2006; Stock et al., 2012). Investigations of large slope failures include a recognition of gravitational drivers of failure alongside the mechanisms of fracture propagation through rock bridges to form shear release surfaces (e.g. Eberhardt et al., 2004a; Stead et al., 2006), with some studies incorporating the impact of thermal or pore pressure fluctuations (e.g. Gischig et al., 2011; Gunzburger et al., 2005; Moore et al., 2011; Preisig et al., 2016), but little consideration of weathering beyond this.

The exact role of stress, weathering and failure mechanisms is not well constrained for smaller rockfall failures (Figure 1.1), though evidence of each is observed within the detachment surface of a rockfall, known as a rockfall scar (Figure 1.2). Weathering and gravitational stresses are often only considered in terms of whole slope collapses, with

its influence on the surficial shallow zone or 'skin' of a rock slope, where smaller rockfall occur, little quantified.

As outlined above, understanding the interactions between the spatial distribution of stress and temporal control of weathering on rock strength may determine the patterns and mechanisms of rockfall failure – essential for accurate hazard assessment. This thesis therefore aims to investigate the controls on and interaction of weathering and stress within intact rock to determine the impact on mechanical detachment of rockfalls.

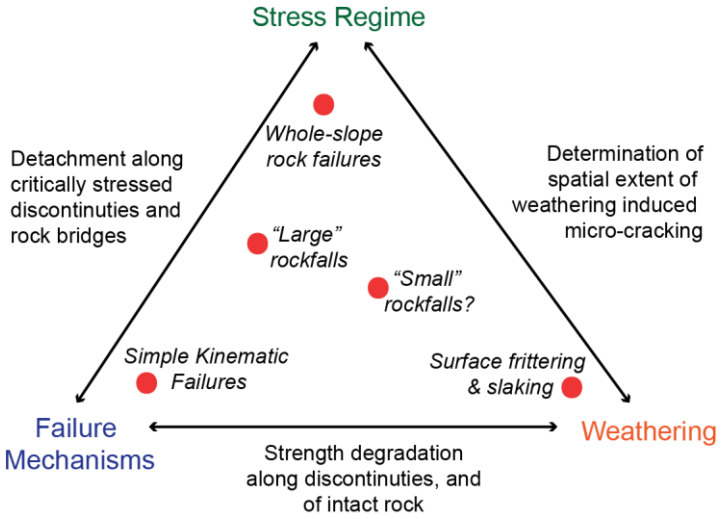

Figure 1.1: Schematic of the competing influence of weathering, the slope stress distribution and failure mechanisms on slope instability.

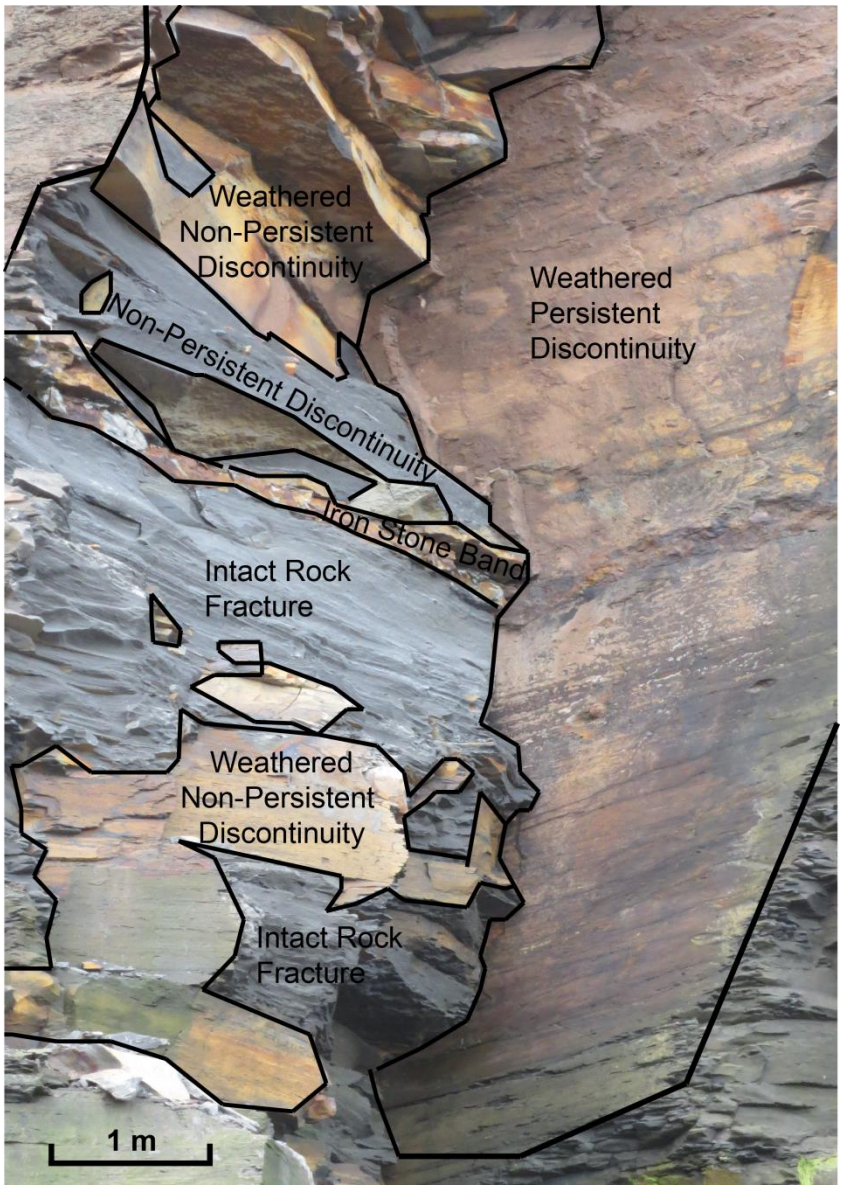

Figure 1.2: Photo of a recent rockfall scar from the North Yorkshire coast (November 2014). The scar displays weathered discontinuities of varying persistence, unweathered discontinuity surfaces, and fractured rock bridges. A band of iron stone is also visible in the middle of the rockfall scar (Author's own photo, 2014).

1.2 Novelty of Approach

Recent advances in remote sensing techniques, such as terrestrial laser scanning (TLS), have revealed a variety of patterns of progressive failure of rockfall, and mechanical sequences of detachment from the wider slope (see reviews in Abellan et al., 2014; Eitel et al., 2016; Jaboyedoff et al., 2012). A correct interpretation of this behaviour requires a detailed understanding of the processes that drive rockfall detachment.

Central to this, is an understanding of the strength properties of a rock slope that control stability. Rock bridges are an important component of stability, but traditionally have been difficult to quantify due to their being concealed within a slope (e.g. Einstein et al., 1983). This thesis develops an alternative approach by forensically analysing rock bridges within post-failure rockfall scars, captured via field observations using high resolution terrestrial laser scanning and photography, and compiling for the first time a database of rock bridge attributes.

Strength degradation, as induced by weathering, is important for controlling the timing of failure (Gunzburger et al., 2005; Viles, 2013a). Weathering induced strength degradation may vary spatially across a slope as function of gravitationally induced ambient stress (Brain et al., 2014; Bruthans et al., 2014). An understanding of both temporal and spatial controls on strength degradation, will therefore inform the observed temporal and spatial patterns of failure recorded within remote sensing data. The investigation of the role of weathering in the zone of rock mass, where strength degradation is crucial for stability, provides quantitative links to rock slope instability, which have previously been difficult to upscale (Hall et al., 2012; Viles, 2013a).

Within this thesis, exploratory numerical modelling is used to assess the potential spatial control of gravitationally induced ambient stress on rockfall failure. The influence of weathering on strength degradation of strong rock (as defined by: ISRM, 2015), subjected to ambient stress and environmental conditions experienced by a rock slope, is investigated via novel experimental set-ups. Using laboratory analogue models, the stress conditions, equivalent to those within a natural rock slope allow the experiments to be up-scaled to understand the field and numerical observations (Viles, 2001). This unique integration of high resolution field observations, geotechnical laboratory testing and numerical modelling allows the controls on weathering induced damage accumulation to be analysed over a variety of spatial scales, from the whole slope to the micro-crack (Viles, 2013a).

The thesis evaluates the role of weathering on the occurrence and mechanics of rockfall failure, by defining the following aspects:

- The zone in a rock slope where rock strength degradation is important in driving rockfall
- The ambient stresses experienced by such zones
- The rate and magnitude of strength degradation within these zones.

1.3 Research Aim & Objectives

The over-arching aim of this thesis is to *explore the spatial and temporal controls on weathering-induced strength degradation within a rock mass, and the associated implications for the mechanics of rockfall*. The research objectives are:

Objective 1: To characterise the failure surfaces of rockfall via morphological analysis to establish the relative contribution of intact rock fracture, discontinuity release surfaces and surficial weathering in rockfall failure. The purpose is to identify where rock bridges are located within slope, and therefore where stress concentration and/or strength loss is important in controlling stability.

Objective 2: To model the interaction of micro-topography and rock mass structure in concentrating stress within the slope near surface (<1 m depth) and assess the coincidence, both in time and space, between rockfall and stress concentrations. The output determines how the broader structure and topography act to concentrate stress at rock bridges, and the resulting impact on rockfall occurrence.

Objective 3: To measure the degree of strength degradation for a rock subjected to simulated topographic stress loading conditions and natural environmental processes. The geotechnical characterisation investigates the changes to intact rock strength at rock bridges, where stress and weathering processes are concentrated, and provides temporal controls on the resulting instability.

Objective 4: To develop a new conceptual rockfall failure model, based on mechanically correct principles of rockfall evolution. This model specifically incorporates; the mechanical controls on failure, the spatial and temporal relationships between stress and rockfalls, and the temporal control of weathering on strength degradation.

1.4 Organisation of thesis

The thesis is split into six substantive chapters (2 – 7). I use the first person "we" to reflect co-author contribution where appropriate, with relative contributions of each author outlined. The content of the following chapters is described as follows:

1.4.1 Chapter 2

Chapter 2 reviews the literature and identifies current gaps in our knowledge of the controls and roles of strength degradation in determining the temporal, spatial and mechanical aspects of rockfall failure. This includes an overview of the current understanding of rockfall behaviour, the processes by which strength degradation occurs and associated links to the mechanisms of failure. It considers the role of weathering within this and examines the potential spatial control of gravitationally induced ambient stress on weathering. Separate introductions and reviews of literature specific to each objective are included within Chapters 3, 4 and 5.

1.4.2 Chapter 3

de Vilder, S.J., Rosser, N.J., and Brain, M.J., 2017. Forensic analysis of rockfall scars. Geomorphology. 295. 202-214

de Vilder, S.J., Rosser, N.J., Brain, M.J., and Vann Jones, E.C., 2017. Forensic rockfall scar analysis: development of a mechanically correct model of rockfall failure. In: 3rd North American Symposium on Landslides. 829-839

This chapter represents a compilation of two published papers. The *Geomorphology* paper forms the basis of the chapter, with the calibration data published in the conference proceedings of the *3rd North American Symposium on Landslides,* which I insert into the

relevant methodology and results section within the *Geomorphology* paper. The full manuscripts of each paper are included in Appendix A. In these papers, I undertook the data collection, processing and analysis; wrote the manuscript; and drew the figures. All authors contributed ideas and edited the text for each respective paper.

Chapter 3 presents a database of 657 rockfall scars captured using uniquely high resolution terrestrial laser scanning and photography. The rockfall scars represent the detachment surfaces of rockfalls observed over a one-year period from a section of cliff at Boulby, North Yorkshire, UK. Within each scar, rock bridge and weathering attributes are mapped. Research Objective 1 is addressed with rock bridge and weathering proportion within each rockfall scar determined, as well as rock bridge distribution, orientation and location. The chapter ends with a discussion of the controls on rock bridge characteristics and the implications of these for the sequence and style of rockfall failure. Though the results are site-specific, the statistical relationships determined from the database are applicable to rock slopes in general. The results from this chapter are also used to inform the boundary conditions of models developed in Chapter 4.

1.4.3 Chapter 4

Chapter 4 addresses Research Objective 2 and examines the influence of topography and rock mass structure in concentrating stress within a slope. It investigates if a relationship exists, both in space and time, between stress distribution and rockfall occurrence. Exploratory finite element modelling is used to establish general rules of the influence of topography (modelled with varying slope angle and the presence of overhangs) and rock mass structure (modelled with varying joint persistence) on the near surface stress and strain distribution of a cliff. These rules are then mapped onto a DEM of the Boulby cliff to assess the coincidence of these conditions with rockfalls. This analysis addresses the second research objective and provides an indication of the spatial control of topography and rock mass structure on rockfall behaviour.

1.4.4 Chapter 5

de Vilder, S.J., Brain, M.J., and Rosser, N.J., Submitted. Controls on weathering intensity and its effects on the compressive strength and failure style of sedimentary rocks. Earth Surface Processes and Landforms.

In this paper, I undertook the data collection, processing and analysis; wrote the manuscript; and drew the figures. NJ Rosser and MJ Brain contributed ideas and edited the text for the paper.

Chapter 5 presents a series of weathering experiments where samples have been subjected to ambient stresses, which includes gravitationally induced compressive stress, equivalent to those experienced by a natural rock slope. I also explore intensive salt water wetting and drying experiments within a laboratory setting and a unique year-long field experiment with samples subjected to natural environmental conditions. This chapter addresses Research Objective 3 and establishes the influence of weathering on rock strength degradation by undertaking comparative analysis of unconfined compression strength between baseline and weathered samples. This chapter ends with a discussion on the influence of ambient compressive stress on the strength degradation, the broader impact of weathering on mode of failure and the implications of this for rockfalls. The complete monitoring data-sets are included in Appendix B.

1.4.5 Chapter 6

Chapter 6 brings together the findings of Chapters 3 to 5 to analyse the spatial and temporal controls on weathering induced strength degradation within a rock mass. From this, a new conceptual model is used to explore the impact of rock weakening through time on the nature and characteristics of brittle rock fracture and rockfall detachment. The development of the conceptual model addresses Research Objective 4. The implications of this model are discussed with reference to observed pre-failure deformation and magnitude -frequency characteristics of rockfall falling from a slope.

1.4.6 Chapter 7

Chapter 7 presents the conclusions of this study in the context of the four research objectives. Here the most novel findings are outlined and recommendations for future research are discussed.

2 Current understanding of controls on rockfall failure

2.1 Driving forces of failure

For failure to occur, the stresses experienced by a slope must be greater than the resisting strength of the slope. Much research has focussed on understanding the environmental stresses which can trigger failure (e.g. Amato et al., 2016; Frayssines and Hantz, 2006; Ishikawa et al., 2004; Lim et al., 2010; Matsuoka and Sakai, 1999; Rosser et al., 2007; Sass, 2005; Strunden et al., 2015; Vann Jones et al., 2015; Wieczorek and Stefan, 1996). However, correlations with environmental conditions are often low and rockfall failure can occur in the absence of any discernible triggers (e.g. Lim et al., 2010; Rosser et al., 2007; Wieczorek et al., 1992). Correlations between environmental conditions and failure decrease for increasing rockfall size (Rosser et al., 2007; Strunden et al., 2015).

As the links between environmental conditions and rockfall failure are low, the strength of the rock mass (i.e. the resisting force) is an important control on failure, with its evolution through time determining the temporal and spatial patterns of rockfall. This literature review aims to assess our current understanding of the role of rock strength and its degradation in controlling rockfall failure. It identifies gaps in knowledge, including the location of strength degradation within a slope, the controls on the intensity of such strength degradation and the associated implications for the mechanisms of failure.

2.2 Resisting forces of failure

The strength of the rock mass is a function of discontinuities of various orientations and attributes, which are separated from each other by zones of intact rock, termed as rock bridges. Both of these components can be variously weathered. Rock mass structure, comprising the presence and characteristics of discontinuities, is a crucial control on stability (Stead and Wolter, 2015 and references therein) and acts to lower rock mass strength (Hoek, 1983; Selby, 1982; Terzaghi, 1962). The orientation of discontinuities with respect to each other and the slope itself can determine failure location by providing

zones that enable kinematic release. This can be broadly classified into the categories of sliding, toppling or wedge failure (Goodman and Shi, 1985; Wyllie and Mah, 2004). However, as rockfall scars indicate, intact fracture through rock is also commonly required for rockfall release (Figure 1.2). These rock bridges act to increase stability, with numerical analysis suggesting that if rock bridges account for even a single digit percentage of a slope, the overall factor of safety will be substantially higher (Diederichs, 2003; Einstein et al., 1983; Frayssines and Hantz, 2006; Jennings, 1970; Scavia, 1995). However, due to the difficulty of characterising internal features of a rock mass (Einstein et al., 1983), slope stability studies have often conservatively assumed that discontinuities are fully persistent and therefore structural controls on rockfall failure are purely kinematic (e.g. Goodman and Shi, 1985; Wyllie and Mah, 2004). Failure requires step path style breakage via development of a failure plane through rock bridges, which may occur progressively due to the time-dependent nature of fracture propagation (Eberhardt et al., 2004b; Kemeny, 2005; Scavia, 1995). Progressive failure has long been recognised within hard rock and soil failures and involves the time-dependent propagation of a discontinuity driven by the redistribution of stress in front of the propagating discontinuity crack tip (Bjerrum, 1967; Terzaghi, 1962). The strength characteristics of intact rock will therefore influence the nature of this progressive failure.

2.3 The role of weathering

For failure to occur under environmental stresses lower than that required to drive fracture propagation through pristine intact rock, this rock must have been weakened prior to failure. Weathering, as defined as the in situ breakdown of rock at or near the Earth's surface (Yatsu, 1988), via the mechanical means of micro- and macro-scale crack growth (Eppes and Keanini, 2017), acts to prepare a slope for failure (Viles, 2013a)

Rock slopes are a weathering-limited environment, where weathering is the rate-limiting process that can determine the erosion of a slope (Viles, 2013a). Weathering research has largely been concerned with the mechanisms of weathering processes at

increasingly smaller scales, with limited links to its effect on rock slope emergent larger scale behaviour (Hall et al., 2012). This thesis aims to identify and characterise these links, firstly by identifying spatially where weathering is a control on rockfall behaviour (i.e. where rock strength degradation is required for failure to occur) and secondly by examining its temporal control on failure.

Weathering is often assessed within rock mass classification systems, such as the Rock Mass Rating System (Selby, 1980), Geological Strength Index (Hoek and Brown, 1997) and the Q System (Barton et al., 1974). These semi-quantitative systems classify rock mass strength as a function of discontinuity density and orientation, surficial characteristics of weathering along these discontinuities and estimates of rock strength, often obtained from surface hardness measurements (e.g. Borrelli et al., 2007). They provide an indication of the global role of weathering in determining the susceptibility of a slope to failure, but as they do not explicitly consider the location, timing or mechanisms of such failures, they provide little information on the role of weathering in driving rockfall detachment itself.

However, numerous studies have shown a link between some measure of weathering intensity and rockfall occurrence, especially in alpine environments (Ishikawa et al., 2004; Krautblatter et al., 2013; Matsuoka and Sakai, 1999; Sass, 2005; Viles, 2013a). Sass (2005), in a study of rockfall occurrence, implicitly indicates a relationship between weathering and rockfall intensity, with areas of more prolonged freeze-thaw events experiencing greater occurrence of rockfalls. This relationship exists as weathering reduces the strength of the rock mass gradually over time (Gunzburger et al., 2005). This is displayed conceptually in Figure 2.1, whereby the strength of the rock mass decreases slowly in response to environmental cyclic loading, until the point of final failure is reached. These cycles in stress can result from freeze-thaw, wetting and drying and temperature cycles which alter the stresses in the slope (Yatsu, 1988). It is the repetition and accumulation of weakening during these cycles which may prepare a slope for failure (Gunzburger et al., 2005). The rate of strength degradation and the time needed for

failure to occur is determined by the rate of change of the resisting forces in Figure 2.1. This resisting line is representative of the global strength of the rock mass that ultimately fails.

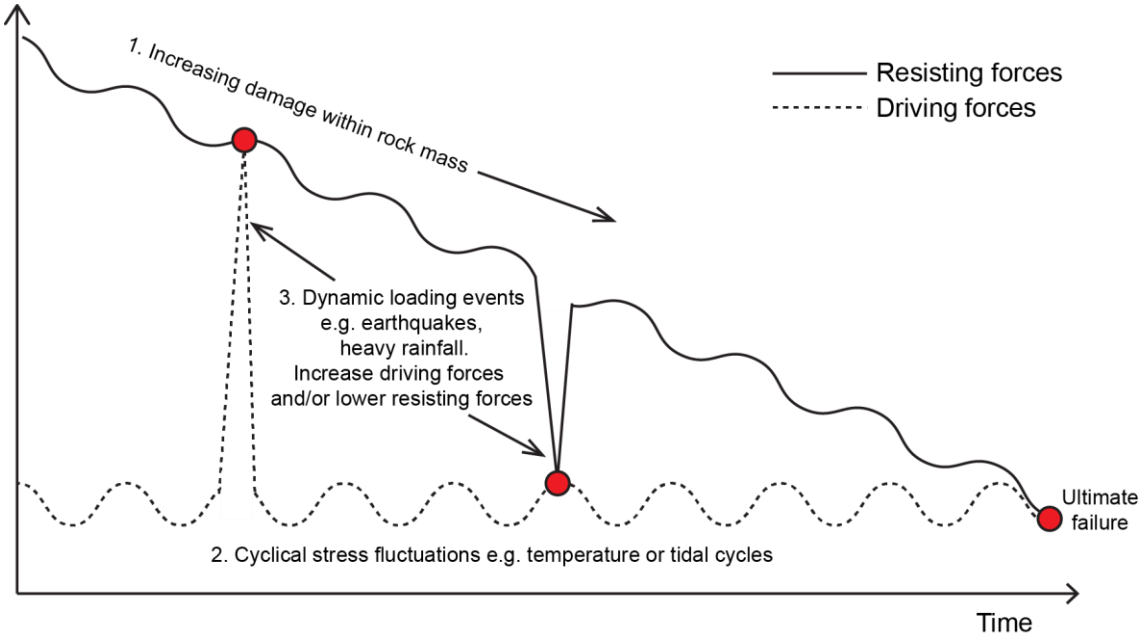

Figure 2.1: The factors which reduce the strength of the rock mass, and increase the stresses acting upon it over time (the x axis). The red dots represent when failure conditions are met. The gradual reduction in rock mass strength is driven by environmental cycles. Dynamic loading events can both increase the stress acting on a slope, or decrease the strength of the slope, which allows failure to occur (modified from Gunzburger et al., 2005).

2.3.1 Weathering along discontinuities

Weathering induced reduction in rock strength occurs in two ways: along discontinuities and within intact rock itself. Weathering along discontinuities can result in a loss of frictional and cohesional strength via both chemical and mechanical weathering mechanisms (Selby, 1980; Yatsu, 1988). Areas of greater fracture density often display greater weathering intensity and a resultant higher rockfall occurrence (Sass, 2005). This may be due to the fact that discontinuities act as conduits for water and air flow, determining and regulating the micro-environmental conditions of the rock slope and therefore the magnitude and extent of the stresses imposed by weathering processes (e.g. V. S. Gischig et al., 2011; Ishikawa et al., 2004; Miller and Dunne, 1996; Moore et

al., 2011; Preisig et al., 2016). Fracture tips may also act as stress concentrators, in the same way as micro-crack tips concentrate stress, therefore allowing macro-crack propagation (and/or micro-crack propagation) to occur (Kemeny, 2005, 2003).

2.3.2 Weathering within intact rock

As rockfalls can occur via a step-path failure process, if the discontinuities are already critically stressed, then the weathering induced strength degradation of a rock bridge(s) is a controlling factor in block release and slope stability. However, due to the location of rock bridges within a slope, their presence and characteristics are often difficult to quantify (Einstein and Baecher, 1983). However, it is here that strength degradation is important for controlling the spatial locations and timing of failure, as these rock bridges form the attachment points to the wider slope, and must break for failure to occur (Kemeny, 2005). This thesis addresses this by examining rockfall scar surfaces, which contain a record of rock bridges, to determine the exact role of rock bridges in controlling failure (Figure 1.2).

Within intact rock, strength degradation is a function of increasing fracture density, both at a macro- and micro- crack scale. In this thesis, the presence and concentration of micro- and macro - cracks within a rock are referred to as '*damage'*, with the processes of crack generation and propagation referred to as '*damage accumulation'*. Weathering not only influences the strength properties of intact rock but can also influence rock rheology, which may change the style of rock failure (Basu et al., 2009; Gupta and Seshagiri Rao, 2000; Viles, 2013a).

2.4 Time dependent damage accumulation processes

2.4.1 Fracture mechanics concepts

This section provides an overview of linear elastic fracture mechanics which underpins brittle fracture propagation within rock, and therefore how damage can accumulate (Anderson, 2005). Griffith (1924, 1921) developed a theory for the initiation of micro-cracks, where micro-cracks initiate at pre-existing open cracks within the rock when

tensile stress concentrations at the crack tip exceed the local strength of the crack tip. These pre-existing micro-cracks include: grain boundaries; inter-crystalline cracks within grains; intra-crystalline cracks; and, mineral cleavage cracks (Kranz, 1983). Initial micro-crack growth is likely to be tensile and parallel to the major principal stress, defined as σ^1 (Lajtai and Lajtai, 1974). The Griffith theory can be expressed in terms of energy, with crack propagation occurring when the energy available for such propagation overcomes the resistance of the material, as:

$$G = \frac{\pi\sigma^2 a}{\varepsilon}$$

Equation 2.1

The energy release rate (*G) i*s a function of external loading *(σ),* 50% the existing crack length (*a),* and Young's Modulus of Elasticity (ε). Young's Modulus reflects the stiffness of the material, indicating how easily it can break or bend, as determined by the ratio of stress to strain (Anderson, 2005). This theory of micro-crack initiation was modified by Irwin (1957) to define the stress experienced at the crack tip as the stress intensity factor (K_I), with this factor dependent on crack geometries and external stress loading conditions. It is defined for tensile fracture as:

$$K_I = \sigma\sqrt{\pi a}$$

Equation 2.2

The stress intensity factor is therefore proportional to the length of the crack and influenced by external loading conditions. Micro-crack growth occurs if K_I exceeds the fracture toughness (K_C) of the material (Anderson, 2005). It is also suggested that a threshold (K_{TH}) exists where no micro-crack initiation and growth can occur.

Within these fundamental equations, the rock properties explicitly, as determined by ε or $K_{C,}$ control micro-crack growth. Understanding how these properties change through

time is therefore important for understanding how damage accumulation results in eventual rock failure (Eppes and Keanini, 2017).

2.4.2 Sub-critical crack growth

Observations and experimental data indicate that cracks can grow sub-critically between K_{TH} and K_I (Atkinson, 1984). The mechanisms which drive sub-critical micro-crack growth have been suggested to include stress corrosion, dissolution, diffusion, ion exchange or micro-plasticity. Stress corrosion is the predominant mechanism within rock, while the role and nature of the other mechanisms are debated and remain not well understood (Anderson, 2005; Atkinson, 1984; Eppes and Keanini, 2017). Stress corrosion is a chemo-mechanical processes which operates at micro-crack tips (Figure 2.2), where the strained molecular bonds react more readily to environmental agents than non-strained bonds (Atkinson, 1984). This reaction process creates weaker bonds, which may allow the micro-crack to propagate under existing stresses. Fluctuations of stresses by weathering processes such as thermal expansion or contraction can create small perturbations in stress that result in fracture propagation. As stress-corrosion requires a reagent, it is dependent firstly on the presence of moisture within a crack, and secondly on the chemical properties of such fluid. Moisture therefore controls the effectiveness of this mechanism, and as such any weathering processes that create stress fluctuations necessary for micro-crack growth (Eppes and Keanini, 2017).

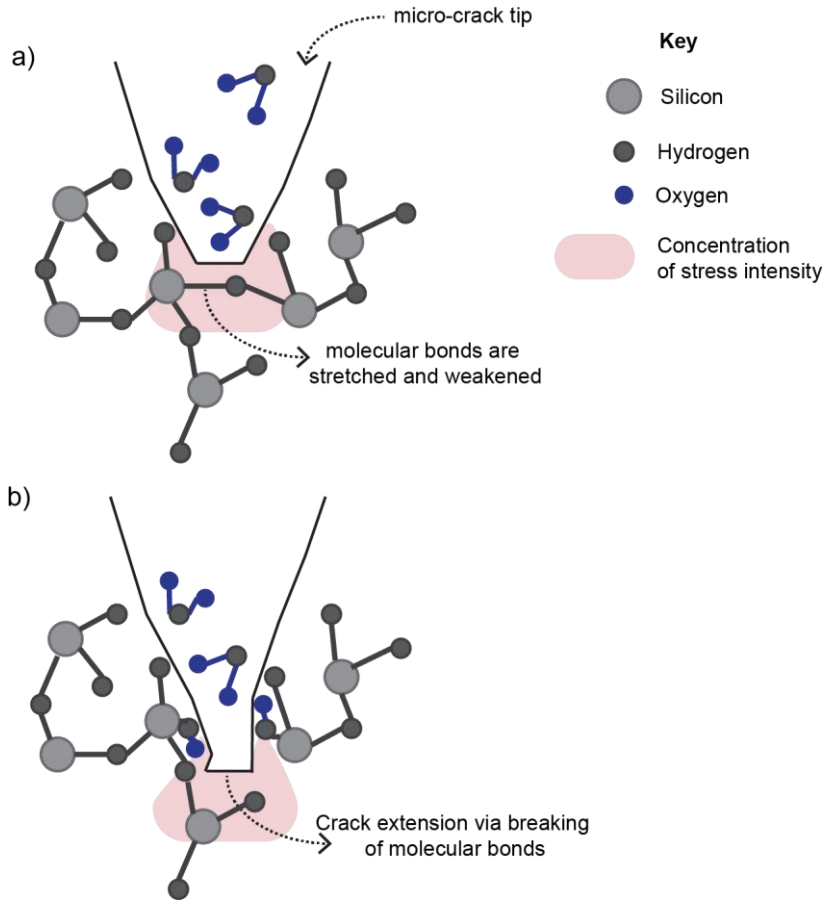

Figure 2.2: Conceptual schematic of the process of stress corrosion in quartz. a) Molecular bonds at the crack tip, where the stress intensity factor (*K*) is concentrated, are stretched and weakened. Due to the weakening, the molecules become chemically reactive with water (either in liquid or vapour form) in the crack. b) The newly formed bonds created by the reaction between quartz and water are weaker and therefore more readily broken by the subcritical stresses allowing the crack to extend (Eppes and Keanini, 2017).

Cyclical fatigue is another suggested mechanism of sub-critical crack growth, which occurs by purely mechanical means, whereby repeated cyclical loading weakens bonds at the micro-crack tip (Attewell and Farmer, 1973). However, distinguishing in reality between stress-corrosion and cyclical loading is not possible. The duration, number of cycles and their amplitudes are known to influence the degree and rate of cyclical fatigue in a rock (Cerfontaine and Collin, 2017 and references therein). This is often expressed in terms of an S-N curve, whereby high amplitude stress processes which cyclically load a slope require a fewer number of cycles before macro-scale fracture and failure can

occur (Figure 2.3). A fatigue limit is proposed with cyclical stress amplitudes lower than this resulting in no damage within the rock (Anderson, 2005).

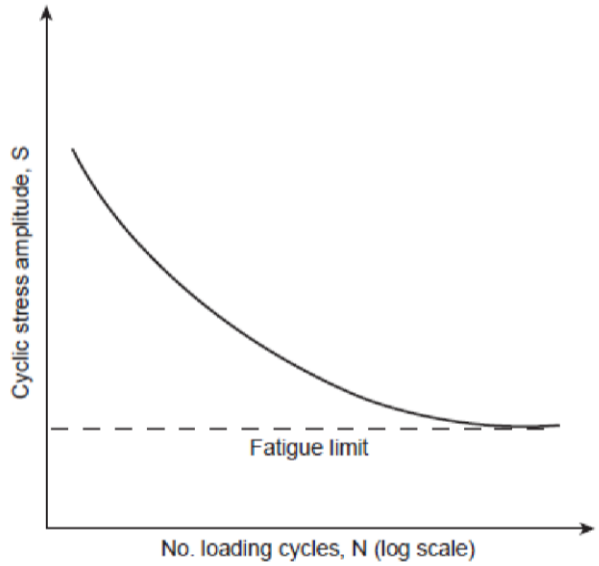

Figure 2.3: Typical S-N curve for material. As the cyclical stress amplitude decreases, the number of loadings cycles required for failure increases. Below a cyclical stress amplitude threshold, an infinite number of cycles can occur, which do not result in failure. This is termed the fatigue limit (Anderson, 2005).

Both mechanisms highlight the importance of fluctuations in stress in driving micro-crack propagation, as evidenced by recent research on thermal cycling controls on rock fracture (Collins et al., 2018; Collins and Stock, 2016; Eppes et al., 2016; Lamp et al., 2017). Collins and Stock (2016) investigated controls on rockfall occurrence in the granitic slopes of Yosemite (USA) and found that stress fluctuations as a function of thermal expansion and contraction of a sheeting joint (i.e. macro-scale fracture) resulted in the transfer of thermal energy to mechanical energy at the joint crack tips. This thermal cyclical and cumulative weathering drives fracture propagation (Collins and Stock, 2016). This occurs firstly at the micro-crack scale, but over time as the density of micro-cracks increases, weakening the rock, at which point they intersect, coalesce, and ultimately lead to unstable runaway macro-fracture propagation and final failure (Cruden, 1974).

2.4.3 Stages of fracture propagation

Analysis of stress-strain data obtained from laboratory experiments reveals that fracture propagation is characterised by several distinct phases, each related to a critical level of stress and strain (Bieniawski, 1967; Brace et al., 1966; Eberhardt et al., 1998; Lajtai and Lajtai, 1974; Martin and Chandler, 1994). Firstly, crack closure occurs as a compressive load is applied (Figure 2.4). As this load increases, linear elastic deformation occurs, until micro-cracks begin to initiate and grow. This crack growth is stable, meaning if the load is removed, crack growth will stop (Bieniawski, 1967). As these cracks grow they tend to follow the local maximum stress trajectory, which may be different from the external applied major principal stress, as a function of energy required for propagation. Nearby micro-cracks and flaws may modify the local stress-field influencing crack propagation pathways (Kranz, 1983).

As micro-crack density increases and cracks start to coalesce, this damage becomes more localised within a sample (Figure 2.4) (Diederichs, 2003; Kranz, 1983). This localisation of damage is important for the formation of a fully persistent macro-scale fracture (Main, 2000). This coalescence may also mark the transition towards unstable propagation, where continued growth is independent of external load (Eberhardt et al., 1998). This accelerating unstable propagation occurs until peak strength and the development of a macro-scale fracture results in final failure. The formation of a macro-scale fracture involves micro-fracturing in front of the propagating macro-crack tip front, allowing the mechanisms which drive micro-crack damage to be upscaled to understand processes of macro-scale damage accumulation.

However, the influence of weathering on this stress-strain behaviour is little quantified, though has been shown to alter failure behaviour (Basu et al., 2009; Gupta and Seshagiri Rao, 2000). Cyclical loading tests, where fluctuations in stress can act as a proxy for environmental cyclical stresses, display a more diffuse and distributed pattern of micro-cracking, influencing the development of the macro-scale fracture required for ultimate failure (Cerfontaine and Collin, 2017). Detailed geotechnical characterisation is therefore

required to understand how weathering influences the mechanical stages of fracture propagation.

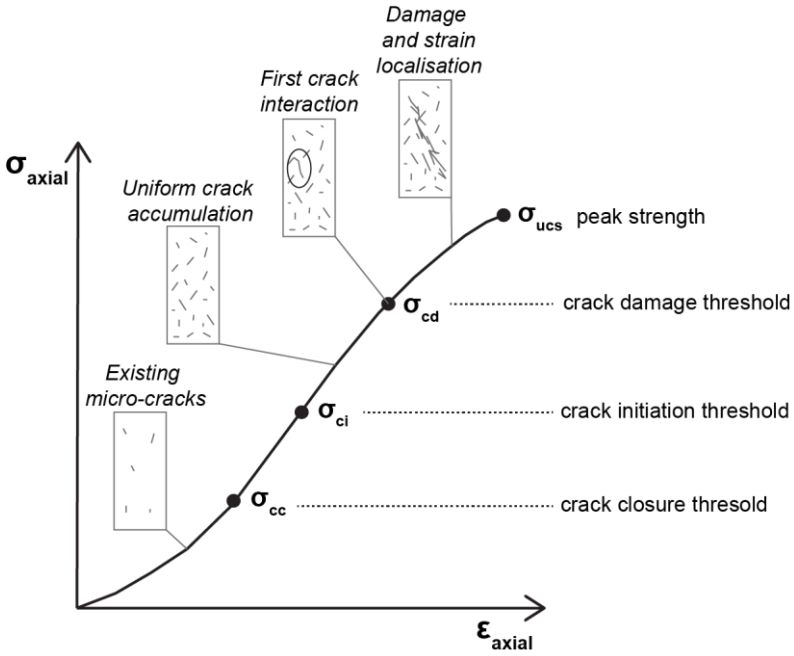

Figure 2.4: Stress-strain curve showing the stages of crack development, with the accumulation and distribution of micro-cracks within a laboratory sample displayed in the box schematics (adapted from Diederichs, 2003; Eberhardt et al., 1998).

2.4.4 Pre-failure deformation

As the failure surface propagates, the stress within the intact rock increases resulting in further fracture propagation with this feedback leading to an acceleration towards failure (Main et al., 1993). This hyperbolic acceleration towards failure has been observed within landslide monitoring studies, where deformation of the surface of the landslide occurs before final failure, and as such forms a possible forecasting tool for failure (Saito, 1965; Voight, 1989).

Conceptually, the development of a macro-scale failure plane that allows complete detachment of a failure mass is characterised by three distinct phases of deformation (Figure 2.5) (Main, 2000; Petley et al., 2005; Varnes, 1978). Firstly, a primary phase

where the failure plane initiates at the micro-crack scale characterised by an initial acceleration in creep as micro-cracks form. Secondly, as the density of micro-cracks increases and they coalesce to form a larger localised failure plane. This stage is characterised by slow constant velocity of creep through time. Finally, a critical threshold of micro-cracks is reached within the rock whereby the feedback between increased stress and further micro-crack growth exists resulting in 'run-away' or unstable fracture propagation and failure (Main, 2000).

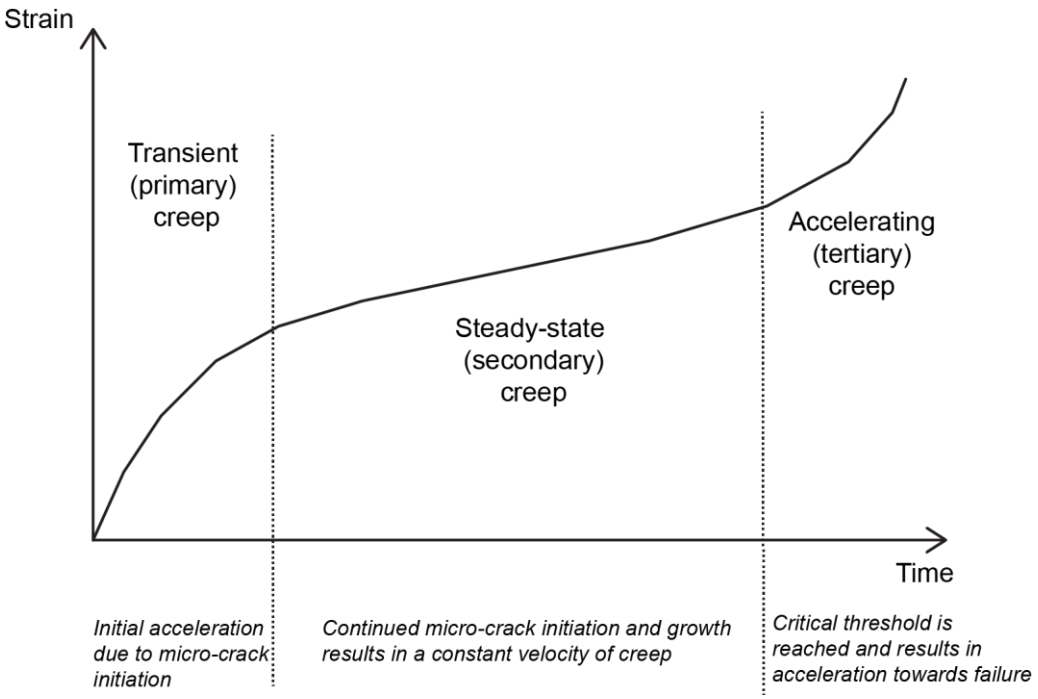

Figure 2.5: Stages of creep observed within laboratory samples and slope failures, with each stage characterised by its relationship of time-dependent strain accumulation (modified from Main, 2000).

Understanding how a fracture propagates within an incipient rock block, resulting in detachment of the rockfall aids in the interpretation of often ambiguous deformation behaviour before failure, which does not necessarily adhere to the simplified conceptual model. Monitored pre-failure deformation of rockfalls clearly show step-like displacement behaviour (Figure 2.6), which has been suggested to be the result of a rock bridge

fracture along the incipient failure plane (Carlà et al., 2017; Kromer et al., 2015; Royan et al., 2015).

Therefore, in order to understand the patterns of pre-failure deformation, an understanding of how weathering induced strength degradation influences the development of a macro-scale fracture necessary for the breakage of rock bridge is needed. This requires a combined knowledge of rock bridge location within a slope, and geotechnical characterisation of the stress-strain behaviour of the rock properties of the rock bridge.

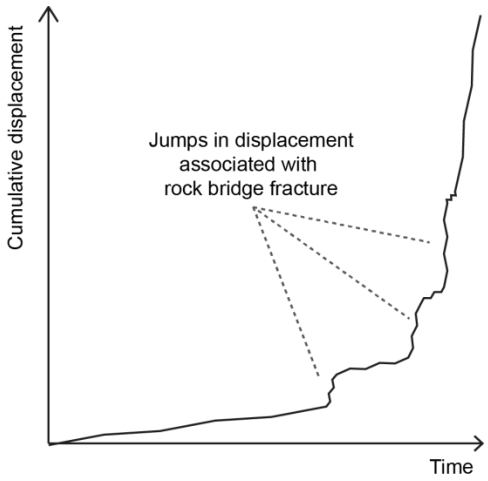

Figure 2.6: Schematic of cumulative displacement observed for failure of brittle slope failures and rockfalls.Steps or jumps in the cumulative displacement may be related to rock bridge fracture events (Carlà et al., 2017; Kromer et al., 2015; Royan et al., 2015).

This time-dependent damage accumulation is also evident in rates of rockfall activity, with Rosser et al., (2007) outlining a conceptual model of damage and strain accumulation through time, which results in a substantial final rockfall failure (Figure 2.7). Within this model, relatively small rockfalls occur continuously as a function of background weathering and surficial material shedding, often in response to environmental forcing events. These precursory rockfalls result in strain redistribution, which drives fracture propagation and further strain accumulation within the slope. They

often occur around the periphery of the eventual larger failure, indicating that incipient larger failure is potentially accommodating a portion of the redistributed stress and strain. Once a critical threshold of strain accumulation has been reached and crossed, controls on further damage accumulation are driven by the internal mechanisms of stress distribution rather than external forcing events. This results in a similar pattern of acceleration as observed for both laboratory and landslide observations. This may also explain the low correlation between environmental conditions and rockfall failure, by introducing a 'lag' effect between an external forcing event which may cross the critical strain threshold but requires further strain accumulation before final failure can occur (Rosser et al., 2007). Damage accumulation at rock bridges is therefore not only a key control on individual failures but influences the temporal patterns of rockfall across a slope.

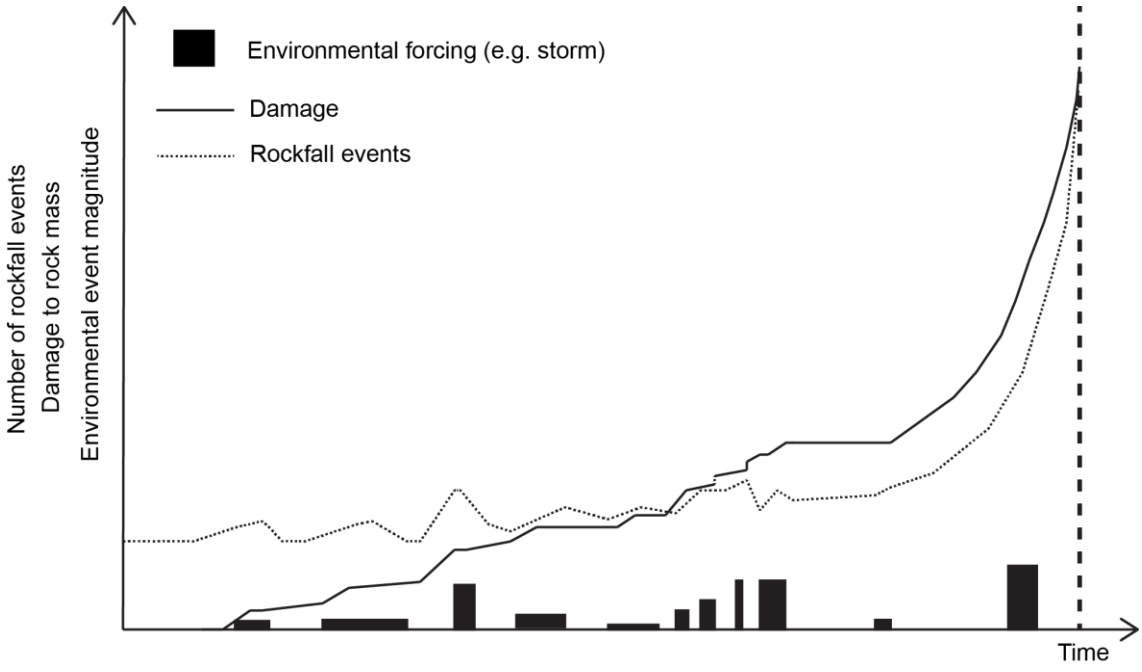

Figure 2.7: Schematic of damage accumulation within a rock mass via background weathering process, environmental forcing events and precursory relatively smaller rockfall activity, which results in a larger slope failure (modified from Rosser et al., 2007).

2.5 The interaction of stress and weathering

Within both laboratory studies and field observations, understanding the critical levels of stress and strain required for unstable micro- and macro- fracture propagation, and the run-away acceleration towards failure, is important in order to understand time and nature of final failure. It may also be important to determine the levels of stress and strain required for fracture initiation. Brain et al., (2014) showed that ground motions in a coastal cliff, considered as representative of marine loading, were only of a sufficient magnitude to result in micro-crack propagation in a very narrow zone of the cliff surface under both high gravitational stress and higher magnitude storm events (illustrated in Figure 2.8).

The confining stress within a rock mass has also been suggested to influence rates of sub-critical cracking, though the exact mechanisms that drive this are unclear (Atkinson, 1984; Eppes and Keanini, 2017). As such, the pattern of micro-crack generation and propagation may not only be controlled by the presence of existing micro-cracks and the magnitude of the loading, but also the stress distribution within and across the slope (Brain et al., 2014). This holds implications for where weathering induced strength degradation is effective in promoting failure.

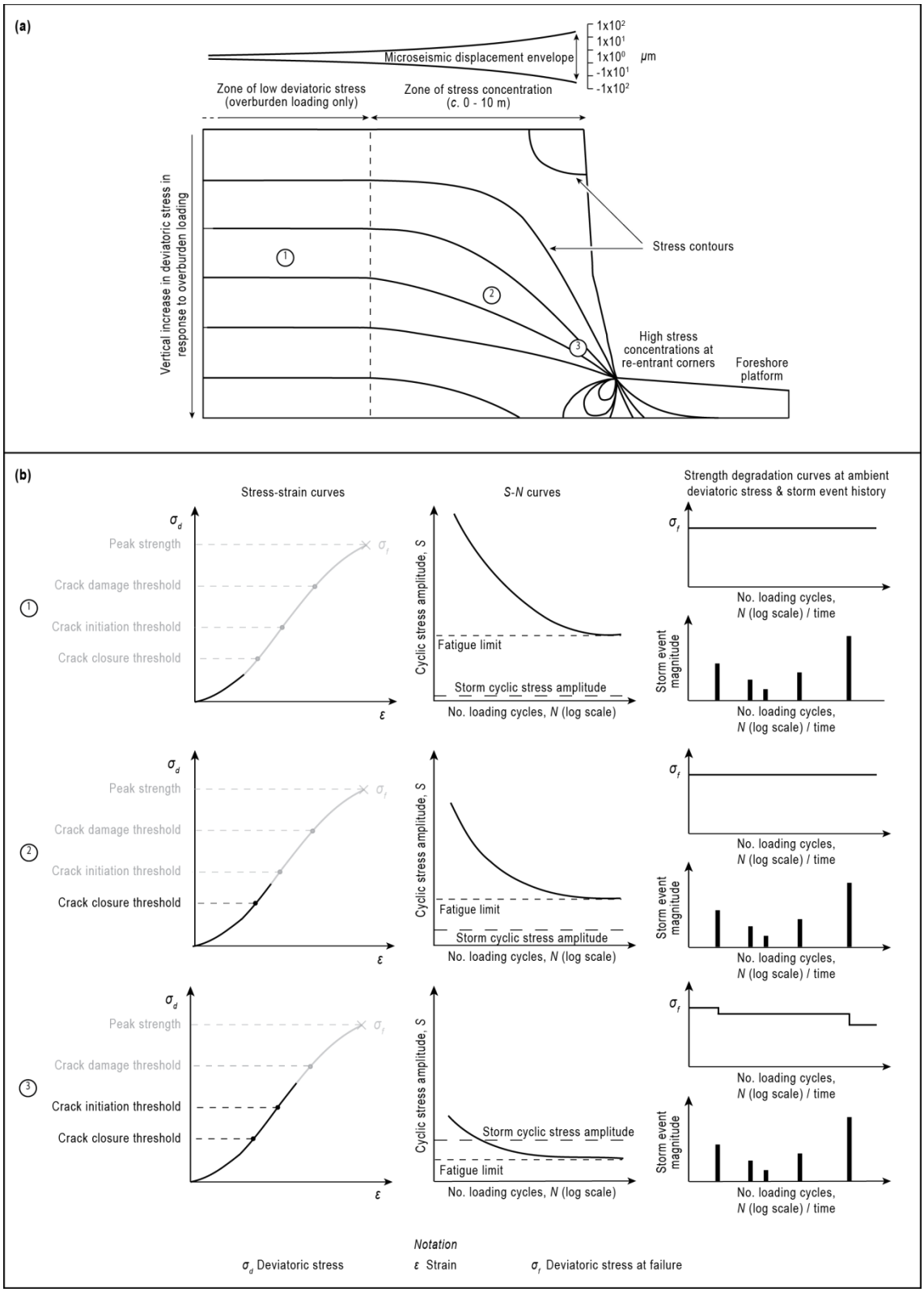

Figure 2.8: Conceptual model of the distribution of rock mass damage as a result of topography and environmental loading conditions. A) An idealised cliff model displaying three stress zones. B) The graphs display the stress-strain curves of each stress zone, indicating their stress state, as well as conceptual S-N and strength degradation curves (Brain et al., 2014).

2.5.1 Conventional view of stresses in rock slopes

The role of gravitational stress is an often-overlooked component within weathering but is one which can potentially play an important role in rock breakdown due to crack generation at various scales. Gerber and Schiedegger (1969) term this endogenic weathering. The traditional view of the role of stress in weathering is that higher stress concentrations result in greater weathering efficacy (Gerber et al., 1973; e.g. Gerber and Schiedegger, 1969; Krautblatter and Dikau, 2007; Miller and Dunne, 1996), and micro- and macro- crack propagation in general (Leith et al., 2014a; Molnar, 2004). These studies hypothesise that the greatest weathering occurs at the base of the slope where stress due to gravitational loading and confining pressure is highest. Large rock slopes have been shown to generate sufficient compressive stresses to drive exfoliation joint formation as the stresses are greater than the resisting tensile strength of the rock (Bahat et al., 1999; Martel, 2017; Stock et al., 2012).

This process represents a first-order control on the weathering processes, and it has been suggested that this may form a positive feedback enhancing other mechanisms of weathering (Selby, 1993). However, smaller slopes may not be massive enough to generate compressive stresses sufficient to drive macro-fracturing (Martel, 2017), but importantly, even here the stress regime may still influence the initiation and propagation of micro-cracks (Brain et al., 2014). An idealised slope can be separated into three stress zones: (1) overburden loading only; (2) increasing stress concentrations near the slope surface; and, (3) stress concentrations at re-entrant corners at the base of a slope (Figure 2.8). In Zone 1 and 2, overburden loading does not cross the crack closure or initiation threshold, and as such the fatigue limit is much greater than the storm cyclic stress amplitude inhibiting the generation of micro-cracks. In Zone 3, the increased stress allows the crack initiation threshold to be passed, lowering the fatigue limit, and resulting in the accumulation of damage in the rock as indicated by the strength degradation curves in Figure 2.8 (Brain et al., 2014).

Areas of high stress may display more rapid weathering, and the time required for failure to occur will in turn be reduced. This is shown in Figure 2.9, which illustrates a modified version of the model proposed by Gunzburger et al., (2005), where 'Enhanced Weathering' achieves final failure more rapidly.

2.5.2 Alternative view of stresses in rock slopes

Recent analogue experiments have suggested a more complex pattern of stress control on weathering and erosion (Bruthans et al., 2014; Zhang et al., 2015). Bruthans et al., (2014) experiments and numerical modelling of sandstone landforms showed that in areas of high stress concentration, grains in a granular material had a greater interlocking strength and were therefore more resistant to erosion which they equate to weathering. Their models of sandstone arches eroded until a critical threshold was reached: When the cross-sectional area of a pillar became small enough and the resultant increased stress concentration was sufficient to allow the frictional strength to resist erosion the model stabilised. Their models displayed a lower stress field around surface protrusions and the areas surrounding discontinuities, which were eroded more rapidly than areas of high stress. This was confirmed via field observations and numerical modelling of sandstone landforms in Petra, Jordan (Rihosek et al., 2016).

Zhang et al., (2015) investigated the properties of soft rock-fill material placed under a compressive load and subjected to weathering, and found that increasing the compressive load resulted in greater frictional strength of material. In this scenario, a modified version of Gunzburger et al (2005) would display a shallower rate of change in resisting strength akin to a – 'Stress Dampening' effect (Figure 2.9). The role of stress in intensifying weathering may ultimately be dependent on the respective in situ orientation of the stress, environmental loading of crack tips (influences stress distribution at the crack tip), and the anisotropic characteristics of the rock (Brain et al., 2014)

This thesis assesses the influence of gravitationally induced ambient stress on weathering induced strength degradation via a series of novel experimental set-ups. Detailed geotechnical characterisation of strength allows an assessment of whether

gravitationally induced ambient stress results in enhanced weathering, dampened weathering or has no effect on weathering rate. This provides spatial controls on the efficacy of weathering, strength degradation and associated susceptibility to rock failure.

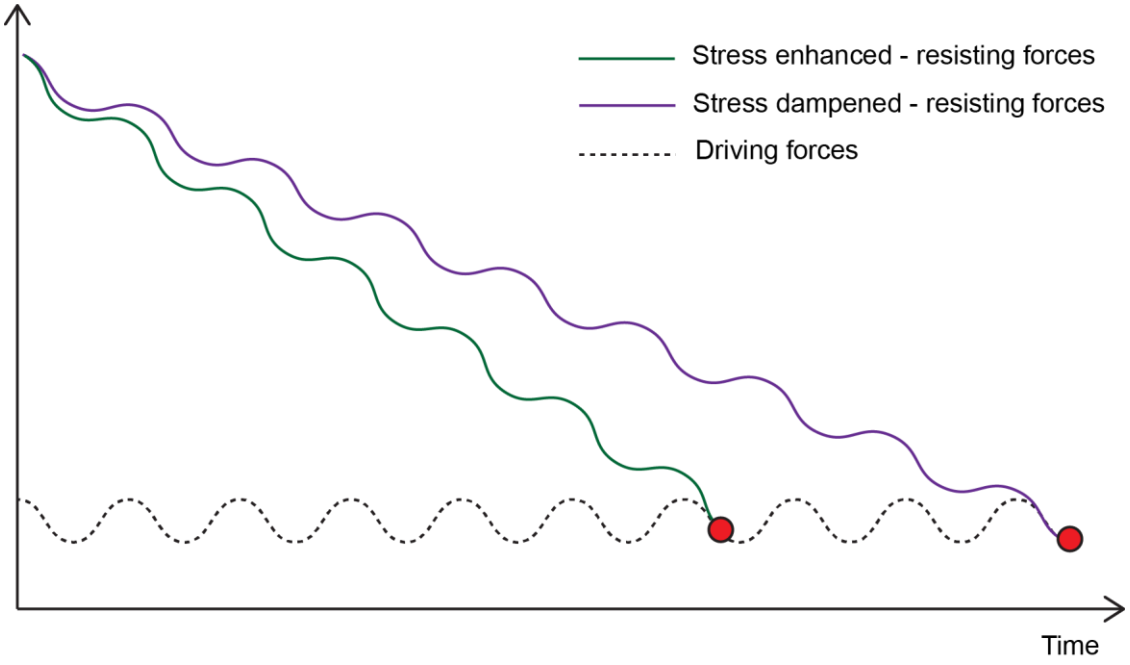

Figure 2.9: A modified version of Gunzburger et al., (2005) displaying the role of stress in controlling the temporal nature of rock failure. The initial temporal stages are similar for each line. The red dots represent where ultimate failure is reached.

2.5.3 The importance of topography

In both scenarios described above, the topography of the rock slope controls the stress regime within the slope. Therefore, understanding how the variations in topography at the scale of individual rockfall failures influence the distribution of stress across a slope; and its resultant impact on weathering effectiveness and rockfall occurrence is important. This includes the micro-topography (at scales of 10 m² to 1 m²) of a slope surface, such as overhangs, concavities or arches, which may act to concentrate and distribute stress locally (Figure 2.10). Areas of greater local curvature can generate larger tensile stresses and drive fracture propagation (Stock et al., 2012), with notches at the base of overhangs forming the locus for failure surface propagation (Kogure et al., 2006; Muller and Martel,

2000; Young and Ashford, 2008). Increased rockfall activity has also been observed for the periphery of overhangs and other protruding features (Rosser et al., 2007), which may be a manifestation of this phenomenon.

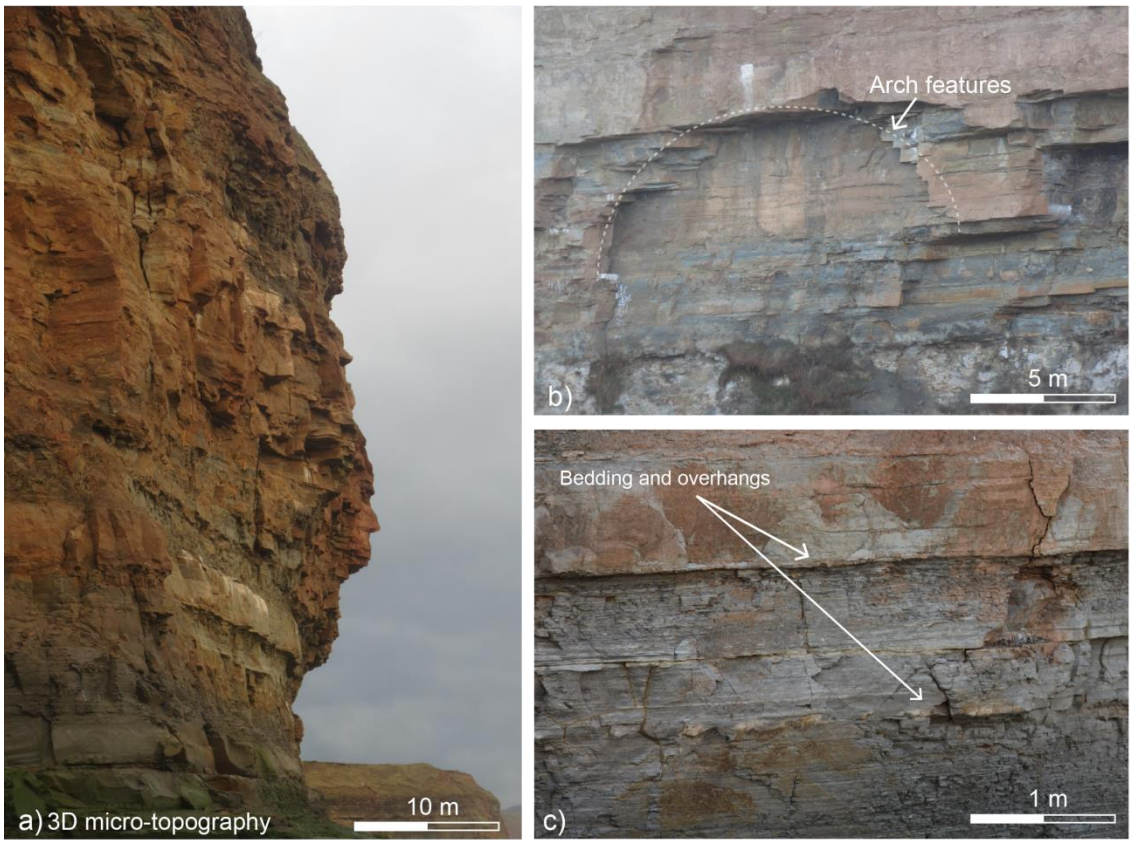

Figure 2.10: Examples of the variable morphology observed at different spatial resolutions along the coastal cliffs between Staithes and Boulby, North Yorkshire, UK. a) Profile view of the cliff face displaying the complexity in micro-topography. b) Arch features are present throughout the cliff face. c) Overhanging blocks associated with bedding and differential lithologies (Author's own photos, 2015).

However, most models that consider the topographic stress field only consider landform-scale features in planform, such as valleys and ridges (Liu and Zoback, 1992; Molnar, 2004; Savage et al., 1994; Slim et al., 2014; St Clair et al., 2015) and deep seated gravitational deformations (e.g. Bachmann et al., 2006; Kinakin and Stead, 2005; Radbruch-Hall et al., 1976), using a simplified 2D topography. Smaller scale studies of vertical cliff slopes also use simple two dimensional profiles which lend themselves to

numerical modelling (e.g. Savage, 1993; Wolters and Müller, 2008), but do not model micro-topography created by overhangs and concavities.

Additionally, within the interior of the rock mass, rock bridges represent areas of high stress concentration, and so may be areas subjected to more effective weathering due to more favourable conditions for micro-crack generation or may represent areas of greater stability. The stresses required for fracture propagation through rock bridges have been modelled (Eberhardt et al., 2004a; Kemeny, 2005, 2003; Scavia, 1995), but the combined effects of rock bridges and topography on stress distribution across a slope, and its resultant impact on rockfall activity are little investigated and unknown.

Exploratory numerical modelling is undertaken within the thesis to determine the combined effect of rock bridges and topography on the stress distribution and strain behaviour of a slope and assess if the resulting stress and strain patterns control the spatial location of rockfalls. This allows a whole slope assessment of the potential controls on damage accumulation and rockfall occurrence.

2.6 Study site: Boulby, North Yorkshire Coast, UK.

The coastal cliffs of North Yorkshire, specifically a two-kilometre section between Staithes and Boulby, provide a natural laboratory for understanding the interactions of rock mass structure, stress and weathering in controlling rockfall behaviour (Figure 2.11). This is due to frequent rockfall activity, variable morphology and lithology of the cliffs, and the coastal setting, which will be explored further within this section.

Figure 2.11: Study site location map, with the cliffs at Boulby forming the main study area, though the observations of rockfalls recorded between Staithes and Boulby are used to interpret style and characteristics of failure.

2.6.1 Rockfall activity

Rockfalls are a dominant mode of erosion and drive coastline retreat (Lim et al., 2010; Rosser et al., 2013). Significant erosion has been quantified over monthly time-scales (Barlow et al., 2012; Lim et al., 2010), providing a sufficient number and range in sizes of rockfall events from which to characterise dominant failure behaviour. Additionally, much research has been undertaken along this coastline (see: Barlow et al., 2012; Brain et al., 2014; Lim et al., 2011, 2010, 2005; Norman et al., 2013; Rosser et al., 2007, 2013; Vann Jones et al., 2015), providing insights into broader-scaler rockfall processes. Some of these observations are particularly pertinent to this study, and include, but are not limited to:

- Rockfalls occur as a time-dependent process, whereby failures propagate up cliff or laterally within lithologies following a process of stress redistribution across the cliff surface (Rosser et al., 2013).

- Failure propagation is moderated by the cliff lithologies (Barlow et al., 2012; Rosser et al., 2013), and certain cliff surface features, such as overhangs and concavities, display greater concentrations of rockfall activity (Rosser et al., 2007).
- Areas of high stress concentration may theoretically be more susceptible to strength degradation (Brain et al., 2014)
- Rock mass structure associated with the different lithologies controls failure volume and shape (Rosser et al., 2013).
- There is limited correlation between regional environmental conditions and rockfall triggers, especially for larger rockfalls (Lim et al., 2010; Rosser et al., 2007).

2.6.2 Geology

The cliffs between Staithes and Boulby comprise a lower shale unit, an upper shale unit, and an interbedded siltstone and sandstone unit capped by a glacial till (Figure 2.12), which are part of the Lower Jurassic Redcar Mudstone and Staithes Sandstone formations (Rawson and Wright, 2000). All units display a bedding dip of 2° to the south-east, which is broadly orthogonal to the northern aspect of the cliff face. The lower shale unit is dark blue-grey, slightly weathered with some algal cover, and is moderately strong to strong (classification based on ISRM, 2015). The upper shale unit is also dark blue-grey, slightly weathered, and is moderately strong to strong. The distinction between the two units is due to subtle differences in rock mass structure. Both units are indistinctly bedded with iron-stone bands throughout, and a widely spaced joint pattern (classification based on ISRM, 2015). However, the upper shale unit displays a greater variance in the spacing of joints than the lower shale unit. The light blue-grey interbedded siltstones and sandstones comprise gradational beds of silt and sand, which can be up to 3 m in thickness. The unit is slightly weathered and moderately strong to strong It displays a widely spaced (~ 2 m) ‘blocky’ joint pattern with narrow to widely dilated joints.

Variations in rock mass structure between the three units, allows the role of structure to be evaluated in determining rockfall failure mechanisms. The response to weathering between the units may also differ due to variations in the composition and fabric of the lithologies (Duperret et al., 2005; Hall et al., 2012). The interactions of all three components (structure, stress and weathering) may influence the temporal and spatial behaviour of rock weakening, and inevitably rockfall occurrence.

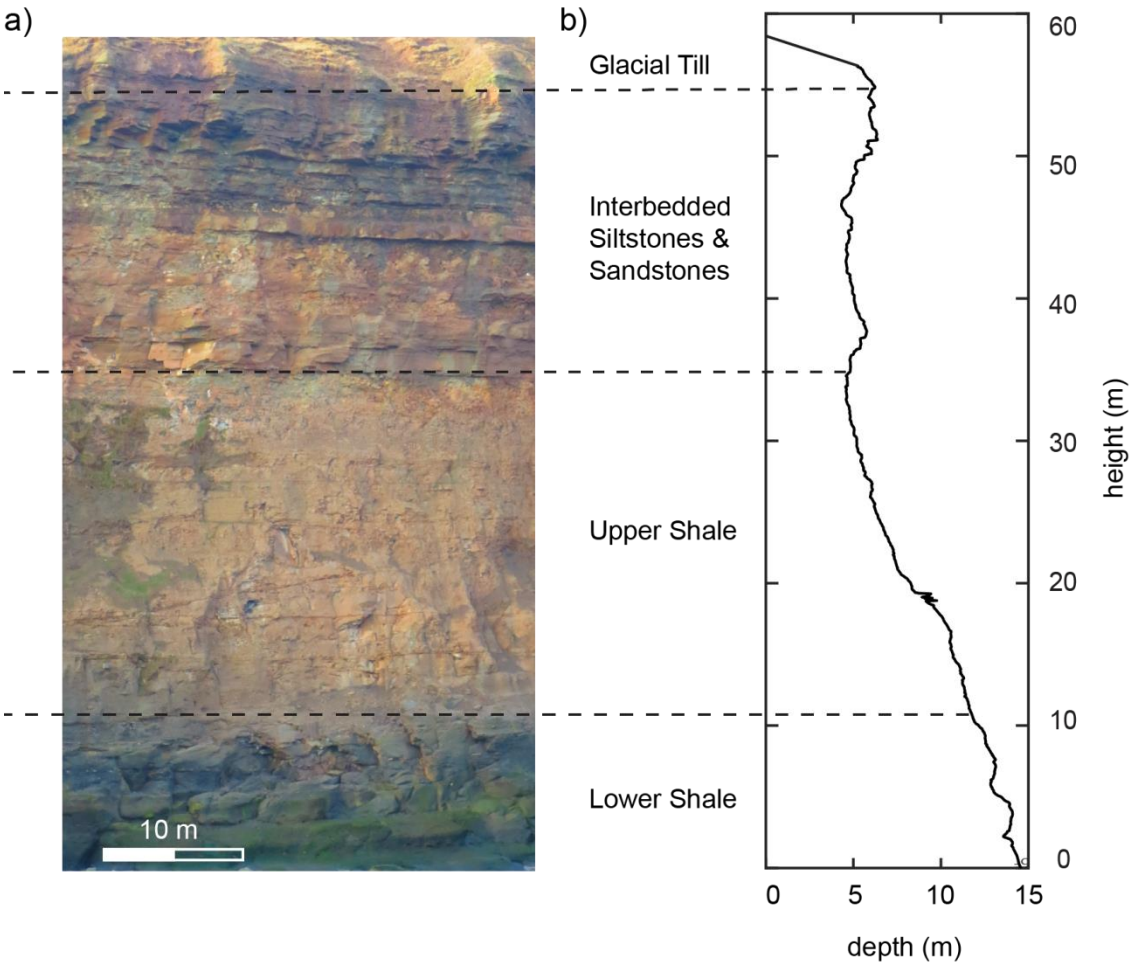

Figure 2.12:Lithological profiles a) Example photograph of lithological units (Author's own photo, February, 2015) and b) Typical lithological profile of the cliff between Staithes and Boulby (obtained via terrestrial laser scanning)

2.6.3 Morphology

The cliffs are near-vertical, up to 60 m high, and are fronted by a wide, gently dipping (2°) shore platform, which extends up to 300 m seawards at low tide. The cliffs show a

wide variation in morphology (Figure 2.10). Features, such as overhangs, concavities and arches, concentrate stress within the slope near-surface, which may determine areas of the slope more susceptible to rock strength degradation (Brain et al., 2014; Bruthans et al., 2016, 2014; Rihosek et al., 2016). The variety in micro-topography allows the coincidence between the topography, resulting stress concentrations and rockfalls to be assessed. From this, this thesis aims to establish broader patterns and topographical based rules on controls on rockfall occurrence.

2.6.4 Environmental setting

The cliffs are located in a storm-dominated environment, subject to northerly and easterly storm events. They experience a macro-tidal range of c. 6 m, with > 3 m inundation of the cliff toe during spring tide conditions, and exposure of the foreshore platform during low tide. Temperature data recorded by the Loftus Meteorological Office weather station for 2016, located 3 km to north and inland of the study site, displays a minimum daily mean temperature of -1.99°C experienced in January, with a maximum daily mean of 21.02°C experienced in September. Snowfall can occur, but rarely settles at the coast, with insolation often reduced in winter months to approximately 1 sunlight hour per day due to low cloud and fog (Lim et al., 2010). The climate is generally drier than the west of the UK, with mean annual precipitation of 567 mm, with hourly rainfall intensities of up to 79.1 mm $^{-hr}$ recorded (Rosser et al., 2007).

This coastal setting is a dynamic high energy weathering environment (Mottershead, 2013). The combination of a maritime setting and a temperate climate result in a suite of potential weathering processes occurring at the coast. These processes are often categorised into physical, chemical or biological mechanisms (Mottershead, 2013, Viles, 2013, Yatsu, 1988). Physical processes can include wetting & drying, insolation, freeze-thaw and salt weathering. The presence of, and fluctuations in, ground/sea water within the cliff near surface can result in chemical weathering processes such as hydration, hydrolysis, dissolution and oxidation (Yatsu, 1988). Finally, algae and microbiological

processes act as biological weathering agents (Naylor et al., 2012, Yatsu, 1988). These weathering processes often act synergistically, enhancing the intensity of weathering (Viles, 2013).

Within the context of the coastal environment of Boulby, salt weathering and wetting and drying are likely to act in conjunction due to tidal cycles and storm conditions. Daily insolation cycles may also cause an important thermal weathering process, with freeze-thaw only occurring for a short duration each winter due to the relatively warmer coastal temperatures. Algae growth at the toe of the cliff at Boulby suggests biological weathering. The nature and intensity of these weathering processes may vary with cliff elevation and profile, due to tidal and storm inundation heights. (Mottershead, 2013). Advantageously, for this study the coastal setting likely permits higher rates of strength change to be recorded over time than compared to non-coastal slopes (Mottershead, 2013).

2.7 Summary

This literature review provides an overview of the fundamental principles which underpin our current understanding of damage accumulation within a rock mass, the mechanisms of rockfall failure, and the potential control of stress on weathering efficacy. On the basis of the literature presented, the following research questions are identified:

- Where within a rock mass is damage accumulation important?

As rockfalls often lack discernible triggers, weakening over time (i.e. damage accumulation) must have occurred to enable failure. Whilst many studies have observed in field or laboratory observations (e.g. Collins and Stock, 2016; Eppes et al., 2016) or via numerical modelling (e.g. Kemeny, 2005) weathering induced strength degradation over time, there is limited understanding of where in a rock slope such strength degradation is crucial in driving the detachment of rockfall. Understanding where this damage accumulation is important requires an assessment of the location of rock bridges

within a slope, which control rockfall release. This is addressed via Research Objective 1.

- What are the controls on damage accumulation within these zones?

As recent research has indicated (Brain et al., 2014; Bruthans et al., 2014), gravitationally induced ambient stress may control the efficiency of damage accumulation, and therefore the timing of failure. This also creates a variation in the spatial intensity of weathering within a slope. This variation creates areas which may be weaker than the surrounding rock mass, and therefore may fail preferentially dictating the spatial pattern of rockfalls (Rosser et al., 2013). Understanding firstly the distribution of stress within a slope, and secondly, the impact of stress on weathering will allow an evaluation of the spatial controls on damage accumulation. This is addressed via Research Objective 2 and 3.

- What is the impact of damage accumulation on the mechanisms of rockfall failure?

The influence of weathering on slope stability has often only been considered for broader whole slope susceptibility to failure and collapse rather than the influence on the mechanisms and timing of individual shallow and smaller rockfall detachments. However, a correct understanding of when and how a rockfall might fail is crucial for the interpretation of pre-failure deformation and establishment of early warning thresholds (Kromer et al., 2017; Petley et al., 2005; Rowe et al., 2017; Royán et al., 2014). This is addressed via Research Objective 4, which brings together the findings of Research Objectives 1, 2 and 3.

3 Forensic analysis of rockfall scars

3.1 Abstract:

We characterise and analyse the detachment (scar) surfaces of rockfalls to understand the mechanisms that underpin their failure. Rockfall scars are variously weathered and comprised of both discontinuity release surfaces and surfaces indicative of fracturing through zones of previously intact rock, known as rock bridges. The presence of rock bridges and pre-existing discontinuities is challenging to quantify due to the difficulty in determining discontinuity persistence below the surface of a rock slope. Rock bridges form an important control in holding blocks onto rock slopes, with their frequency, extent and location commonly modelled from the surface exposure of daylighting discontinuities. We explore an alternative approach to assessing their role, by characterising failure scars. We analysed a database of multiple rockfall scar surfaces detailing the areal extent, shape, and location of broken rock bridges and weathered surfaces. Terrestrial laser scanning and gigapixel imagery were combined to record the detailed texture and surface morphology. From this, scar surfaces were mapped via automated classification based on RGB pixel values.

Our analysis of the resulting data from scars on the North Yorkshire coast (UK) indicates a wide variation in both weathering and rock bridge properties, controlled by lithology and associated rock mass structure. Importantly, the proportion of rock bridges in a rockfall failure surface does not increase with failure size. Rather larger failures display fracturing through multiple rock bridges, and in contrast smaller failures fracture occurs only through a single critical rock bridge. This holds implications for how failure mechanism changes with rockfall size and shape. Additionally, the location of rock bridges with respect to the geometry of an incipient rockfall is shown to determine failure mode. Weathering can occur both along discontinuity surfaces and previously broken rock bridges, indicating the sequential stages of progressively detaching rockfall. Our findings have wider implications for hazard assessment where rock slope stability is

dependent on the nature of rock bridges, how this is accounted for in slope stability modelling, and the implications of rock bridges on long-term rock slope evolution.

3.2 Introduction

The scar left behind after a rockfall from a rock face, commonly comprised of exposed joint surfaces separated by zones of broken intact rock termed *rock bridges*, holds significant insights into the conditions prior to failure, and the mechanics of that failure. Despite this, the analysis of failure scars has been largely restricted to detailed post-failure analysis of single, commonly large, rockfall or rockslides, rather than analysis of an inventory of multiple events (e.g. Frayssines and Hantz, 2006; Paronuzzi and Sera, 2009; Sturzenegger and Stead, 2012). To gain insight into the influence of rock structure on stability, failure mechanisms are commonly inferred from the back analysis of stability based upon the wider slopes' rock mass strength (RMS), which is estimated from the combined influence of pre-existing discontinuities, intact rock strength, and the degree of weathering (Barton, 1974; Hoek and Brown, 1997; Jennings, 1970; Selby, 1980). The control of intact rock strength is most significant at rock bridges, as they form the attachment points holding a failing block to the rock mass (Jennings, 1970) (Figure 3.1a). Failure is known to often occur as a complex, time-dependent interaction between shearing along discontinuities and progressive fracturing through rock bridges, termed 'step-path' failure (Brideau et al., 2009; Eberhardt et al., 2004a; Scavia, 1995).

Structural assessment of stability is routinely undertaken through field investigation by direct observation (e.g. Priest, 1993), remote sensing (e.g. Dunning et al., 2009; Sturzenegger and Stead, 2009), geophysical survey (e.g. Clarke and Burbank, 2011), or intrusive ground investigations such as borehole logging. However, characterising the persistence of discontinuities through a potentially unstable rock slope remains challenging. As such, many studies have assumed that discontinuities are fully persistent and the resulting stability analysis employs a purely kinematic analysis of failure (e.g.

Goodman and Shi, 1985; Wyllie and Mah, 2004). Importantly however, rock bridges influence overall slope stability, and experiments with limit equilibrium modelling shows even a single-digit percentage presence of rock bridges as a proportion of total discontinuity length within a slope will substantially increase the overall factor of safety (Frayssines and Hantz, 2009; Jennings, 1970). Field data from previous failures suggests a wide range in a rock bridge prevalence that is inevitably site specific, including very small percentages (0.2% to 45% as reported by: Tuckey and Stead, 2016 and references therein). In addition, prior to failure the slope can become weakened via a complex suite of weathering processes (Viles, 2013a), which alter the mechanical properties of exposed discontinuities, already broken rock bridges and those, which may break in future.

The identification and attributes of significant intact rock bridges is poorly constrained in field studies, due to the difficulty of assessing their presence within the rock mass. Forensic analysis of a rockfall scar provides the most direct assessment of their role within a rockfall event (Figure 3.1b). However, few studies have fully characterised rockfall scars, with many focussed on specific analysis at single sites. This, combined with the wide range of reported rock bridge presence and only limited and disparate assessment of general characteristics between sites, we argue provides insufficient evidence to fully constrain the role of rock bridges in controlling rockfall (e.g. Frayssines and Hantz, 2006; Lévy et al., 2010; Paronuzzi et al., 2016).

A broader assessment, and detailed analysis of both rock bridges and other scar attributes can be used to infer the nature of stresses at the time of failure (e.g. Paronuzzi et al., 2016; Paronuzzi and Sera, 2009), subsequent failure mode (Bonilla-Sierra et al., 2015; Stock et al., 2011), the sequence of rock bridge breakage (Stock et al., 2012), and the prevalence of weathering, and hence relative age of discontinuities and rock bridge breakage. This has important implications for hazard assessment of individual slopes (Fell et al., 2008), and also for how rock strength and structure influence longer-term landform change (Clarke and Burbank, 2010; Koons et al., 2012).

To address this, we present analysis of a rockfall scar database consisting of 657 individual rockfalls, which range in surface area from 0.1 m² to 27 m². Our aim is to characterise rock bridges within individual rockfall scars in this inventory in order to understand how they determine the type, mode and location of failure.

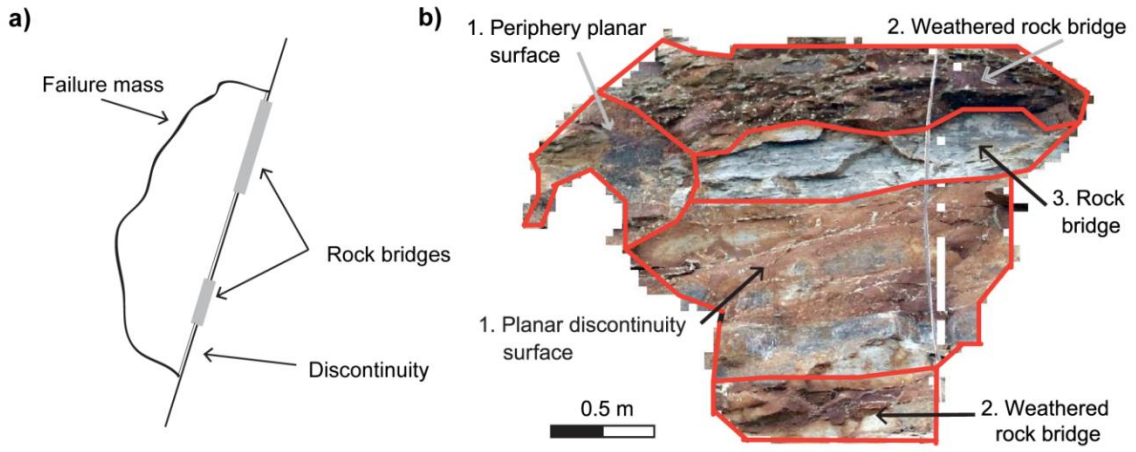

Figure 3.1: Conceptual profile view and example photograph of rockfall scar characteristics. a) Simplified profile view of a rockfall held to a rock slope by rock bridges and a pre-existing yet not fully formed discontinuity. The incipient rockfall requires the rock bridges separating the discontinuities to be broken before failure can occur. b) Example high resolution photograph of a siltstone rockfall scar, from North Yorkshire coastal cliffs, U.K. The scar contains discontinuities of varying persistence, plus three separate broken rock bridges that have been variously weathered, as indicated by the surface colour. Analysis of the age of the features, as indicated by their weathering, suggests the order of failure, with the discontinuity surfaces forming first, before fracturing and weathering of rock bridges, and the final fracture of a freshly exposed rock bridge.

3.3 Study Site

We monitored a 200 m section of near-vertical cliffs at Staithes, North Yorkshire, UK over a 13-month period to document and characterise rockfall activity (Figure 3.2). The rock portion of the cliffs is ~60 m in height and located on a storm-dominated macro-tidal coastal environment. The 200 m survey section contains a lower shale unit (~10 m high, extending from the cliff toe at mean high water level), an upper shale unit (~32 m high) and an interbedded siltstone and sandstone unit (~12 m high), capped by a glacial till

(Figure 3.2c). These form part the of the Lower Jurassic Redcar Mudstone and Staithes Sandstone formations (Rawson and Wright, 2000). All units display a bedding dip of 2° to the south-east, which is broadly orthogonal to the northern aspect of the cliff face, and a complex discontinuity pattern, which varies in orientation and persistence between the interbedded layers in each major rock type. From field mapping, the dark blue-grey lower shale unit is slightly weathered with some surficial algal cover, is moderately strong to strong, and has indistinct bedding with iron-stone bands throughout, as well as a widely spaced joint pattern of varying persistence (classification based on ISRM, 2015). The upper shale unit is similar with a dark blue-grey colouring, slightly weathered, is indistinctly bedded with ironstone bands, and is moderately strong to strong. However, its joint pattern shows a greater variance in spacing. The interbedded siltstones and sandstones are comprised of gradational beds of silt and sand, which can be up to 3 m in thickness, and display a widely spaced (~2 m) 'blocky' joint pattern with narrow to widely dilated joints. It is slightly weathered, is light blue-grey, and moderately strong to strong.

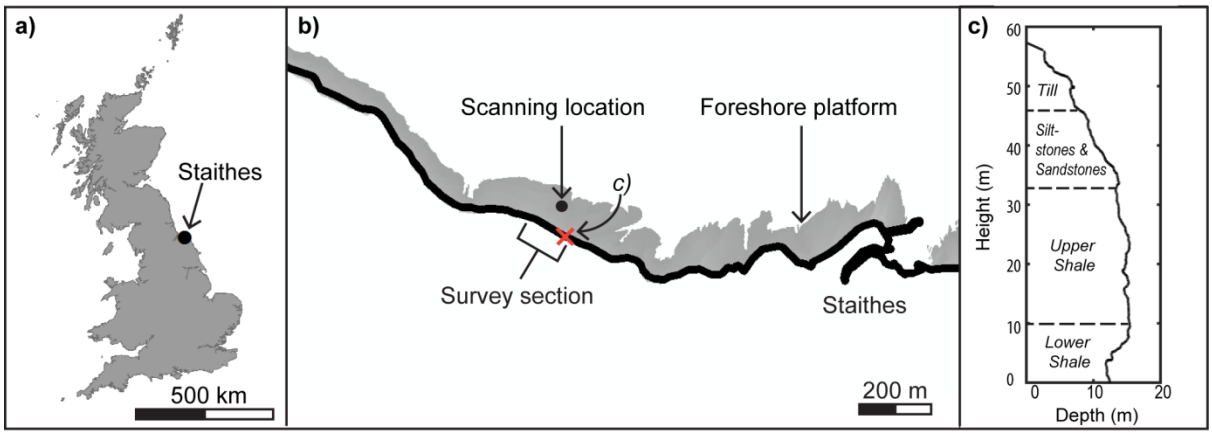

Figure 3.2: Study site location. a) Location of Staithes, North Yorkshire, UK. b) Map view of survey section and scanning location at Staithes. The location of the cliff cross-profile section presented in c)., is indicated by the cross. c) Typical cliff and lithological profile of the survey section.

3.4 Methods

3.4.1 Overview of approach

Understanding the role of rock bridges and weathering in controlling failure behaviour requires complete characterisation of scar surface attributes. Both high resolution imagery and 3D models of the rockfall scars derived from pre- and post-failure topography are required to create and collate the scar database. From this, we undertook detailed analysis of the rockfall scar texture, structure and colour to quantify the properties of broken rock bridges and conversely discontinuities. This involves not only understanding the proportion of each element within an individual failure surface, but also their distribution, orientation and location with respect to the overall rockfall scar. Given the near-vertical cliff face and the typical nature of rockfall on these cliffs (see: Rosser et al., 2013), we assume that blocks delimited by pre-existing discontinuities alone must fall instantly in response to rock bridge failure in an adjacent supporting block and so are indistinguishable from rockfall controlled by rock bridges.

Firstly, we define the areal proportion of rock bridges (*%rb*) and weathered surfaces (*%w*) within each individual rockfall scar as a percentage of the total scar surface area, and proportion of weathered rock bridges (*%wrb*) as a percentage of individual rock bridge area. Respectively, these characteristics control slope stability (Jennings, 1970), indicate the exposure to environmental processes (Viles, 2013a), and places limits on the temporal order of failure (Stock et al., 2011). Secondly, we constrain if fracturing through rock bridges is either uniformly distributed across the rockfall scar or is more locally concentrated. The distribution of rock bridges determines the location, direction and magnitude of stress concentration at each attachment point that supported the rockfall prior to release. Thirdly, we determine the locations of rock bridges with respect to the critical slip path, which influences the stress required for failure along this orientation (Tuckey and Stead, 2016). Fourthly, we analyse the location of a rock bridge within a rockfall scar relative to its centre of mass, which represents the location about which forces act and rotation occurs (Hibbeler, 2010). This places controls on failure mode,

with simple moments indicating if failure was most likely in tension or shear (Bonilla-Sierra et al., 2015; Stock et al., 2011).

3.4.2 Rockfall inventory & descriptors

We collected repeat terrestrial laser scanning (TLS) surveys of a 200 m section of coast on an approximately monthly basis over a 15-month period (June 2015 to September 2016) (Figure 3.2). A Riegl VZ -1000 laser scanner was consistently positioned ~100 m from the cliff toe to collect 3D point clouds with spacing of 0.01 m to 0.02 m. From this, we undertook 2.5D change detection of the sequential cliff surfaces using the approach detailed in Rosser et al. (2005), which assumes that the cliff face can be approximated to a 2D planar surface. Triangular irregular network (TIN) models were created of the pre- and post-failure topography and combined to form a 3D rockfall model, from which we calculated centre of the mass, volume and dimensions, assuming a uniform rock density.

We captured high resolution photography to provide information on surface texture, discoloration due to weathering and context for interpreting the 3D scan data. We collated gigapixel panoramic images of the cliff face on an approximately monthly basis over 13 months (August 2015 to September 2016) from the same foreshore position as the TLS (Figure 3.2). We used a 50 MP Canon EOS 5DS R camera with a 300 mm telephoto lens, in conjunction with a Gigapan Epic Pro mount. The individual photos were stitched into one panoramic image (8,688 by 5,792 pixels), achieving an on-cliff pixel resolution of 0.001 m to 0.002 m (Figure 3.3). We manually adjusted aperture, shutter speed and ISO depending on conditions to capture sharp, high-quality images.

Each panoramic image was overlaid on the DEM collected in the same month. We geo-referenced the image using a spline transformation with at least 200 control points. Rockfall scars were extracted from the Gigapan images using the rockfall locations extent from the change measured using the TLS data comparison. Rockfall scar images

that had undergone distortion or warping of pixels during geo-referencing were manually deleted from the database.

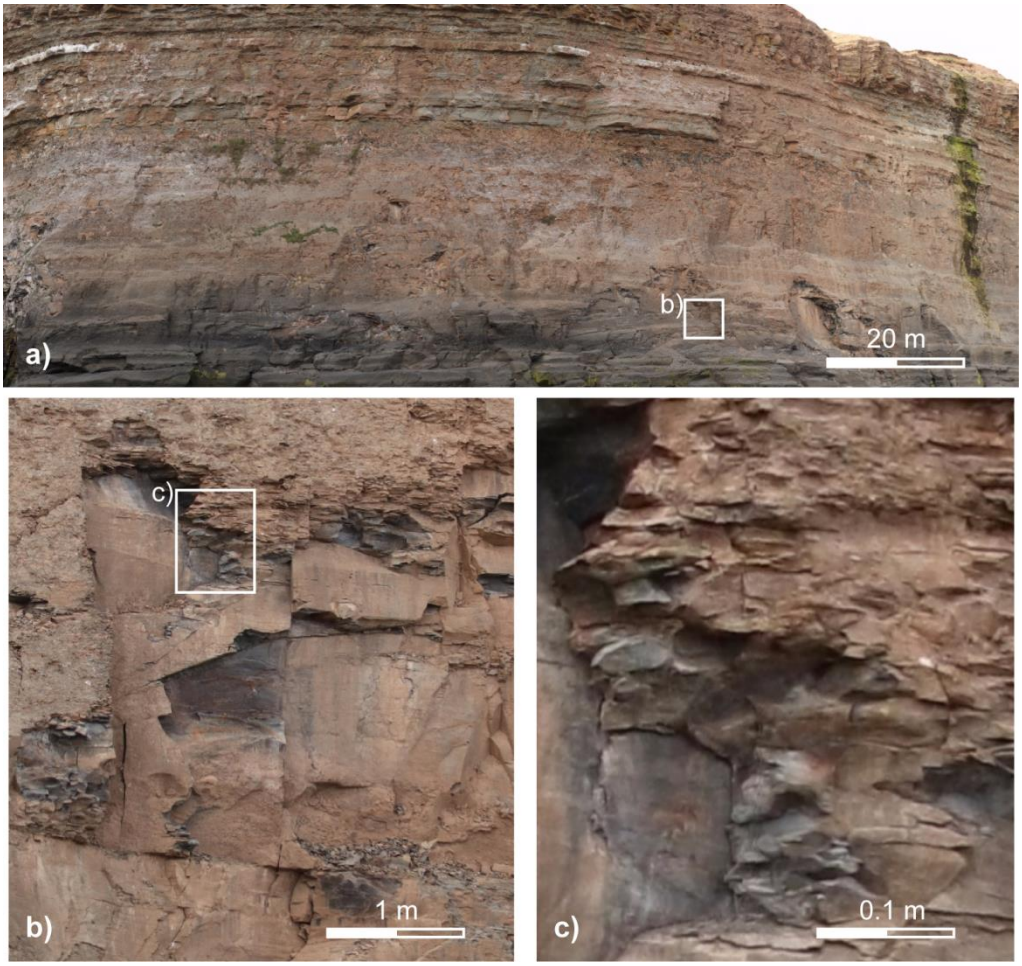

Figure 3.3: Gigapixel imagery of the monitored cliff section. a) Panoramic image. b) Close-up of a rockfall scar. c) Close-up of a freshly broken rock bridge.

3.4.3 Data Processing

Over the survey period we identified a total of 657 rockfall scars with > 0.1 m² surface area. We consider it unlikely that failures smaller than 0.1 m² are controlled to the same degree by the interaction of discontinuity release surfaces and rock bridges due to large discontinuity spacing (> 2 m) and the relatively high strength of the cliff rock as compared to small rockfall volume (mass), and so these were not included in the analysis.

We automated the classification of rockfall scar features to avoid the subjectivity associated with manual classification. This automated process involved a routine to classify areas of fracture through rock bridges within the scar surface imagery. Inspection of the imagery revealed that broken rock bridges in rockfall scars on these cliffs are characterised by rough surfaces with micro-topography comprised of small (cm – scale) planar segments separated by small (10^{-1} - 10^{1} cm) linear edges, as compared to the smooth and planar pre-existing discontinuity surfaces. High numbers of contiguous small segments and edges represent the remnants of failed rock bridges in the scar surface. We also undertook automated colour classification to identify discoloured surfaces indicative of weathering.

3.4.3.1 Edge Detection

To discretize the scar surface into zones of broken rock bridges and pre-existing discontinuities, we developed a method to delimit areas of similar texture within the scar. We employed an automated image classification technique, based upon the RGB values in the high-resolution optical imagery, adapting an approach used for petrographic grain boundary detection, developed by Li et al. (2008). This involves four stages outlined in Figure 3.4, namely: edge detection, noise reduction, vectorisation and density classification. Edges were detected by the contrast of light to dark tones in pixel values, indicative of shadowing created by rough surfaces (Figure 3.4a). To enhance contrast, images were converted to grey-scale and smoothed by obtaining and applying a median pixel value over a specified area to reduce small scale noise (Figure 3.4b). As fractures are likely to have linear features and be continuous within patches, pixel contrasts less than the smoothing area were considered noise. The range in pixel values was calculated over a kernel size of 12 by 12 pixels or 0.018 m by 0.018 m, which retained resolution but remained insensitive to gradual shifts in tone and/or colour due to natural lithological or weathering variations (Figure 3.4c). This kernel highlighted only abrupt changes in pixel values, and as such identified those areas more related to fracturing of

intact rock. As an individual rockfall scar assessment of relative pixel value range, this approach is insensitive to larger scale (e.g. month to month) variations in ambient colour, and lighting. The pixel value range was converted into a binary using Otsu's (1979) thresholding algorithm, allowing classification of the scar surface into zones of 'non-edges' and 'edges' (Figure 3.4d). As this was a relative threshold value set via cluster analysis of grey-scale pixel histogram rather than a pre-determined absolute value – it allowed areas of relatively higher pixel contrast to be separated from areas of relatively lower pixel contrast for each rockfall scar. As a second stage of noise reduction, fracture zones < 0.002 m in length were omitted and those with tips within a 0.01 m area were conjugated to form a continuous single 2D zone feature (Figure 3.4e). Zones of fracture edges were converted into polylines using a centre-line vectorisation, whereby proximal collinear edges within 0.0225 m were merged (Figure 3.4f). The line features allowed densities of fractures to be obtained using a kernel with radius of 0.25 m (Silverman, 1986), which retained detail whilst simplifying small-scale noise (Figure 3.4g). This produced coherent zones, which described low to high edge densities across the rockfall scar surface (Figure 3.5). Areas of higher density indicated fracturing through a broken rock bridge (Figure 3.4h), verified by visual comparison of a subsample of the classified inventory.

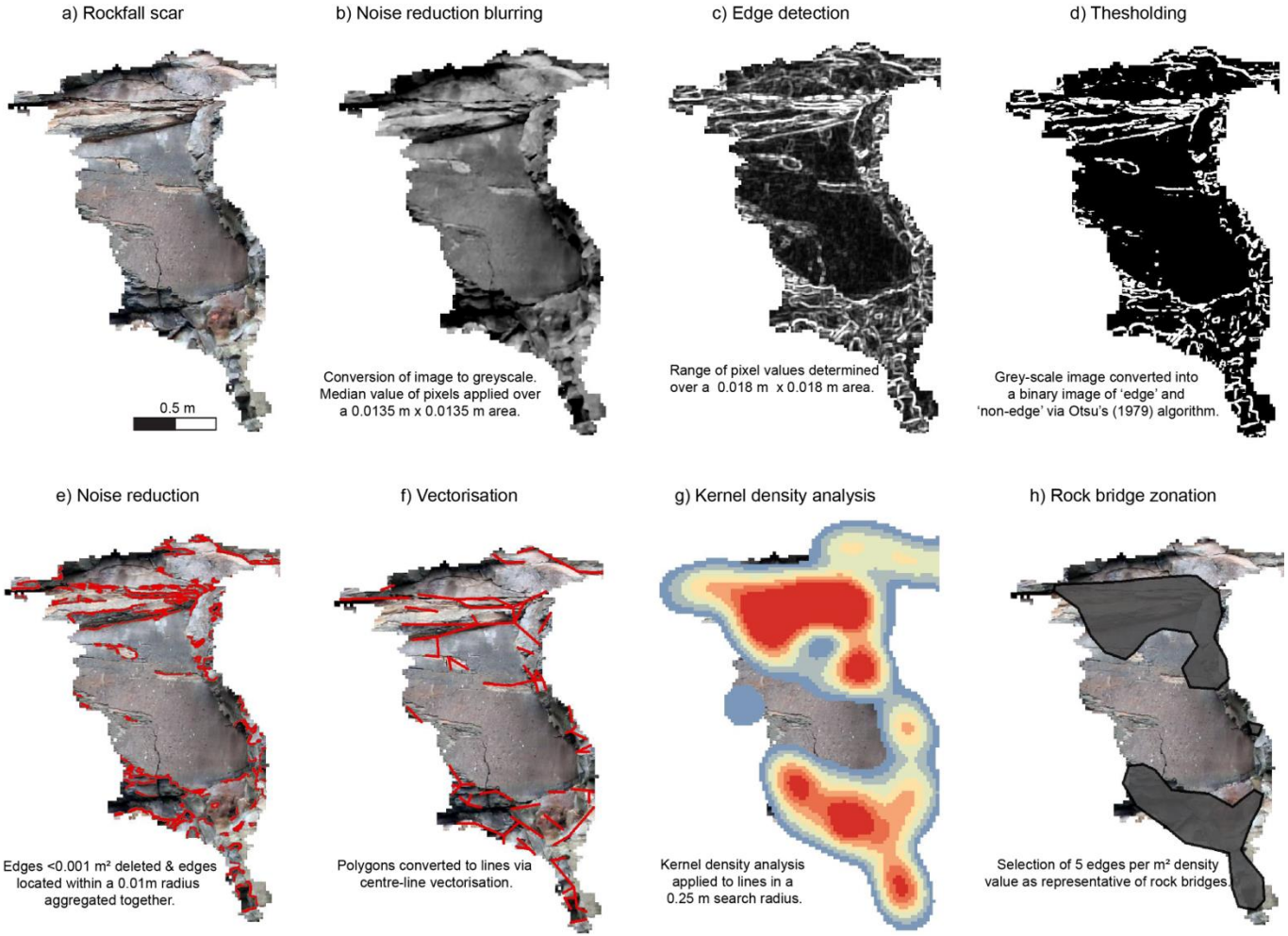

Figure 3.4: Detailed stages of edge detection from the original image (a), through initial noise reduction (b), to edge detection algorithms(c-d), further noise reduction (e), and density analysis of edges (f-h)

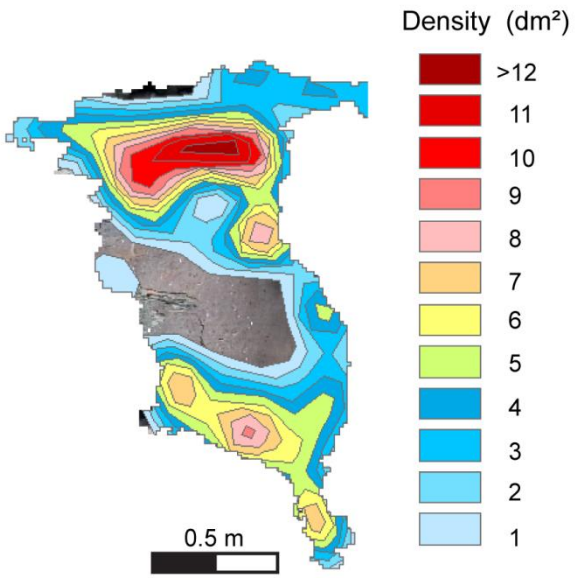

Figure 3.5: Density classes derived from kernel density analysis of edges within rockfall scars. Density increases from 1 edge per m² to ≥12 edges per m² within this rockfall, though densities >15 edges per m² occur within the database. The incremental density value is simplified as *dm².*

3.4.3.2 Rock bridge determination

Based upon the density of features derived using the image classification, a threshold that identifies a 'rock bridge' from other areas is needed. To determine the edge density range over which features are classified as rock bridges we analysed a subset of the rockfall database, which consisted of a random sample of 163 rockfall scars > 0.1 m² recorded between the two monitoring intervals of 25/11/2015 and 26/01/2016. This sub sample contained a wide range of rockfall sizes and respective lithologies. Individual rock bridge areas were derived from incrementally increasing density values between 1 - 15 edges per m² (*dm²*). Mean, median, interquartile range and the number of observations of individual rock bridges (*rb_count)* for each *dm²* value were determined to evaluate the success of the classification (Figure 3.6). The *rb_count* within a scar peaks at density values of five *dm²* before decreasing. At lower *dm²* rock bridges are conjoined, resulting in a lower number of observations, before features become separated into several individual rock bridges when using higher *dm²* (Figure 3.5). Above five *dm²* the numbers

of observations decrease as some areas no longer contain enough features to be classified as a rock bridge by the kernel density analysis.

The mean, median and interquartile range of individual rock bridge areas decreases with increasing *dm²*. On the basis of this, and in consideration with the peak *rb_count*, we selected a density of five *dm²* for classification. Visual assessments of (>50) rockfalls scars confirmed that this was a 'best-fit' for areas of dense fracturing.

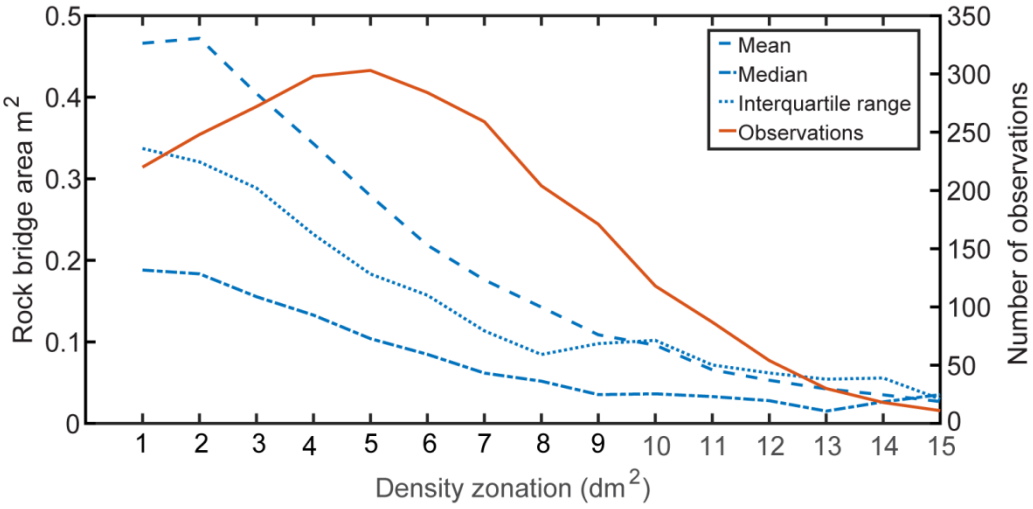

Figure 3.6: Descriptive values of rock bridge area recorded from different density values. These densities are determined from kernel density analysis of edges recorded within rockfall scars. They increase from 1 *dm²* to ≥15 *dm².*

3.4.3.3 Weathering surface classification

We classified rockfall scars into categories to constrain the role of weathering-controlled strength degradation along discontinuities, and within rock bridge fracture (Viles, 2013a). Classification was based on RGB pixel values to represent the intensity of rock weathering relative to virgin rock (Figure 3.7a). We manually chose characteristic RGB histogram ranges, consisting of 25 RGB samples selected to cover a wide range of different surfaces and lithologies exposed upon the cliff. These 25 samples were further classified into five categories determined via histogram evaluation and visual

assessment as: unweathered, shadow, biologically weathered, slightly weathered/till covered and moderately weathered. The glacial till that caps the cliff (Figure 3.2) and drape debris over the cliff face making the distinction between the till cover and slightly weathered surfaces at times ambiguous. Biologically weathered surfaces contain a coating of green algae and are often present on rockfall scars within the tidal inundation zone at the base of the cliff. To characterise the broader pattern of weathering within rockfall scars, we selected the dominant weathering types (Figure 3.7c). As part of this broad assessment, moderately weathered, slightly weathered/till covering and biologically weathered surfaces were combined and simplified to create a single weathered category.

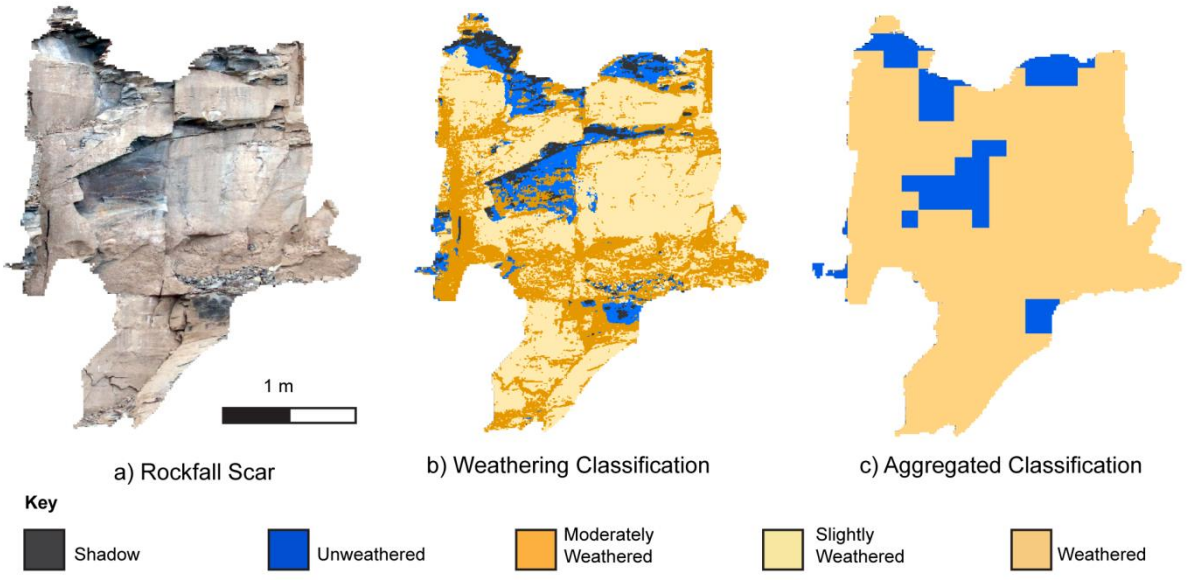

Figure 3.7: Automated weathering surface classification of rockfall scar surface (a) into a detailed 5 category classification of individual pixels (b) and a broader classification of 3 categories based on a 100 by 100 pixel area (c). Categories are outlined in the key.

3.4.4 Calibration data-set

We calibrated both automatic methods with a manually mapped database of 15 rockfall scars. The selected 15 rockfall scars range in scar surface areas from 0.11 m² to 26.9 m², with an approximately equal representation of the three lithologies (Table 3.1). The features of the rockfall scars were mapped and separated into three categories; fractures/edges, planar surfaces, and weathered surfaces (Figure 3.8). Mapping of each individual fracture allowed high concentrations of these fractures to be identified visually. We defined these zones of higher fracturing as broken rock bridges (Figure 3.8a). We mapped each individual planar surface within a rockfall scar, with the number of planar surfaces per scar, their total area, location and resulting geometry within the rockfall scar noted (Figure 3.8b). We defined their proportion (*%ps)* as percentage of total scar surface area. We considered a planar surface to be indicative of pre-existing (pre-failure) joints and bedding faces, with a 'smooth' texture and limited fracturing evident. Weathering classification was based on colour differential relative to the overall cliff face, with the total area of weathered surfaces, and their location recorded within the scar (Table 3.1 and Figure 3.8c.). From this information for each rockfall scar, an interpretation of failure sequence and associated controls was constructed, as displayed in Figure 3.8d.

Comparison of descriptive statistics for both automatic and manual methods (Table 3.2), reveal that the mean and median values of rock bridge and weathered surface area are comparable and within the calculated margin of error. As both areal measurements form the basis from which *rb%* and *w%* are calculated – it was important to quantify their accuracy. Visual assessment of automated results is comparable to the hand mapped interpretations (Figure 3.9). The hand mapped datasets confirm the validity of the automated methods.

.

Table 3.1: Rockfall scar database of 15 rockfall scars containing information relating to rock bridges, planar joint surfaces and weathering.

ID	Date	Area (m^2)	Vol (m^3)	Lithology	Rock bridge proportion (*% rb*)	No.of rock bridge zones	Rock bridge location*	Planar surface proportion (*% ps*)	No. of planar surfaces	Planar surface location*	Weathered Proportion (*% w*)	Weathered Location*	Shape
1	Mar- 16	0.11	0.02	Lower Shale	18	1	T(LS)	64	1	T, M, B	0	NA	Planar
2	Mar-16	0.11	0.03	Upper Shale	36	2	T, B	57	4	M	38	M	Wedge
3	Mar-16	0.15	0.02	Siltstone	7	1	M	76	5	T, M, B	80	T, M, B	Wedge
4	Mar-16	0.15	0.03	Lower Shale	13	1	T, M (LS & RS), B	53	4	M	39	B (LS)	Planar
5	Mar-16	0.43	0.11	Lower Shale	21	1	M (LS)	58	5	M (RS)	30	M (LS)	Arch
6	Mar-16	0.45	0.07	Siltstone	7	2	NA	67	1	T, M, B	56	T, B	Planar
	Mar-16	0.88	0.52	Lower Shale	14	2	M	48	4	T, M (LS & RS), B	20	T, M (LS & RS), B	Wedge
8	Aug-15	1.01	0.2	Lower Shale	13	2	T, B	73	3	T, M, B	85	T, M, B	Planar
9	Jan-16	1.81	0.35	Siltstone	43	3	T, B	29	5	T, M	66	T, M, B	Planar
10	Oct-15	2.56	1.24	Lower Shale	8	3	M	55	3	M, B	6	T, B	Wedge
11	Aug-15	3.34	1.07	Siltstone	.42	2	T, B	51	5	M	65	T, M, B	Planar
12	Nov-15	4.09	2.12	Upper Shale	39	3	M (LS), B (LS)	47	1	M (RS)	19	M	Planar
13	Aug-15	4.8	2.01	Upper Shale	35	2	T, B	44	9	M	13	T	Planar
14	Aug-15	6.37	3.04	Lower Shale	18	9	T, M	44	14	M (LS)	4	T, M (LS)	Arch
15	Jan-16	26.9	27	Siltstone	19	30	T, B	32	32	M & B	45	T, B	Planar

* Location abbreviations: T = top, M= middle, B = base, LS = left side, RS = right side

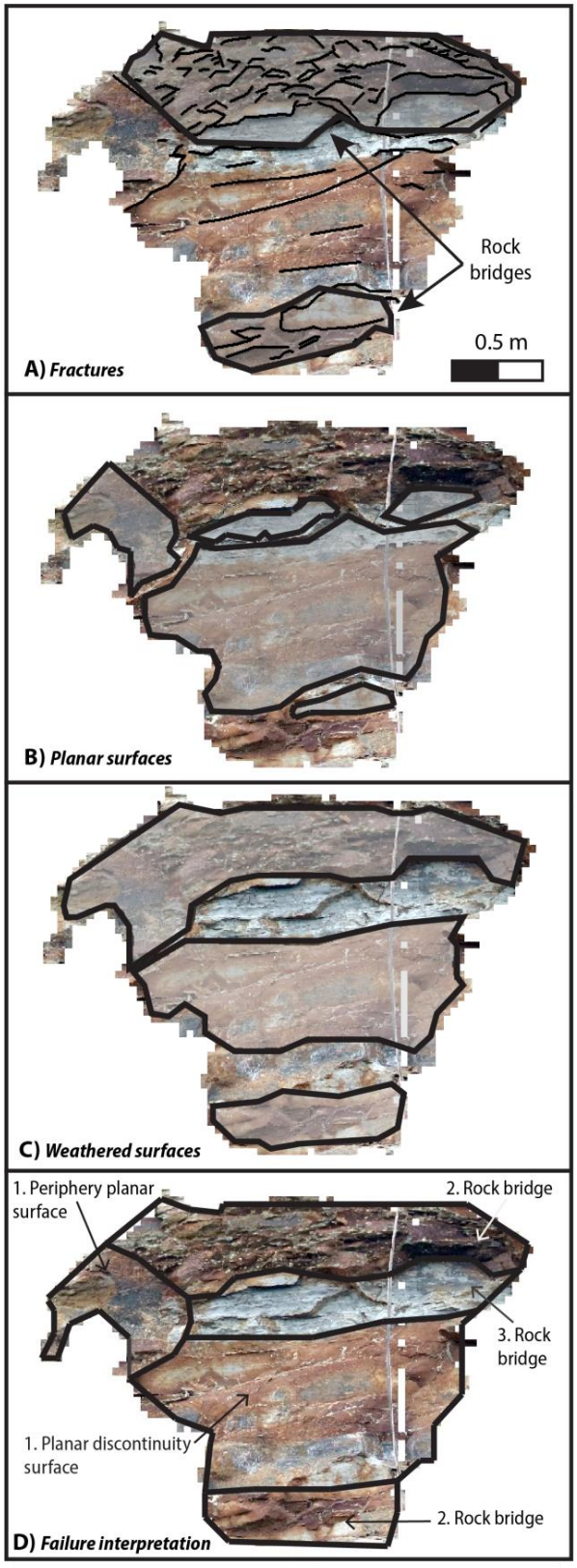

Figure 3.8: Manual mapping of rockfall scars. A) Mapped edges with fracture zones B) Mapped planar surfaces, C) Mapped weathered surfaces and D) Interpretation of failure mechanisms in rockfall scar, with the numbers (1 to 3) representing the components of failure.

Table 3.2: Descriptive statistical comparison between automatic and manual classification of rock bridge and weathered scar surface area.

		Mean (m^2)	Std.dev. (m^2)	Median (m^2)	Margin of error (99% confidence)*	Count
Rock bridge area	Automatic	0.318	0.499	0.102	0.100	74
	Manual	0.191	0.238	0.100	0.157	64
Weathered area	Automatic	0.264	1.044	0.025	0.212	148
	Manual	0.237	0.351	0.089	0.194	82

*Due to differences in sample size a *z (99%)* and *t (99%)* confidence intervals were used for the automatic (n >30) and manual methods (n <30) respectively.

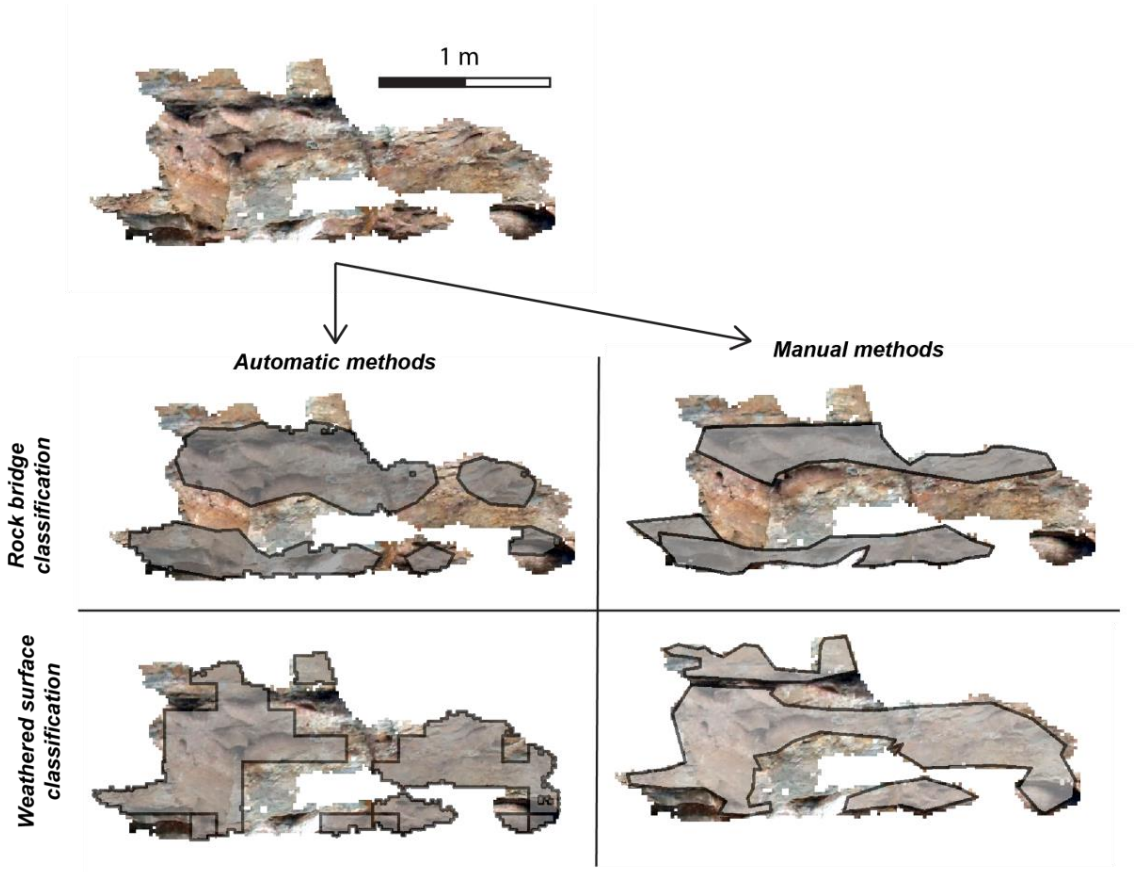

Figure 3.9: Example visual comparison between the respective methods of classifying rock bridges and weathered surfaces.

3.5 Results and Interpretation

3.5.1 Rockfall characteristics

Rockfall scars in the database (n = 657) had a mean surface area of 0.652 m² (Table 3.3), with 13% of rockfall scars having a surface area > 1 m². We use scar surface area as a metric for rockfall size, as it provides a consistent comparison with *%rb* and *%w* and has positive linear relationship with measured rockfall volume (*r =0.927, p = -0.033*). Rockfalls are distributed from across the cliff face, with the highest concentration observed in the shale units (54% in the upper shale and 28% in the lower shale). Fewer interbedded siltstone and sandstone rockfalls are captured due to their location within the cliff face. These events were commonly discarded due to pixel distortion as a result of both the relative steep angle of data capture and nature of 'stretching' the panoramic image over the protruding sandstone and siltstone beds.

Table 3.3: Characteristics of rockfall volume, area and simple geometric variables within the database.

	Area (m²)	Volume (m³)	Width (m)	Height (m)	Depth (m)
Mean	0.652	0.236	1.076	0.893	0.652
Median	0.233	0.043	0.760	0.660	0.494
Std.dev.	1.534	1.208	0.971	0.722	0.547
Min	0.100	0.010	0.260	0.083	0.175
Max	26.912	27.003	9.560	6.160	3.956
Range	26.812	26.993	9.300	6.077	3.781

3.5.2 Rockfall scar characteristics

3.5.2.1 Rock bridge and weathering proportions

The distribution of %rb displays a wide range in values with a skewness of 0.4, and peak in observations for < 2 %rb (Figure 3.10a). This includes rockfalls with no rock bridges, which account for 20% for rockfalls within the database. Such rockfall are predominately

< 0.2 m² with a maximum scar surface area of 1.66 m² (Figure 3.11). Excluding this subset, %rb values are normally distributed with a wide range in values from 0% to 97.6%, and a mean value of 31% ± 26% and a median of 29% (Figure 3.10a and Table 3.4). Individual rockfall scars therefore display a large range in the proportion of their surface that comprises broken rock bridges.

To understand what drives this large range in *%rb* values, we assessed rockfall volume and lithological differences. Rockfall scar area showed no correlation with *%rb* ($r = -0.122$, $p = 0.006$), with a wide scatter in *%rb*. Comparison of descriptive statistics between the three lithologies revealed a 10*%rb* difference by rock type (Table 3.4). The lower shale displayed the lowest *%rb* (26.7%) and interbedded siltstones and sandstones displayed the highest (*%rb* = 34.7%). A similar pattern is observed for the median values of *%rb*. Analysis of variance indicates that the lower shale unit had a statistically-significant ($p = 0.01$) lower mean *%rb* than that of the upper shale and siltstone/sandstone units. Therefore, *%rb* varies as a function of lithology but not with increasing rockfall size. The different lithological units, and their associated rock mass structure, can be considered a critical influence on the prevalence of rock bridge proportion within the scars (and therefore rockfalls) that each unit generates.

%w has a bimodal distribution whereby rockfalls are generally characterised by either <4 *%w*, or more strongly at values of >98 *%w* surface weathering (Figure 3.10b). There is a wide but consistent range in values between these two end members, which generates a mean value of 49.7 % ± 34.9%, and a median of 48.9%. Surfaces with >98 *%w* correspond to the peak in values for <2*%rb,* suggesting that rockfalls with nearly 100*%w* contain 0*%rb*. However, as the peak is larger for *%rb*, some of these scar surfaces with no rock bridges must have been partly unweathered prior to failure. This suggests that *%w* is not solely related to discontinuity occurrence within the rockfall scar, and as such must be related to weathering of already broken rock bridges. The wide range in values also indicates that discontinuity connectivity within the rock mass influences the distribution of weathering across the scar surface prior to failure.

%wrb has a similar bimodal distribution to %w with rock bridges strongly >98*%wrb* or <20 *%wrb,* and a wide consistent range in values (Figure 3.10c). *%wrb* has a mean value of 43.51% ±35.19%, and a median value of 35.5%. Most rock bridges however are only partly weathered, with 79.95% of all rock bridges containing <50*%wrb*, and *%wrb* overall accounts for 12.99% of total rock bridge area. This may be a function of the areal aggregation during classification and the ambiguity of classifying till covered/slightly weathered surfaces (Figure 3.7), introducing an element of uncertainty in this result. As such, we suggest that the broad pattern of these results rather than the exact *%wrb* value is more important. The result implies that some rock bridges within the rock mass have been either partially or completely fractured before final failure of the rockfall, and these fractured surfaces have been exposed for significant periods of time for surficial weathering and discolouration to take place.

Table 3.4: Descriptive statistics for *%rb* based on geology

	Mean	Std.dev.	Median	Max	Min	Count
All	30.8	25.8	28.9	97.6	0	657
Lower Shale	26.2	26.7	20.3	97.6	0	184
Upper Shale	31.9	25.1	31.2	95.3	0	356
Siltstone/Sandstone	34.7	25.9	36.2	93	0	117

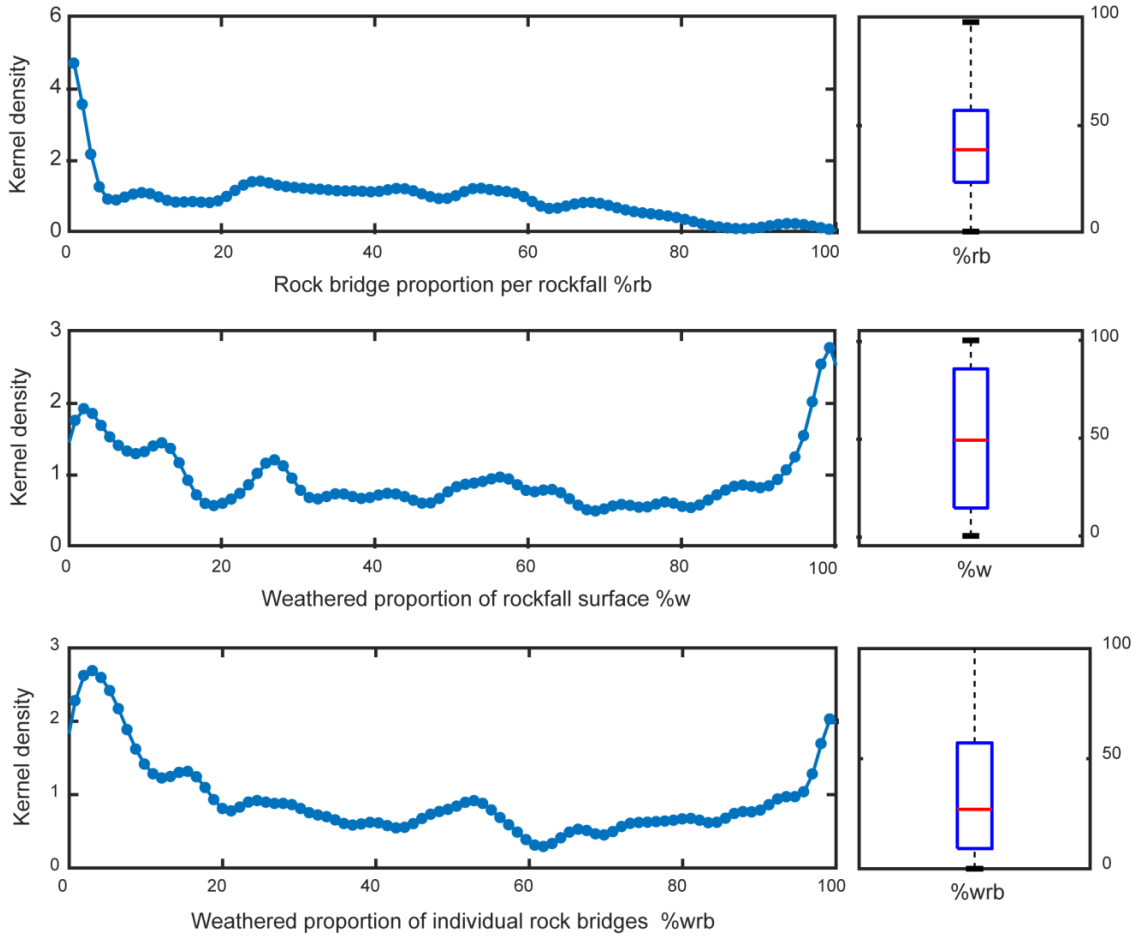

Figure 3.10: Histograms and box plots of a) *%rb* and b) *%w* and c) *%wrb*.

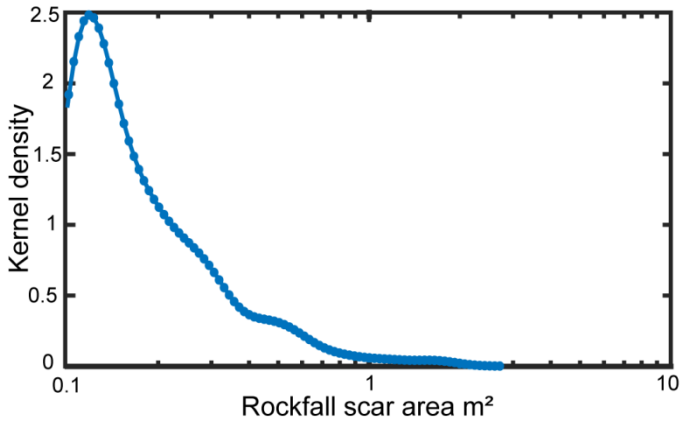

Figure 3.11: Kernel density plot of the area distribution of rockfall scars recorded with no rock bridges.

3.5.2.2 Rock bridge distribution

Rockfalls have a median value of one rock bridge per scar, with a mean value of 1.8 ± 2.2. The number of rock bridges per scar has a significant positive linear correlation with increasing rockfall scar area (r = 0.928; Figure 3.12a). This demonstrates that larger rockfalls contain more individual rock bridges, as opposed to larger rockfalls purely being larger versions of their smaller counterparts. Failure interpretations of the manually mapped data-set confirm this increase in complexity with rockfall size (Figure 3.13). Mechanically, larger rockfalls may therefore behave and fail in a manner quite different to smaller rockfall, and so may be sensitive to a different set of conditions, controls or thresholds on failure. Around 0.5 m² scar surface area, rockfalls tend to contain ≥2 rock bridges, with the trend indicating that rockfalls with 1 m² surface area are most likely to contain two or more rock bridges. This indicates that, in broad terms for every 0.5 - 1 m² of increasing rockfall scar surface area, there is one additional rock bridge holding the block to the rock face. Individual rock bridge area is predominantly measured to be *c*. 0.1 m² (Figure 3.12). A 0.5 m² rockfall surface area that contains a 0.1 m² rock bridge adheres to the mean *%rb* estimate.

Within each rockfall scar, we examined the areal extent of the individual rock bridge(s) (Figure 3.12b). We compared the relative area of the largest rock bridge within the scar to all the other rock bridges within the same scar. Our analysis identifies that for rockfalls with <5 rock bridges, one main rock bridge dominates the scar surface, with smaller peripheral bridges. As the number of rock bridges increases the dominance of a single bridge decreases, as the fraction of the scar rock bridge area occupied by the largest rock bridge as compared to all other rock bridges reduces. This suggests that for larger rockfalls with > 5 rock bridges in the inventory, rock bridges tend to be of a similar surface area. Conceptually, and assuming a homogenous rock mass structure, as the failure scar surface area grows it incorporates more rock bridges. With increasing rockfall volume, fractured rock is distributed across multiple bridges of similar size, rather than concentrated in one primary rock bridge. By implication the perimeter to area ratio of rock

bridges changes with rockfall volume, which exposes a greater area of the supporting rock bridges to be exposed to weathering within the rock mass.

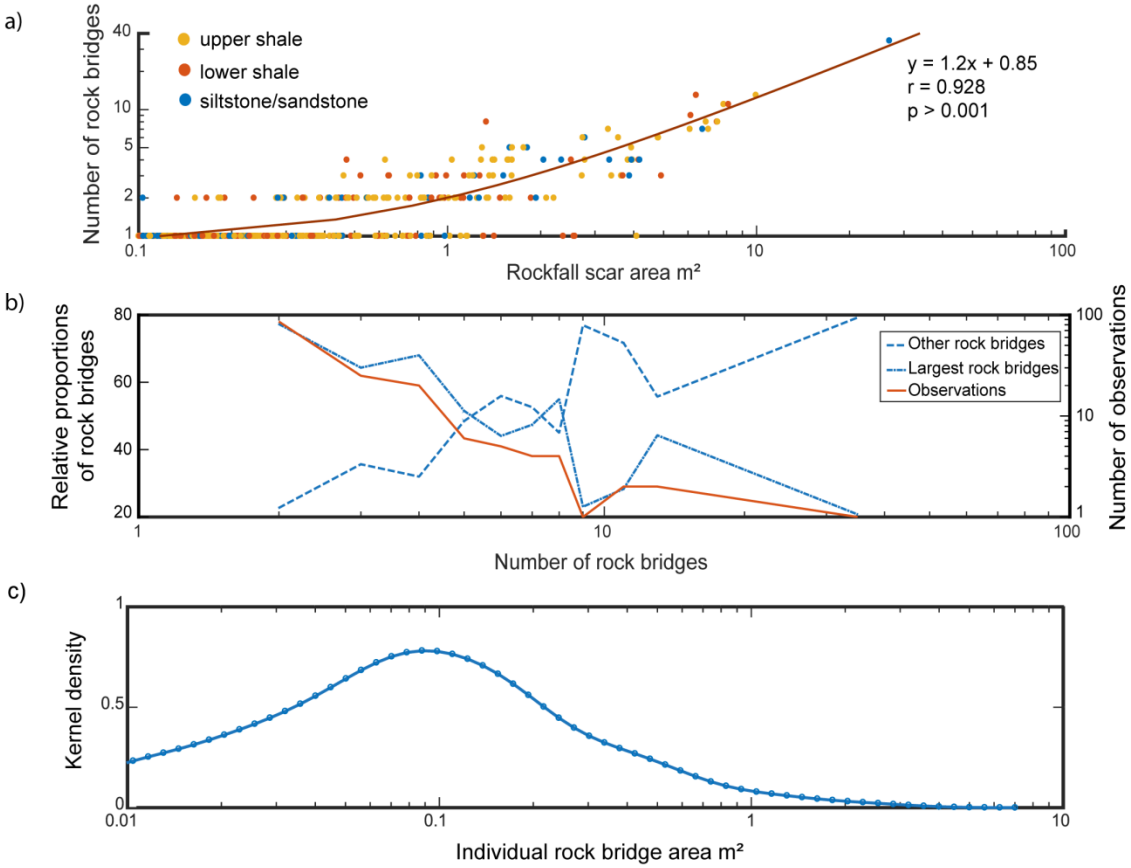

Figure 3.12: Rock bridge distribution within each rockfall scar. a) Scatter plot displaying a positive linear trend between number of rock bridges per scar and rockfall scar area. b) Mean values of the relative proportion of the largest rock bridge within an individual scar compared with the proportion of all other rock bridges within an individual scar. For example, if a rockfall scar contains two rock bridges, the largest accounts for 80% of rock bridge area while the other accounts for only 20 %. The number of observations for the calculation of mean values is plotted on the right axis and descreases with increasing rock bridges. c) Kernel density plot of individual rock bridge area distribution, displaying that most rock bridges are 0.1 m².

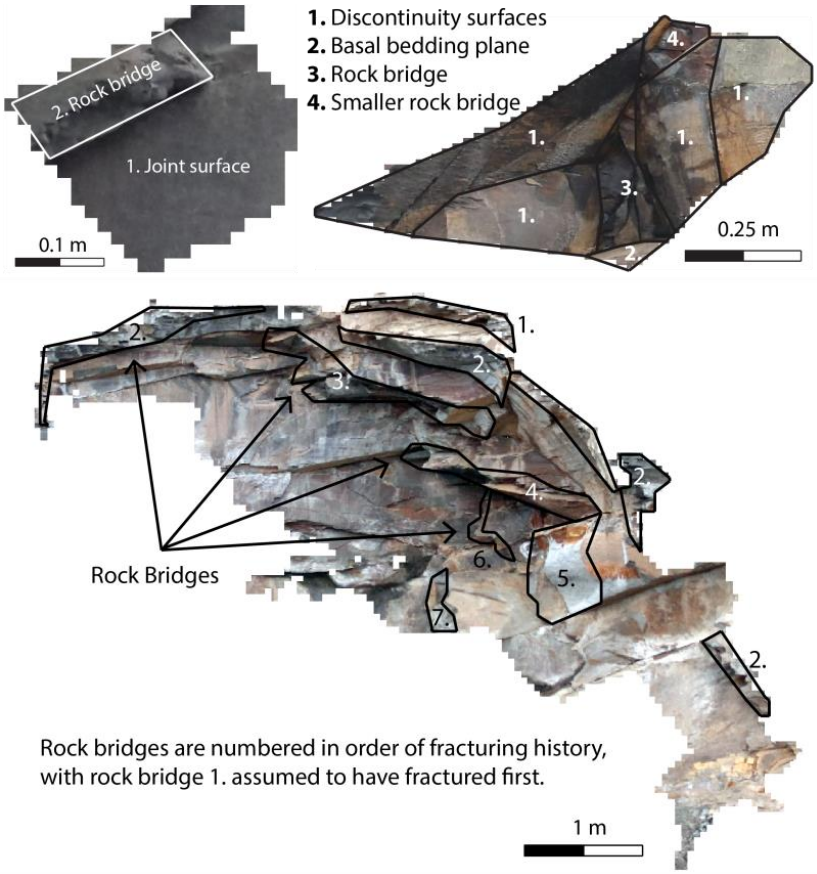

Figure 3.13: Failure interpretations of rockfall scars from the manually mapped database. With increasing area, the number of rock bridges and discontinuity surfaces increase, as do the stages required for failure.

3.5.2.3 Rock bridge orientation

We assessed the orientation of rock bridges with respect to rock bridge planarity relative to the main failure surface. We compared the mean slope and aspect (derived from the cliff face surface topography model) of the rock bridges with that of the overall aspect and slope of the scar surface (Figure 3.14a). Slope and aspect are comparable to the dip and dip direction, respectively, of a discontinuity given the projection of the cliff face data employed here. Scar aspect was measured relative to cliff normal (Figure 3.2b) and as such represents deviations from the cliff face aspect. From this we derived a mean aspect value of 173.7° ± 53.1°, indicating that the most rockfall scars are oriented approximately parallel to the cliff face.

We define rock bridges as co-planar with the main failure surface, if both slope and aspect are ≤15° from scar surface orientation. Due to the relatively small failure size and based on field observation, we assumed rockfalls scar surfaces contained one main planar failure surface, and therefore co-planar rock bridges are also in-plane with this surface. We define rock bridge deviations in slope and aspect of >15° as non-planar. Our definition of non-planar bridges does not necessarily distinguish in-plane rock bridges along intersecting joints from out-of-plane rock bridges located between discontinuities of differing orientations. 69.5% of rock bridges were defined as predominately co-planar, with 30.5% predominantly non-planar. Rockfalls that contain both non-planar and co-planar rock bridges account for 14.8% of events in the inventory. For these rockfalls, scars are dominated by co-planar rock bridges (97%), with non-planar rock bridges forming only a minor component of the total scar. Therefore, nearly all rockfalls which contained both non-planar and co-planar bridges were accounted for within the 69.5 % of rock bridges which are predominately co-planar. This suggests that lateral release surfaces related to discontinuities striking perpendicular to the cliff face contain fewer rock bridges. Assessment of mean *%rb* between co-planar and non-planar rock bridges reveals that non-planar rock bridges show a higher proportion (51.1*%rb*) compared to co-planar (35.4*%rb*) (Figure 3.14b). Analysis of variance indicates that this difference is statistically significant ($p > 0.001$), so although non-planar rock bridges are less prevalent in our dataset, when they are recorded, their *%rb* is normally higher. Analysis of the distribution of co-planar versus non-planar rock bridges shows that (larger) rockfalls with multiple rock bridges are less likely to contain non-planar rock bridges (Figure 3.14c). Therefore, non-planar rock bridges are limited to smaller rockfalls, which as identified previously, tend to contain only one rock bridge. These smaller rockfalls are more likely to be associated with discontinuity surfaces, which comprise rock bridges, whereas the larger rockfalls have fractured both through and across discontinuities.

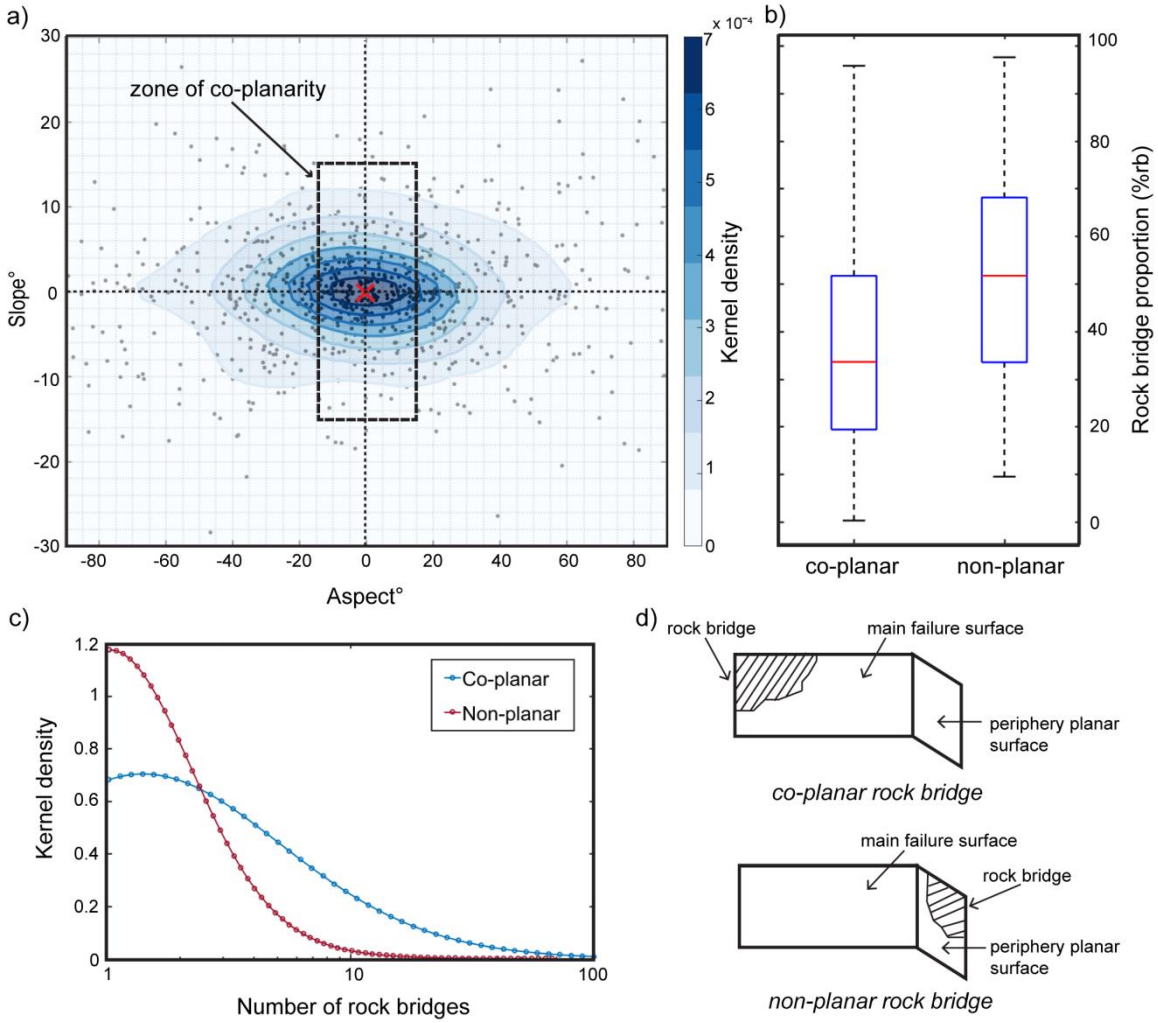

Figure 3.14: Rock bridge orientation within each rockfall scar. a) Kernel density plot displaying the difference in mean slope and mean aspect between rock bridge and the rockfall scar surface. Co-planarity defined as change in slope & aspect of < 15 °. b) Box plot displaying difference in *% rb* between co-planar and non-planar rock bridges. c) Kernel density plot of the number of rock bridges for either co-planar or non-planar rock bridges. d) Conceptual end-member examples of co-planar and non-planar rock bridges.

3.5.2.4 Rock bridge location

We normalise the coordinates of the position of the centre of the rock bridge relative to the coordinates of the 3D centre of mass projected back onto the cliff face for each rockfall. The centre of the rockfall is located at coordinates {1,1}, and rock bridge positions are displayed relative to this point (Figure 3.15). The highest density of rock bridges is generally located just above the rockfall centre of mass. Overall, more rock bridges are located above the rockfall centre of mass (52.4%), as opposed to below

(47.6%), although this distinction is not clear. Rock bridges are however clustered around the projection of the rockfall centre of mass onto the cliff, with a decreasing density in bridge position with increasing radial distance relative to the scar extent. Rock bridges are broadly represented in all areas of the rockfall scar, except on the very periphery. Rock bridges therefore may not define the perimeter of the rockfall, but rather support a mass of which the extent is defined by the rock mass structure.

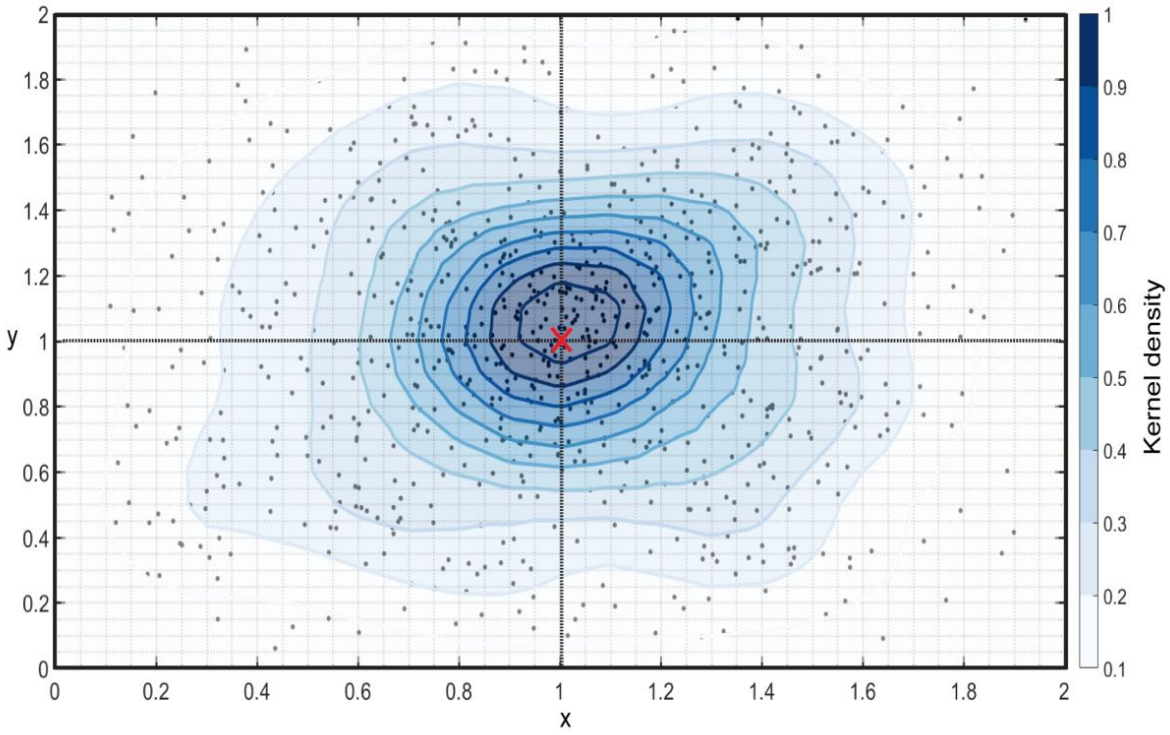

Figure 3.15: Kernel density plot of rock bridge centres normalised to the rockfall centre of mass. The rockfall centre is located at the x of 1, 1- with y values < 1 located below the rockfall centre and y values > 1 located above the rockfall centre.

3.6 Discussion

3.6.1 Rock bridge role in failure

Our results demonstrate that a wide range of *%rb* is possible within failures from the same rock type and structure. This holds across a range of rockfall sizes but varies with source rock lithology. The mean *%rb* value of 31% ±26% is higher than previously

reported for other rockfall scar analysis case studies, which invariably focus on larger volume events, often in more competent or massively jointed rock. Previous studies, comprising of individually mapped rockfall scars, displayed a range of 0.2% to 26% (Frayssines and Hantz, 2006; Lévy et al., 2010; Paronuzzi et al., 2016; Paronuzzi and Sera, 2009; Stock et al., 2012, 2011). Estimates obtained from discontinuity persistence mapping and back analysis modelling display a larger range of 1% to 45% (Elmo et al., 2011; Gischig et al., 2011; Grøneng et al., 2009; Karami et al., 2007; Matasci et al., 2015; Sturzenegger and Stead, 2012; Tuckey and Stead, 2016). All of these estimates, including our dataset, display a six order of magnitude range in rockfall size (from 0.01 m^3 to 10,000 m^3) and consider various rock types.

We suggest that the large recorded variance in *%rb,* which we report here, is due to the spatial distribution of rock bridges within the slope, as determined by the persistence and spacing of discontinuities within the rock mass (Tuckey and Stead, 2016). To account for this variance, robust sensitivity analysis within modelling to determine failure susceptibility is needed. Through analysis of rockfall scars from the three rock types considered here, it is evident that lithology is an important control on rock mass strength in defining the nature of rock bridges, and even subtle changes in rock mass structure between the three lithological units results in significant *%rb* differences. This indicates that not only the wider geology, but also the local scale lithology changes control rock mass characteristics that are important controls in releasing blocks as rockfall. Joint density, a proxy for joint spacing, varies with bed thickness (e.g. Huang and Angelier, 1989; Ladeira and Price, 1981; Narr and Suppe, 1991), indicating that within interbedded sedimentary sequences rock bridge characteristics will vary as function of mechanical stratigraphy.

The distribution of these rock bridges influences the stress within the incipient failing mass, determining its eventual failure mode (Bonilla-Sierra et al., 2015; Stock et al., 2011). Our dataset demonstrates that most rockfalls in our inventory will contain a singular rock bridge, which may be located throughout the scar, except on its periphery,

with an approximately equal location probability above or below the rockfall centre of mass. Bonilla-Sierra et al., (2015) modelled rock bridge location in relation to a translational failure. Higher concentrations of tensile cracking were associated with rock bridges located at the top of the failure surface, a steeper slope angle and a lower centre of mass. When the rock bridge is located above the centre of mass, and assuming simplified geometry, the force acting on the failure mass generates a bending moment that results in greater tensile cracking and associated rotation (Hibbeler, 2010). Conversely, shear cracking was associated with a more shallow failure surface and rock bridges located in the centre or lower parts of failure (Bonilla-Sierra et al., 2015). Using a similar simplification, we suggest that rockfalls with rock bridges located above the centre of mass likely fail predominantly in tension, while rockfalls with rock bridges in line with or below centre of mass are likely to predominantly fail in shear (Figure 3.16). The degree of deviation of rock bridge location from the rockfall centre needed to generate sufficient bending moment and associated tensile failure is unknown. Further modelling would reveal if even slight deviations in rock bridge location results in an imbalance of forces, affecting those acting on a failing block and resulting in a change to the dominant failure mode.

Additionally, rock bridges that are non-planar to the main failure surface or located to the side of the centre of mass introduce an element of twisting or torsion into the mechanical analysis, which is rarely considered within the 2-dimensional analysis of slope failure mechanics (e.g. Wyllie and Mah, 2004), but is standard practice for structural engineering (e.g. Hibbeler, 2010). These require a fully 3D approach to account for dilation and rotation of blocks within the rock mass. Analysis of the stresses experienced by the rock bridges will determine which strength characteristics, such as tensile or shear, are most important for stability. We show here that with increasing rockfall size, more rock bridges are likely to be incorporated into the eventual failure surface. This increases the complexity of the forces acting on the incipient failure mass due to their multiple attachment points to the slope. This also highlights the potential for the

sequential failure of one rock bridge at a time, and the subsequent transfer of and changes in the nature of stress on remaining intact bridges.

Our results show that smaller rockfalls containing <5 rock bridges are commonly dominated by one large main rock bridge, which dictates the potential for failure and release. The mechanical and compositional characteristics of this main bridge will determine its strength, and the magnitude and trajectory of stress required for failure to occur. Within a heterogeneous (sedimentary) lithology, small scale (10^{-3} m to 10^{0} m) intrinsic flaws such as, micro-cracks, grain boundaries and sedimentary structures, such as ripples or concretions may predispose the rock bridge to failure by forming initiation points for micro- and macro- crack propagation (Kranz, 1983; McConaughy and Engelder, 2001; Pollard and Aydin, 1988). As such, the temporal behaviour of these smaller rockfalls may be difficult to predict.

As a failure develops, it remains unclear how the failure responds to, accommodates and incorporates smaller peripheral rock bridges, or includes the partial failure of larger rock bridge located on the edge of failure scar. In the case of a partial failure of a larger rock bridge, questions concerning controls on termination of fracture within that rock bridge and the impact on the dimensions of the failure mass are raised. This point of termination may be determined by intersecting cliff perpendicular discontinuities or non-persistent bedding, whereby fracture propagation deflects and stops at these boundaries due to changes in the near–field stresses experienced by the propagating crack tip, influenced by changes in lithological composition and mechanical interactions with discontinuities (Pollard and Aydin, 1988; Scavia, 1990). Therefore, discontinuity spacing may control rockfall geometry and the amount of partial and complete fracturing required through rock bridges contained within the incipient failure mass.

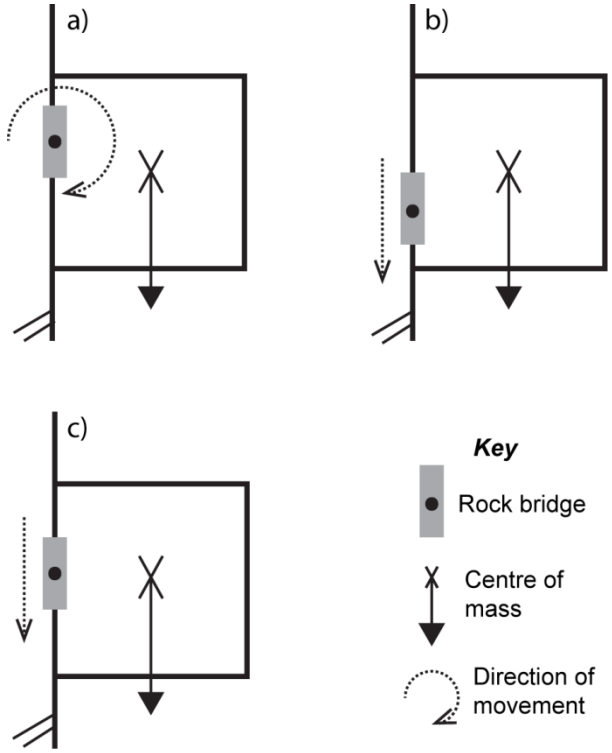

Figure 3.16: Conceptual model of rock bridge attachment points and potential failure directions. a) Rock bridges located above centre of mass may result in outward rotation of the incipient rockfall block and associated tensile failure. b) & c) Rock bridges located below centre of mass may fail in shear due to downward forces acting on the rock bridges.

3.6.2 Implications for progressive failure

For larger rockfalls, fracturing through each of the multiple rock bridges is required. The order through time in which rock bridges fracture remains poorly constrained but is likely to be complex. This order must have important implications for progressive failure and stress redistribution within the incipient scar (Eberhardt et al., 2004a; Kemeny, 2003; Stead et al., 2006). For instance, the fracture of minor rock bridges may result in significant enough changes to stress distribution to create instability, or it may only be the fracture of larger bridges that are the catalyst for acceleration towards final failure and block release. Fracturing may represent or may drive pre-failure deformation (e.g. Rosser et al, 2007; Kromer et al., 2015) whereby observed surface deformation may be a manifestation of fracturing of rock bridges within the rock mass. Our analysis of *%wrb* distribution has indicated that substantial weathering of fractured rock bridges can occur

before final failure, suggesting that pre-failure deformation may not always result in a sudden acceleration towards failure and may evolve over a period sufficiently long enough for weathering to take hold. In these circumstances the redistribution of stress may result in a new prolonged (quasi-)equilibrium state (Leroueil, 2001). Modelling of progressive failure may help understand this temporal pattern by accounting for the distribution of fracturing and stress between these multiple rock bridges (Stead et al., 2006).

Rockfall failure is commonly poorly correlated with environmental conditions and can occur entirely independently of environmental triggers (Lim et al., 2010; Rosser et al., 2007). However, smaller rockfalls (< 0.1 m^3) can be more successfully correlated to, for example, mean air temperature and wind velocity (Lim et al., 2010). These correlations may exist for small rockfalls that display no rock bridges, and as such require no fracturing through intact rock to instigate release. For rockfalls with rock bridges, some form of rock strength weakening is needed for failure to occur at low magnitude environmental stress triggers that are otherwise insufficient to fracture intact rock (Gunzburger et al., 2005). This weakening is likely to be driven by processes such as weathering or stress redistribution as described here (Collins and Stock, 2016; Gunzburger et al., 2005; Viles, 2013a). These processes can create stress fluctuations within the slope that drive the development and coalescence of micro-cracks, eventually reducing the strength of rock to the point of failure (Attewell and Farmer, 1973; Cruden, 1974; Stock et al., 2012).

Our analysis shows that the rockfalls considered here display a wide range of exposure to weathering prior to failure, as represented by the variation in *%w* and *%wrb*. However, not all discontinuity surfaces may be weathered, with the prevalence determined by the connectivity of the discontinuity sets and the intensity and efficacy of environmental conditions acting on and within the slope. The relationship between this exposure and connectivity influences weakening within the slope (Gischig et al., 2011; Viles, 2013). Weathering at the interface between a rock bridge and a discontinuity, known as the

crack tip, where stress is concentrated, is an important control on weakening and fracture propagation (Collins and Stock, 2016). The rock bridge perimeter to rock bridge area ratio must to some extent dictate this rate of weakening of rock bridges. For example, two slopes with the same overall rock bridge proportion may weaken at different rates depending on rock bridge size, shape, area and distribution. A slope that contains smaller but more abundant rock bridges may weaken at a faster rate due to high perimeter to area ratio.

As attachment points to the slope, rock bridges represent zones of stress concentration. Recent research has shown a complex relationship between weathering and stress prior to failure, which suggests that stress concentrations may either enhance or dampen the efficiency of weathering events (Brain et al., 2014; Bruthans et al., 2014). Understanding the stress regime that rock bridges experience can determine their temporal and spatial response to weakening (Kemeny, 2003). Micro-cracks may be preferentially oriented with respect to the applied stress (Brain et al., 2014), impacting overall strength. For example, mode 1 cracking will reduce tensile intact rock strength. The models presented by Scavia and Castelli (1996) indicate that fracture propagation is dependent on rock bridge size, with larger rock bridges requiring tensile σ_3 conditions - the minimum principal stress, for fracture to occur. Defining rock bridge proportion and distribution, along with failure mode, is critical for assessing the failure stress regime. The exact nature of feedbacks between weakening, the stress regime and individual failures, and how these interactions drive the propagation of further failure requires detailed quantification. These interactions affect the timing of rockfall failure, which holds implications for the frequency and magnitude of rockfall activity, a critical input of hazard assessments (Fell et al., 2008) and slope erosion rate calculations (Barlow et al., 2012; Dussauge et al., 2003; Malamud et al., 2004).

3.6.3 Influence on rock mass strength

We observe that while most rock bridges are co-planar to the main failure surface, ~30% are not. These non-planar rock bridges may represent fracturing through intact rock

along discontinuity sets, or the partial fracturing of peripheral rock bridges co-planar to the failure surface. Non-planar rock bridges are largely absent from larger rockfalls, suggesting that they are representative of partial fracturing through peripheral rock bridges, or that they have been subsumed into the failed mass and so are not visible within our analysis. This indicates that most rock bridges are located co-planar to the main failure surface, which in this instance is cliff parallel. The prevalence of rock bridges along cliff parallel discontinuities may be related to the conditions of joint formation. These cliff-parallel joints may be formed in response to local scale topographic stress and slope curvature (Gerber and Schiedegger, 1969; Martel, 2017). It is unlikely that these discontinuities represent large scale sheeting joints, like those observed in the granitic rocks of Yosemite Valley, due to the lower magnitude of overburden stress and weaker lithologic characteristics of the rocks considered here (Martel, 2017). We however assume that smaller scale topographic stresses may generate smaller scale fracturing comparable in form if not scale.

These localised topographic stresses may result in an intermittent smaller-scale joint propagation. Additionally, as joint density increases within a rock mass, the interactions between the individual joints inhibit each other's expansion (Pollard and Aydin, 1988), by changing the stress intensity factor of the propagating crack tip of a joint (Scavia, 1990). This results in less persistent but higher density jointing with a greater prevalence of rock bridges, distributed in distinct zones within the slope. In contrast, intersecting joints, which may have been formed by larger regional scale stresses associated with tectonics and uplift, may be more persistent separated by larger rock bridges (Brideau et al., 2009; Tuckey and Stead, 2016). Our analysis reveals that non-planar bridges account for a higher proportion of scar surface area. Therefore, the spatial prevalence and pattern of rock bridges within a slope is related to its rock mass strength characteristics as determined by joint type. The propagation and persistence of joints in turn is influenced by lithology (Pollard and Aydin, 1988). Defining the conditions of joint formation and their resulting characteristics will enhance our understanding of rock mass

strength (Moore et al., 2009). Consequently, this has implications for slope evolution, with numerous studies outlining the influence of rock mass strength on differential slope forms (Augustinus, 1992; Moore et al., 2009; Selby, 1982). Understanding the intrinsic properties of rock mass strength, as represented by rock bridges, discontinuities and weathering, will better inform the parameters of larger scale landscape evolution models (Moore et al., 2009).

3.7 Conclusions

We present the first large scale database of rock bridge and rockfall scar weathering characteristics (0.1 m² to 27 m²). Our analysis reveals:

- Rock bridges account for 31% ±26% of failure scar surface area. The wide range in *%rb* is related to subtle changes in lithology and rock mass structure.
- Failure mode is dependent on the imbalance of mass created by the deviation between the rockfall centre and rock bridge attachment point. This point may be subjected to tensile, shear and torsional stresses, which influences the parameter of strength critical for stability. 3D modelling is required to provide a comprehensive slope stability analysis.
- The number of rock bridges within a scar, and associated failure complexity, increase linearly with rockfall size. The majority of rockfalls are dominated by one main rock bridge, which is critical for maintaining stability. For larger rockfalls to fail, progressive failure and fracturing is likely required through multiple rock bridges. Through time the stress applied to each rock bridge may change as it tends towards being the next in sequence to fail.
- Rock bridges must have been weakened prior to failure, with the rock bridge perimeter to area ratio determining weathering exposure at the discontinuity/rock bridge boundary. Not only is rock bridge proportion a control on stability, but other

rock bridge attributes are important to provide a full explanation of the spatial and temporal occurrence of failure.

- Rock bridges provide controls on the mode, spatial pattern, and temporal behaviour of failure, which influences slope stability as a whole.

This analysis provides insights into the relative contribution of surficial weathering, rock bridges and conversely discontinuity release surfaces to rockfall instability, as outlined in Objective 1. From this analysis, the stresses acting upon a rockfall scar and rock bridges within such a scar can be inferred, providing information about how stress is concentrated within individual rock-bridges. This information provides boundaries for exploratory numerical modelling outlined in chapter 4. In addition, the characteristics of rock bridges within individual failures determine where strength degradation is an important control on failure.

4 Topographic and structural controls on cliff slope stability

4.1 Introduction

The ratio of stresses acting on a slope to the resisting strength controls its stability. Stresses experienced by the slope are often considered in terms of episodic external environmental events, such as earthquakes (e.g. Keefer, 1994) or heavy rainfall (e.g. Iverson, 2000), which may act as triggers for failure. These lower-frequency, higher-magnitude events are superimposed on a quasi-constant lithostatic vertical stress (σ_v) which is a function of the height of the overlying column of rock (*h),* the unit weight of the material *(p)* under gravity (*g)* (9.8 m/s²), as outlined below:

$$\sigma_v = \rho g h$$

Equation 4.1

Topography at a range of scales has been recognised to modify vertical lithostatic stresses, concentrating stress within specific areas (Radbruch-Hall et al., 1976; Savage et al., 1994). For example, previous work has considered the impact of valley and ridge systems on concentrating stress, such that stresses are compressional along ridges and tensile in valleys, and where these stresses exceed local rock strength, subsequent fracturing can occur within a rock mass (Leith et al., 2014a, 2014b; Liu and Zoback, 1992; McTigue and Mei, 1981; Miller and Dunne, 1996; Molnar, 2004; Savage et al., 1994; Savage and Swolfs, 1986; Slim et al., 2014). However, few studies have analysed the near-surface stress distribution of steep slopes (Bruthans et al., 2014; Martel, 2006; Savage, 1993), where high slope angles are identified as a key control on the magnitude of stresses (Wolters and Müller, 2008).

The micro-topography (i.e. features with an areal footprint of 10 m² to 1 m²) of the surface of steep slopes, comprised of convex and concave morphology, may also act to concentrate stress locally (Figure 4.1). This chapter defines areas of protruding (convex) rock as overhangs, which are often observed within interbedded sedimentary

sequences. These bedding-related overhangs have been shown to influence erosion rates, and represent boundaries where instability can concentrate, or be halted from migrating across the surface further (Barlow et al., 2012; Lim et al., 2010; Rosser et al., 2007). Above and below an overhang, re-entrant corners, with concave or flat areas, represent the zones which separate overhangs (Figure 4.1). These re-entrant corners form areas where stress and strain is concentrated, and therefore are areas where failures surfaces may preferentially occur and then can propagate (Kogure et al., 2006; Muller and Martel, 2000; Young and Ashford, 2008). The nature of these stresses may determine if this failure surface propagates in tension (e.g. Herterich et al., 2018) or shear (e.g. Muller and Martel, 2000). Greater overhang depths (Figure 4.1) are linked with generating greater differential and tensile stresses that result in an enhanced fracture propagation likelihood (Martel, 2017; Stock et al., 2012).

In addition, the (internal) rock mass structure of the slope also concentrates stress at rock bridges – the zones of intact rock which separate discontinuities within the rock mass (Jennings, 1970). Rock bridges form areas where failure surfaces need to develop in order for the complete detachment and failure of a rock block (Eberhardt et al., 2004a; Jennings, 1970; Kemeny, 2005; Scavia, 1995). The percentage of rock bridges within a rock slope has been observed to vary from 0.2% to 45% (Tuckey and Stead, 2016 and references therein), influencing the areas in which stress is concentrated and strain can therefore accumulate (Figure 4.1). A higher persistence of discontinuities will result in smaller rock bridges, potentially increasing stress concentration in these areas, while for lower persistence discontinuities with larger rock bridges, stress may be more evenly distributed. The exact impact of rock bridges on the wider stress distribution within a slope, and the influence on subsequent instability, has not been investigated. Consideration of rock mass structure is largely limited to kinematic controls on failure, and their contribution to the wider rock slope strength (Goodman and Shi, 1985; Hoek, 1983; Selby, 1980; Wyllie and Mah, 2004). The combined influence of slope shape and

rock mass structure on near-surface stress concentrations and patterns of strain is not fully constrained.

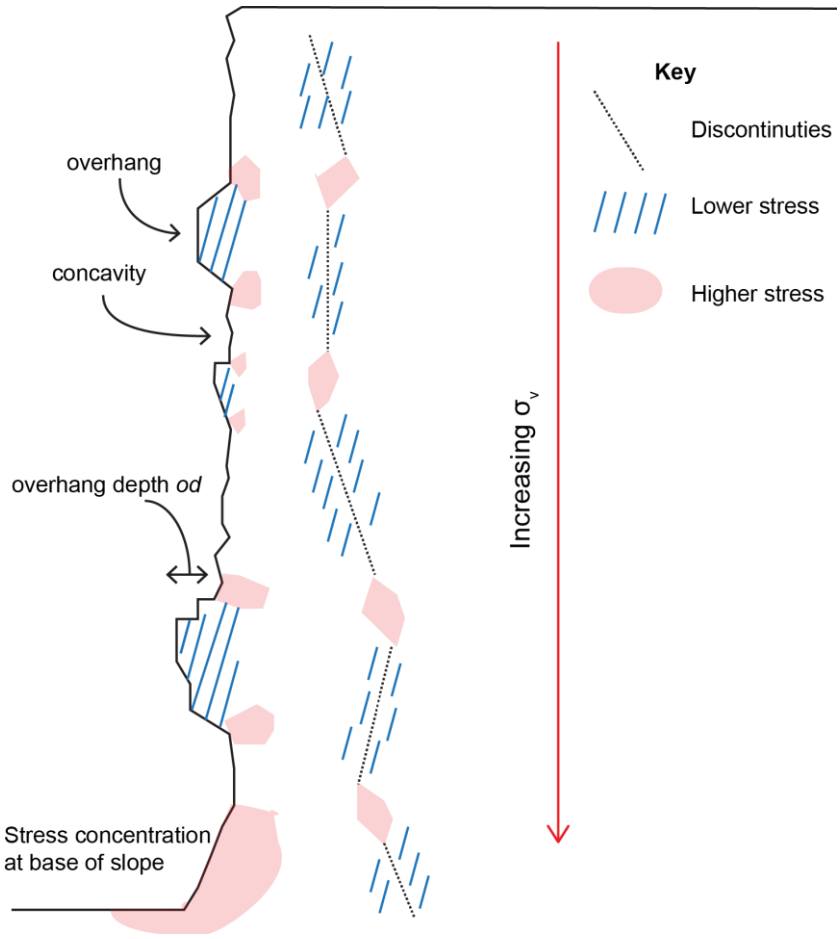

Figure 4.1: Schematic of the potential influence of topography, including overhangs and discontinuities, in concentrating increasing σ_v in the slope near surface.

The near surface zone is important as recorded rockfall depths for near-vertical slopes display mean rockfall depths in the order of 1 m or less (e.g. Dewez et al., 2013; Lim et al., 2010; Stock et al., 2011), as also observed in the rockfall characteristics reported in Chapter 3 (Table 3.3). These shallow rockfalls dominate the erosion of steep slopes (e.g. Dewez et al., 2013; Lim et al., 2010; Moore et al., 2009; Stock et al., 2011). An improved understanding of the link between the distribution of stress and strain within a slope and

failure potential can, therefore, provide a susceptibility analysis tool for future instability assessment.

This chapter uses a numerical modelling approach to explore the relationship between slope angle, overhang depth and discontinuity persistence on the subsequent distribution of stress and strain within the slope near-surface, and the resulting impact on the spatial patterns of rockfall occurrence. The chapter is divided into two sections. Firstly, the stress and strain distribution of idealised slopes are examined via 125 exploratory finite element models (FEM). In these models, slope angle, overhang depth and discontinuity persistence to understand how each model variable influences the stress distribution and strain behaviour of a slope. The first half of the chapter concludes by deriving general rules and broad scale observations on how the nature and values of stress and strain in a slope are dictated by the aforementioned variables.

The second half of the chapter examines the coincidence between rockfall failure and model variables, using a real-world rock slope and rockfall dataset. This assesses if the general stress and strain patterns determined via numerical modelling dictate the spatial patterns of rockfall failure. The combination of numerical modelling and real-world dataset constrains the relationship between stress distribution and strain behaviour with failure.

4.2 Exploratory numerical modelling

This chapter investigates the bulk and emergent behaviour of stress and strain in steep rock slopes in response to varying slope angle, surface geometry and structure. Most traditional modelling approaches often consist of back analysis case-studies of a previously failed slope (e.g. Brideau et al., 2011; Eberhardt et al., 2004a; Sturzenegger and Stead, 2012), in order to understand the triggers and mechanisms of the specific failure. The outputs from this type of modelling are inevitably site-specific and tailored to the particular topographic, structural and geological setting of the failed rock slope.

Modelling in this chapter considers an alternative approach, by determining the interactions and net effect of varied conceptual topography and rock structure on the stress and strain distribution of slope. This is intended to identify any unexpected behaviour (e.g. thresholds in response), and macro-scale variations in stress and strain, which can potentially control and explain patterns of rockfall occurrence.

4.2.1 Finite element modelling

A series of conceptual 2D slope profiles with varying slope angle (*sa)*, overhang depths (*od)*, and discontinuity persistence (*dp)* (Figure 4.2) were created, and their stress and strain values calculated using the finite element model (FEM) RS2 (RocScience, 2017). FEM solves for stress and strain by sub-dividing the slope into much smaller finite elements connected within a mesh structure, with instantaneous stress and strain calculated for each element (Cook, 1995). A FEM mesh consists of mesh elements joined to each other by mesh edges. The mesh of the models within this chapter consisted of triangles with 6 mesh elements, separated by 0.5 m long mesh edges. This mesh density captures the fluctuations in stress and strain caused by metre-scale micro-topography and discontinuities. As this chapter is concerned with near surface stress concentrations and strain behaviour, this high-density zone of mesh extended back 10 m from the slope surface (Figure 4.2). Sensitivity analysis was undertaken to determine the key values required for *sa*, with the values for *od* and *dp* sourced from a review of the literature (see Section 4.2.5).

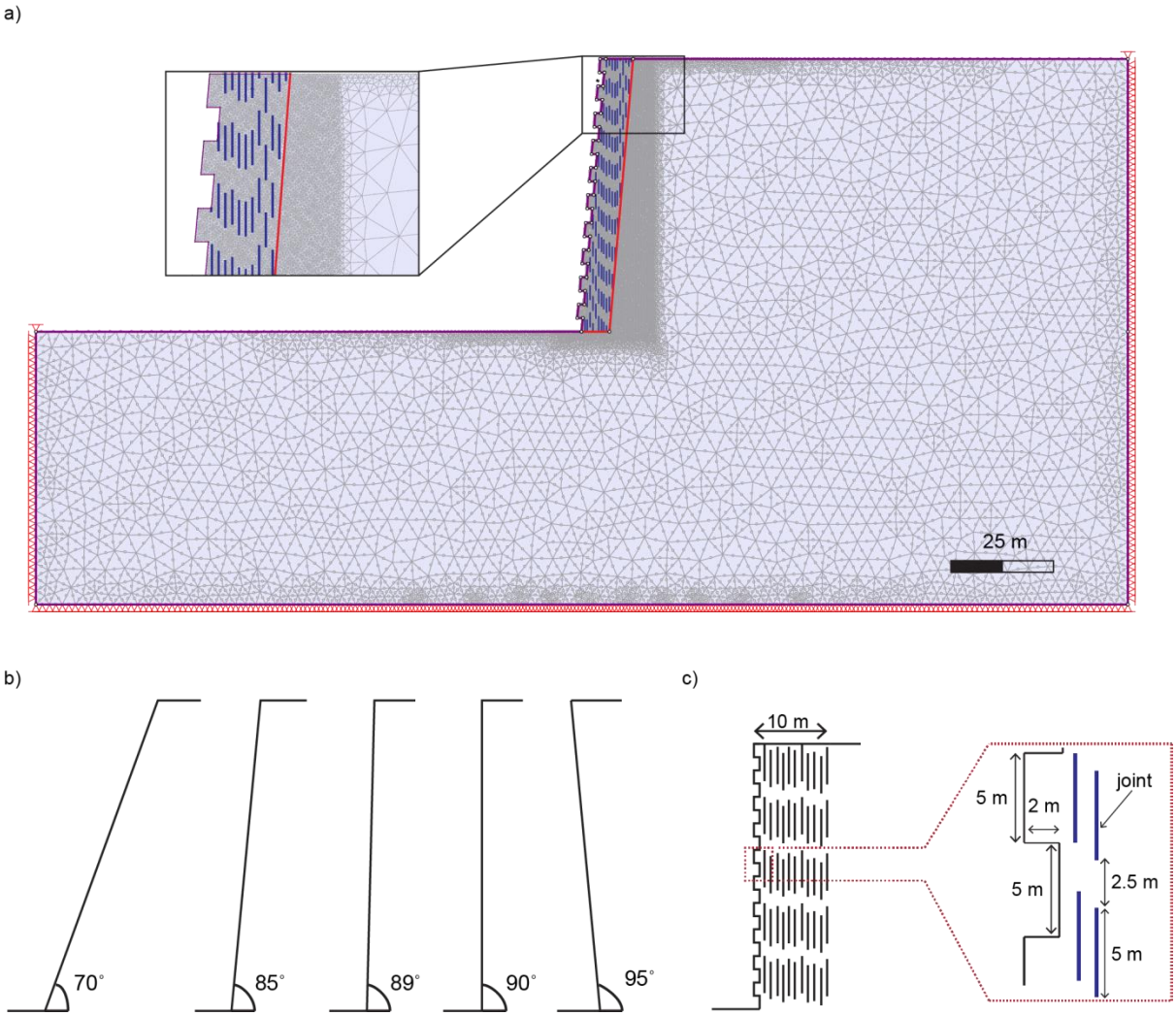

Figure 4.2: Schematic of FEM model geometries. a) Example model set-up, with a *sa* of 85°, *od* of 2 m, and *dp* of 50 %. Inset displays the high-density mesh b) The various slope angles modelled. c) Example schematic of a 90° slope with 2 m *od* and 50% *dp*. The overhanging sections are 5 m high, and separated from each other by 5 m. The discontinuities are 5 m long and spaced 1 m apart from each other. Discontinuities are located within 10 m of the slope face

4.2.2 Model outputs

125 models were created from combinations of the selected 5 values of *sa*, 4 values of *od* and 4 values of *dp*, including models with no discontinuities or overhangs (Table 4.1). For each model configuration, the sigma 1 stress (σ^1), sigma 3 stress (σ^3), volumetric strain (ε_v) and maximum shear strain (ε_{xy}) values at each finite element were exported (Table 4.2). σ^1 stress represents the in-plane (2D) major principal stress, while σ^3 is the in-plane (2D) minor principal stress (Twiss and Moore, 1992). The relationship between

σ^1 and σ^3 determines if a failure occurs in tension or compression as determined by Mohr-Coloumb failure criterion (Figure 4.3a). The criterion is defined by cohesional strength (*c),* the internal angle of friction (*φ)* and the normal stress ($\sigma_{n)}$ acting on a parcel of rock:

$$\tau = c + \varphi\sigma_n$$

Equation 4.2

Failure occurs when the line defined by the Coulomb criterion intersects the Mohr circles. The relationship between σ^1 and σ^3 defines the mode of failure from extensional shear through to compressional -shear (Figure 4.3b). Changes in stress are related to changes in strain via Hooke's Law, where the strain ($\boldsymbol{\varepsilon}$) experienced by parcel of rock is proportional to the applied stress (σ), within the elastic bounds of the rock, as defined by Young's Modulus of Elasticity (*E)*:

$$\sigma = E\varepsilon$$

Equation 4.3

Strain can be characterised by $\boldsymbol{\varepsilon}_V$, which defines the volume change of a parcel of rock, either dilation or contraction, and $\boldsymbol{\varepsilon}_{xy}$, which refers to shape change of the same parcel of rock (Figure 4.3c)(Twiss and Moore, 1992).

From the modelled results, mean values of each of the key exported variables were calculated over 0.5 m depth intervals from the base to the top of the slope for every node within 1 m of the slope surface (Figure 4.4). This is consistent with the mesh edge length. The 1 m depth zone over which the data is averaged also incorporates the effect of discontinuities on stress, with the first discontinuity located at 0.9 m depth at the top of the slope (Figure 4.2), providing an accurate analysis of stress and strain at the critical depths over which rockfall detachment occurs (e.g. Dewez et al., 2013; Lim et al., 2010; Stock et al., 2011).

Table 4.1: Model ID numbers (in bold) and associated configurations for each of the various variable combinations of overhangs and discontinuities. For each of the five slope angles 25 models were created and run.

dp (%)	*od* (m)				
	0	0.25	0.5	1	2
0	1	2	3	4	5
50	6	10	14	18	22
70	7	11	15	19	23
90	8	12	16	20	24
96	9	13	17	21	25

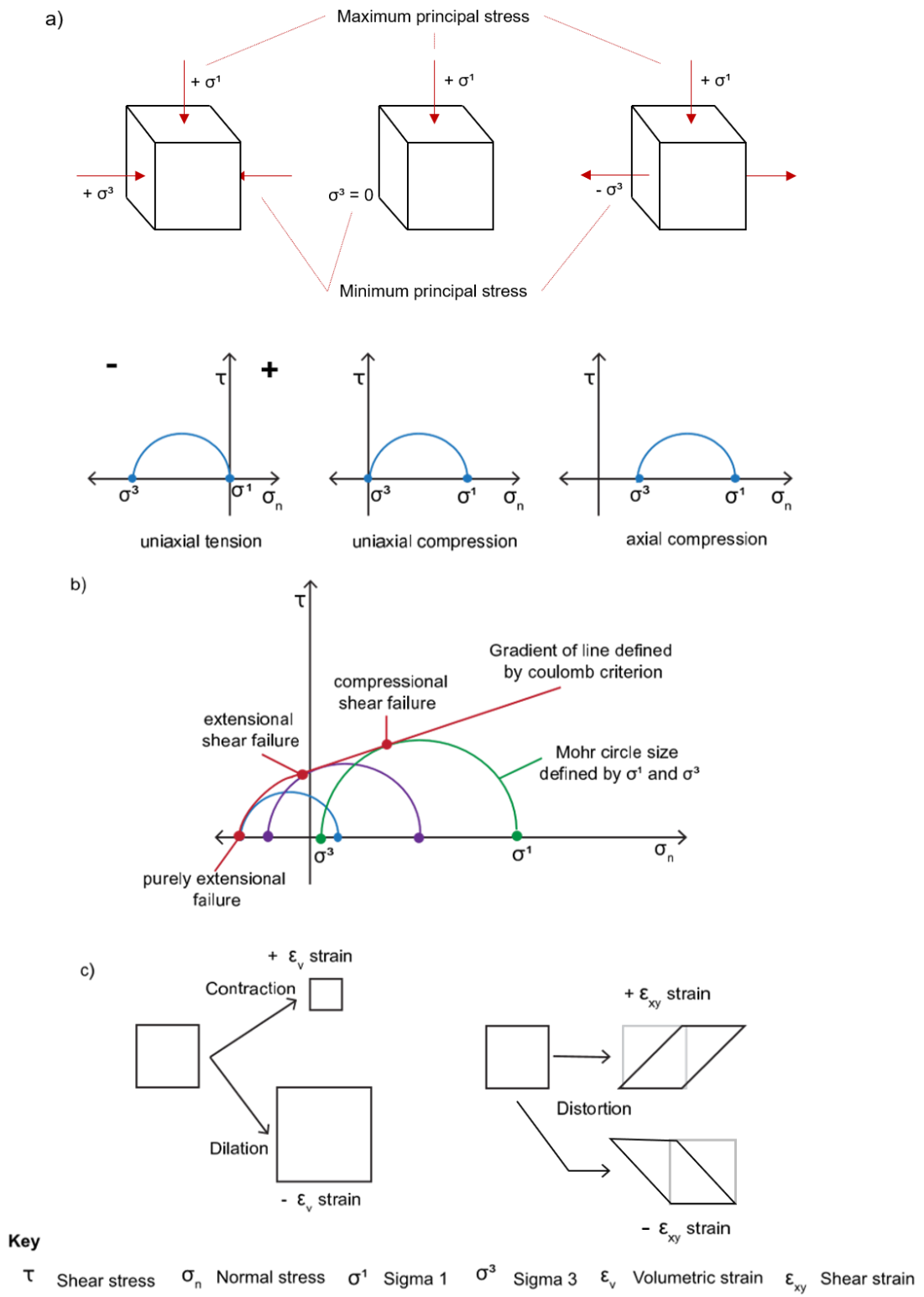

Figure 4.3: Key stress and strain variables. a) Schematic of states of stress as experienced by a parcel of rock within a slope, with confining pressure determining if σ^3 is positive or negative. These states of stress are represented by Mohr circles, with σ^1 and σ^3 defining the location and size of the circles. b) Schematic of Mohr-Coulomb failure criterion, where failure occurs when the Coulomb line intersects a Mohr circle. The location of this intersection with respect to σ_n and τ determine if failure mode is extensional, extensional-shear or compressional-shear. c) Schematic of volumetric strain and shear strain (Modified from: Twiss and Moore, 1992).

Table 4.2: Notation of stress and strain attributes, and associated descriptions and interpretations of the stress and strain experienced by a parcel of rock within a slope

		Interpretation of values			
Notation	*Property*	*Positive values*	*Negative values*	*Relative increases*	*Relative decreases*
σ^1	*Sigma 1*	Compressive stress	Extensional stress	Increased compressive stress	Decreased compressive stress
σ^3	*Sigma 3*	Compressive stress	Extensional stress	Increased compressive stress and/or decreased tensile stress	Decreased compressive stress and/or greater tensile stress
ε_{xy}	*Maximum shear strain*	Clockwise distortion of rock	Anti-clockwise distortion of rock	Increased distortion	Reduced distortion.
ε_v	*Volumetric strain*	Contraction of rock	Dilation of rock	Increased contraction	Increased dilation.

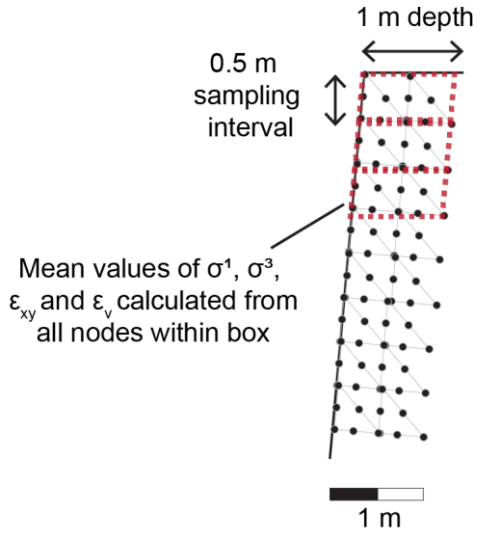

Figure 4.4: Calculation of mean values of σ^1, σ^3, ε_{xy} and ε_v. All nodes within sampling boxes are included in calculation of mean

4.2.3 Model implications

Analysis of the exploratory model results considers the interaction of *sa*, *od* and *dp* in creating topographic stress concentrations and determining the strain behaviour in a slope. From this, general rules were established. These rules were applied to two rockfall datasets captured over both monthly and annual time scales at Boulby, North Yorkshire,

UK. Slope angle and overhangs were characterised from digital elevation models (DEM) of Boulby, with the rockfall scar database of Chapter 3 providing information on *dp* (i.e. the opposite of *rb%*). Coincidence between classified features and rockfall occurrence was used to determine the influence of stress distribution and strain behaviour on rockfall failure.

4.2.4 FEM model constants

4.2.4.1 Material properties

Material properties, outlined in Table 4.3, were those of a generic isotropic sedimentary rock, which behaved elastically. The isotropic and elastic nature of the rock were selected to model a slope with properties constant in every direction (i.e. no anisotropy), which exhibited brittle fracture (Hoek and Brown, 1997). The strength properties were equivalent to those of Skinningrove Siltstone, a lithological unit that forms part of the slope at Boulby (see Chapter 5 for geotechnical testing results). These properties were chosen so that the stress and strain experienced by the FEM models were similar to those of the rockfalls recorded at Boulby.

As outlined above, vertical stress (σ_v) is a function of depth and the mass of material. The horizontal stress at a point in a slope is determined via the *k* ratio (Twiss and Moore, 1992). The *k* ratio is calculated from material properties as represented by Poisson's Ratio (*v)* and the vertical stress, via the equation outlined below:

$$k = \frac{v}{1 - v}\,\sigma_V$$

Equation 4.4

Poisson's Ratio measures elasticity via the ability of a rock to expand in response to applied compression (Jaeger et al., 2007). A *k* ratio of 0.43 was calculated from an assumed Poisson's Ratio of 0.3, derived from data on the geotechnical properties of the different lithological units present in Boulby as outlined in Lim et al., (2010).

4.2.4.2 Discontinuity properties

Discontinuities were incorporated as discrete breaks within the mesh and assigned very weak strength properties (Table 4.3), as the modelling is aimed at better understanding stress and strain concentrations at rock bridges, rather than the absolute failure of rock. Once these rock bridges break, kinematic release along discontinuities which daylight at the slope surface occurs, and as such discontinuities provide little frictional or cohesional resistance to overall stability (e.g. Einstein et al., 1983; Goodman and Shi, 1985; Wyllie and Mah, 2004).

For simplicity, one vertical (90°) discontinuity set located within 10 m of the slope surface was considered within the conceptual models. The analysis in Chapter 3 indicates that rockfall scars are parallel to the slope face, with rock bridges predominantly (70%) located co-planar to these scar surfaces (see Figure 3.14).

Discontinuity length was kept constant at 5 m (Figure 4.2). Overhangs were defined as 5 m high blocks of protruding rock within the model, separated from each other by a 5 m vertical spacing (Figure 4.2). This geometry is similar to that of a horizontally-bedded cliff face with variations in mechanical strength of rocks creating overhangs. The spacing of overhangs and discontinuity length were chosen to be the same, with the implicit assumption that discontinuity length interacts with bedding to dictate the shape of overhangs. Discontinuity spacing is kept constant at 1 m, with the first discontinuity located 0.9 m back from the slope surface (Figure 4.2), as rockfalls are shallow (< 1 m depth) and require fracturing through a rock bridge (i.e. separating the discontinuities) co-planar to the discontinuity release surface (Chapter 3).

4.2.4.3 Overhang properties

Overhangs are considered here as 5 m high protruding blocks, which can be split into four components based on their influence on the stress distribution and strain behaviour of a slope (Figure 4.5). The greatest increases or decreases in stress and strain are experienced at the base of the overhang (Figure 4.5: 2.) and at the top of the overhang (4.), with a higher magnitude of stress and strain observed between overhangs (3.).

Overhangs themselves display a relative decrease in stress and strain (1.). Overall, the differences in values between geometry types 2, 3 and 4 are minimal compared with geometry type 1 (Figure 4.6). As such, geometry types 2, 3 and 4 are combined and defined as a concave area, with overhangs representing convex areas.

Table 4.3: Model parameters and values of the slope geometry, material properties and discontinuity characteristics of the conceptual FEM models.

	Parameters	Values	Justification
	Model constants		
Slope properties	Slope height (m)	100	Same magnitude as cliff height at Boulby
Material properties	Cohesion (MPa)	1.141	Generic sedimentary rock properties based on geotechnical testing (see Chapter 5) to create generic sedimentary rock properties
	Friction angle °	44.02	
	Tensile strength (MPa)	0.446	
	Unit weight of rock (MN/m³)	0.022	
	Young's Modulus (MPa)	10000	
	Poisson's Ratio	0.3	Lim et al., (2010)
Discontinuity properties	Normal stiffness (MPa/m)	1000	Provide limited strength, and allow stress and strain to be concentrated at rock bridges
	Shear stiffness (MPa/m)	100	
	Discontinuity dip (°)	90	Chapter 3 observations
	Discontinuity length (m)	5	Coincident with overhang geometry
	Discontinuity spacing (m)	1	Rockfall depths
	Model variables		
Topography	Slope angle (°)	70, 85, 89, 90, 95	Chapter 4 analysis
	Overhang depth (m)	0.25, 0.5, 1, 2	Cai et al., 2004
Rock mass structure	Discontinuity persistence (%)	50, 70, 90, 96	Tuckey and Stead, 2006 & Chapter 3 observations

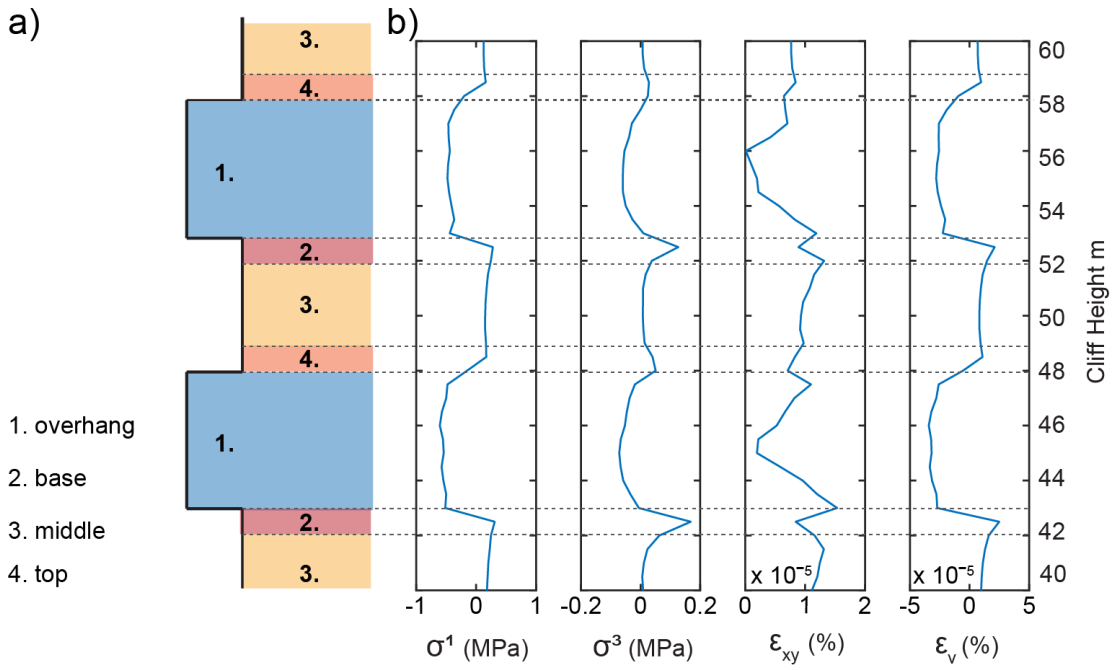

Figure 4.5: Schematic of the influence of overhangs on stress and strain, here showing the values of stress and strain for a section of a 90° slope with 2 m overhangs.

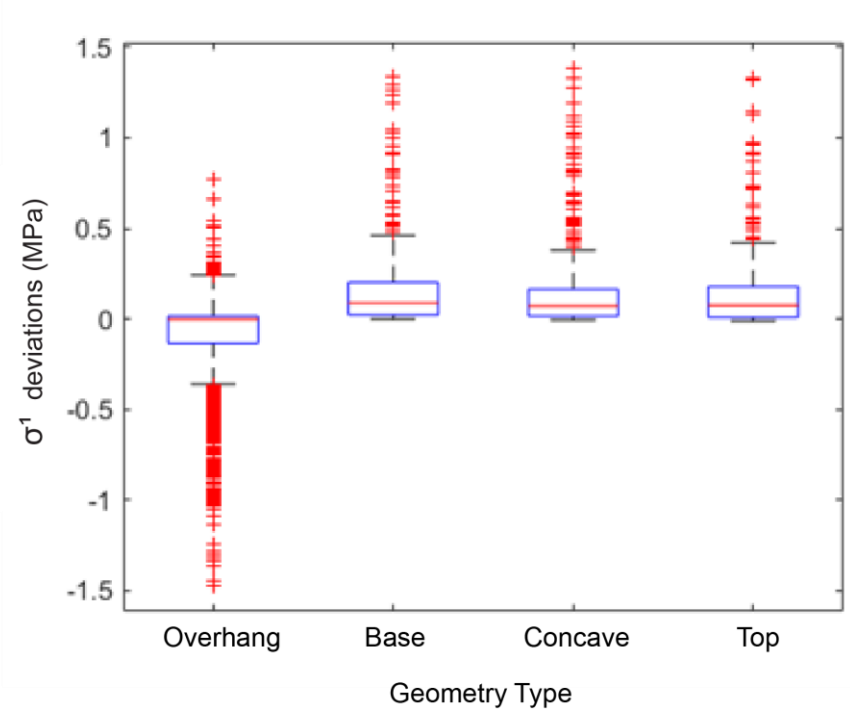

Figure 4.6: Boxplot of all σ¹ values by the four-geometry type for all models with overhangs. The geometry types are: 1) overhang, 2) base of overhang, 3) in-between the overhang and 4) top of the overhang

4.2.5 FEM model variables

4.2.5.1 Slope angle (*sa)*

Slope angles < 60° were not considered as rockfalls occur predominantly on slopes > 60° (Guzzetti et al., 2003; Loye et al., 2009). Analysis of 12 slope angles was undertaken to determine the key values of *sa* for exploratory models, which included end-member scenarios such as overhanging slopes (95° and 100°). Four characteristic slope behaviours are identified in response to changes in slope angle and height (Figure 4.7).

The first of these behaviours is manifest in slopes at 60°, 70°, 75° and 80°, characterised by a steep increase in σ^1 up to 0.1 MPa in the upper 10 m of the cliff, followed by a decrease in σ^1 to 0.01 to 0.05 MPa between 90 m and 20 m. Below 20 m a steep increase in σ^1 to 1.1 MPa occurs, indicating that for these slope angles σ^1 is concentrated primarily in the base of the slope (Figure 4.7). Secondly, slope angles of 85°, 86°, 87° and 88° are characterised by a similar increase in σ^1 of 0.1 MPa to 0.5 MPa in the upper 10 m of the cliff. This value of σ^1 is constant from 90 m to 10 m cliff height, with a steep increase in σ^1 to 1.1 MPa below 10 m occurs (Figure 4.7). Thirdly, a slope angle of 89° is characterised by a steep increase in σ^1 to ca. 0.75 MPa in the upper 30 m of the cliff. This value of σ^1 is constant from 70 m to 5 m cliff height. Below 5 m, a steep increase in σ^1 is observed to 1.1 MPa (Figure 4.7). Fourthly, slope angles of 90°, 95° and 100° are characterised by steep increases in σ^1 in the upper 20 m of the cliff to 1 MPa. This is followed by a more gentle increase in σ^1 between 2 MPa to 3 MPa at 5 m cliff height. Below this, a steep increase in σ^1 of between 2 and 8 MPa occurs (Figure 4.7). Therefore, single-degree variations in slope angle can result in an order of magnitude difference in σ^1.

Based on these four characteristic responses, slopes angles of; 70°, 85°, 89°, 90° and 95° were selected for further consideration (Figure 4.2). Both 90° and 95° were selected from one category for the models to contain both a vertical and overhanging slope.

Additionally, the basal zone displays a substantially different response in σ^1. The processes which drive rock failure in this zone may be different to the processes operating more widely across the slope face. As rockfall occurs the entire area of the cliff face (Rosser et al., 2007), the basal 5 m is not included within the following analysis of the models.

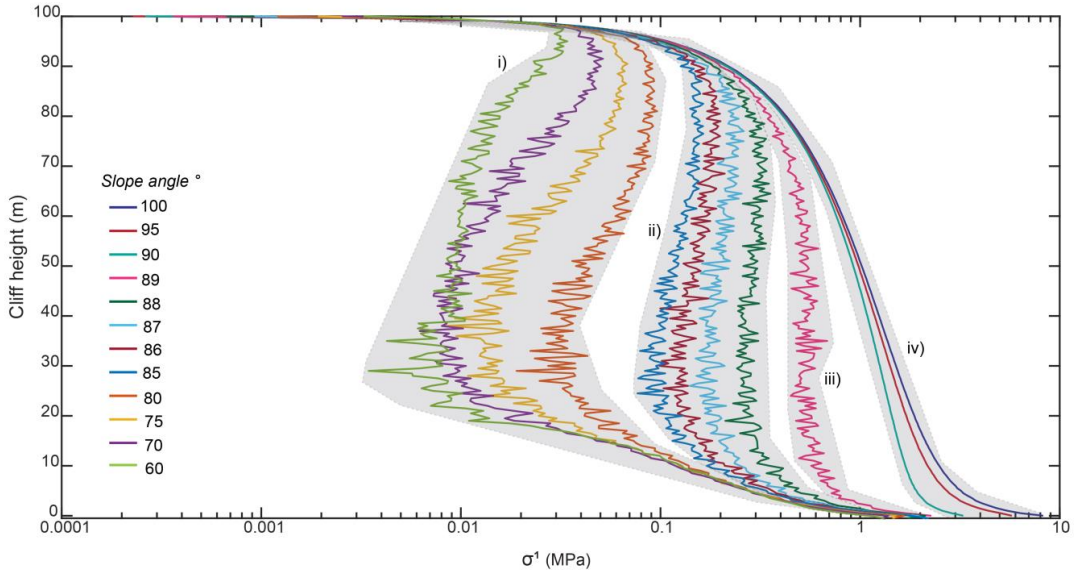

Figure 4.7: Change in σ^1 for changes in *sa* and cliff height. The different grey-shaded areas i), ii), iii) and iv) represent four characteristic behaviours.

4.2.5.2 Overhang depth (*od)*

Four values of *od* were modelled to determine the impact of protrusion on stress distribution and strain, as increases in protruding depth of material has been shown to generate greater differential and tensile stresses (Stock et al., 2012). The selected overhang depths of 0.25 m, 0.5 m, 1 m and 2 m (Table 4.3) reflect the general block size characteristics involved in brittle rockfall, as determined by Cai et al., (2004) in their study of controls on rockfall failure. Larger overhang depths result in bigger failures (Lim et al., 2010), such that if a rockfall consists of a broken overhang, the post failure surface is planar to the surrounding surfaces rather than protruding. Therefore, use of the block sizes determined by Cai et al., (2004) can reflect *od.*

4.2.5.3 Discontinuity persistence (*dp)*

Discontinuity persistence was incorporated into the models to understand how the percentage of intact rock located between individual discontinuities influences topographic stress concentrations (Jennings, 1970). The value of discontinuity persistence was based on minimum, mean and maximum estimates derived from the literature (Tuckey and Stead, 2016 and references therein), and the mean estimate derived from the dataset in Chapter 2. Analysis of literature estimates reveals minimum and mean *dp* of 50% and 90% respectively (Tuckey and Stead, 2016), while the mean rock bridge proportion (*%rb*) in Chapter 3 determined a mean *dp* of 70%. The maximum modelled persistence was 96%; this was due to difficulty in creating meshes with no acute angles for discontinuity persistence values that are >96%, as acute angles may result in inaccurate calculations of stress and strain.

4.3 Results and analysis

4.3.1 Baseline characterisation

This section details the influence of changing values of *sa* on the stress distribution and strain behaviour experienced by slopes, which contain no overhangs or discontinuities. These models form the baseline conditions from which the effects of overhangs and discontinuities on stress and strain are compared in the subsequent result sections.

4.3.1.1 Changes in σ^1

As shown in the model variable explanation (section 4.2.5.1), a single-degree variation in slope angle can have a significant impact on σ^1 (Figure 4.8a). Slope angles of 70° and 85° display an approximately constant low stress value of < 0.3 MPa for changes in cliff height. A *sa* of 89° displays 'noisier' data, with a constant σ^1 of < 0.75 MPa for changes in cliff height. The variability of the data (i.e. 'noise') may be a function of the trajectories of σ^1, which are close to, but not quite, vertical. Slope angles of 90° and 95° display an increase in σ^1 with increasing distance from cliff top (i.e. decreasing cliff height values),

reaching 2 MPa and 2.7 MPa at the cliff base. For slopes of < 90°, σ^1 is constant with change in cliff height, while for slopes of ≥ 90°, σ^1 increases with increasing overburden.

4.3.1.2 Changes in σ^3

For nearly all slope angles, σ^3 remains near zero. The exception to this is a *sa* of 70°, where values of σ^3 are negative up to a maximum of -0.044 MPa between 70 m and 20 m cliff height, and a *sa* of 85° where a steep increase in σ^3 below 10 m to 0.026 MPa occur (Figure 4.8b). The negative 'bulge' for a *sa* of 70° may be a function of a similar decrease in σ^1 observed over the same cliff heights (Figure 4.7).

4.3.1.3 Changes in ε_{xy}

Increases in slope angle result in increases in ε_{xy} (Figure 4.8c). ε_{xy} values are near zero for changes in cliff height for *sa* of 70° and 85°. A steep increase in ε_{xy} occurs below 10 m cliff height, which reaches a maximum of 0.12 x 10^{-4} % and 0.16 x 10^{-4} % for the respective slope angles. For a *sa* of 89°, a constant value of ca. 0.18 x 10^{-4} % is observed between 90 m and 10 m cliff height. Slope angles of 90° and 95° display a gentle increase in ε_{xy} with decreasing cliff height, until 10 m where more rapid increases in ε_{xy}, of up to 0.53 x 10^{-4}% and 0.92 x 10^{-4}% occur, for the respective slope angle. Patterns of increasing ε_{xy} for each slope angle are similar to the patterns displayed in response to varying σ^1, indicating that changes in σ^1 may result in changes to ε_{xy}, and vice versa. Distortion as a result of increased ε_{xy} is greatest at the base of the slope.

4.3.1.4 Changes in ε_v

Increases in slope angle result in decreases in ε_v (Figure 4.8d). Slope angles of 70° and 85° display near zero ε_v with changes in cliff height. A rapid increase in ε_v occurs below 5 m cliff height of up to 0.7 x 10^{-4}% and 0.95 x 10^{-4}% for the respective slope angles. For a *sa* of 89°, a decrease in ε_v value of ca. -0.2 x 10^{-4}% is observed between 80 m

and 5 m cliff heights. For a *sa* of 90°, a gentle decrease in ε_v of up to -0.4 x 10^{-4}% occurs between 100 m and 15 m cliff height. For a *sa* of 95°, a gentle decrease in ε_v to -0.43 x 10^{-4}% occurs between 100 m and 5 m cliff height. All slopes display an increase in ε_v at the base of the slope. The negative values of ε_v recorded for *sa* of 89°, 90° and 95° indicate that rock may be more able to dilate (Figure 4.3). The low σ^1 and σ^3 values for *sa* of 70° and 85° may not be great enough to result in volume changes and vice versa.

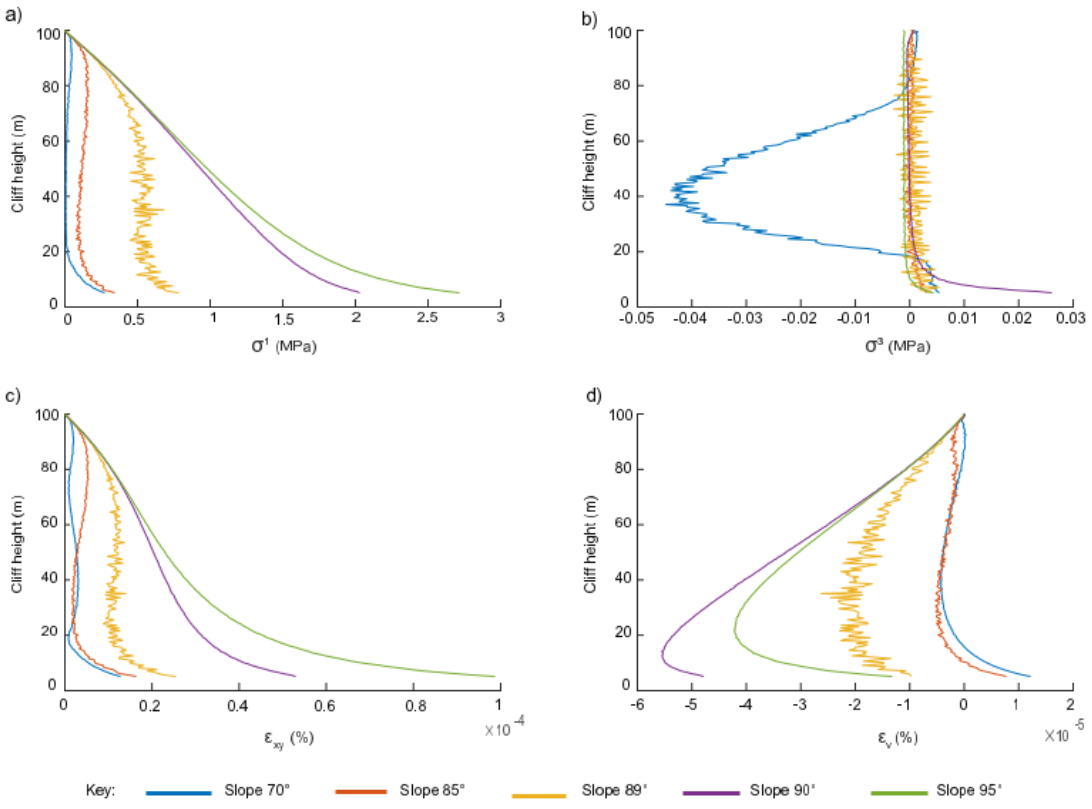

Figure 4.8: Baseline trends for each value of *sa*, of a) σ^1, b) σ^3, c) ε_{xy} and d) ε_v.

4.3.2 Impact of overhangs

Overhangs result in deviations of stress and strain away from baseline values. To analyse the magnitude of these deviations, the baseline trend for each slope angle is subtracted from the response of models with overhangs (Table 4.1). The values in this section are therefore de-trended relative values of stress and strain, and not the actual

absolute modelled values (Table 4.2). Data is presented as scatter plots for σ^1. The other variables display the same response as seen in the scatter plots of σ^1 in Figure 4.9 and Figure 4.10, and therefore for brevity, analysis of their modelled results have been summarised in boxplots in Figure 4.11 and Figure 4.12. Geometry (i.e. concave or overhang), *sa* and *od* influence the nature and magnitude of deviations of stress and strain from the baseline values.

4.3.2.1 Influence of slope angle (*sa*)

For overhangs, each overhang depth in slopes at 70° and 85° displays an approximately constant value of σ^1 with respect to changes of cliff height, with a steep decrease in σ^1 relative to baseline below 10 m cliff height (Figure 4.9a & Figure 4.9b). Concave geometries at 70° and 85° also display approximately constant values (i.e. no trend in response to an increase or decrease in σ^1) for each overhang depth, but with no increase relative to baseline below 10 m (Figure 4.10).

For concave geometries, the deviations in σ^1 for slopes at 89°, 90° and 95° linearly increase with decreasing cliff height (Figure 4.10). A *sa* of 89° displays the highest increases in σ^1 relative to baseline, with a maximum value of σ^1 of ca.1.4 MPa. The boxplots of Figure 4.11 indicate that σ^3, ε_{xy} and ε_v also increase relative to baseline with decreasing cliff height for these slope angles. However, the shifts in ε_{xy} are an order of magnitude lower than those of baseline values (x 10^{-5}: Figure 4.11, x 10^{-4}: Figure 4.8) while for σ^1 and σ^3 they are comparable to baseline values (x 10^0 : Figure 4.11, x 10^0 : Figure 4.8).

A *sa* of 89° returns the highest deviation from baseline in σ^1 with an increase of 1.4 MPa (Figure 4.10c). The trajectories of σ^1 may act in such a way to create greater topographic stress concentrations than observed for the slopes at 90° and 95°.

Overhangs on the 89° slope switch mid-slope (40 m to 60 m cliff height) from decreasing σ^1 relative to baseline in the upper half of the slope, to increasing σ^1 relative to baseline

in the base (Figure 4.9c). For overhangs, σ^1 decreases relative to baseline for 90° and 95° slopes, with decreasing cliff height up to maximum relative decrease of -1.5 MPa for a 95° slope (Figure 4.9d & Figure 4.9e). σ^3 values in overhangs show a general reduction relative to baseline for 89°, 90° and 95° slopes, with the largest decrease of up to -1.1 MPa recorded for the 90° slope. ε_{xy} and ε_v also decrease relative to baseline for 89°, 90° and 95° slopes (Figure 4.11).

Overall, observations of the data indicate:

- For both overhang and concave geometries deviations from baseline are lowest for 70° and 85° slopes, for all values (σ^1, σ^3, ε_{xy} and $\varepsilon_{v)}$ (Figure 4.11).
- An increase in the magnitude of deviations from baseline occurs between 85° and 89°. This step-change coincides with a change from constant to increasing σ^1 values with changes in cliff height (Figure 4.9 and Figure 4.10).
- This means that for 70° and 85° slopes, the impact of overhangs on stress distribution and strain behaviour does not change with cliff height, while for ≥ 89° slopes, overhangs located at the base of the slope have an amplifying effect compared to those located at the top of the slope.

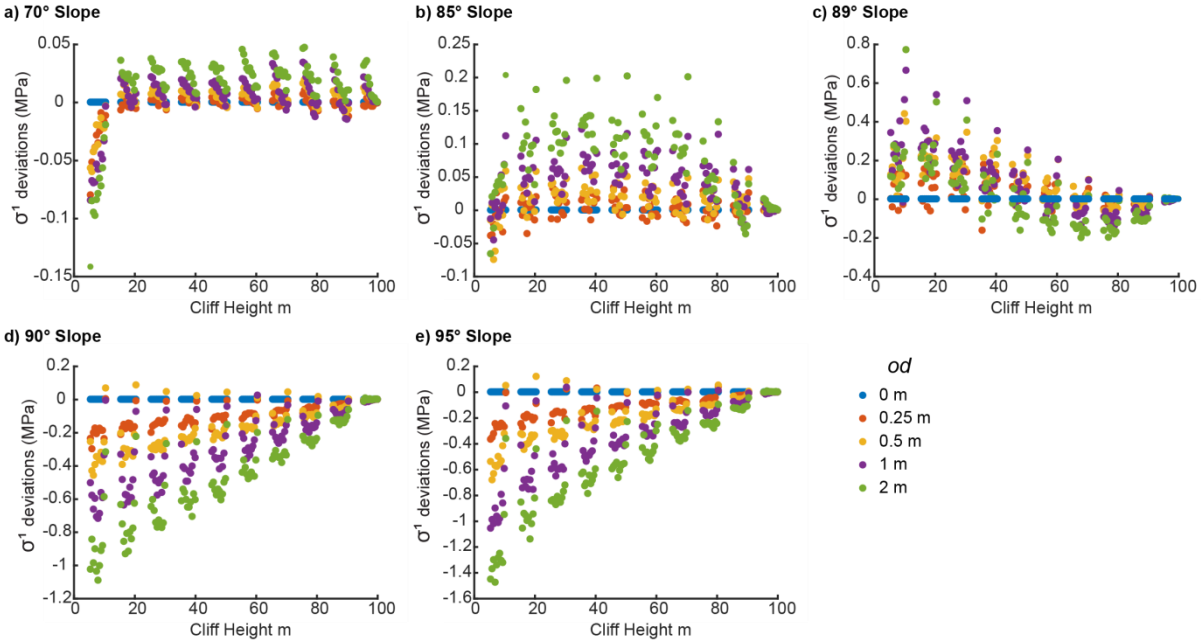

Figure 4.9: The impact of cliff height and value of *od* on deviations of σ¹ from baseline, at overhangs. Positive de-trended σ¹ values indicate elevated σ¹ values relative to baseline, while negative values indicate a decrease in stress relative to baseline. a) to e) represent the different modelled slope angles (*sa*). It is important to note that the scale between each scatter plot changes.

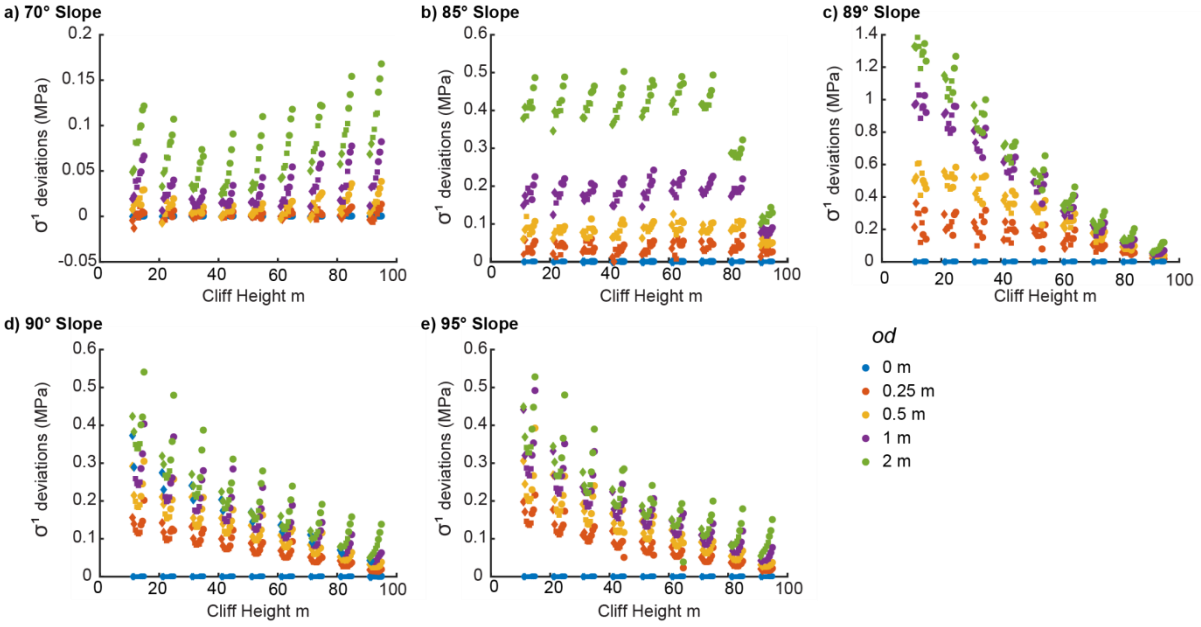

Figure 4.10: The impact of cliff height and values of *od* on deviations of σ¹ from baseline, at concavities. Positive de-trended σ¹ values indicate elevated σ¹ values relative to baseline, while negative values indicate a decrease in stress relative to baseline. a) to e) represent the different modelled slope angles (*sa*). It is important to note that the scale between each scatter plot changes.

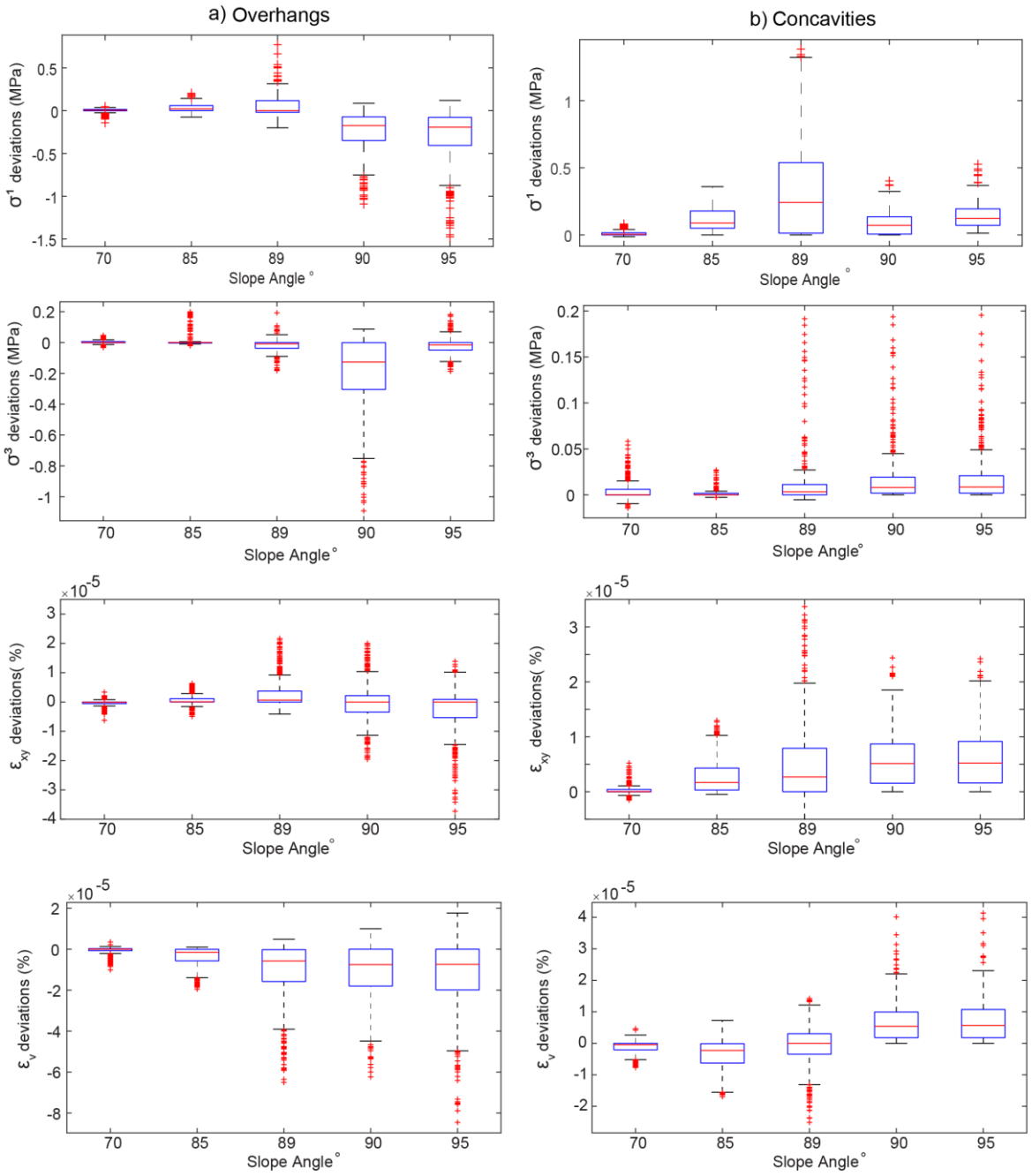

Figure 4.11: Response of σ^1, σ^3, ε_{xy} and ε_v at a) overhangs and b) concavities to differences in the value of *sa*.

4.3.2.2 Influence of overhang depth (*od)*

For overhang geometries, increases in overhang depth (*od)* are associated with larger ranges in values for σ^1, and σ^3, and slight increases in ε_{xy}. The mean values of ε_v show the clearest decrease, from -0.32 x 10^{-5} at an *od* of 0.25 m to -1.92 x 10^{-5}, at an *od* of 2 m (Figure 4.12).

Concave geometries display increasing σ^1, σ^3, ε_{xy} and a wider range of ε_v with increasing *od* (Figure 4.12). The mean value of σ^1 shifts from 0.02 MPa to 0.13 MPa from an *od* of 0.25 m to an *od* of 2 m, as does the mean of σ^3 from 0.006 MPa to 0.12 MPa. Mean values of ε_{xy} increase from 0.17 x 10^{-5}% at an *od* of 0.25 m to 0.93 x 10^{-5} % at an *od* of 2 m.

Overall, observations of the data indicate:

- Larger overhang depths result in a greater range of deviation from respective baseline values. This is true for both geometry types, and all values of σ^1, σ^3, ε_{xy} and ε_v (Figure 4.12).
- For slopes ≥ 89°, where the effects of overhangs are amplified with depth (Figure 4.9 and Figure 4.10), the influence of increasing *od* will therefore be greatest at the base of the slope, with deviations in σ^1 of ca. 1.4 MPa from baseline (Figure 4.10).
- For slopes < 89° the influence of increasing *od* will be constant with changes in cliff height.

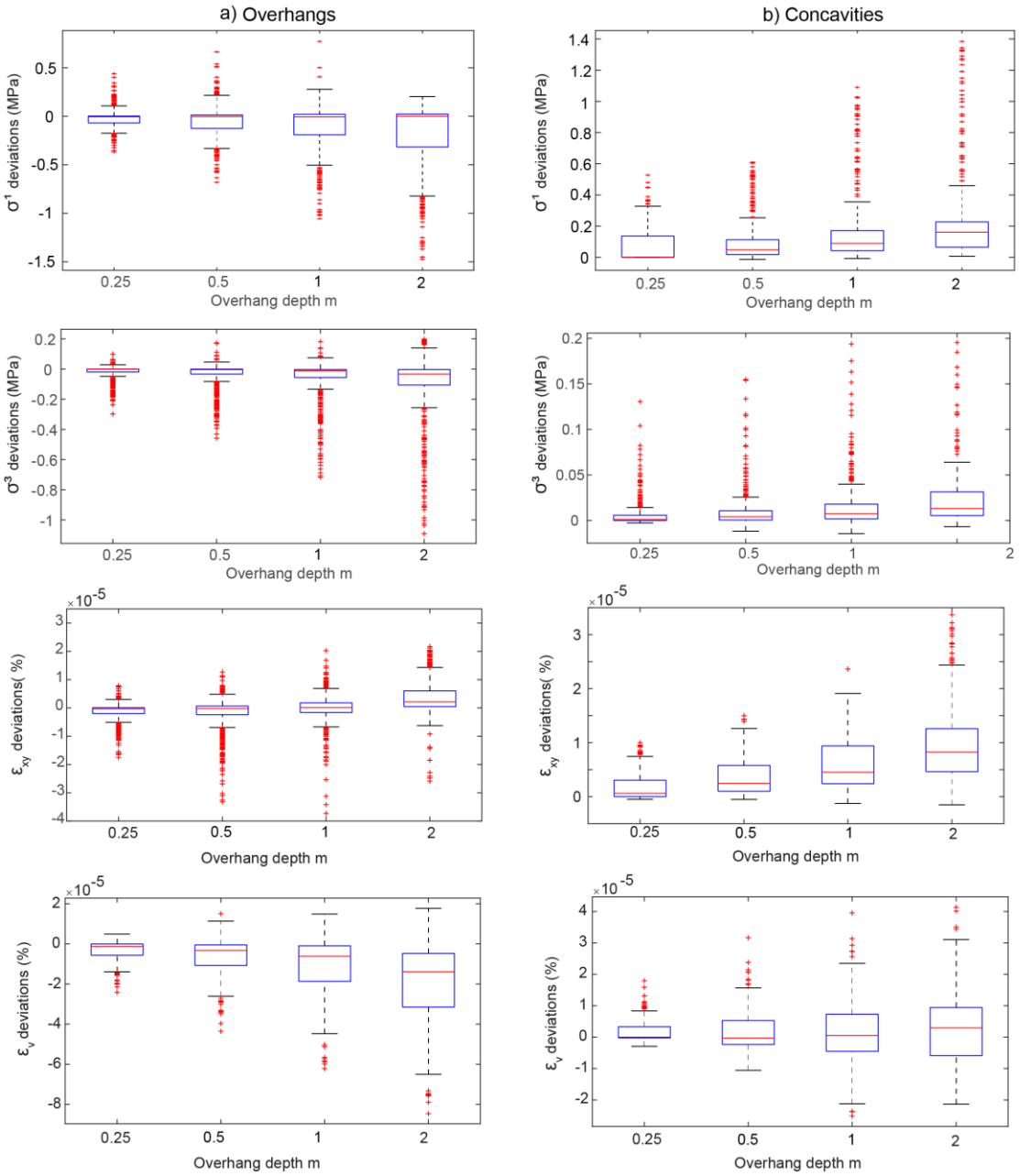

Figure 4.12: Response of σ^1, σ^3, ε_{xy} and ε_v at a) overhangs and b) concavities to changes in value of *od*.

4.3.3 Impact of discontinuities

To understand the impact of discontinuity persistence on stress distribution and strain behaviour, the representative baseline trend for each model with discontinuities was subtracted, as was the trend of the corresponding representative *od* model (Table 4.1). This de-trending removed both the effect of stress and strain as a result of slope angle

and overhang topography, to highlight the impact of discontinuities only. Deviations in σ^1, σ^3, ε_{xy} and ε_v, reported below, are only a result of discontinuities (Table 4.2).

The inclusion of joints within the model resulted in an increase in the range of recorded stress and strain values, with both positive and negative deviations observed for all variables regardless of *sa* or geometry type (Figure 4.13). The magnitude of the deviations as a result of discontinuities observed at overhangs (Figure 4.13) are the same order of magnitude as modelled values for overhangs with no discontinuities (Figure 4.11). Maximum deviations in σ^1 are ca. 0.5 MPa for models with discontinuities (Figure 4.13), and ca. 1.5 MPa for models with overhangs (Figure 4.11), while for σ^3 they are ca. 0.2 MPa for models with discontinuities (Figure 4.13), and ca. 1 MPa for models with overhangs (Figure 4.11). For ε_{xy} and ε_v, maximum deviations are both ca. 4 x 10^{-5}% and ca. 8 x 10^{-5}%, respectively (Figure 4.11 and Figure 4.13). Discontinuities and overhangs, therefore, have a similar influence on the stress distribution and strain behaviour of the near-surface of a slope.

A less distinct stress and strain pattern is observed for models with only discontinuities (Figure 4.14) in comparison to models with only overhangs (Figure 4.5). The data is noisy, but generally higher values of σ^1 and ε_{xy} relative to baseline are observed at discontinuity tips. The pattern of σ^3 and ε_v is variable with respect to rock bridge and discontinuity location. Lower values of σ^1 of up to -0.037 MPa, and ε_{xy} of up to -0.81 x 10^{-6}% are observed along the extent of discontinuities (Figure 4.14). The discontinuities located closest to the slope surface record the highest deviations from baseline for σ^1, σ^3 and ε_{xy}.

Within the 1 m zone of the near-surface, the location of discontinuities relative to the slope surface, and the effect of overlapping discontinuities, may create the observed heterogeneity.

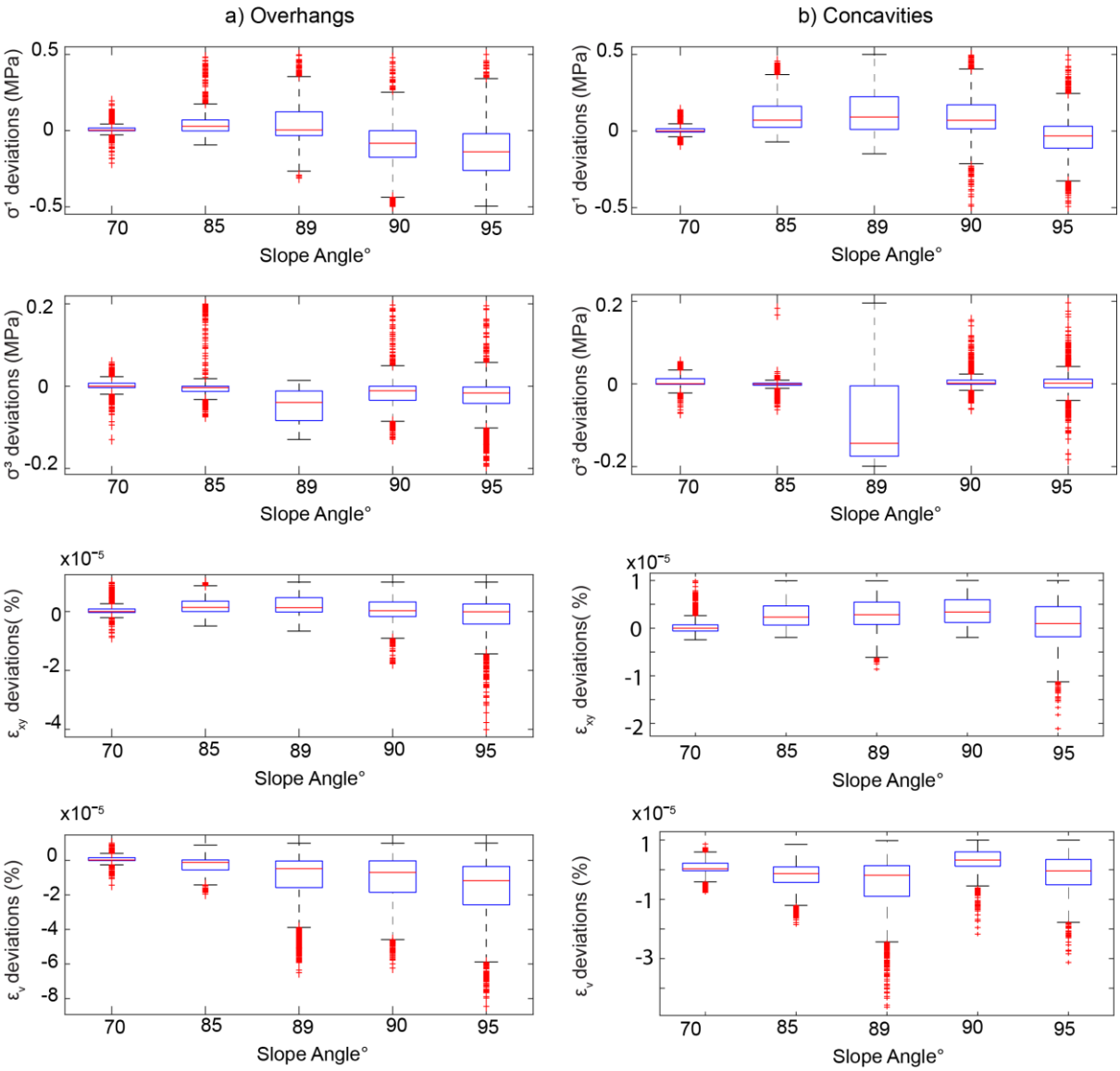

Figure 4.13: Response of σ^1, σ^3, ε_{xy} and ε_v deviations at a) overhangs and b) concavities to differences in values of *sa.*

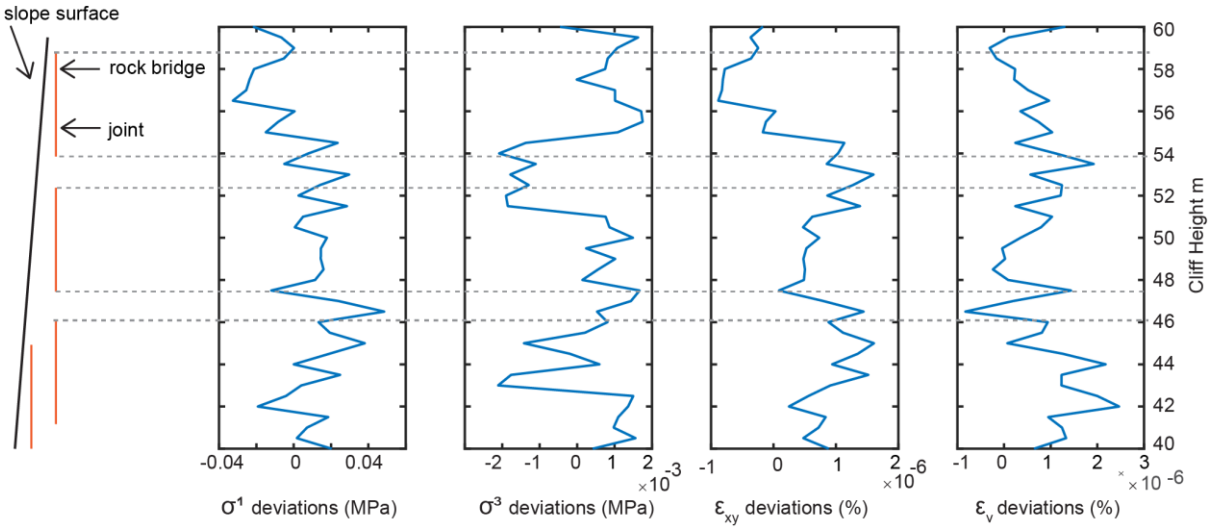

Figure 4.14: Schematic of the influence of discontinuities on stress and strain, here showing the de-trended values of a section of an 85° slope with a *dp* of 70 %.

4.3.3.1 Influence of slope angle *(sa)*

For each value of *od* in slopes at 70° and 85°, the value of σ¹ remains constant with respect to changes in cliff height, apart from cliff heights > 10 m where a steep increase in both negative and positive deviations of σ¹ of up to 0.2 MPa occurs (Figure 4.15 and Figure 4.16).

For overhangs on a slope of 89°, values of σ¹ relative to baseline decrease in the upper half of the cliff between 90 m and 40 m, before increasing relative to baseline below > 40 m (Figure 4.15). For concave geometries on a slope of 89°, σ¹ increases with decreasing cliff height. (Figure 4.16).

For concave geometries on a 90° slope, each value of *od* displays an increase in σ¹ relative to baseline with decreasing cliff height (Figure 4.16). For overhang geometries in the same models, a decrease in σ¹ relative to baseline occurs with decreasing cliff height (Figure 4.15). At the edges of overhangs, each value of *od* increases in σ¹ relative to baseline. These positive σ¹ deviation edge values represent the transition from overhanging to concave geometries.

For concave geometries in a slope of 95°, each value *od* displays both an increase and decrease in σ^1 with decreasing cliff height. This range in deviations increases towards the base of the cliff, with this zone recording the largest range of σ^1 from 0.4 MPa to -0.4 MPa (Figure 4.16). For overhang geometries in a slope of 95°, each value of *od* displays a decrease in σ^1 with decreasing cliff height, though positive deviations in σ^1 of up to 0.5 MPa occur (Figure 4.15). These positive deviations are more prevalent below > 40 m.

Overall, observations of the data indicate:

- The influence of discontinuities on the stress and strain behaviour of a slope increases with increasing slope steepness (Figure 4.13).
- The effect of discontinuities for slopes of < 89° does not change with decreasing cliff height, apart from at the base of the slope. Conversely, the effect of discontinuities for slopes ≥ 89° increases with decreasing cliff height. Therefore, discontinuities are more important at the base of the slope for stress and strain distribution.
- For both geometry types, the magnitude of deviation of σ^1, σ^3, ε_{xy} and ε_v for 70° and 85° slopes is smaller compared to slopes ≥ 89°, apart from σ^3 values in concave geometries (Figure 4.13).
- The effect of discontinuities on values of stress and strain is similar to models with overhangs only. An 89° slope does not appear to delineate step-changes in behaviour as seen for models with overhangs only, apart from the larger interquartile range (*iqr*) of negative deviations in σ^3 modelled at concavities (Figure 4.13b)

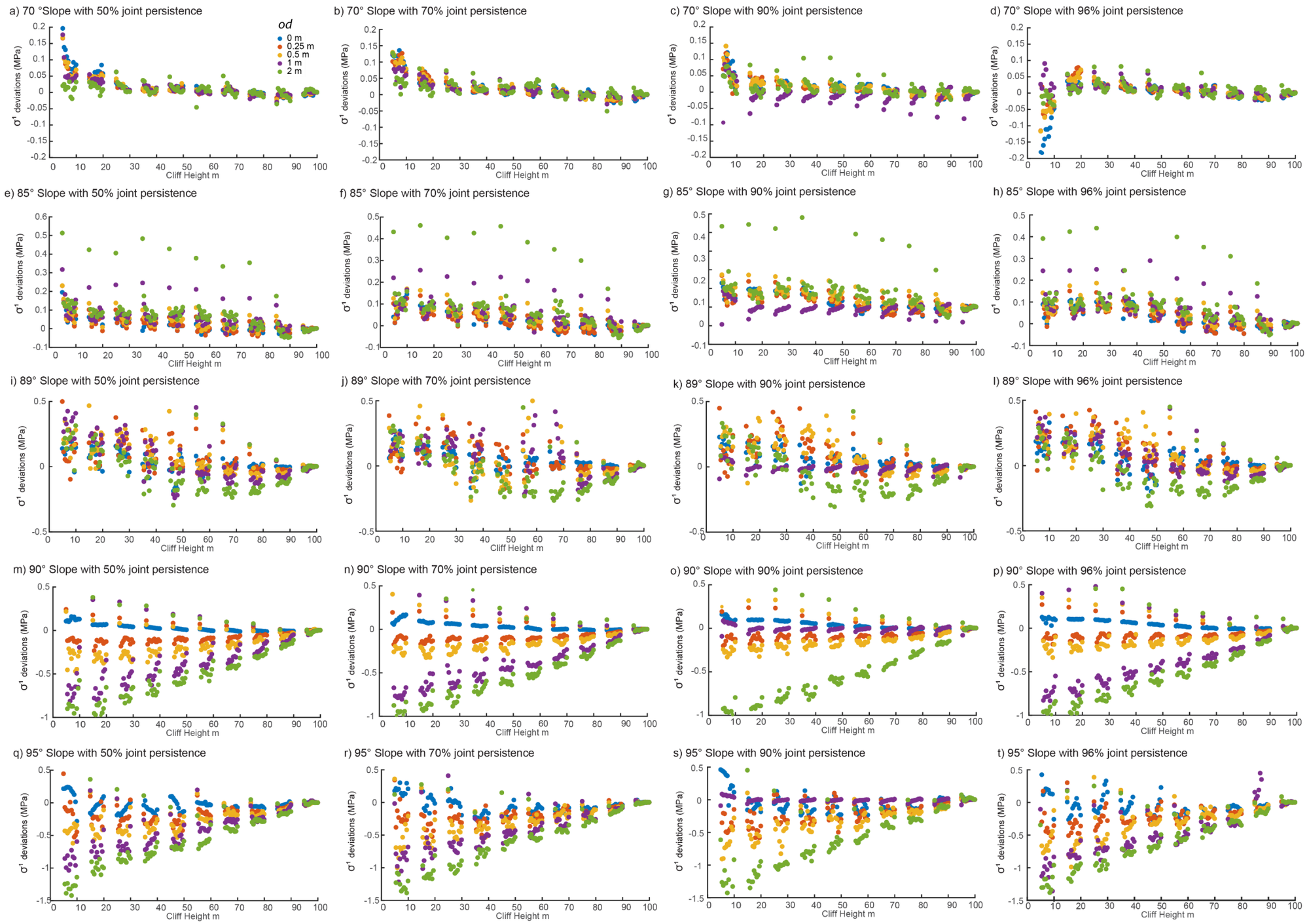

Figure 4.15: The influence of changes in value of *dp*, with respect to changes in cliff height and *od*, on deviations of σ¹ from baseline at overhangs. Positive de-trended σ¹ values indicate elevated σ¹ values relative to baseline, while negative values indicate a decrease in stress relative to baseline. The scatter plots a) represent the various modelled *dp* values for: a) to d) a 70° slope. e) to h) an 85° slope, i) to l) an 89° slope, m) to p) a 90° slope, and q) to t) a 95° slope. It is important to note that the scale between each scatter plot changes.

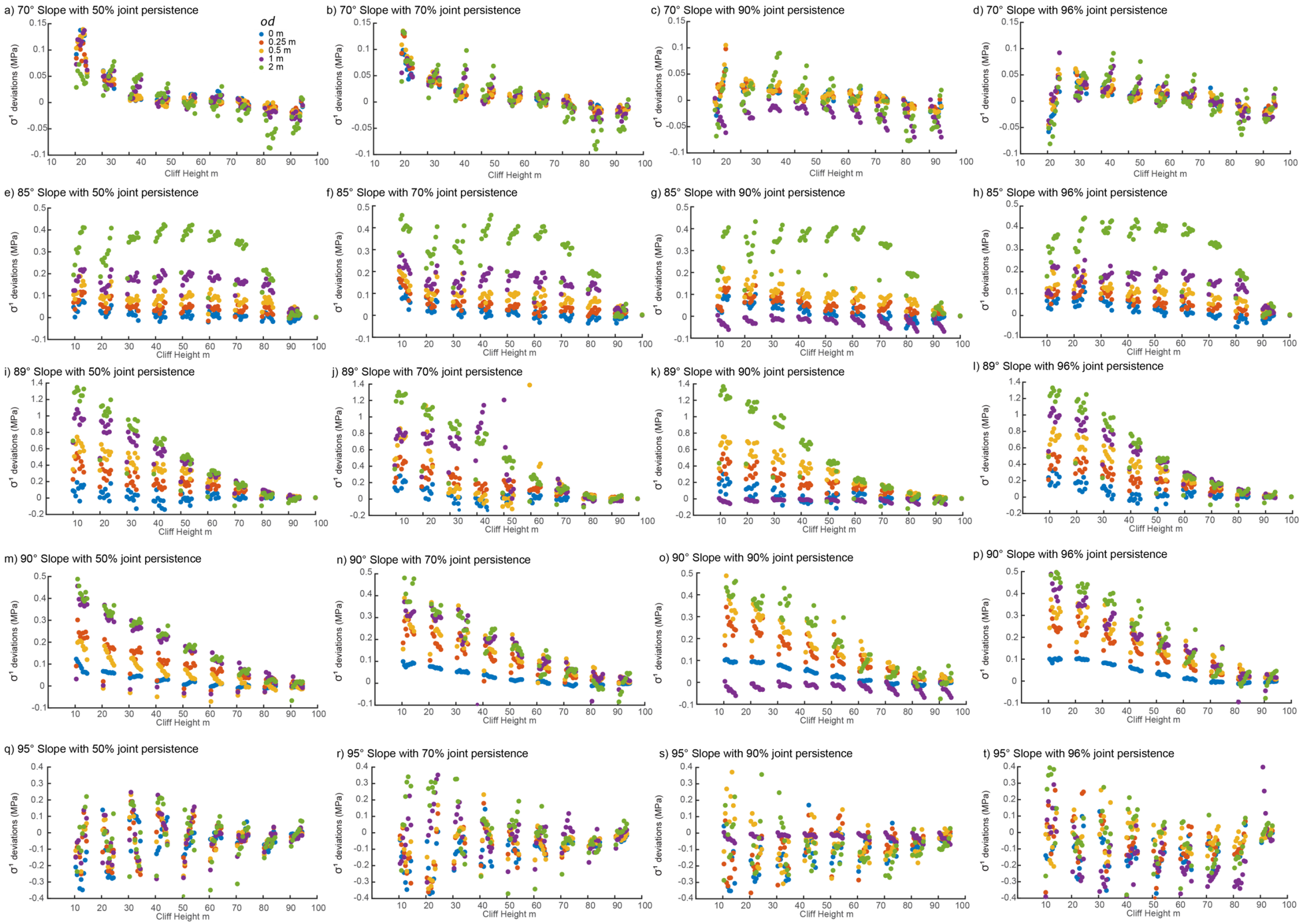

Figure 4.16: The influence of changes in value of *dp*, with respect to changes in cliff height and *od*, on deviations of σ¹ from baseline at concavities. Positive de-trended σ¹ values indicate elevated σ¹ values relative to baseline, while negative values indicate a decrease in stress relative to baseline. The scatter plots a) represent the various modelled *dp* values for: a) to d) a 70° slope. e) to h) an 85° slope, i) to l) an 89° slope, m) to p) a 90° slope, and q) to t) a 95° slope. It is important to note that the scale between each scatter plot change

4.3.3.2 Influence of overhang depth (*od)*

For overhang geometries, increases in *od* are associated with larger interquartile ranges (*iqr)* in values for σ^1 and σ^3, along with a decrease in mean ε_v, while there is no change in the distribution of ε_{xy} values (Figure 4.17). For σ^1, an *od* of 0.25 m displays an *iqr* of 0.04 MPa, while an *od* of 2 m has an *iqr* of 0.06 MPa. The same can be seen for σ^3, where an *od* of 0.25 m has an *iqr* of 0.008 MPa, while an *od* of 2 m has an *iqr* of 0.06 MPa. The mean values of ε_v show the clearest decrease from -0.033 x 10^{-5} % at an *od* of 0.25 m to -0.11 x 10^{-5} % at an *od* of 2 m*.*

Concave geometries display a larger *iqr* in σ^1, σ^3, ε_{xy} and ε_v values with increasing *od*. The *iqr* of σ^1 shifts from 0.04 MPa at an *od* of 0.25 m to 0.077 MPa at an *od* of 2 m. Similarly, for σ^3, where an *od* of 0.25 m has an *iqr* of 0.007 MPa, while an *od* of 2 m has an *iqr* of 0.07 MPa. The *iqr* in ε_{xy} increase from 0.5 x 10^{-5} % at an *od* of 0.25 m to 1.15 x 10^{-5} % at an *od* of 2m, as does the *iqr* of ε_v increases from 0.29 x 10^{-5} % at an *od* of 0.25 m to 0.42 x 10^{-5} % at an *od* of 2m.

Overall, observations of the data indicate:

- Increases in *od* result in greater deviations of σ^1 from baseline for both geometry types (Figure 4.15 and Figure 4.16).
- The lack of a definitive increase or decrease in all four stress and strain values, apart from ε_v in overhangs, suggests that changes in overhang depth are not a dominant control on stress distribution and strain behaviour within models with discontinuities.

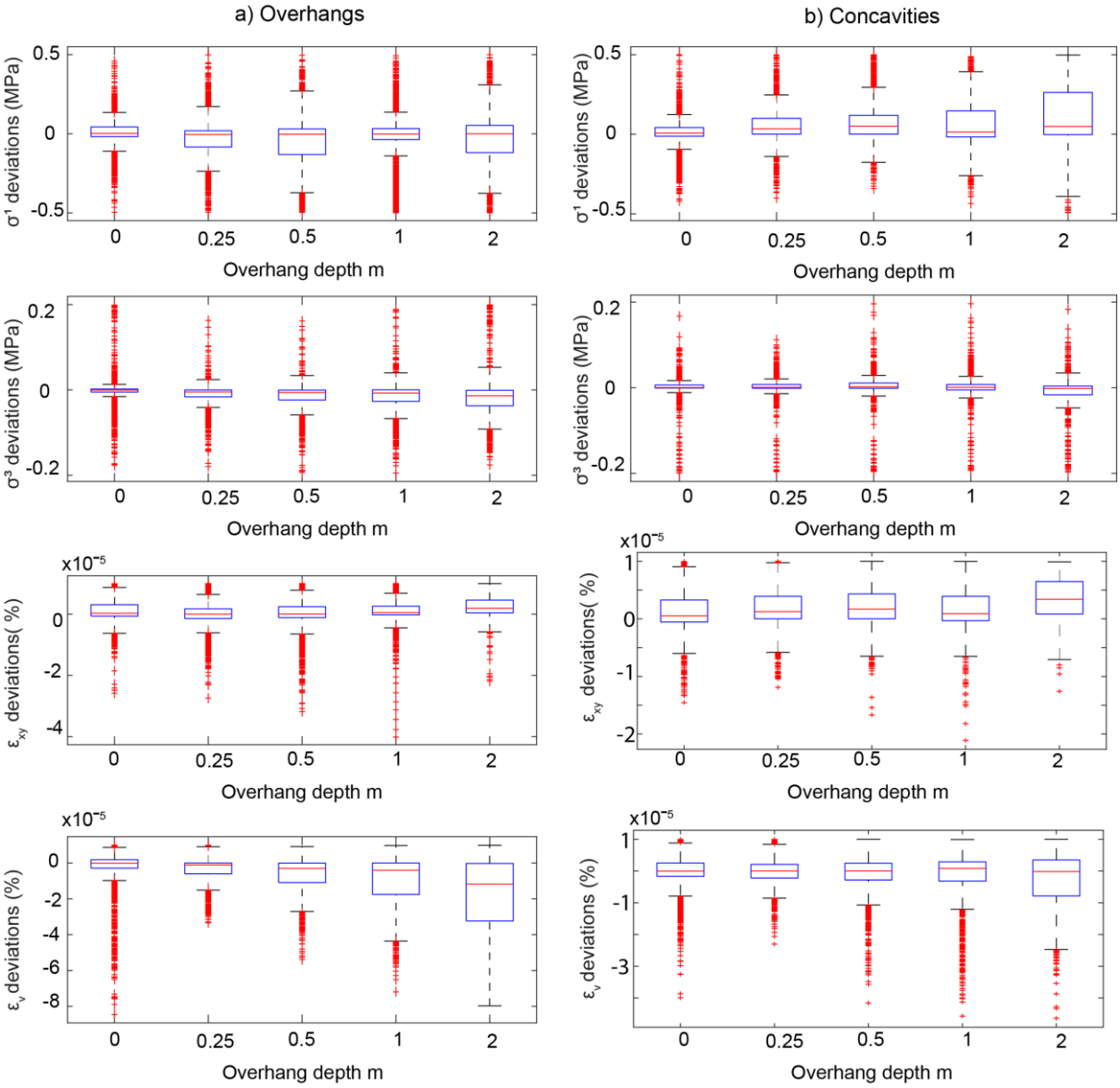

Figure 4.17: Response of σ^1, σ^3, ε_{xy} and ε_v deviations at a) overhangs and b) concavities to differences in values of *od*.

4.3.3.3 Influence of discontinuity persistence (*dp)*

Changes in the value of *dp* have a limited influence, with the range and values of σ^1, σ^3, ε_{xy} and ε_v deviations from baseline similar for each value of *dp* (Figure 4.18). ε_{xy} in concave geometries display the greatest change, with the *iqr* of values increasing from 0.7 x 10^{-5} % at a *dp* of 50% to 0.81 x 10^{-5} % at a *dp* of 96%. This increase in ε_{xy} suggests that greater distortion may occur as the value of *dp* increases, and rock bridges proportion is less.

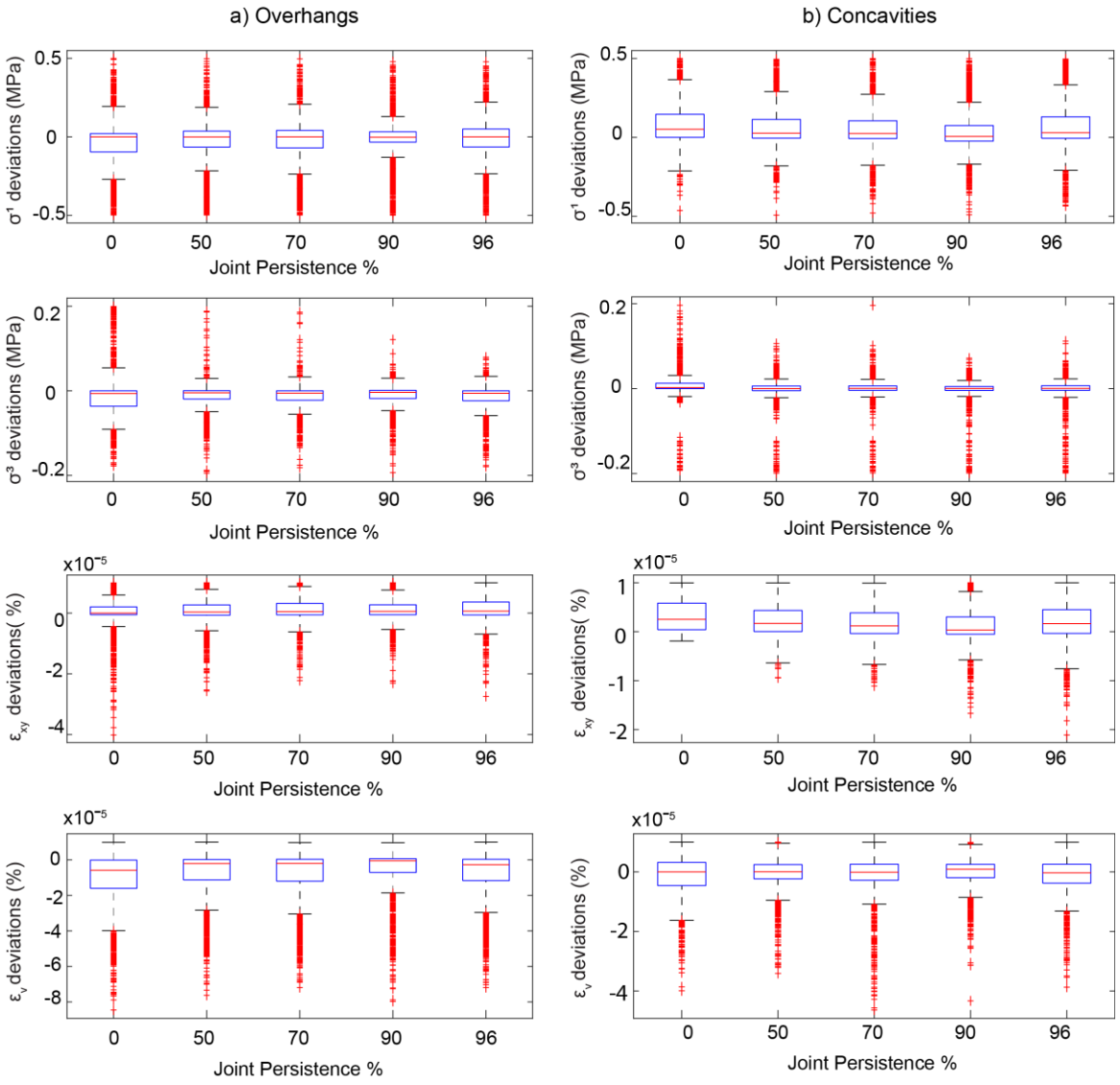

Figure 4.18: Response of σ^1, σ^3, ε_{xy} and ε_v deviations at a) overhangs and b) concavities to differences in values of *dp*.

4.4 Stress intensity indexes

A stress intensity index represents a qualitative scale of the impact of topography and rock mass structure on the stress distribution and strain behaviour, where 0 represents no influence, and 1 a major influence. These indexes were created from the observations of the modelled outputs to understand how overhangs and discontinuities interact. As outlined in section 4.2.4.3, geometry type is a first order control on stress and strain, alongside slope angle, as indicated by both models with overhang and discontinuities

(Figure 4.11 and Figure 4.13, respectively). These variables determine the baseline value of σ^1, σ^3, ε_{xy} and ε_v experienced within the near-surface of a slope.

4.4.1 Implications of models with overhangs only

Theoretical bounds were determined from slope angle model variability (Figure 4.19). This variability can be linked to overhang depth, with increasing values of *od* resulting in greater deviations from baseline (Figure 4.12). The bounds of the stress index are defined by the *iqr* of each value of *sa.* The *iqr* represents the transition from a slope with no overhangs to one with an *od* of 2 m (Figure 4.19)

However, there is a no direct correlation between values shown within the stress index and the corresponding value of *od.* This is due to the effect of cliff height, with deviations from baseline increasing towards the base of the slope (i.e. Figure 4.9). Therefore, these plots must be interpreted qualitatively to represent either areas of increased (1), or decreased (-1) stress and/or strain (Figure 4.19)

General observations from these conceptual stress indexes indicate that:

- A rock parcel located in a ≤ 89° slope will experience increased σ^1 as a result of both overhangs and concavities, though σ^1 is greatest for concavities.
- For these concavities, higher levels of ε_{xy} and lower levels of ε_v indicate that distortion rather than dilation of the rock parcel is more likely to occur (Figure 4.3). This is particularly important at an 89° slope. Increases in σ^1 relative to baseline, along with positive σ^3 values as determined by positive deviations relative to the near-zero values of baseline (Figure 4.8), indicate that this rock parcel is potentially likely to fail by compressional-shear mechanisms (Figure 4.20a).
- A parcel of rock within an overhang in ≤ 89° slope will also experience slight reduction in σ^3, more substantial reductions in ε_v and slight increases in ε_{xy}. This suggests that dilation of the rock parcel may be occurring; as baseline values of ε_v are already negative (Figure 4.8). This dilation may be accompanied by

distortion of the rock parcel. The reductions in σ^3 relative to baseline result in tensile stresses acting on the slope, allowing to rock to potentially fail by extensional shear mechanisms (Figure 4.20a).

- A rock parcel located within an overhang on a ≥ 90° slope will experience an overall reduction in σ^1, σ^3, ε_{xy} and ε_v, especially when compared with parcels of rock located between overhangs which experience heightened σ^1, σ^3, ε_{xy} and ε_v. Overhangs in these ≥ 90° slopes will potentially fail by extensional–shear mechanisms and concavities by compressional shear.

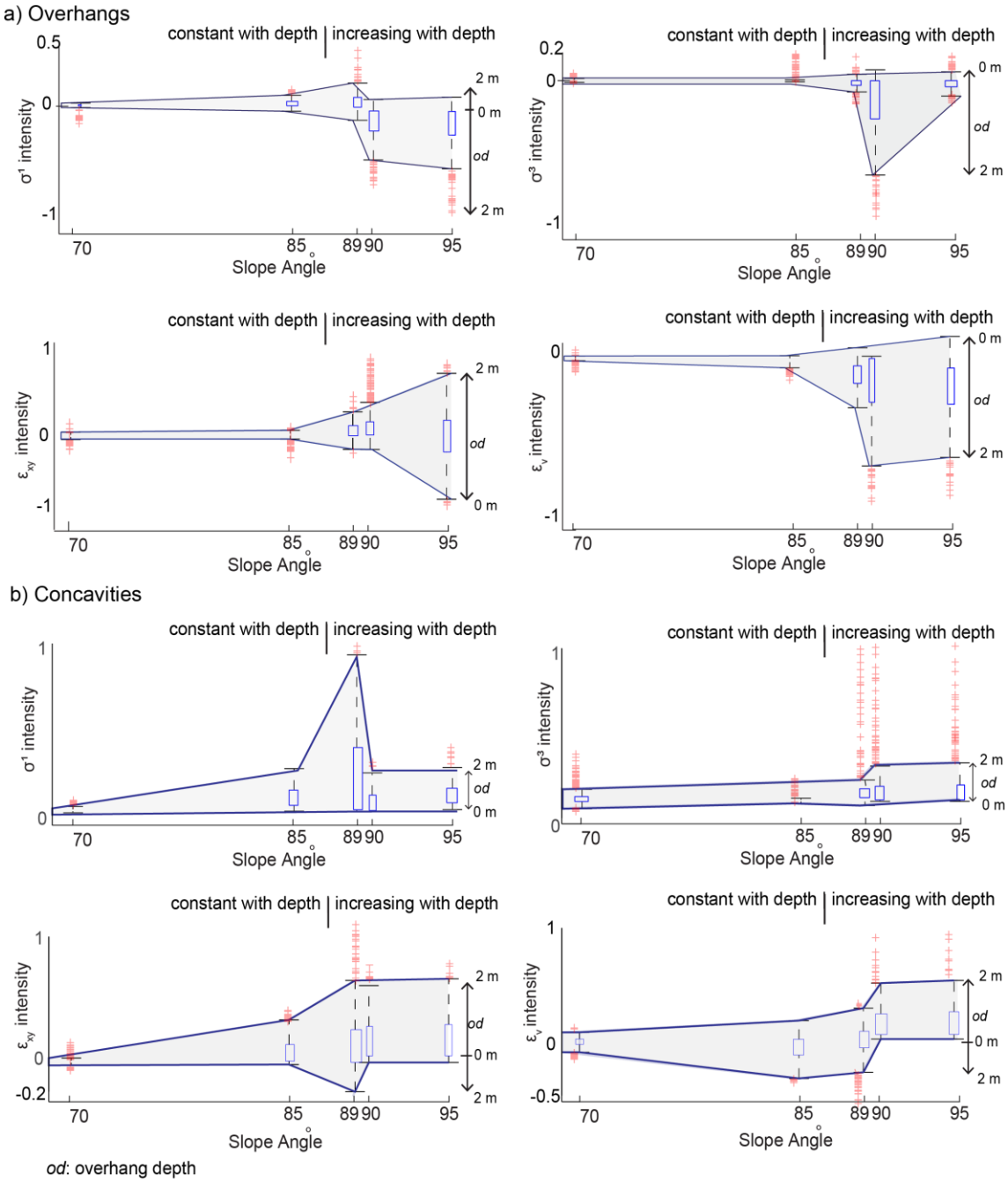

Figure 4.19: Stress intensity indexes for the impact of overhangs on stress and strain at a) overhangs and b) concavities, as determined by the value of *sa*. The *iqr* represents variations in *od*. Values are constant with increasing distance from cliff top for slopes of 70° to 85°, whereas slopes of 89° or greater show increasing amplification with depth from cliff top.

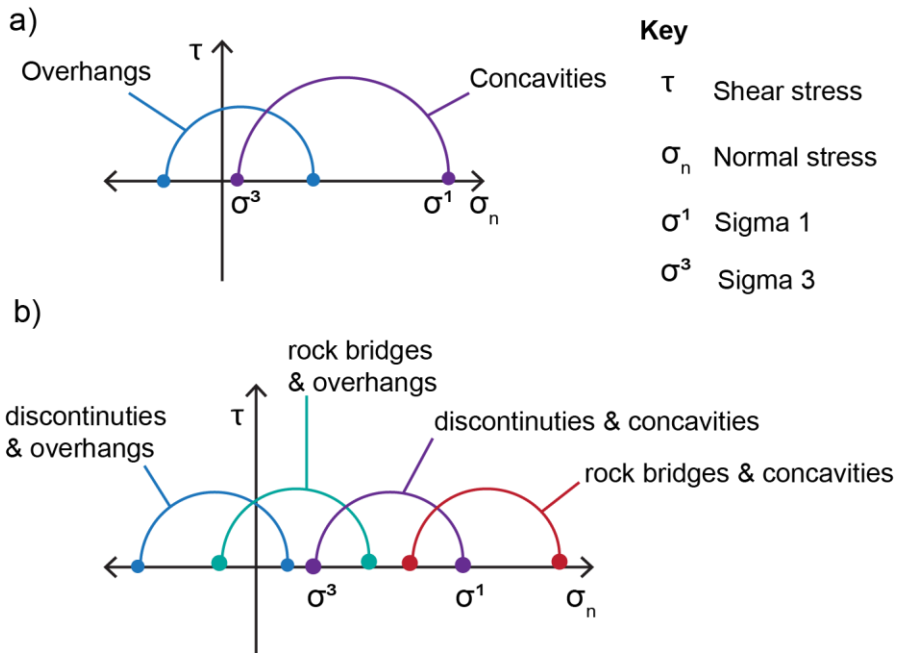

Figure 4.20: Schematic Mohr circles for overhangs and discontinuities. a) Mohr circles for slopes with overhangs and no discontinuities. b) Mohr circles for slopes with discontinuities and overhangs.

4.4.2 Implications of models containing discontinuities

The impact of discontinuities within a slope increases with increasing slope steepness, as indicated by the increase in range of values for σ^1, σ^3, ε_{xy} and ε_v (Figure 4.21). Broadly, changes in these values are similar for both overhanging and concave geometries, except for certain model values, such as σ^3 within a *sa* of 89°. General observations from these results indicate:

- Rock bridges represent zones where topographic stress is concentrated due to the higher σ^1 relative to baseline, while the higher values of ε_{xy} relative to baseline suggest distortion of rock located at the discontinuity tip is more likely to occur (Figure 4.3)
- Along discontinuity surfaces, σ^1 and ε_{xy} are reduced relative to baseline. This indicates that distortion is less likely to occur, and the reduction in σ^1 will result in greater tensile stresses.

- The relative location of rock bridges and discontinuities with respect to overhangs and concavities influences stress and strain. For example, the coincidence of an overhang with a discontinuity surface will result in enhanced reduction in σ^1, σ^3, ε_{xy} and ε_v relative to baseline. This in turns results in greater tensile stress and extensional-shear failure (Figure 4.20b).
- The coincidence of an overhang and rock bridge will act to cancel out the effects of one another. For example, lower σ^1 recorded at overhangs, but higher σ^1 recorded at rock bridges. Tensile stresses in overhangs are reduced and extensional-shear failure may be less likely to occur (Figure 4.20b).
- The coincidence of concave geometries and discontinuities also cancel out one another's effect on stress and strain, which may result in a reduction of compression, but not an increase in tension (Figure 4.20b)
- The coincidence of concave geometries and rock bridges results in elevated values of σ^1, σ^3, ε_{xy} and ε_v with greater compression and distortion occurring and compressional-shear failure more likely (Figure 4.20b).

Changes in the value of *dp* have limited influence on the stress distribution and strain behaviour. Therefore, the *iqr*, which defines the theoretical bounds in Figure 4.21, is related to the location of discontinuities and rock bridges with respect to overhangs. Increases in σ^1 and ε_{xy} are a function of rock bridge location, with decreases in σ^1 and ε_{xy} a function of discontinuity location (Figure 4.21). The pattern of increases or decreases in σ^3 and ε_v with respect to rock bridges or discontinuities is unclear. Increases in values of *od* act to amplify this effect, with increased variability of stress and strain values observed for larger values of *od* (Figure 4.17). This amplification effect is visible in Figure 4.15 and Figure 4.16, though does not display as distinct a pattern as observed for overhang only models (Figure 4.12). Overhangs and discontinuities therefore interact to determine the influence of discontinuities on the stress distribution and strain behaviour of a slope.

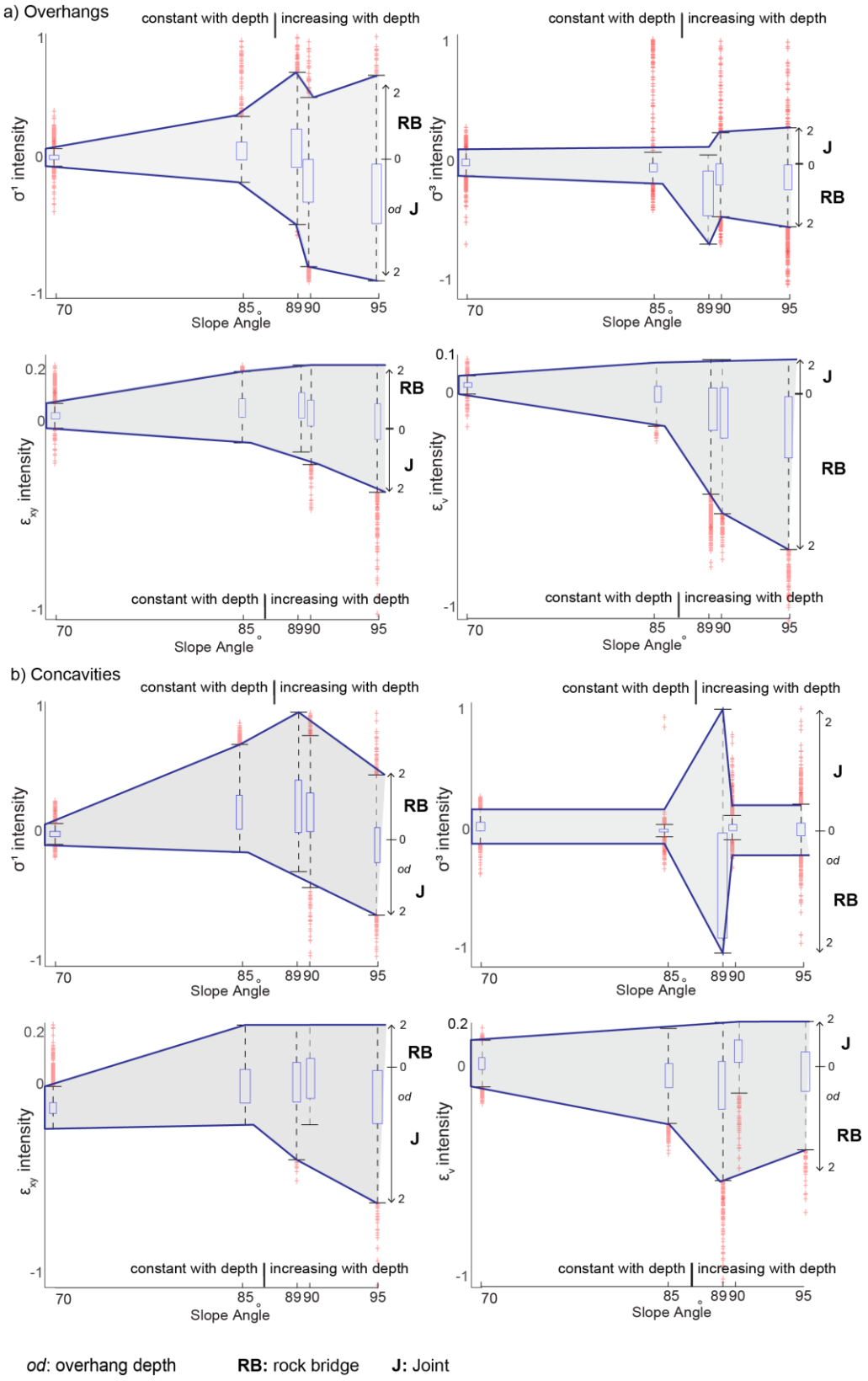

Figure 4.21: Stress intensity indexes for the impact of discontinuities on stress and strain for a) overhangs and b) concavities as determined by values of *sa*. Values are constant with increasing distance from cliff top for 70° to 85°, whereas slopes of 89° or greater show increasing amplification with depth from cliff top.

4.5 Topographic controls on spatial patterns of failure

4.5.1 Overview of approach

This section aims to understand if the stress distribution and strain behaviour of a cliff face, as determined by the presence or absence of overhangs and joints, dictates where rockfalls occur in a real-word slope. Slope angle and overhang locations are determined from digital elevation models (DEM), with the coincidence between these topographic features and rockfalls occurrence assessed. From this, the preferences of rockfalls to fail either at overhangs via extensional-shear mechanisms, or at concavities via compressional-shear mechanism are analysed.

Rockfalls recorded from monthly terrestrial laser scanning (TLS) of the hard rock coastal slopes located at Boulby, North Yorkshire, UK form the basis of the rockfall dataset (Figure 4.22). This is the same location as described in Chapter 3, though the time-frame and scanning resolution of the monitored data differ. The rock bridge proportions determined in Chapter 3 reveal that a wide range of rock bridge proportions and conversely discontinuity persistence (*dp)* is observed in individual rockfall scars (Figure 3.10). The mean *dp* is 69% ± 26%. However, the FEM results suggest that changes in the value of *dp* do not influence stress or strain patterns. Overhangs do influence the patterns of stress and strain observed for FEM models which contain discontinuities, even when the baseline overhang trend has been subtracted from the discontinuities models. Therefore, this section focusses on mapping overhang locations to understand if they can be used as a predictor for rockfall failure.

4.5.2 Rockfall dataset

The rockfall dataset consists of two different time intervals over which the TLS monitoring data was recorded. This allows for the examination of the temporal scales over which topography may control rockfall character and pattern. For both datasets the base 5 m of the rock slope was excluded for consistency with the finite element modelling and analysis.

The first timescale represents scans captured at an approximately monthly basis from 25th July 2008 to 28th June 2010. Sequential scans were registered to within an RMSE of ±0.1 m, and change detection undertaken following the procedure outlined in Rosser et al., (2005). The resultant digital elevation models (DEMs) of the TLS point clouds have a grid resolution of 0.125 m by 0.125 m. This resolution and accuracy allowed rockfalls of greater than 0.00156 m^3 to be detected and, as outlined in Vann-Jones et al., (2015), 31,987 rockfalls were recorded over this time period, with volumes ranging from 0.00156 m^3 to 12.73 m^3 (Figure 4.23a) . Table 4.4 presents mean rockfall characteristics for this inventory.

The second time-interval consists of twelve years of annual change observed at Boulby from 2003 to 2015 (Figure 4.23b). Due to the improvements of TLS technology over this time period, these scans have a slightly coarser resolution of 0.15 m by 0.15 m as result of the initial scans from 2003. The dataset consists of 20,087 rockfalls, with a higher mean volume and depth as compared with the monthly dataset (Table 4.4). This is a function of the monitoring epoch over which change has been determined, with discrete rockfall events over the annual timescales amalgamated into larger areas of mass wasting (Figure 4.23). Rockfalls recorded within this period have formed part of the rockfall datasets reported in numerous previous studies (Barlow et al., 2012; Lim et al., 2010; Rosser et al., 2007, 2013; Vann Jones et al., 2015).

Table 4.4: Geometrical characteristics of rockfalls recorded for the monthly and annual datasets.

	Area m^2		Depth m		Volume m^3	
	Mean	Standard deviation	Mean	Standard deviation	Mean	Standard deviation
Annual dataset	0.0676	0.3385	0.4884	0.0949	2.2204	11.817
Monthly dataset	0.0687	0.3543	0.002	0.0013	0.0134	0.138

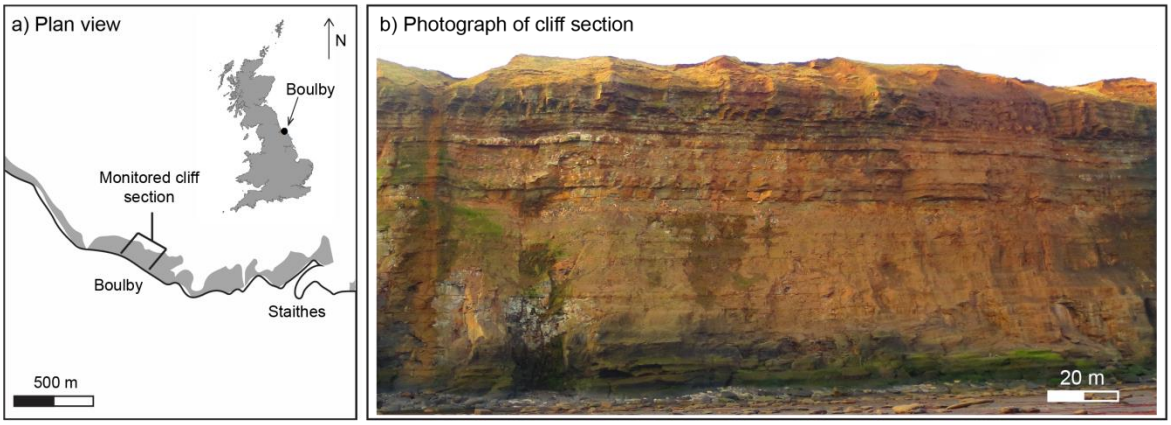

Figure 4.22: Rockfall dataset location map a) Map of the extent of the monitored cliff section located at Boulby, North Yorkshire, U.K. b) Photograph of the monitored cliff section.

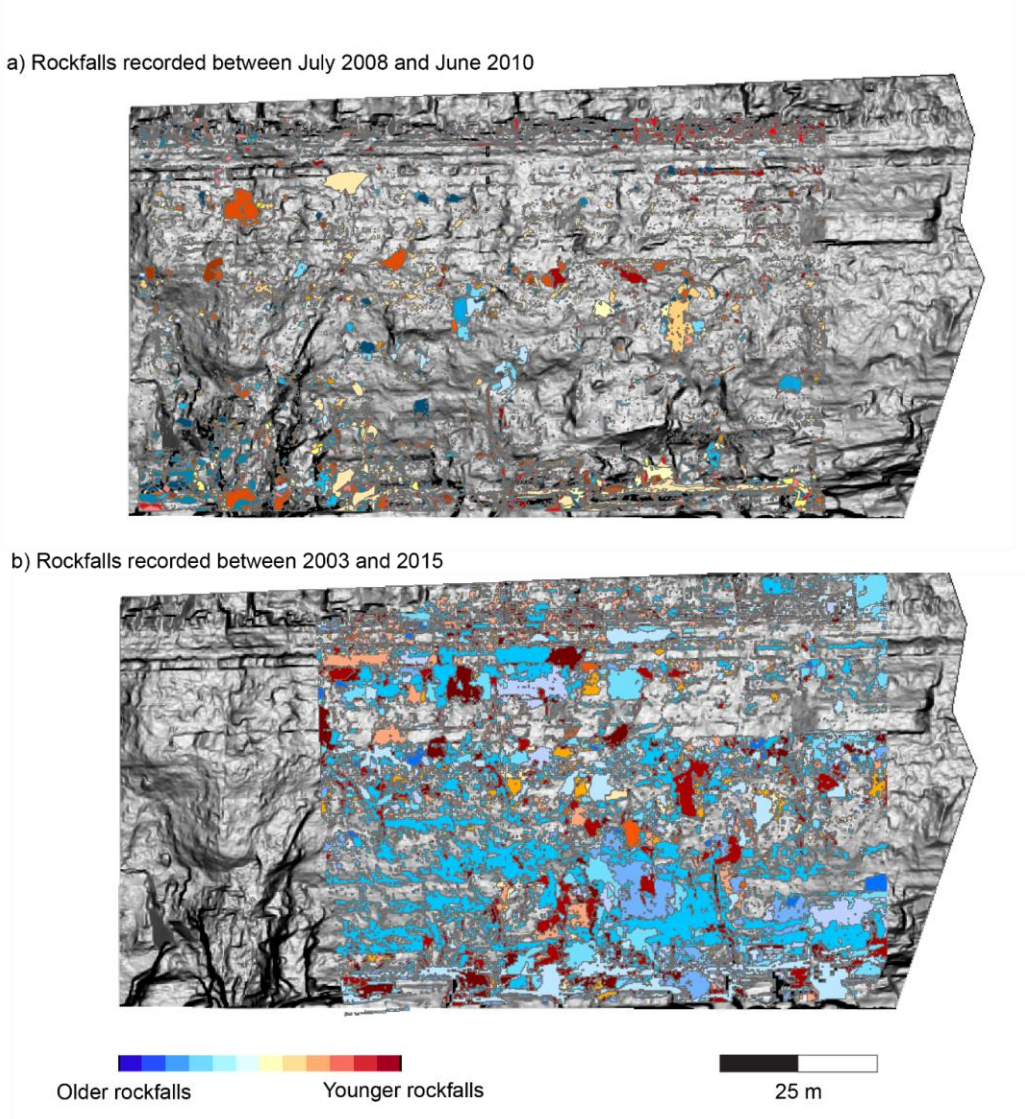

Figure 4.23: Observed rockfalls for a) the two-year dataset of monthly cliff changes and b) the twelve-year dataset of annual cliff changes. The extents of the dataset differ due to the spatial extent of the initial scans collected for the annual dataset. Rockfalls observed during each respective monitoring epoch are represented by a different colour within the Figure. Grid size of DEM is 0.15 m².

4.5.3 Topographic classification

4.5.3.1 Slope angle

The effect of overhangs and discontinuities on stress and strain increases with increasing slope steepness, therefore changes in slope angle may influence where along a section of cliff, stress and strain potentially become more important for controlling rockfall behaviour. As such, slope angles were calculated from 2D profiles, located at 1 m spacing across the width of the DEM. The lower and upper coordinates of the profiles were used to calculate overall slope angle via trigonometry, while the mid-point coordinates of the profiles allowed the upper and lower slope angle to be determined (

Figure 4.24a). The choice of using the mid-point was based on qualitative observations of the data. Rockfalls were assigned to calculated upper or lower slope angles where they intersected the one-metre spaced profiles. The distribution of all recorded slope angles versus rockfall slope angles was assessed to understand if rockfalls preferentially occurred for certain angles.

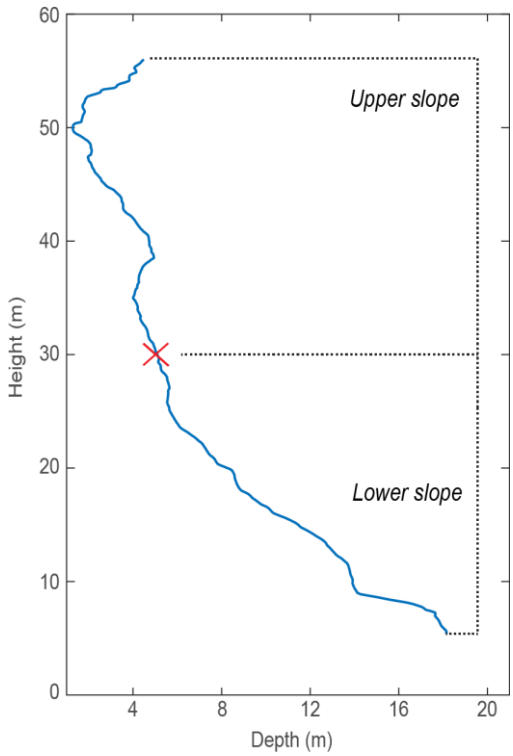

Figure 4.24: Example slope profile , displaying the dichotomy of slope angles between the upper and lower cliff section. Overhangs

The presence of overhangs was determined via profile curvature analysis, where curvature represents the second derivative of local slope for a DEM grid cell calculated from the surrounding eight cells (Figure 4.25). Negative curvature values indicate areas of convexity, positive values indicating concavity and values of zero indicate flat surfaces. Convex zones therefore represent overhangs, with the degree of convexity indicating the local steepness of the profile.

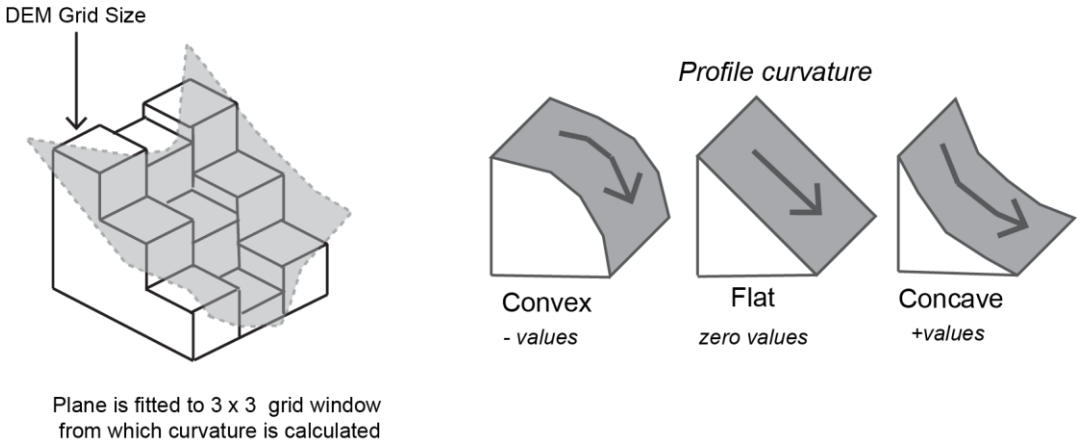

Figure 4.25: Calculation of curvature from a local plane fitted to a 3 x 3 grid cell window of a DEM. Curvature is convex, concave or flat.

The resolution of the DEM is important for determining the wavelength over which curvature is calculated using a moving 3 x 3 cell window. This may indicate at what scale overhangs, as determined by convexity, are an important control on rockfall occurrence. As such, for this analysis curvature has been calculated for the following monthly time-scale DEM resolutions: 0.125 m², 0.25 m², 0.5 m², 1 m², 2 m² and 5 m². For annual timescales the following resolutions were used: 0.15 m², 0.3 m², 0.6 m², 1.05 m², 2.1 m², and 5.1 m². The different DEM resolutions were created from the mean value of aggregated cells from both the 0.125 m² DEM, and 0.15 m² DEM for each respective time-scale DEM.

Alongside this, the range in depth values normal to the cliff face is calculated to determine overhang depth. The range of values is calculated over a 3 x 1 window for each DEM resolution, designed to complement the window over which curvature is calculated. For example, a DEM with a grid cell resolution of 0.5 m² will have curvature calculated over a 1.5 m² square while range in depth values is calculated over a 1.5 m by 0.5 m rectangle. Though there is no linear correlation between increasing convexity and increasing overhang depth. Increases in both convexity and concavity are associated with higher magnitude curvature values (Figure 4.26). These higher depth ranges may indicate the point of transition from convexity to concavity, or vice versa (Figure 4.26).

Rockfalls were assigned curvature values based on their pre-failure surface morphology. On a monthly timescale these curvature values were calculated from the preceding month's DEM. For example, a rockfall recorded in August 2009 would be assigned the curvature values of the July 2009 DEM. On an annual timescale these curvature values were calculated from the preceding year's DEM. The distribution of rockfall curvature values versus the whole slope curvature values was assessed to determine if rockfall preferentially occur in convex or concave areas.

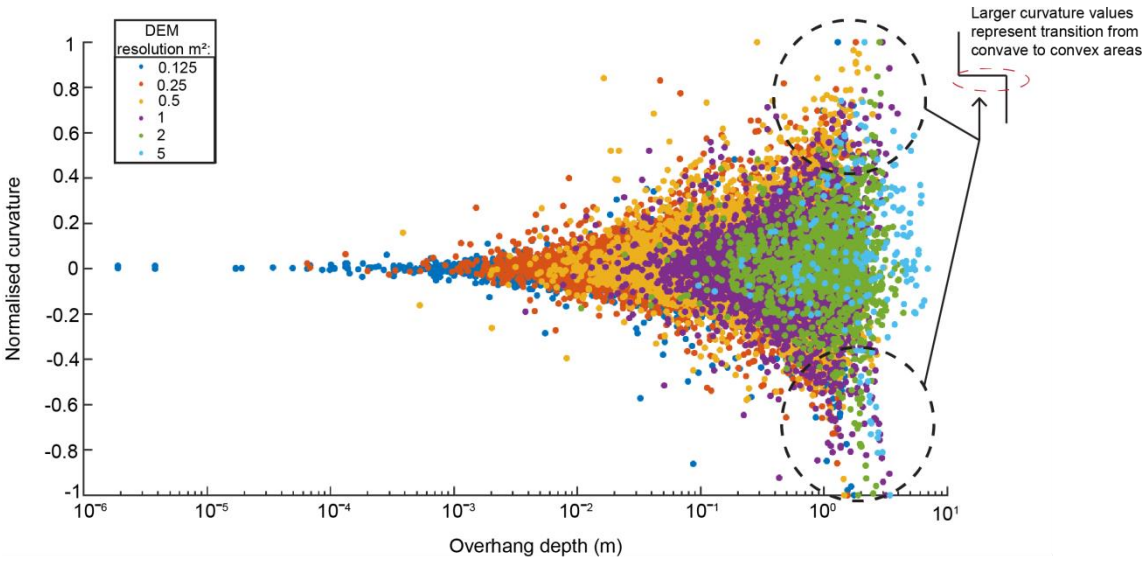

Figure 4.26: Relationship between curvature values and their associated range in depth for the DEM. Normalised curvature values are plotted to allow the different values for each curvature wavelength to be plotted on the same scale.

4.5.4 Topographic analysis

4.5.4.1 Slope angle and rockfalls

The overall mean slope angle is 79.6° ± 2.27°, with the upper slope displaying a mean angle of 87.82° ± 1.48°, while the lower slope is shallower with a mean angle of 68° ± 3.3°. Neither the lower slope or upper slope contain slope angles of ca. 80°, as indicated by its absence in the distribution of slope angles illustrated in Figure 4.27. The small range in standard deviations indicates that these slope angles are consistent along the extent of the monitored section. Comparison of the distributions of the upper and lower slope angle with the slope angle associated with rockfalls indicates that rockfalls do no preferentially occur for certain angles (Figure 4.27).

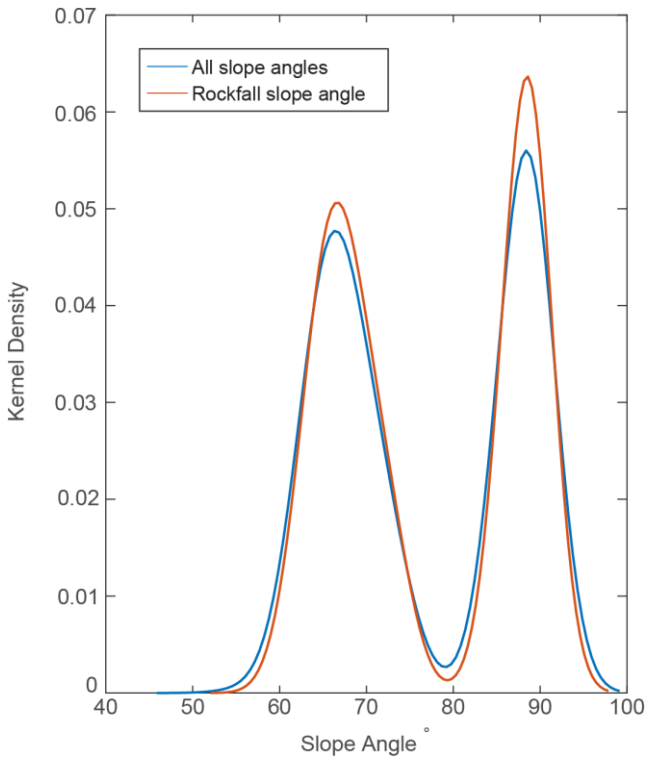

Figure 4.27: Distribution of recorded slope angles for the whole slope and slope angles recorded for rockfalls.

4.5.4.2 Overhangs and rockfall on monthly timescales

Rockfalls recorded over monthly time-scales are more likely to occur in convex areas of the slope for all DEM resolutions (Table 4.5). This is particularly true for curvature recorded over 0.125 m², where rockfalls are likely to occur 80.95% of the time within convex areas, while the proportion of convex areas of the whole slope accounts for only 50.52% of the available area (Table 4.5). All other DEM resolutions show small increases of approximately 5% to 15% in the proportion of rockfalls occurring within convex areas, relative to the overall proportion of convex areas in the slope. These changes in the distribution of curvature recorded for rockfalls versus whole slope curvature are all significantly different ($p > 0.001$). Furthermore, this relationship is strongest for larger rockfalls, with rockfalls greater than 1 m² likely to occur in convex areas 86.9% of time for curvature resolutions of 0.125 m².

Table 4.5: Percentage of rock slope which is convex, compared with the percentage of rockfalls occurring in convex areas of the slope over monthly timescales. Percentages are determined from cumulative frequency distributions of the data.

DEM Resolution (m²)	Convex percentage for whole slope (%)	Percentages of rockfalls occurring in convex areas (%)			
		All rockfalls	Rockfall area (m^2)		
			<0.1	0.1 - 1	>1
0.125	50.52	80.95	80.6	83.87	86.9
0.25	49.88	62.88	61.69	72.76	67.38
0.5	48.63	53.39	52.71	58.82	63.95
1	47.48	52.23	51.98	53.8	61.5
2	45.93	51.75	51.68	52.43	50.8
5	41.08	57.26	52.09	58.23	63.37

4.5.4.3 Overhangs and rockfalls on annual timescales

Curvature values for rockfalls recorded over annual time-scales are similar to the overall distribution of curvature recorded for the slope, with rockfalls slightly more likely to occur

in concave areas (Table 4.6), in contrast to monthly time-scales (Table 4.5). This contrast is most pronounced for larger rockfalls, where they are less likely to occur in convex areas over annual time-scales, especially for curvature resolutions of 2.1 m² and 5.1 m² (Table 4.6). These subtle changes in distribution of curvature values between rockfalls and the whole slope curvature are all statistically significant ($p > 0.001$). Overhanging geometry for longer timescales therefore shows a different control on recorded rockfall activity than compared to that over shorter timescales.

Table 4.6: Percentage of rock slope which are convex, compared with the percentage of rockfalls occurring in convex areas of the slope over annual timescales.

DEM Resolution (m²)	Convex percentage for whole slope (%)	Percentage of rockfalls occurring in convex area (%)		
		All	Rockfall area (m²)	
			< 1	> 1
0.15	50.35	49.70	46.96	50.08
0.3	49.99	47.28	47.28	47.21
0.6	48.67	43.72	44.12	41.21
1.05	47.66	41.51	47.73	40.61
2.1	46.27	42.81	43.08	34.55
5.1	41.36	40.16	40.21	37.18

4.5.4.4 Curvature changes through time

Rockfall activity can change the curvature of a slope via block release both at a local 'rockfall' scale, and at a whole slope scale. Analysis of curvature change over time was undertaken to understand how rockfalls influence curvature, in the absence of evidence of any long-term change in slope profile form from historical mapping data. Comparison between the first and last scan data for both time periods reveals that at the scale of the whole slope, the majority of the slope maintains a constant curvature form - either convex, flat or concave (Figure 4.28). For example, at a DEM resolution of 0.125 m², 59% of the cliff surface displays the same level of curvature (i.e. convex, concave or flat)

in the first and last DEM, while approximately 20% of the cliff surface is calculated as either convex in the last DEM that was not convex in the first DEM, or is calculated as concave in the last DEM that was not concave in the first DEM. As the DEM resolution increases, the percentage of the slope surface which displays a constant curvature through time increases to 92% for a DEM resolution of 5 m².

This classification does not consider if areas which are already convex or concave have increased or decreased in their relative values. The proportion of curvature which remains constant is slightly higher for monthly monitoring intervals with annual time series displaying more change in curvature. Curvature at smaller spatial scales displays the most change, particularly on annual time-scales where up to 49% of the slope is either more concave or convex. Larger DEM resolutions represent areas of larger convexity or concavity, which are also more likely to be constant over time. Qualitatively, as Figure 4.29 illustrates, the areas of constant curvature in Figure 4.28 may coincide with overhanging lithological layers, where limited rockfall activity is recorded.

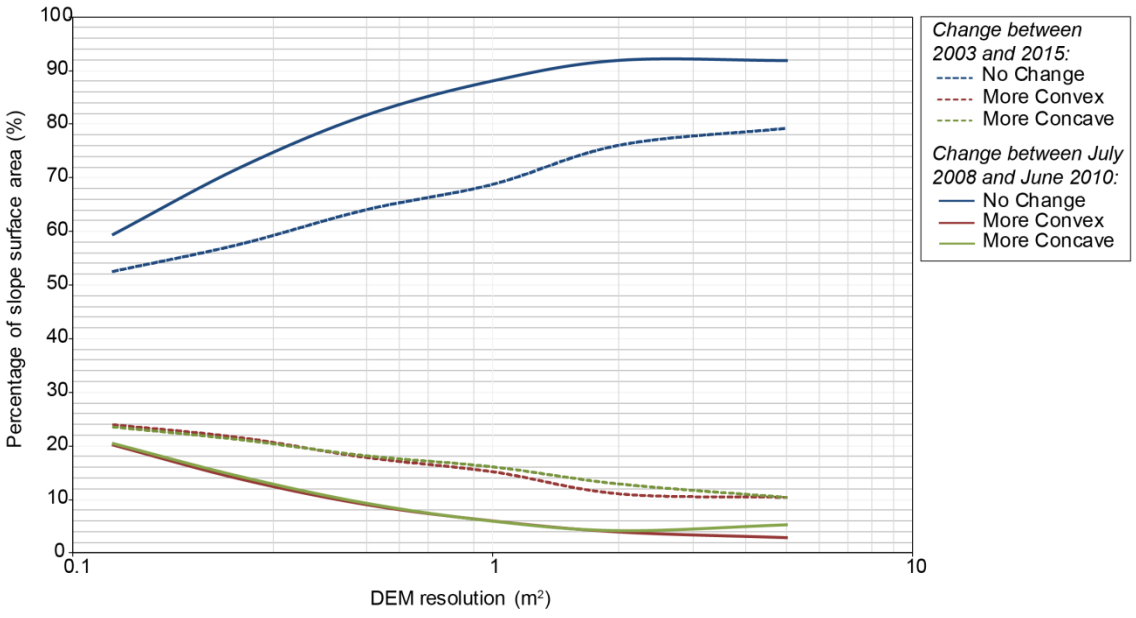

Figure 4.28: Proportion of rock slope which has remained constant, or that become more convex or more concave between the first and last monitoring interval. This change is curvature is calculated for each DEM resolution, with both the proportion of change for monthly and annual time-scales is plotted.

.

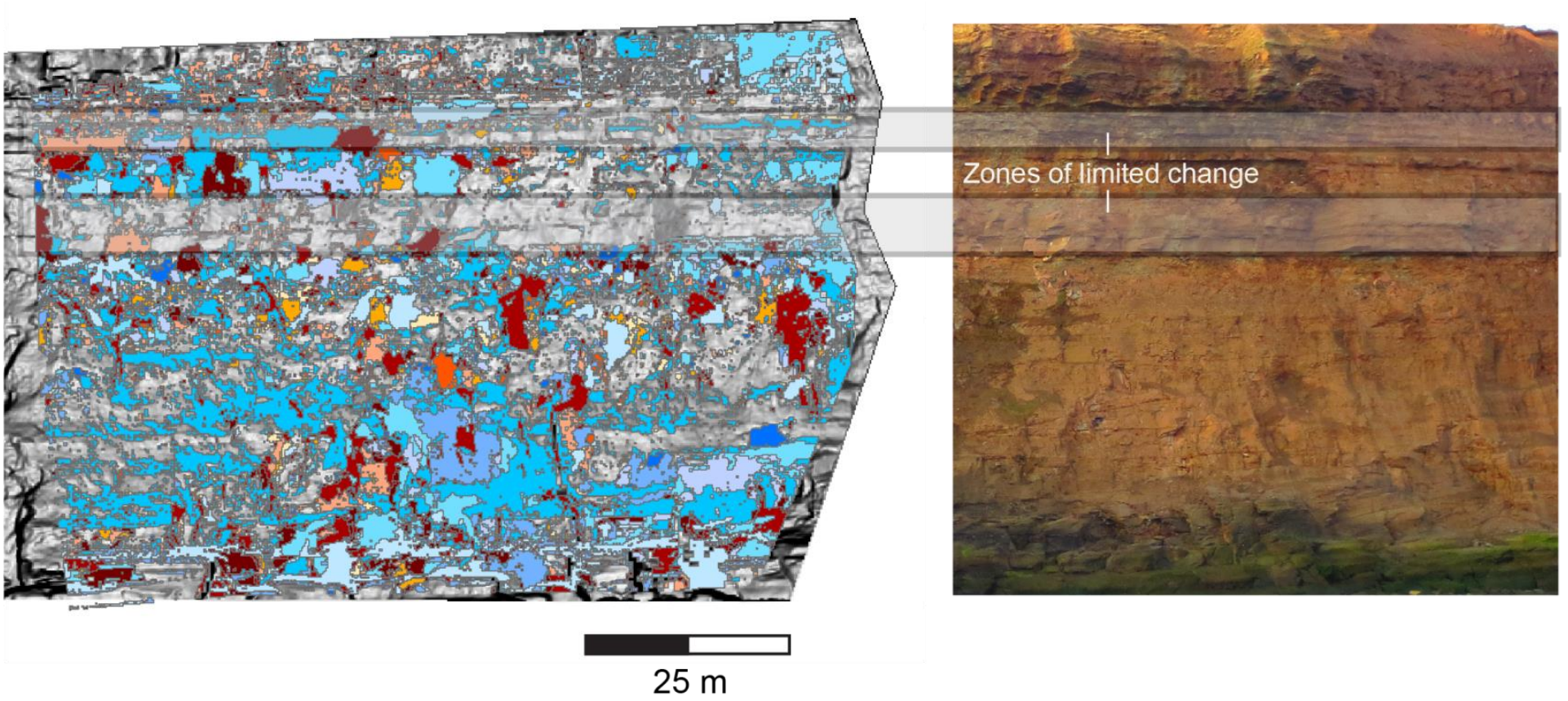

Figure 4.29: DEM and photograph displaying the two zones of limited erosion for the monitoring period between 2003 and 2015.

4.6 Discussion

4.6.1 Controls on stress distribution and strain behaviour

Slope angle and overhang geometry are important controls of the stress distribution and strain behaviour as shown by the exploratory FEM models, even when their respective baseline trends have been removed from the data. In other words, slope angle and overhang geometry affect the ability of various overhang depths and levels of discontinuity persistence to concentrate and distribute stress and strain. Overhang depth in turn affects the ability of discontinuity persistence to concentrate stress and strain. The modelled patterns of stress and strain within the near surface of a slope suggest that topographic features, such as slope angles and overhangs, are the predominant control on stress distribution and strain behaviour.

Generally, concavities represent areas of the greatest stress and strain in the FEM analysis, with overhangs themselves characterised by lower stress and strain. Discontinuities are characterised by decreased stress and strain, with this stress and strain concentrated at rock bridges. Increases in overhang depth have been shown to amplify this effect. Variations to these generalised and simplified observations exist and are often dependent on slope angle.Variations of ≤ 5° in slope angle result in substantial variations in the modelled stress distribution and strain behaviour. As slope angle increases, the influence of overhangs and discontinuities also increases. Wolter and Müller (2008) investigated the influence of slope shape on stress distribution, with steeper angles increasing stress particularly at the base of the slope. In their models, undercutting at the base of the slope to form a slope angle ≥90° did not result in significant increases in stress. Similarly, the FEM models presented here indicate that increases in slope angle beyond 89° do not necessarily result in greater levels of stress or strain. Within these models, an 89° slope angle represents an apparently critical value, potentially due to changes in trajectories of stress and strain as a slope transitions from near-vertical to vertical. The 1° shift in slope angle from 89° to 90° may have important implications for failure behaviour and rockfall activity.

4.6.2 Implications for failure mode

As outlined in section 4.4, slopes ≥ 90° display a clear distinction in failure mechanisms between overhangs and concavities, with overhangs potentially failing exclusively by extensional-shear mechanisms, and concavities by compressional-shear mechanisms. This distinction is likely to increase towards the base of the slope and with increasing levels of *od*, as the amplification effects on stress and strain increases. Failure mode is therefore not only dependent on slope angle, but also the location upon a cliff coupled with the overhang depth. However, slope angles ≤ 89° do not display the same pattern of a reduced level of σ^1 at overhangs. Additionally, for slope angles ≤ 85°, stress and strain are not amplified with depth, indicating that for these slope angles, failure mode is unlikely to change with cliff height, and the smaller changes in stress and strain values from baseline may not influence failure mechanisms to the same extent as steeper slopes.

Interpretations of failure mode from Mohr-Coulomb criterion are similar to those specified for trilinear fracture envelope (Diederichs, 2003). This envelope indicates that for shear failure to occur, both increases in σ^1 and σ^3 are required. However, when the ratio between σ^1 and σ^3 is high, particularly when σ^3 is near zero, tensile micro-cracking may dominate leading to spalling extensional failures. In addition, σ^1 is an important control on micro-crack initiation, which is insensitive to confining pressures (Diederichs, 2003).

Understanding the failure mechanisms of rockfalls is necessary for the correct interpretation of the pre-failure monitoring data (Petley et al., 2005). The modelled decrease in ε_v and associated increased dilation at overhangs, and contraction at concavities, suggests that pre-failure deformation manifest as surface displacement may be more detectable for overhangs as compared to concavities. Analysis of pre-failure monitoring data indicates that toppling and tensional failures are more detectable, with planar sliding and associated propagation of shear fracture displaying less measurable deformation (Kromer et al., 2017; Rowe et al., 2017). The success of detection of pre-

failure deformation may be dependent on the interactions between failure mechanisms and surface topography.

4.6.3 Controls on rockfall patterns

4.6.3.1 Influence of slope angle

The coincidence between rockfall activity recorded at Boulby and certain slope angles was limited, with no greater concentrations of rockfalls in steeper sections of the slope, where modelled stress and strain tend to be higher. This may be a function of the steeper sections of slope were only recorded in the upper half of the cliff, where the impact of slope angle and overhangs is less than that experienced at the base of the slope, with the shallower slope angles of the lower slope, and their associated topography, may have more limited influence on rockfall occurrence. The cliffs at Boulby display a limited range of slope angles which prevents a broader analysis of the preference of rockfalls to fail in steeper slope angles from this dataset, where otherwise in other circumstances stress and strain may be higher.

Conflicting views exist on regional influence of slope angles on rockfall activity, with some studies indicating slope angles control rockfall occurrence (e.g. Messenzehl et al., 2017), while others find no significant correlations with rockfall activity (e.g. Moore et al., 2009). None of these studies considered the role of subtle single-degree variations in slope angle in controlling rockfall activity. A more regional assessment of these subtle changes is needed to more fully explore the relationship between stress-strain, slope angle and rockfall characteristics.

4.6.4 Influence of overhangs

FEM analysis has showed that overhangs influence the stress distribution and strain behaviour of a slope. Areas of stress concentration, which include concavities, may form the locus for failure by promoting the propagation of failure surfaces through intact rock. Previous analysis of rockfalls at Boulby show that they occur around the edges of large-scale overhangs and similar protruding features, which are areas of high stress and strain concentration, with these failures concentrated along structural boundaries

including bedding (Rosser et al., 2007). Stress concentrations at re-entrant corners can also form the locus from which failure surface propagation through an overhang results in a wider scale release of the overhanging block above (Kogure et al., 2006; Stock et al., 2012; Young and Ashford, 2008). This may be a similar mechanism to an enhanced level of propagation of sheeting joints with respect to greater slope curvature (Martel, 2006). FEM modelling here, alongside other studies (e.g. Herterich et al., 2018), indicates that greater overhang depths will yield higher stresses and promote failure. However, the topographic analysis within this chapter shows that for larger areas of convexity, representative larger scale overhangs, rockfalls fail in approximately equal amounts for convex and concave areas.

Topographic analysis indicates rockfalls preferentially occur in smaller scale convex areas (0.125 m to 0.25 m) over monthly timescales. This coincidence is likely driven by upward and lateral propagation of rockfall scars, whereby notches created by rockfall activity apparently migrate upslope as failure grows (Rosser et al., 2013). Rockfalls are time-dependent phenomena whereby after a failure occurs, stress redistributes within the surrounding rock mass, leading to fracture propagation and subsequent further failure (Eberhardt et al., 2004a; Rosser et al., 2007; Stock et al., 2012). As these failures propagate they create areas of localized convexity. Concentrations of stress and strain induced by large scale topographic features may play roles in determining areas more susceptible to failure when progressively growing areas of failure intersect areas of high stress and strain. The small and abrupt nature of changes in local slope for these smaller convex features may drive a greater degree of relative change in stress and strain, which potentially could be of greater importance to rockfall failure than the absolute magnitudes of stress or strain.

Over longer (annual) timescales, this analysis shows that rockfalls are slightly more likely to occur in concave areas over larger spatial scales. The upward and lateral propagation of rockfalls, which coincide within smaller convex features, may occur within the larger scale concave features of a cliff. Both levels of temporal resolution explored here capture

small-scale changes in curvature of the slope of between 40% and 50% which may be related to rockfall propagation. However, rockfalls occur in both convex and concave areas apparently at both monthly and annual time-scales. The higher levels of modelled stress and strain in concave areas do not necessarily result in greater rockfall occurrence, and vice versa for overhangs. Other factors including discontinuities might control rockfall patterns. This also suggests that observed rockfalls fail via extensional shear or compressional shear in approximately equal amounts.

4.6.5 Influence of discontinuity persistence

The exploratory models reveal that discontinuity persistence had limited influence on stress and strain. The inclusion of discontinuities within the FEM models results in greater heterogeneity of stress distribution and strain behaviour, which may be potentially explained by the location of discontinuities with respect to overhangs and concave surface topography. This increased heterogeneity may also explain the limited coincidence between overhangs, concavities and rockfalls. The analysis within chapter 3 revealed that rock bridges accounted for 31% ± 26% of rockfall scar surface area, with discontinuity persistence higher (69% ± 26%.) The limited influence of persistence on stress and strain may explain the consistency of rockfall patterns observed at Boulby, as the 52% range in discontinuity persistence is unlikely to affect stress and strain values. Discontinuity persistence may be more influential for the exact characteristics of individual failures, with their impact on stress and strain important at the micro-scale, within the area surrounding the propagating discontinuity tip (Scavia, 1995). Discontinuity persistence may determine the amount of micro-cracking needed, and associated time required to accumulate such damage for rock block release (Kemeny, 2005). As the mesh density of the FEM models (ca. 0.5 m) is several orders of magnitude larger than the micro-crack scale (ca. 1×10^{-3} m), stress and strain concentrations at the discontinuity crack tips are not detected.

As the FEM modelling represents a static, time-independent model, the temporal influence of damage accumulation over time may explain why joint persistence appears

to have a limited influence on stress and strain. Further modelling combined with field observations of rockfall behaviour could asses this time-dependent characteristic (Kemeny, 2005; Stead et al., 2006). Additionally, the FEM models assessed only one discontinuity orientation, spacing and length, with the analysis of the variability of these parameters beyond the scope of the present study. Incorporation of multiple discontinuities sets within a 3D model, which intersect each other, increases the freedom of movement of the incipient failing block, and may result in greater dilation of the rock mass (Brideau and Stead, 2010; Havaej and Stead, 2016). Bonilla-Sierra et al., (2015) modelled the influence of joint orientation on modes of failure, revealing that rock bridges located planar to discontinuities with dips > 50° are more likely to fail via tensile cracking, with greater shear cracking observed for discontinuities < 50°. This suggests that the rock bridges located planar to discontinuities within the exploratory models here are more likely to fail via a tensile extensional mechanism. However, if such rock bridges are located within a concavity, the concentration of σ^1 and ε_{xy} likely suppress this tensile cracking, while a coincidence with an overhang will enhance this. The influence of discontinuity characteristics and topography on instability potential and associated modes of failure therefore cannot be considered separately.

4.6.5.1 Other controls

As both the higher and lower zones of stress and strain established from the FEM modelling do not explain the range of observed rockfall activity, other processes may be controlling the spatial occurrence of rockfalls. Along with progressive failure and stress distribution, this may include:

- The interactions of weathering process, which gradually weaken the rock mass over time, resulting in non-linear and spatially varied damage accumulation across the rock slope (Viles, 2013b). Discontinuity connectivity, as determined by rock mass structure, has been shown to influence weathering process via enabling or limiting thermal or pore-pressure fluctuations (e.g. Moore et al., 2011; Preisig et al., 2016), where a greater number of discontinuities within a rock mass

is associated with a greater degree of rock fatigue (Gischig et al., 2016). Discontinuity persistence may be more important in this context.

- Lithology, which has been shown to influence erosion rates and magnitude-frequency behaviour of rockfalls (Barlow et al., 2012; Lim et al., 2010; Rosser et al., 2007). Changes in key characteristics between lithological units can result in deflections or suspension of the propagating failure surface (Gudmundsson et al., 2010). Lithological layers, associated with overhangs appear to have undergone limited change over the course of the 12 years at Boulby.

4.7 Conclusion

This chapter has considered the bulk influence of slope angle, overhang geometry, discontinuity persistence and rock mass structure on near-surface stress and strain distribution within an idealised rock slope. This has been used to explore the relationship between modelled distributions of stress and strain and the observed spatial patterns of rockfall activity at Boulby, North Yorkshire, UK.

The key conclusions of this chapter are as follows:

- Topographic characteristics of a slope as represented by overall slope angle and overhang geometry are an important control on the near surface stress distribution and strain behaviour.
- Overhangs and discontinuities have a larger impact on stress and strain for increasingly steep slopes. Subtle changes in slope angle (single degrees), particularly for slopes between 85 and 90 are shown to substantially alter the stresses and strains experienced.
- Concavities between overhangs display heightened stress and strain concentration, especially at re-entrant corners beneath and above overhangs, while overhangs themselves experience lower stresses and strains.
- Failure mechanisms are dependent on location relative to overhangs and discontinuities. Extensional-shear failures are associated with overhangs and discontinuities, while compressional-shear failures are linked to concavities and

rock bridges. A single parameterisation of rock strength is therefore inadequate for explaining the absolute and relative likelihood of failure across a complex, natural rock slope.

- Analysis of the coincidence between rockfalls and overhangs reveals that for smaller spatial scales and shorter temporal scales, rockfalls are more likely to occur in convex areas, while over longer time scales they are slightly more likely to occur in concave areas. This process may potentially reflect upward and lateral propagation of rockfalls following stress-redistribution in the surrounding rock mass, which reflects kinematics and rock structure, in addition to topography and time.

This chapter addressed research objective 2, by first, modelling the interaction of micro-topography and rock mass structure in concentrating stress and strain within the slope near surface. This was achieved using a series of exploratory FEM models, from which general observations have been made. This numerical modelling revealed that stress is concentrated at concavities and is reduced at overhangs. Variations to this simplified rule are dependent on changes of slope angle and the presence or absence of discontinuities. The resulting stress distribution and strain behaviour influence the failure mechanisms of an individual rockfall, with concavities potentially failing by compressional shear mechanisms and overhangs by extensional shear. Secondly, the coincidence between rockfall activity and areas of stress and strain concentration were assessed using rockfall datasets recorded at Boulby, North Yorkshire, UK. Rockfalls occur preferentially for small scale convex features over monthly timescales, with these convex features created by upwardly propagating rockfalls. The lack of agreement between the spatial locations of rockfalls and topographic features suggest that the resulting near surface stress and strain distribution is not the sole control on spatial patterns of rockfall failure, with other factors such as weathering and lithology potentially important controls.

5 Controls on weathering intensity and the associated impact on the compressive strength and failure style of sedimentary rocks.

5.1 Abstract:

Weathering alters the physical and mechanical characteristics of rock. The links between weathering, micro-crack damage and rock strength are not well constrained, including not only the potential for strength reduction, but the broader rheological response of intact rock to weathering that is important in determining slope failure styles. We investigated the controls on weathering-induced strength degradation to understand how the intensity of weathering may vary spatially in a rock slope, as a function of the ambient stress field induced by overburden loading and local slope geometry. Both of these factors may influence the efficacy of weathering. We conducted experiments using sedimentary rock samples to determine the influence of ambient stress, local slope geometry and previously-existing micro-crack damage on weathering and subsequent changes in rock strength. We placed samples under a constant vertical compressive stress using a novel experimental set-up and subjected samples to either intensive short-term laboratory-based salt-water wetting and drying conditions, or field-based long-term coastal conditions. Unconfined compression testing was undertaken to determine the changes in stress-strain characteristics due to weathering. Our analysis reveals that compressive ambient stress conditions alongside local slope geometry and existing damage do not influence weathering intensity, with the stresses imparted by weathering equal to or greater than the stresses imposed by the range of conditions we simulate. Weathering does, however, significantly reduce intact rock strength, which results in a change in macro-scale failure style, with samples becoming less brittle and developing post-peak residual strength. Multiple stages of brittle failure are required before residual strength is reached, with this sequence of failure manifested in pre-failure deformation data. These results also indicate that as a rock weathers the magnitude of triggering events required to promote ultimate failure changes.

5.2 Introduction

Rock slope failures are a significant hazard (Dussauge-Peisser et al., 2002; Fell et al., 2008; Guzzetti et al., 1999) and contribute to landscape evolution over a variety of timescales (e.g. Clarke and Burbank, 2010; Korup et al., 2007; Moore et al., 2009). The intrinsic properties of a rock slope, such as the strength of intact rock bridges (Jennings, 1970) and nature of joint sets (Einstein et al., 1983; Goodman and Shi, 1985), along with their physical setting, which includes slope angle, aspect and curvature (e.g. Matsuoka and Sakai, 1999; Messenzehl et al., 2017; Sass, 2005) predispose a slope to failure. Slopes can be destabilised rapidly in response to sudden and short-lived increases in driving stresses that trigger failure, such as those resulting from strong earthquake ground shaking or heavy rainfall (Iverson, 2000; Keefer et al., 1987; Keefer and Keefer, 1994). Rock slope instability can also develop over longer (10^0 - 10^3 years) timescales in response to incremental and cumulative reductions in rock mass strength driven by preparatory micro-fracture development and weathering (Collins and Stock, 2016; Eppes and Keanini, 2017; Gunzburger et al., 2005). Weathering is an umbrella term for a suite of geomorphic processes that result in the in situ breakdown of rock at or near the ground surface (Yatsu, 1988). In light of this definition, we view weathering as any process which generates and propagates micro-cracks in rock within the earths near surface, with this micro-crack (i.e. damage) accumulation necessary for the physical breakdown and brittle fracture of rock required for rockfall or shallow rock slope failure detachment.

The significance of weathering on modifying rock characteristics has been widely observed (e.g. Durgin, 1977; Migon, 2010; Thomson et al., 2014) and the significance for rock slope stability has been demonstrated in numerical and analogue studies (e.g. Bachmann et al., 2004; Huisman et al., 2011). Understanding the controls of weathering-induced strength loss in rock slopes is important for understanding how weathering can predispose a rock slope to failure. Engineering classifications provide a descriptive insight into the nature of weathering along discontinuities (e.g. Selby, 1980; Hoek, 1983),

but such schemes do not sufficiently consider weathering-induced strength degradation of intact rock bridges that critically influence rock slope stability (de Vilder et al., 2017; Jennings, 1970; Kemeny, 2005). Similarly, many weathering studies have typically only considered surficial changes to rocks (Moses et al., 2014, and references therein), with few considering associated changes in rock strength at a scale relevant to rock slope failures, particularly for small and shallow rockfalls where stability is controlled by one critical rock bridge (de Vilder et al., 2017). In addition to decreases in rock strength, changes to rock rheology can be caused by weathering (Fookes et al., 1988). In turn, this may result in a change in the nature and style of failure (Basu et al., 2009; Gupta and Seshagiri Rao, 2000; Viles, 2013). This aspect of rock response is rarely directly considered in weathering studies.

Conventional weathering studies undertaken under laboratory conditions replicate environments where ambient compressive, shear or tensile stress conditions are considered negligible, such as desert surfaces or foreshore platforms (e.g. Coombes et al., 2013; Mottershead, 2013; Viles, 2005; Warke, 2007). However, rock slopes experience stresses resulting from temporal and spatial variations in topography, overburden load and macro- and local-scale slope geometry (Brain et al., 2014; Leith et al., 2014a, 2014b; Martel, 2006). Recent analogue experiments have suggested that the effects of weathering on rock mass strength may differ where gravity-induced ambient stress conditions exist (Bruthans et al., 2014; Rihosek et al., 2016; Zhang et al., 2015). Indeed, weathering processes operate concurrently and/or interact with a range of other processes that prepare slopes for macro-scale fracture (Aldred et al., 2016; Atkinson, 1984; Collins and Stock, 2016; Eppes and Keanini, 2017b; Eppes et al., 2016; Gischig et al., 2011; Lamp et al., 2017; Rosser et al., 2013; Stock et al., 2012) but their combined effect on rock mass strength and failure style remains unknown. This is due to the inherent complexity and non-linearity of weathering (Phillips, 2003; Viles, 2005), and associated unquantified influence on rock mass strength (Viles, 2013) within the context of an ambient gravitational stress field (Bruthans et al., 2014).

To improve our understanding of these controls on rock slope stability, we undertook a testing program that subjected cylindrical rock samples to weathering processes typically experienced by coastal rock cliffs. Our experimental design allowed us to determine the effects, if any, of ambient compressive stresses on the nature and rate of weathering and its effect(s) on rock strength, and failure style. Within these experiments we also analysed the influence of pre-existing microcrack populations and stress concentrations resulting from variable sample geometry on the strength and deformation behaviour of rock.

5.3 Materials and Methods

5.3.1 Sample lithology

We selected two lithologies for use in our study: Staithes Formation Siltstone ('siltstone') and Catcastle Buff Sandstone ('sandstone') (Figure 5.1). These rocks have different grain-size characteristics and, hence, associated differences in their potential susceptibility to weathering-driven weakening (cf. Eberhardt et al., 1999). The Siltstone forms part of the Lower Jurassic Staithes sandstone Formation (Rawson and Wright, 2000). It is light grey-blue, with 2 mm to 6 mm thick banding (classification based on ISRM, 2015). Samples were drilled from blocks collected at Skinningrove, North Yorkshire, UK (30 U 636318 m E 6049138 m N). The Catcastle Buff Sandstone forms part of the Millstone Grit Group (BGS, 2017). It is light grey-brown, massive and medium grained with minor (10%) coarse grains (ISRM, 2015). Samples were drilled from blocks collected from Dunhouse Quarry, Staindrop, UK (30 U 575875 m E 6047486 m N).

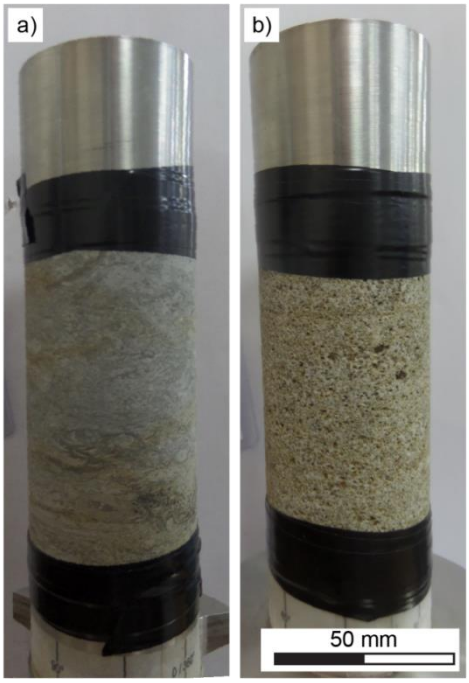

Figure 5.1: Photographs of samples a) Example siltstone sample core. b) Example sandstone sample core. Both cores are 96 mm high, and 48 mm in diameter.

5.3.2 Overview and experimental design

The first stage of our experimental program involved determining the baseline geochemical and geotechnical behaviour of the siltstone and sandstone lithologies. We considered the elemental composition of unweathered samples to characterise the geochemistry. To assess strength, we determined the unconfined compressive strength (UCS). UCS is a widely-used measurement of strength in rock mechanics and slope engineering (e.g. Jaeger et al., 2007), and also is closely related to other key measurements of intact rock strength (Perras and Diederichs, 2014). The UCS testing also allowed us to obtain a detailed understanding of stress-strain and, hence, fundamental rheological behaviour of the sample and the nature of failure. For the latter, we considered the number and nature of failure ‘events' that occurred until near or total strength loss had occurred in each sample. These failure events were defined as substantial, near-instantaneous reductions in stress with drops evident in stress-strain curves.

For our baseline dataset, we used cylindrical samples that are typical of standard geotechnical testing procedures (ASTM, 2008). These standard, unmodified samples are henceforth referred to as *U* (unmodified) samples. In addition, we undertook baseline tests on modified cylindrical samples. Firstly, we were interested in the influence of an elevated density of micro-cracks (and so the damage condition) on susceptibility to weathering processes, rates and associated changes in behaviour (Røyne et al., 2008; Viles et al., 2018; Warke, 2007). We refer to these pre-damaged samples using the notation *P*. Secondly, we were interested in the effects that variations in surface geometry may have on the effectiveness of weathering processes. To do so, we cut vertical notches into cylindrical samples. Such geometric modifications to the samples were designed to mimic the influence of daylighting discontinuities. This allowed us to assess if stress concentrations in the areas surrounding these notches created any evidence that resultant enhanced micro-cracking can be subsequently exploited by weathering processes (Lajtai and Lajtai, 1974). In addition, the increase in surface area of the sample as a result of the notch may affect the nature, rate and effectiveness of weathering (Robinson et al., 1982). Samples with modified geometry are referred to using the notation *G*. We also considered the combined effects of both modified geometry and pre-damage conditions; these are referred to as *PG* samples.

The second stage of our testing program involved assessing the effects of weathering on the key geochemical and geotechnical properties determined in our baseline characterisation stage, namely geochemical composition, strength and rheological behaviour. There were two elements to our experiments. Firstly, we considered the effects of weathering in a controlled laboratory environment. These tests focussed on the effects of salt-water wetting and drying cycles on rock properties, typical of those conditions experienced in coastal rock slopes (Mottershead, 2013). Secondly, since weathering processes do not operate in isolation (Viles, 2013), we also undertook set of field-based weathering experiments where rock samples were exposed to weather/environmental conditions and their combined effects at a coastal cliff-top in

North Yorkshire, UK. For both laboratory and field experiments, we considered the effects of weathering on *U*, *G*, *P* and *PG* samples. In addition, our experimental design allowed us to assess the effects of an elevated ambient compressive stress on weathering impacts on *U*, *G*, *P* and *PG* samples. In both laboratory and field weathering experiments, we placed samples under a constant vertical compressive stress for the full duration. This was achieved using hanging weights and a lever system. For every sample placed under stress, there was an equivalent control sample that was not subjected to vertical stresses but had been subjected to the same pre-test modifications and/or conditions (Table 5.1).

5.3.3 Geotechnical testing methods

5.3.3.1 Sample preparation

We prepared 96 mm high, 48 mm diameter cylindrical rock cores following ASTM D4543 (2008). We measured the mass and volume of each sample and subsequently calculated sample bulk density (Head, 2006).

We created pre-existing damage within the samples by loading them in unconfined compression to 75% of the median UCS observed in standard baseline tests (see results). This magnitude of loading was chosen as it is typically considered to exceed the crack initiation threshold, c_i, and, hence generate a population of distributed micro-cracks, but without causing macro-scale fracture (Figure 5.2a) (Eberhardt et al., 1998).

For *G* samples, we cut three 5 mm wide by 5 mm deep vertical ‘notches’ spaced 50 mm apart along the sample circumference, equivalent to a 120° circumferential offset between notches (Figure 5.2b). The reduction in cross-sectional area was accounted for in the calculation of compressive stress.

PG samples were firstly modified in terms of geometry and then pre-damaged using the same procedures as above.

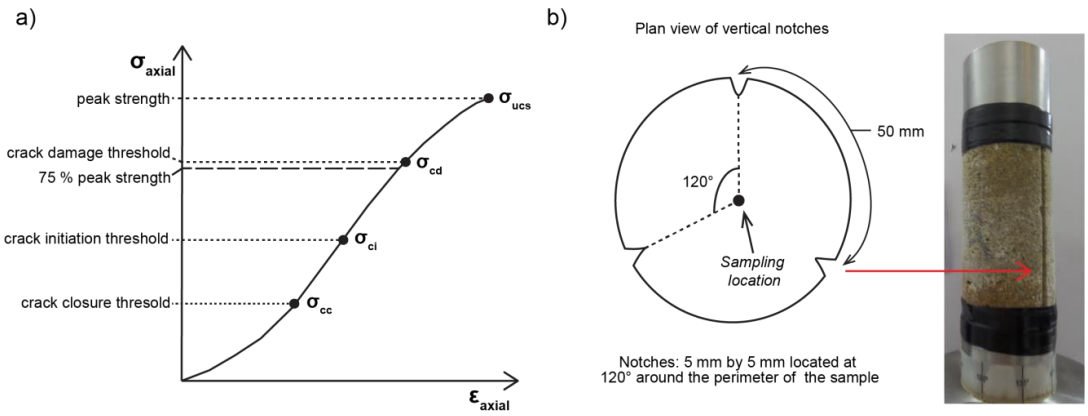

Figure 5.2: Sample Modifications. a) Stress-strain curve showing the different stages of micro-crack development under conditions of uniaxial compression (adapted from: Eberhardt et al., 1998). Samples were preloaded to 75% of peak strength in order to surpass exceed the crack initiation threshold but not exceed that of the crack damage threshold. b) Geometry of notches cut into sample, showing the conceptual plan view and an example notch within a sandstone core.

5.3.3.2 Surface hardness measurements and visual appearance

We measured baseline surface hardness of samples using a standard (d – type) Equotip portable hardness testing device (Viles et al., 2011). We measured the surface hardness of the rock in Leeb numbers (*L*); a higher *L*-value indicates a harder rock surface hardness. For each baseline rock core sample, we recorded the mean of ten measurements, obtained at random locations on the sample. These measurements were accompanied by qualitative descriptions and photographs of sample condition, noting in particular how the surface texture and colour changed through time.

5.3.3.3 Unconfined compression tests

We determined the UCS of samples in broad accordance with ASTM D7012-14 (2014) using a compressive load frame and cell manufactured by GDS Instruments Ltd. (Barla et al., (2010). Samples were loaded under compressive strain control at a rate of 0.1% min^{-1}; this strain rate reflects the net strain recorded by the apparatus and is comprised of both deformation of the rock sample and the apparatus itself in response to load (so-called 'machine strain'). The magnitude of deformation of the apparatus is constant for a given applied stress. As such, we were able to directly compare strain values between samples using net (machine) strain. This was an important consideration because use

of direct, local measurements of rock sample deformation were not always possible following completion of weathering tests, where the fragile and highly-friable nature of the weathered core surface prevented appropriate attachment of displacement transducers (LVDTs). However, for all baseline samples and for suitable post-weathering samples, we directly monitored sample deformation using two orthogonally mounted LVDTs on the rock surface. Where possible, these local strain measurements were used to calculate Young's Modulus of Elasticity and characterise the local stress-strain behaviour (ASTM D7012-14, 2014).

5.3.4 Geochemical testing methods

We determined the geochemical properties of samples via X-ray fluorescence (XRF) using a hand-held Niton XL3t XRF (ThermoScientific, 2017) to assess the elemental composition of selected samples. As these tests were conducted after the UCS tests, an approximately disc-shaped segment was cut from the broken samples to ensure a flat surface from which accurate readings could be obtained (ThermoScientific, 2017). For each, two sample spot measurements (3 mm diameter sampling area) were undertaken from the circumferential centre point of each sample (i.e. mid inner core, shown in Figure 2b) on a surface which had not been exposed previously. Elements were only recorded if their concentration was greater than 1% within the sample (ThermoScientific, 2017).

5.3.5 Baseline characterisation

We determined the baseline geochemical characteristics of siltstone (n = 4) and sandstone (n = 4) samples. We determined baseline UCS and stress-strain behaviour of standard (*U*) siltstone (n = 12) and sandstone (n = 11) samples. We also measured baseline UCS and stress-strain behaviour of modified geometry *(G*) samples *(*siltstone: n = 2 & sandstone n = 3). This included mean and standard deviations of UCS compressive strength and axial strain at the point of failure. From this, we calculated baseline failure envelopes. All baseline samples were instrumented with two LVDTs to record the strain response of the samples.

5.3.6 Weathering Experiments

5.3.6.1 Laboratory weathering experiments

We used front-loading oedometers ((Head and Epps, 2011), Figure 5.3) to place samples under a constant vertical compressive stress of 3.8 MPa, equivalent to approximately 150 to 200 m of vertical overburden. Using the pump system detailed in Figure 3, rock samples were subjected to six-hour wetting and drying cycles consisting of 30 minutes of submersion in sodium chloride solution (200 g/l), followed by drainage of the cell and subsequent exposure to ambient air for 5.5 hours. These six-hour cycles mimic semi-diurnal tidal flooding conditions experienced at the coastal cliff toe at Boulby. The experiments were undertaken in a climate-controlled laboratory (temperature: 20.9˚C ±0.24; humidity: 45% ±5.3), allowing us to isolate the effects of saltwater wetting and drying on the samples.

We subjected a total of 32 (16 sandstone and 16 siltstone) rock samples to laboratory weathering conditions for a total of 90 days. A summary of the type of samples tested (*U*, *P*, *G* or *PG*) is detailed in Table 5.1. For each type, the vertical compressive stress was applied to two samples, and two samples acted as non-stressed control samples that experienced the same weathering cycles. We monitored the net vertical deformation of the four 'stressed' samples with LVDTs (Figure 5.3). Vertical displacement of the sample was recorded as mean measurements observed over a one-minute interval. We also monitored the surface appearance and texture of rock samples and measured surface strength using the Equotip device on a weekly basis.

Following completion of the weathering test, we carefully removed the rock samples from their containers. We took two XRF measurements from 16 samples that were selected to cover all the representative sample combinations for both lithologies outlined in Table 5.1. We also measured the post-test mass of the air-dry samples.

Next, we determined the UCS and associated stress-strain behaviour of all 32 samples. This allowed us to quantify the degree of strength degradation and any changes in failure style in response to weathering. Half of these samples (n = 16) were instrumented with

two axial transducers to characterise local strain, while for the remaining half (n = 16) only net strain values were obtained.

In order to determine the impact of weathering on strength, we determined if statistically significant differences existed between the means and distributions of UCS compressive strength of weathering samples compared to baseline samples. For each of the weathered siltstone sample subset groups, which include stressed or non-stressed samples and all sample types (*U, P, G, and PG),* we used Wilcoxon rank sum test to determine these statistical differences, as the data is non-normally distributed with equal variances (see results), as determined by Lilliefors tests and Levene's tests respectively (Hollander et al., 2015). The UCS data for sandstone was normally distributed with equal variance (see results), as determined by Lilliefors tests and Bartlett's tests (Hollander et al., 2015). As such, we used one-way analysis of variance (ANOVA) to test for significant difference(s) in the distribution and means between the weathered samples and baseline samples. Student's t-tests were used to determine statistically-significant differences between pairs of groups.

Table 5.1: Sample types tested with each weathering experiment. For each of the sample types (e.g. *U, P, G, PG)*, two of the samples were placed under a constant vertical stress, while the other two samples were controls.

	Unmodified standard samples (U)	Pre-damaged samples (P)	Modified geometry samples (G)	Pre-damaged and modified geometry samples (PG)
Laboratory–Sandstone	4	4	4	4
Laboratory - Siltstone	4	4	4	4
Cliff – Sandstone	4	4	4	4
Cliff - Siltstone	4	4	4	4

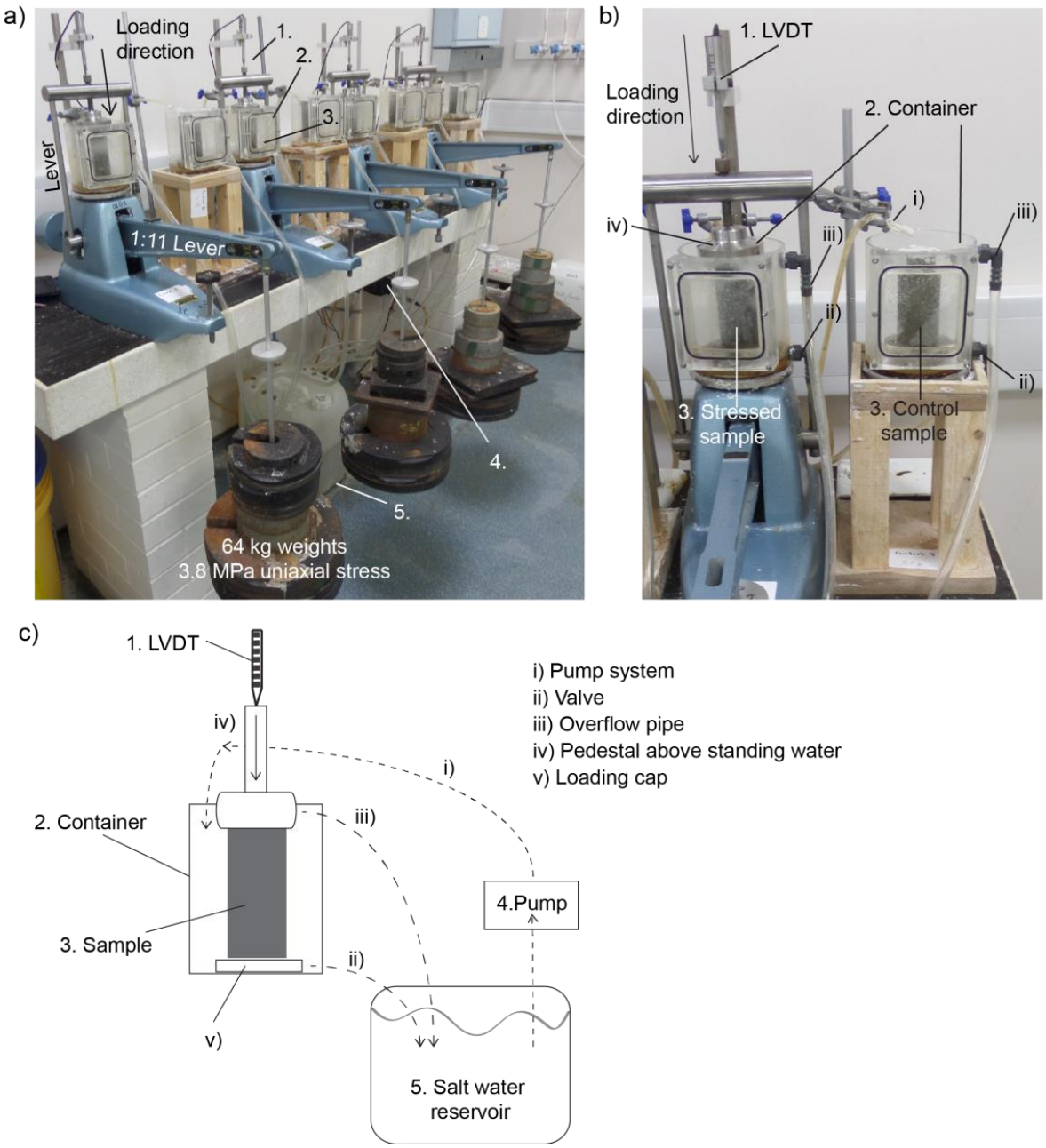

Figure 5.3: Laboratory set-up for saltwater wetting and drying experiments a) and b) Photographs of the laboratory set-up. The saltwater wetting and drying system operates by pumping water into the containers via a pipe (i) from the saltwater reservoir and draining via a valve (ii) after 30 mins of inundation. To prevent over-topping of the containers an overflow pipe (iii) was inbuilt. A small amount of standing water was present below the valve line within the container, and so samples were placed on a pedestal (iv) above this water line. The load applied via the loading cap (v). c) Schematic of the saltwater wetting and drying.

5.3.6.2 Field weathering experiments

We undertook a year-long (19th August 2016 – 30th August 2017) field experiment in which we used a purpose-built loading frame at the cliff top at Boulby, North Yorkshire, UK (Figure 5.1) to subject 32 (16 sandstone and 16 siltstone) rock samples to field conditions. The loading frame placed stressed samples under a constant vertical compressive stress of 2 MPa, equivalent to 80 to 100 m of vertical overburden and representing the height of the cliffs at Boulby (Figure 5.4). Control samples (i.e. those that were not placed under vertical stress) were located adjacent to the corresponding stressed sample. A summary of the type of samples tested (*U*, *P*, *G* or *PG*) is detailed in Table 5.1. For each type, the vertical compressive stress was applied to two samples, and two samples acted as non-stressed control samples that experienced the same environmental conditions. During the field experiment, we qualitatively monitored and described the surface appearance and texture of rock samples and measured surface strength using the Equotip device on a monthly basis.

Following completion of the field experiments, we again determined the geochemical properties of 16 samples using XRF, considering a sample from each experimental treatment (Table 5.1). We also measured the post-test mass of the samples. We then determined the UCS and associated stress-strain behaviour of all 32 samples. Half of these samples (n = 16) were instrumented with two axial transducers to characterise local strain, while for the remaining half (n = 16) only net strain values were obtained.

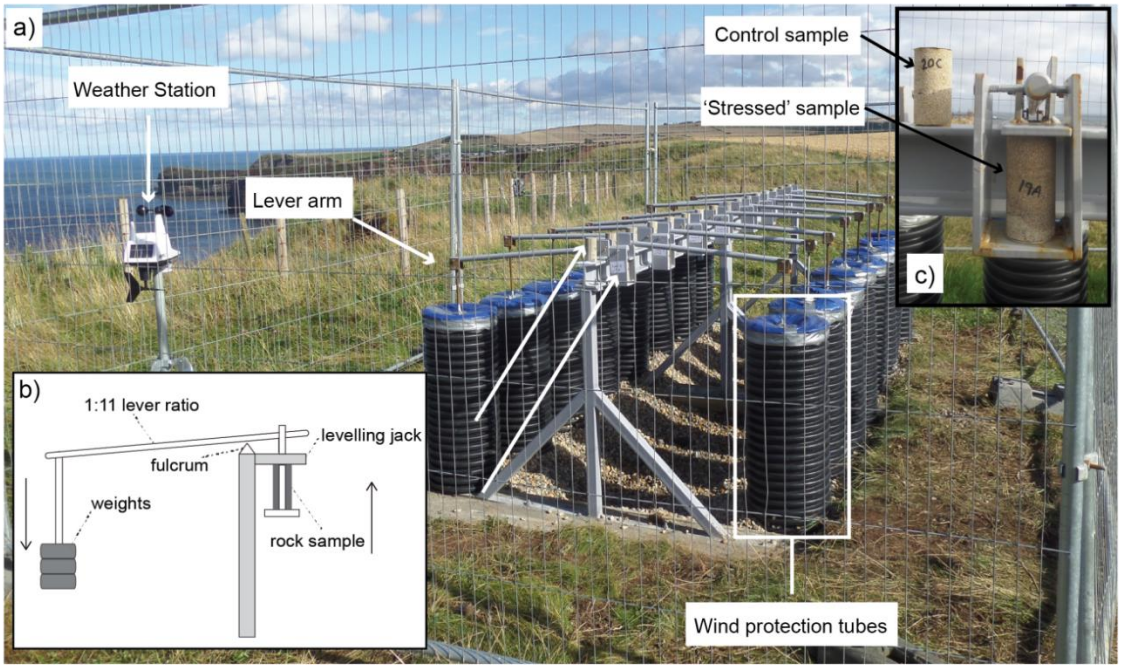

Figure 5.4: Field set-up for natural environmental condition experiment a) Field compression apparatus used to place samples under a constant vertical compressive stress. Non-stressed samples were placed on top of the beam, while 'stressed' samples were placed under load using a simple lever system. The weights for each lever arm were contained within protective tubes to prevent the hanging weights from moving due to wind. b) The general apparatus set-up, whereby the rock samples are subjected to a load applied via the levelling jack. The sample is compressed against the levelling jack when weights are applied on the opposite lever arm. Schematic is not to scale. c) Non-stressed and 'stressed' samples, with the load applied to the stress sample via the levelling jack.

5.4 Results

5.4.1 Sample baseline characterisation

5.4.1.1 Siltstone baseline characterisation

Our geochemical analysis indicates that the unweathered siltstone lithology is dominated by silicon, with aluminium, iron, potassium and titanium forming minor (> 0.1%) elements, and chlorine a trace element (< 0.1%: Table 2). We recorded a mean Equotip *L*- value of 397.5 ±126.7.

The mean UCS was 34.15 MPa ± 6.43 MPa, with failure occurring at a mean local strain of 0.46% (Table 5.3: Figure 5.5). We calculated a mean Young's Modulus of 8.99 GPa, with the local axial strain at failure ranging from 0.2% to 0.68% (Figure 5.5). All samples exhibited a brittle failure style, with most (n = 10) samples requiring either one or two

stages of brittle failure before residual or zero strength was reached. UCS tests for the modified geometry (*G*) samples displayed mean peak strength of 33.69 MPa ±1.57 MPa. These samples displayed a single-stage brittle failure.

We undertook linear regression analysis of UCS as a function of bulk density and found a reasonably-strong, statistically-significant relationship (r^2 = 0.61, p = 0.0026; Figure 5.6). This modelled envelope (Figure 5.6) allowed us to determine the representative baseline mean from which to compare the effect of weathering in absolute and percentage terms. If the initial starting bulk density of the siltstone samples was less than or greater than the range of bulk density values measured in the baseline tests, they were not used in analysis. This permitted more direct comparison of the effects of weathering on UCS and ensured the rock samples had comparable physical and geotechnical properties at the start of the experiments.

5.4.1.2 Sandstone baseline characterisation

The unweathered baseline sandstone samples were geochemically dominated by silicon, with aluminium, iron, and potassium forming major elements, while titanium and chlorine are minor elements (> 0.1 %; Table 5.2). We record a mean Equotip *L*- value of 564.87 ± 68.73.

UCS tests of standard (*U*) baseline sandstone samples were 55.69 MPa ±7.61 MPa, with failure occurring at a mean local strain of 0.24% (Table 5.3: Figure 5.5). We calculated a mean Young's Modulus of 5.69 GPa, with the local axial strain at failure ranging from 0.06% to 0.44% (Figure 5.5). All sandstone samples exhibited a single stage brittle failure (Figure 5.5). Stress strain curves obtained for the *G* samples displayed mean peak strength of 48.75 MPa ± 3.2 MPa. These samples exhibited two stages of brittle failure. We did not observe a strong and statistically-significant correlation between UCS peak strength and bulk density for the sandstone samples (r^2 = *0.1626, p = 0.2188*). To consider the effects of weathering on the strength of sandstone, we therefore compared absolute and percent changes in strength for weathered samples to the overall baseline mean value.

Table 5.2: Baseline elemental concentrations obtained from XRF analysis.

	Elemental concentrations (%)	Chlorine (Cl)	Silicon (Si)	Aluminium (Al)	Iron (Fe)	Potassium (K)	Titanium (Ti)
Silt-stone	Mean	0.08	27.03	5.0	3.78	1.15	0.41
	Standard Deviation	0.19	33.48	4.18	4.44	0.89	0.3
Sand-stone	Mean	0.02	42.49	2.17	1.04	0.79	0.05
	Standard Deviation	0.09	33.27	5.37	3.83	2.13	0.23

Table 5.3: Baseline geotechnical characteristics derived from UCS testing.

	UCS compressive strength (MPa)		Mean bulk density (g cm^{-3})	Mean Young's modulus (GPa)	Mean axial strain at failure (%)	
	Mean	Standard deviation			Machine strain	Local strain
Siltstone	34.15	6.43	2.31	8.99	1.47	0.46
Sandstone	55.69	7.61	2.4	5.69	1.25	0.24

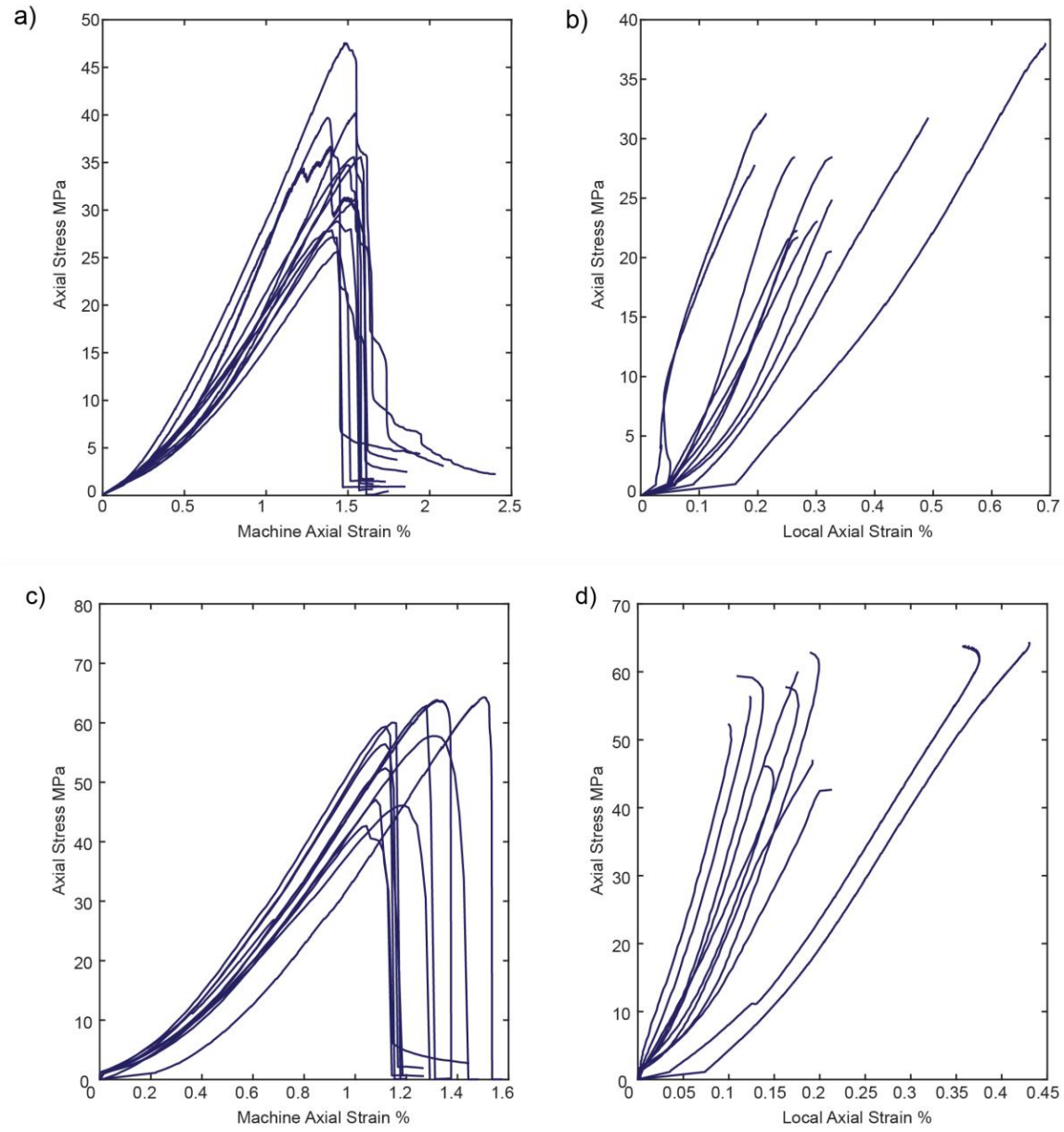

Figure 5.5: Stress-strain curves for siltstone of recorded a) machine and b) local axial strain, and stress-strain curves for sandstone of c) machine and d) local strain.

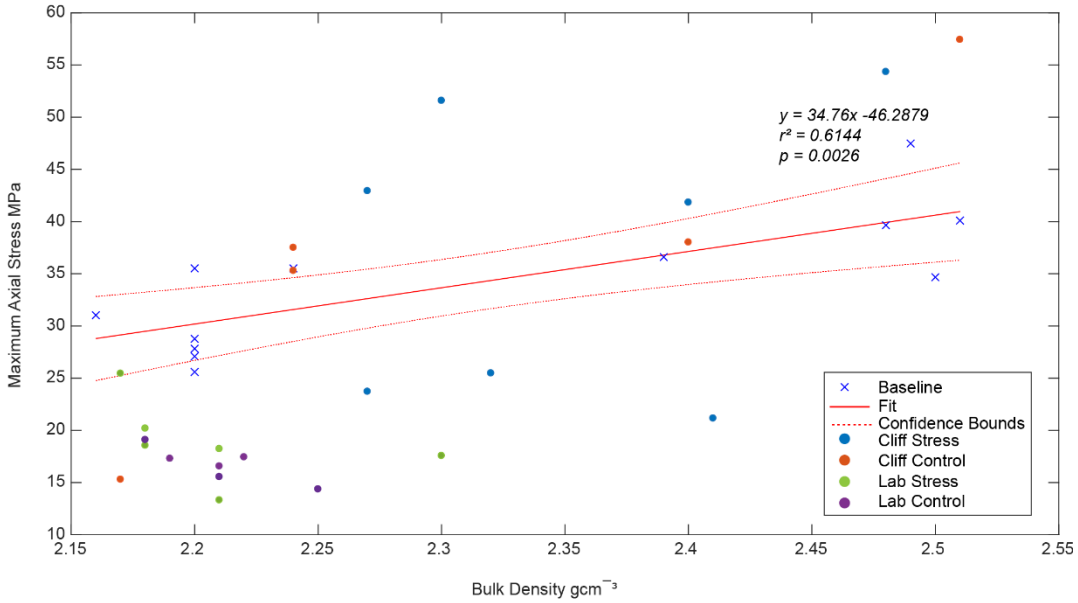

Figure 5.6: Scatter plot of maximum axial stresses for baseline siltstone samples displaying a positive linear relationship with increasing bulk density. 95% confidence bounds of this relationship are plotted on the graph, and weathered samples (with bulk densities values measured prior to weathering experiments) which plot outside of these bounds are significantly different to baseline results.

5.4.2 Weathering Experiment Analysis

5.4.2.1 Laboratory non-stressed siltstone samples

After the completion of the laboratory weathering, siltstone samples displayed an increase in chlorine content of 97% and a decrease in concentration for all other elements of up to 0.46 % of respective baseline values (Figure 5.7a). Iron leaching occurred in five samples, including two *G* and two *PG* samples (Figure 5.8a). Grain loss occurred in all cores, with slaking observed for all samples apart from one *G* sample. Slaking was characterised by loss of fragments of core (on average 5 mm high by 2 mm wide, and 2 mm deep) (Figure 5.8b). These fragments could be identified several weeks prior to detachment, characterised by sub-vertical cracks with a 1 to 2 mm aperture (Figure 5.8c). Tight (< 2 mm aperture), stepped, sub-horizontal cracks up to 50 mm long were observed in two *G* samples. However, this change in surface texture over the course of the experiment did not result in a decrease in surface hardness ($r = -0.21$, $p = 0.08$), with the change in mean *L*-value for each sample within the standard deviation of the samples (Figure 5.9a).

Non-stressed siltstone samples have a mean UCS value of 16.72 MPa, failing at 1.15% and 0.25% machine and local strain, respectively, with a mean Young's Modulus of 2.69 GPa (Table 5.4). All four of these values are lower than baseline. *U* and *P* samples displayed two stages of brittle failure before residual strength was reached, while *G* and *PG* displayed three or more stages (Table 5.4: Figure 5.10a).

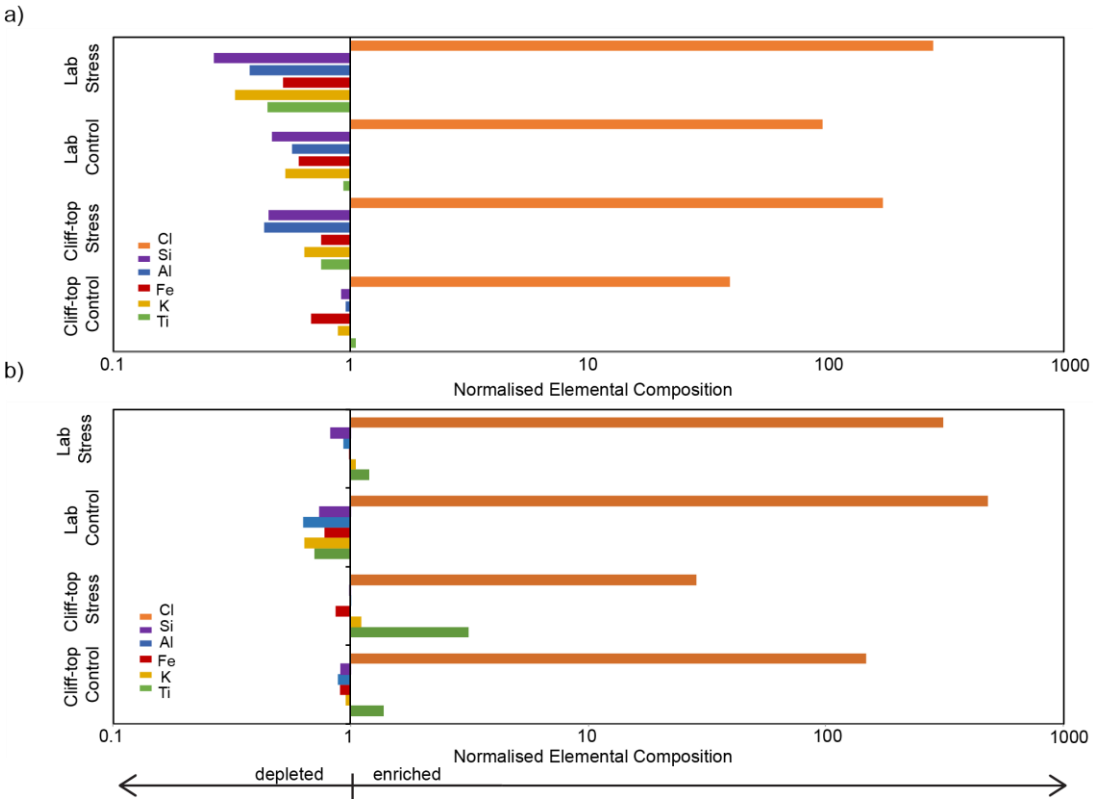

Figure 5.7: Mean elemental compositions of stress and non-stressed sample for both laboratory and cliff-top experiments normalised to mean baseline values of each element (Table 2) for a) Siltstone and b) Sandstone samples. Values greater than 1 are enriched in the elements relative to baseline concentrations, while values less than 1 are depleted relative to baseline concentrations.

Figure 5.8: Photographs of weathered samples taken during monitoring. a), b), and c) were subjected to laboratory weathering conditions. d), e) and f) were subjected to field weathering conditions. a) A sandstone sample with modified geometry (G) displaying iron leaching. b) Siltstone sample displaying slaking, with detached fragments evident around the base of the container. c) Siltstone core displaying an incipient slaking event characterised by a vertical shallow crack with a narrow aperture. d) The surface of the siltstone sample is powdery to touch, with many individual grains at the base of the core. e) Siltstone sample with multiple sub-horizontal cracks at the top and mid of core. This sample failed in situ two months after this photo was taken. f) Sandstone sample displays an area of concentrated grain loss (boxed).

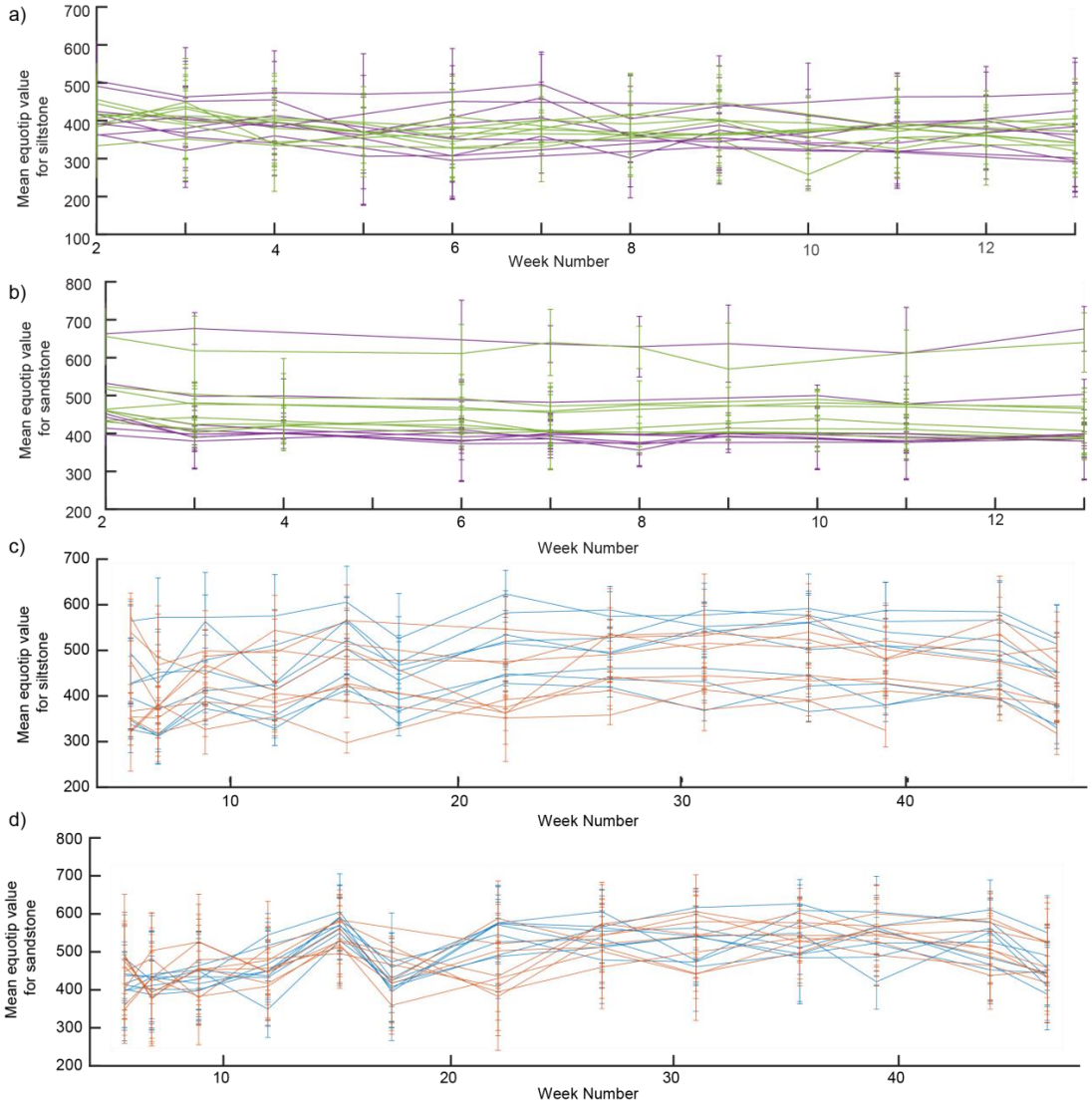

Figure 5.9: Mean Equotip values per sample and their associated standard deviations recorded over the course of a) & b) the laboratory experiments and c) & d) the field experiment. For a) & b) green lines represent stressed samples, while purple lines represent control samples. For c) & d) blue lines represent stressed samples, while red lines represent control samples. a) Siltstone laboratory samples. b) Sandstone laboratory samples. c) Siltstone field samples. d) Sandstone field samples.

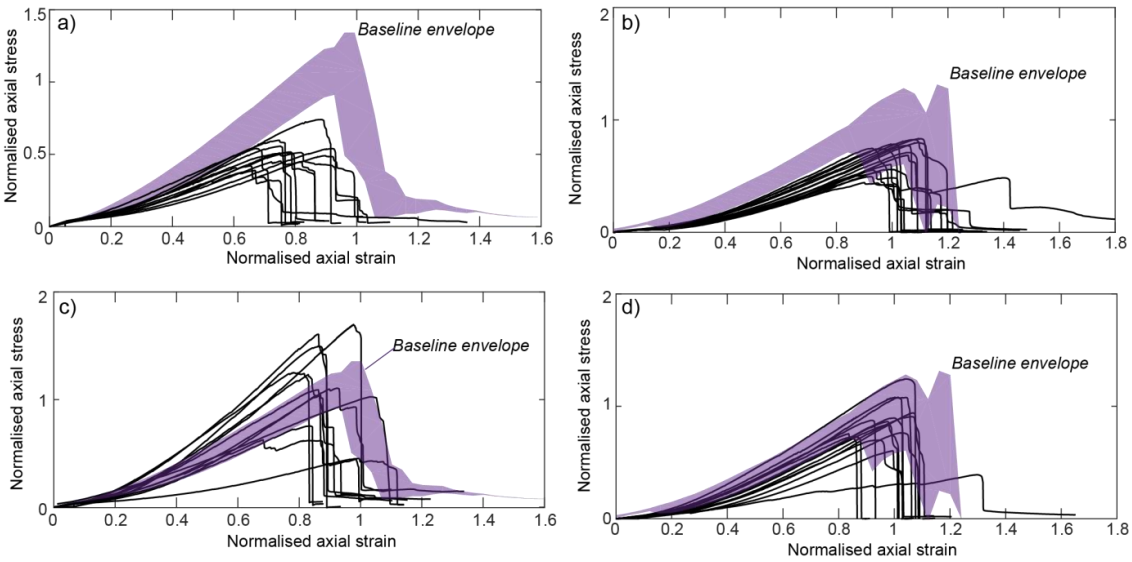

Figure 5.10: Normalised stress-strain curves obtained from UCS testing for a) & c) siltstone and b) & d) sandstone. The purple shaded area is an envelope of the range of baseline values. a) Siltstone laboratory samples. b) Sandstone laboratory samples. c) Siltstone field samples. d) Sandstone field samples.

5.4.2.2 Laboratory stressed siltstone samples

Geochemically, stressed siltstone samples display an increase in chlorine that is 218% greater than that observed in baseline samples, with all other elements displaying a decrease in concentration of up to 0.27% less than baseline (Figure 5.7a). Iron leaching and grain loss were evident for all samples (Figure 5.8a). All *U,* and *PG* samples, one *G* and one *P* sample displayed varying intensities of slaking. Sub-horizontal cracks were also observed in one *U* and one *P* sample. No significant changes in surface hardness occurred over the course of the experiment (*r = -0.18, p = 0.14:* Figure 5.9*a*).

Vertical strain measurements recorded during the weathering experiments indicated that each of the 8 stressed samples in the laboratory experiments compressed over the duration of the laboratory weathering test. Small-scale expansion events (-0.01 % to -0.02 % strain) are on a time-scale greater than that of the wetting and drying cycles and lasted for week long periods. Elastic rebound of the samples occurred at the end of the tests when the load is removed, with *U* and *P* samples displaying no permanent strain over the course of the experiment This is in contrast to the *G and PG* samples, which

displayed permanent strain values of 0.01 % to 0.16 % at the end of the weathering experiment.

Stressed siltstone samples have a UCS value of 18.89 MPa, failing at 1.19% and 0.27% machine and local strain, respectively, with a mean Young's Modulus of 1.69 GPa (Table 5.4). All four of these values are lower than baseline. The *U* sample displayed one stage of brittle failure, while the *G* and *PG* samples displayed two stages of brittle failure, and the *P* sample three or more stages (Table 4:Figure 5.10a).

5.4.2.3 Laboratory non-stressed sandstone samples

Non-stressed sandstone displayed an increase in chlorine content of 480% and a decrease in concentration for all other elements of up to 0.63% of respective baseline values (Figure 5.7b). One *PG* sample displayed iron leaching, while grain loss occurred for all samples. No cracking associated with slaking was observed. A significant decrease in surface hardness was observed over the experiment ($r = -0.26$, $p = 0.023$), though the change in mean *L*-value for each sample is within the standard deviation of the respective sample (Figure 5.9b).

Non-stressed sandstone samples have a UCS value of 35.76 MPa, failing at 1.23% and 0.22% machine and local strain, respectively, with a mean Young's Modulus value of 6.58 GPa (Table 5.4). The samples display a decrease in strength relative to baseline but fail at equivalent strain values and a higher Young's Modulus. *U* and *G* samples displayed two stages of brittle failure, while *P* and *PG* samples displayed three or more stages (Table 5.4: Figure 5.10b).

5.4.2.4 Laboratory stressed sandstone samples

Stressed sandstone displayed an increase in chlorine content of 311%, an increase in titanium and potassium of up to 1.2% and decrease in concentration for all other elements of up to 0.83% of respective baseline values (Figure 5.7b). Iron leaching was observed for all samples, along with grain loss in cores. No slaking was observed for any sandstone samples. One *G* sample contained a sub-horizontal crack. A significant

reduction in surface hardness was detected (*r = -0.36, p = 0.001),* with a decrease in mean *L*-value from 506.12 to 461.75, though the change in mean *L*-value for each sample is within the standard deviation of the samples (Figure 5.9b).

The same behaviour as seen in the monitored strain measurements for stressed siltstone samples is seen here, with six samples compressing in the direction of load over test duration. Expansion events on the order of days to weeks were also observed and exerted –0.025 % to -0.1 % strain (Figure 5.11). Rebound of samples occurred at the end of the tests when the load was removed, with *U* and *P* displaying no permanent strain while *G* and *PG* samples displayed permanent strain values of 0.01% to 0.05% strain.

Stressed sandstone samples have a UCS value of 38.73 MPa, failing at 1.25% and 0.27% machine and local strain, respectively, with a mean Young's Modulus value of 5.49 GPa (Table 5.4). The sample displayed a decrease in strength relative to baseline but fail at equivalent strain and Young's Modulus values. All samples displayed two stages of brittle failure (Table 5.4: Figure 5.10b).

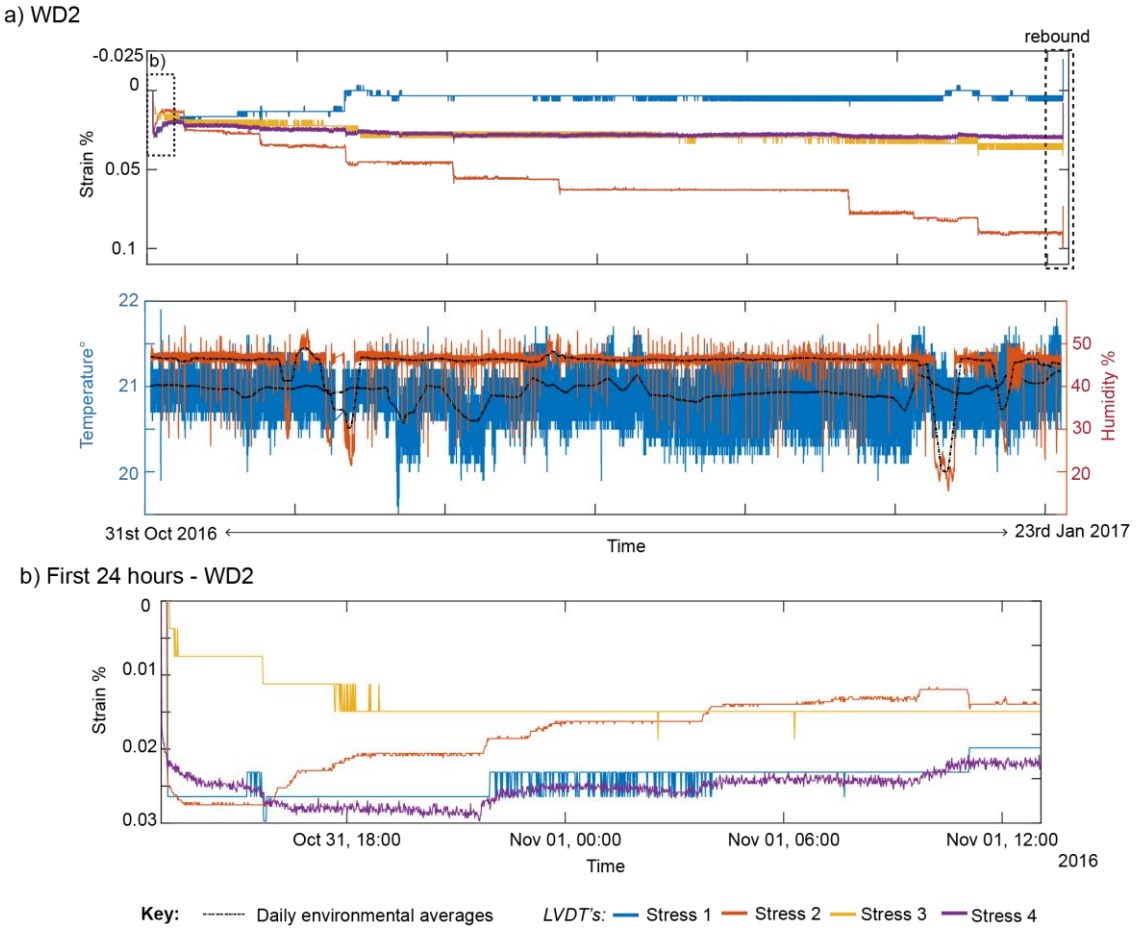

Figure 5.11: Monitoring strain data a) Strain response for each of the four stressed siltstone samples within the laboratory experiments (Table 1). An increase in strain values reflects compression of the sample, while decreases in strain values reflect expansion of sample. Rebound occurs at the end of the experiment for all samples once the constant uniaxial compressive stress is removed. b) First 24 hours of experiment, displaying an initial compression for all samples, followed by either further compression as is the case for Stress 3, or expansion as seen for Stress 1, 2 and 4.

Table 5.4: Mean geotechnical characteristics obtained from UCS testing for both siltstone and sandstone laboratory experiments.

				Mean Geotechnical Characteristics				
Rock Type	Test conditions	Sample variables	No. of samples	Peak UCS strength (MPa)	Machine axial strain at failure (%)	Local axial strain at failure (%)	Young's Modulus (GPa)	Brittle failure stages
Siltstone	Stressed	All	6	18.89	1.19	0.27	1.69	2
		U	1	18.23	1.39	NA	NA	1
		P	1	20.19	1.13	NA	NA	2
		G	2	22.00	1.18	0.15	1.70	3
		PG	2	15.45	1.12	0.12	1.70	2
	Control	All	6	16.72	1.15	0.25	2.69	2
		U	2	18.73	1.17	0.24	5.40	2
		P	1	16.57	1.36	NA	NA	2
		G	1	15.55	1.14	0.27	2.18	3
		PG	2	16.74	1.02	0.20	2.66	3
Sandstone	Stressed	All	8	38.73	1.25	0.27	5.49	2
		U	2	42.73	1.33	0.28	5.78	2
		P	2	39.39	1.31	0.28	5.47	2
		G	2	36.01	1.14	0.33	5.74	2
		PG	2	36.79	1.23	0.21	4.96	2
	Control	All	8	35.76	1.23	0.22	6.58	2
		U	2	27.73	1.18	0.13	8.60	2
		P	2	31.11	1.20	0.22	6.67	3
		G	2	42.00	1.34	0.15	5.85	2
		PG	2	42.21	1.22	0.37	5.22	3

*Where there is only 1 sample the other corresponding sample has been removed as its bulk density lay outside the baseline siltstone bulk density bounds.
**This represents where no local axial data and associated Young's' Modulus values were obtained.

5.4.2.5 Field non-stressed siltstone samples

Non-stressed siltstone displayed an increase in chlorine content of 39% and a decrease in concentration for all other elements of up to 0.68% of respective baseline values (Figure 5.7a). Grain loss occurred for all samples, creating a powdery core surface texture for a *U, P,* two *G* and *PG* samples. Tight (< 2 mm aperture), stepped sub-horizontal cracks which were 2 to 10 mm long, were observed in two *U,* and one *P* sample(s) (Figure 5.8e) along with tight, sub-vertical cracks, 5 to 20 mm long in the *U*

samples. One *U* sample, shown in Figure 8e, failed along a sub-horizontal crack in month 10 of the experiment. A significant increase in surface hardness was detected over the course of the experiment (*r = 0.21, p = 0.04),* though the change in mean *L*-value for each sample is within the standard deviations of the samples (Figure 5.9c).

Non-stressed siltstone samples have a UCS value of 36.71 MPa, failing at 1.4% and 0.26% machine and local strain, respectively, with a mean Young's Modulus value of 5.0 GPa (Table 5.5). The samples display equivalent or higher strength, strain and Young's Modulus values to baseline. *U* and *PG* samples displayed two stages of brittle failure, with *P* samples displaying three stages (Figure 5.10c).

5.4.2.6 Field stressed siltstone samples

Stressed sandstone displayed an increase in chlorine content of 175% and a decrease in concentration for all other elements of up to 0.43% of respective baseline values (Figure 5.7a). Red-coloured grains were observed at the base of the cores during monitoring. Grain loss occurred for all samples, which over the course of the experiment created a surficial powdery texture (Figure 5.8d). No cracking was observed in these samples. A significant increase in surface hardness was detected over the course of the experiment *(r = 0.22, p = 0.025)* though the change in mean *L*-value for each sample is within the standard deviation of the samples (Figure 5.9c).

Non-stressed siltstone samples have a UCS value of 37.30 MPa, failing at 1.12% and 0.29% machine and local strain, respectively, with a mean Young's Modulus value of 3.63 GPa (Table 5.5). The samples display equivalent or higher strength to baseline, while strain and Young's Modulus values are lower than baseline. The *P* samples displayed a single stage of brittle failure, while the *U* sample displayed two stages, and the *G* and *PG* samples displayed three stages (Table 5; Figure 5.10c).

5.4.2.7 Field non-stressed sandstone samples

Non-stressed sandstone displayed an increase in chlorine content of 148%, an increase in titanium of 1.3% and a decrease in concentration for all other elements of up to 0.89%

of respective baseline values (Figure 5.7b). Loss of surface grains was recorded in all samples. Significant increases in surface hardness were observed *(r = 0.4, p>0.001*: Figure 5.9d).

Non-stressed sandstone samples have UCS value of 49.93 MPa, failing at 1.23% and 0.22% machine and local strain, respectively, with a mean Young's Modulus value of 7.07 GPa (Table 5.5). The samples display a lower strength than mean UCS baseline, but the lower strength of *P*, *G* and *PG* samples are within the standard deviation of UCS baseline, while *U* samples fail at a lower strength value that is greater than standard deviation (45.31 MPa). All samples fail at equivalent strain levels to baseline apart from *P* samples, which display the lowest machine strain values with 1.16%, and *G* samples, which display the lowest local strain values at 0.14%. Young's Modulus values are equivalent or higher to baseline, apart from *PG* samples, which have a value of 4.89. All samples exhibit two stages of brittle failure (Table 5.5: Figure 5.10d).

5.4.2.8 Field stressed sandstone samples

Stressed sandstone displayed an increase in chlorine content of 29%, an increase in titanium of 3.1%, and a decrease in concentration for all other elements of up to 0.91% of respective baseline values (Figure 5.7b). Red-coloured grains were observed at the base of samples. Grain loss occurred for all samples, with this grain loss concentrated in pockets on the core surface for 3 samples (Figure 5.8f). One *G* sample displayed a tight, stepped, sub-horizontal 20 mm long crack. Significant increases in surface hardness were observed (*r = 0.44, p>0.001:* Figure 5.9d).

Stressed sandstone samples have a UCS value of 44.53 MPa, failing at 1.23% and 0.17% machine and local strain, respectively, with a mean Young's Modulus value of 6.90 GPa (Table 5.5). *PG* sample have a higher UCS of 59.99 MPa, while all other samples are weaker than baseline. Failure occurs at equivalent machine strain values to baseline, apart from *U* samples, while all values are equivalent or lower than baseline for local axial strain at failure, with *U* samples displaying the lowest value of 0.04%. *PG*

samples displayed a single stage of brittle failure, while *U and G* samples displayed two stages of brittle failure, with *P* samples displayed three stages (Table 5.5, Figure 5.10d).

Table 5.5: Mean geotechnical characteristics obtained from UCS testing for both siltstone and sandstone siltstone experiments.

				Mean Geotechnical Characteristics				
Rock Type	Test conditions	Sample variables	No. of samples	Peak UCS strength (MPa)	Machine axial strain at failure (%)	Local axial strain at failure (%)	Young's modulus (GPa)	Brittle failure stages
Siltstone	Stressed	All	7	37.30	1.21	0.29	3.63	2
		U	1*	23.72	1.12	0.41	1.81	2
		P	2	39.92	1.28	0.25	0.73	1
		G	2	47.27	1.24	0.24	6.45	3
		PG	2	31.50	1.14	0.27	5.53	3
	Control	All	5	36.71	1.40	0.26	5.00	2
		U	1	37.51	1.30	NA**	NA	2
		P	2	25.30	1.41	0.15	3.93	3
		G	0***	-	-	-	-	-
		PG	2	47.73	1.44	0.38	6.08	2
Sandstone	Stressed	All	8	44.53	1.23	0.17	6.90	2
		U	2	43.68	1.14	0.04	7.40	2
		P	2	31.99	1.33	0.17	6.01	3
		G	2	42.44	1.21	0.24	6.37	2
		PG	2	59.99	1.22	0.23	7.85	1
	Control	All	8	49.93	1.23	0.22	7.07	2
		U	2	45.31	1.25	0.25	6.69	2
		P	2	52.51	1.16	0.21	6.25	2
		G	2	51.51	1.28	0.14	10.47	2
		PG	2	50.41	1.21	0.27	4.89	2

* Where there is only 1 sample the other corresponding sample has been removed as its bulk density lay outside the baseline siltstone bulk density bounds
**No local axial data and associated Young's' modulus values were obtained.
*** Both samples had bulk density values greater than the baseline bounds and so were not included in the analysis.

5.4.3 Weathering-induced changes in geotechnical properties

We grouped the different test conditions into broad categories to determine statistical differences from baseline data, as well as difference between these category types. The categories outlined below are the same for both lithologies:

- Sample Modifications: *U, P, G, PG* samples for both laboratory and field experiments
- Test conditions: 'Stressed' or 'non-stressed' samples
- Environmental setting: Laboratory or field

5.4.3.1 Sample modification analysis

Overall, *U* samples were significantly weaker than baseline samples for siltstone and sandstone ($p = 0.001$ and $p > 0.001$, respectively). They show the greatest strength reduction for all sample modifications, being 38.28% weaker for siltstone and 24.60% for sandstone (Table 5.6). *P* samples were significantly weaker than baseline by 20.38% for siltstone and 22.93% for sandstone ($p = 0.0424$ and $p = 0.008$, respectively: Table 5.6). *G* samples were significantly weaker than baseline for sandstone ($p = 0.008$) but not for siltstone ($p = 0.159$) with a 12.7% strength decrease (Table 5.6). *PG* samples do not result in significant decreases in strength from baseline for either lithology ($p = 0.116$ and $p = 0.089$, respectively. All sample modification types for siltstone show a decrease in strain relative to baseline (Figure 5.12), reflected in lower Young's Modulus values indicating a decrease in stiffness (Table 5.6). Sandstone sample modifications display a similar distribution in strain values to baseline (Figure 5.13), with Young's Modulus values all higher indicating an increase in sample stiffness (Table 5.6). No statistically-significant differences exist between the different sample modification types for both siltstone (Figure 5.12) and sandstone (Figure 5.13).

5.4.3.2 Test condition analysis

All stressed samples were significantly weaker than baseline (siltstone: $p = 0.043$ and sandstone: $p = 0.001$), as were non-stressed samples (siltstone: $p = 0.035$ and

sandstone: *p = 0.001)*. However, no statistically-significant differences exist between stressed and non-stressed samples for either lithology (Figure 5.12c & Figure 5.13c). This similarity in distributions also exists for strain values at failure for both siltstone and sandstone sample types displaying a decrease relative to baseline (Figure 5.12d &Figure 5.13d).

5.4.3.3 Environmental setting analysis

Field siltstone samples display an increase in strength of 5.23% with no statistical difference to baseline (Table 5.6). However, the strength of field sandstone samples does decrease significantly by 15.19% (*p = 0.042*: Table 5.6). Both siltstone and sandstone samples in the laboratory tests show significant reductions in strength (*p > 0.001)* with siltstone displaying a 41.4% decrease (Table 5.6). These larger reductions in strength for laboratory experiments result in significant differences between the test types for both lithologies (siltstone: *p = 0.022* – Figure 5.12e, and sandstone: *p = 0.006* – Figure 5.13e). Strain values decrease for laboratory siltstone samples, with a wider range in values for the field experiment (Figure 5.12f). Both laboratory and field sandstone samples display similar strain values to baseline (Figure 5.13f).

Table 5.6: Strength properties of weathered samples for the different environmental setting and test conditions for both siltstone and sandstone, including absolute and percentage differences from equivalent baseline samples.

		UCS				Young's Modulus absolute difference(GPa)**	Absolute difference in machine axial strain at failure (%)8
		Mean (MPa)	Standard deviation (MPa)	Absolute difference (MPa)*	Percent difference (%)*		
Sandstone	All samples	27.43	13.76	-5.25	-18.10	-5.52	-0.24
	All field	37.10	13.57	2.21	5.23	-5.63	-0.18
	All lab.	17.81	3.10	-12.70	-41.36	-5.61	-0.3
	Stressed	28.80	13.86	-4.33	-14.52	-5.63	-0.27
	Control	25.81	14.13	-6.34	-22.26	-5.37	-0.21
	U	19.17	3.06	-11.79	-38.28	-5.13	-0.29
	P	27.86	14.94	-5.95	-20.38	-5.36	-0.26
	G	29.6	14.88	-3.64	-12.70	-5.64	-0.23
	PG	27.85	16.01	-6.94	-22.84	-5.38	-0.28
Siltstone	All samples	42.24	10.70	-13.45	-24.15	0.82	-0.01
	All field	47.23	11.40	-8.46	-15.19	0.77	-0.02
	All lab.	37.24	7.32	-18.45	-33.12	0.78	-0.01
	Stressed	41.63	11.29	-14.06	-25.25	0.82	-0.01
	Control	42.85	10.41	-12.84	-23.06	0.77	-0.02
	U	42.00	5.49	-13.69	-24.60	0.04	-0.02
	P	42.92	13.15	-12.77	-22.93	1.43	-0.04
	G	44.11	11.77	-11.58	-20.80	0.11	-0.01
	PG	47.10	13.12	-8.59	-15.42	0.73	-0.01

*Difference from mean baseline values.
**Calculated from local strain data.

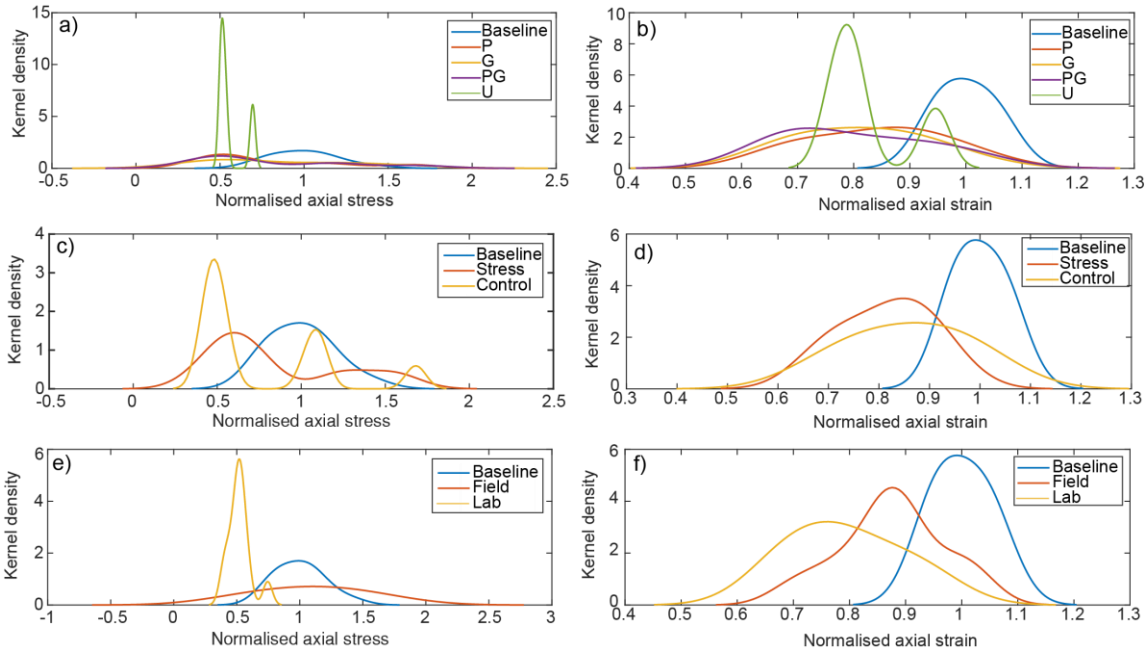

Figure 5.12: Siltstone stress and strain distributions a) & b) Kernel density plots displaying the distributions of peak normalised peak axial stress and normalised axial strain for the modified siltstone samples compared with those of baseline tests. c) & d) Kernel density plots displaying the distributions of normalised peak axial stress and normalised axial strain for the stressed and control siltstone samples compared with baseline e) & f) Kernel density plots displaying the distributions of peak normalised axial stress and axial strain for cliff-top and laboratory siltstone experiments compared with baseline test results.

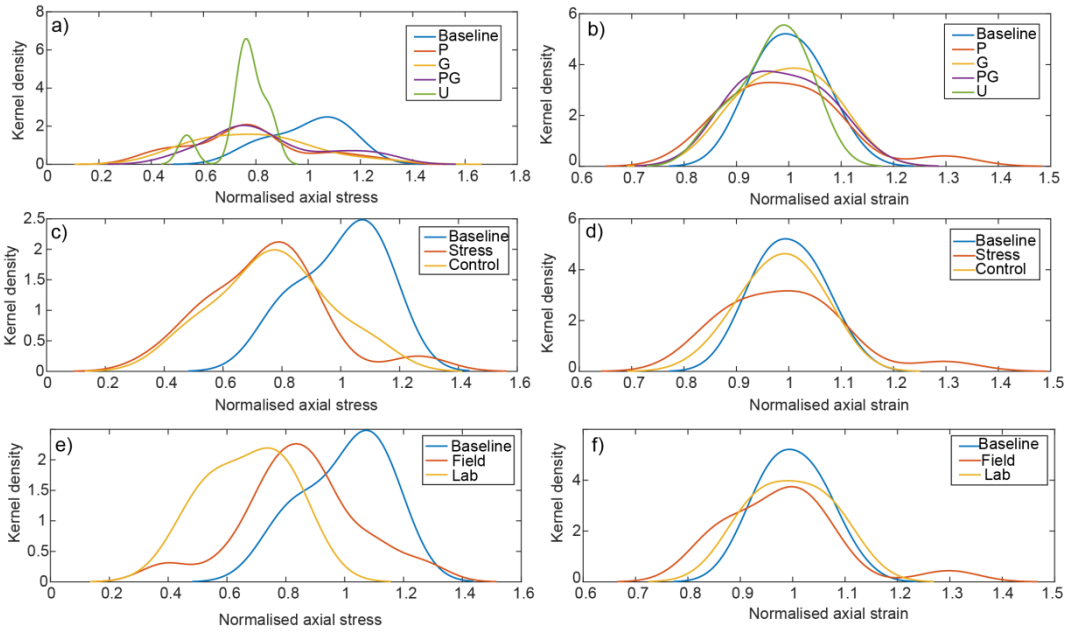

Figure 5.13: Sandstone stress and strain distributions a) & b) Kernel density plots displaying the distributions of peak normalised peak axial stress and normalised axial strain for the modified sandstone samples compared with those of baseline tests. c) & d) Kernel density plots displaying the distributions of normalised peak axial stress and normalised axial strain for the stressed and control sandstone samples compared with baseline e) & f) Kernel density plots displaying the distributions of peak normalised axial stress and axial strain for cliff-top and laboratory sandstone experiments compared with baseline test results.

5.4.3.4 Failure Mode

Generally, as UCS sample strength decreased, failure mode changes to include more brittle stages of failure. Both lithologies displayed this behaviour (Figure 5.14), with significant differences in strength for each failure type existing for sandstone ($p > 0.01$; Figure 5.14b). Multi-stage failures are characterised by a mean strength of 24.46 MPa for siltstone and 32.9 MPa for sandstone. These multi-stage failures may often sustain stresses slightly lower (~1 MPa to 2 MPa) than peak strength of the sample until further or final failure occurs (Figure 5.14c). Along with changes in stress-strain behaviour a greater number of cracks and associated complexity of failure morphology are observed within the samples with increasing number of brittle failure stages (Figure 5.14d). No correlation existed between failure mode and environmental setting, test conditions or sample modifications.

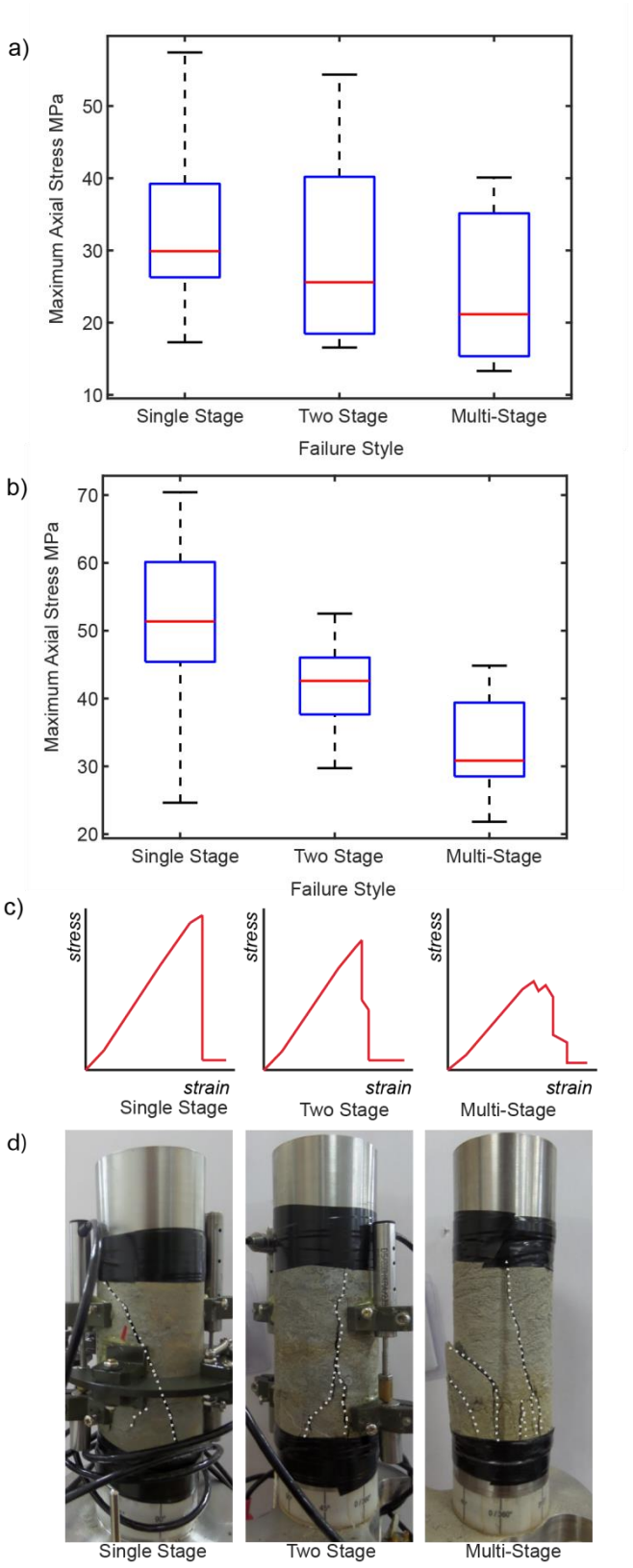

Figure 5.14: Changes in failure style a) Boxplots of a decrease in strength with failure style for sandstone. b) Boxplots of a decrease in strength with failure style for siltstone. c) Conceptual stress-strain graphs displaying the different brittle failure styles. d) Post failure siltstone sample photographs of different failure styles displaying an increase in complexity of failure surfaces with failure mode.

5.5 Discussion

5.5.1 Controls on weathering intensity

Our geotechnical analysis indicates that pre-existing micro-crack damage, modified sample geometries and/or samples subjected to a constant compressive vertical stress do not result in enhanced strength degradation relative to samples that have undergone no modification. A greater density of initial micro-cracks, as present in *G* samples, does not necessarily result in a greater degree of strength reduction, resulting from exploitation of micro-crack populations by weathering processes. This is in contrast to other studies, where increased surface area as a result of micro-cracking, or pre-existing damage within a sample due other weathering processes have been observed to accelerate the rate of weathering (Røyne et al., 2008, Viles et al., 2018). The degree of geometric modification in *P and PG* sample mays have been insufficient to create stress concentrations of sufficient magnitude to result in enhanced micro-cracking (Lajtai and Lajtai, 1974). The shape of the modifications may have determined weathering efficacy, with concavities and curved areas within Robison et al., (1982) study displaying reduced surficial disintegration in response to weathering as compared to sharp protrusions.

Additionally, within this experimental set-up and over the time-scale of the experiments considered, a constant compressive stress has a negligible effect on strength degradation resulting from weathering processes. This result is in contrast to experiments conducted using sediments with no cementation (Bruthans et al., 2014; Zhang et al., 2015) or weak cementation (Bruthans et al., 2016; Rihosek et al., 2016). These previously-published experiments showed a temporal component of stress influence on weakening, displaying faster erosion rates (Bruthans et al., 2014) and strength degradation (Zhang et al., 2015) until a ‘critical’ stress value was reached. The interlocking strength of the grains was great enough to slow or prevent further erosion and weathering from occurring. The frictional properties of these materials were the dominant components of strength, rather than cohesional properties of intact rock. Martin and Chandler (1994) propose that the strength of intact rock is controlled primarily by

cohesion up until 75% to 80% of UCS. Our findings suggest that gravitationally-induced compressive stress (here 2 MPa and 3.6 MPa) has a limited impact on the processes which result in cohesional strength reduction. This imposed topographic stress may also be of an insufficient magnitude when combined with stresses generated by weathering to result in the crack initiation threshold being exceeded (Figure 2a). As consequence, a higher degree of cracking to occur relative to 'stress-free' rock was not observed (Eberhardt et al., 1998).

The range in UCS values we recorded post weathering experiments may mask subtle changes in strength related to different variables groups, such as *U, P, stressed* and non-stressed. However, where statistically-significant relationships existed between bulk density and UCS, we accounted for this variability by using bulk density as an indicator of anticipated strength. The similarity of the distributions and variance between each of the variable groups (*U, G, P* and *PG*) and with baseline data itself indicates that the variance recorded within each group remains constant. We infer that this variance is a function of inherent sedimentological variability (e.g. Ghobadi and Babazadeh, 2015; Nicholson and Nicholson, 2000). As such, comparison between the means reveals shifts in the entire sample population of each variable towards a weaker strength value.

5.5.2 Effect of weathering on compressive rock strength

Overall, we demonstrate that weathering results in a significant reduction of strength for all laboratory samples and even for rock that has been exposed to natural environmental conditions for a year, as demonstrated by the 15.19% loss in strength for sandstone samples placed at the cliff-top. The loss of strength we record can be driven by sub-critical crack growth where micro-crack growth occurs under stress amplitudes lower than the crack initiation threshold within a rock mass (Atkinson, 1984). Small amplitude stress as a result of environmental processes such as insolation or wetting and drying can therefore drive micro-crack growth (Eppes and Keanini, 2017). This can occur via stress corrosion cracking where molecular bonds are strained and stretched at crack tips

by a chemically active environmental agent, such as water (Atkinson, 1984; Eppes and Keanini, 2017)

Our geochemical analysis and monitoring observations indicate that the weathering processes within our experiments change the geochemical composition of samples, both in terms of increases in chlorine content and a leaching effect, with iron leachate observed for stressed samples during the laboratory experiments. As the field samples were exposed to the effects of weather (notably wind and rain), evidence of iron leachate may have been removed. However, the potential increased rates of chemical alteration associated with observations of iron leaching from all stressed samples, does not result in a discernible degree of strength loss greater than that of non-stressed samples. In addition, the geochemical data revealed that a decrease in iron is observed for all sample types. This loss of iron may be a result of enhanced permeability due to increasing micro-crack density or micro-crack opening occurring within the sample (Mitchell and Faulkner, 2008; Nicholson, 2001; Oda et al., 2002). Changes in the geochemistry, as evidenced by leaching, may subsequently change sub-critical cracking characteristics, though little is known about the exact controls on this process (Atkinson, 1984; Freiman, 1984). This change in geochemistry may result in a change of failure style, with increases in pore water acidity resulting in more diffuse cracking (Dunning and Huf, 1983).

We also observed significant periods of expansion within the laboratory strain data, indicating that such expansion was able to counteract the 3.6 MPa vertical stress acting on the sample. This potentially explains the limited influence of topographic stress on strength as weathering can generate stresses that counteract those generated by overburden loading. We suggest that salt crystallisation pressures may be a possible mechanism for this expansion, as evidenced by post-test chlorine content, with micro-cracking also occurring when crystallisation pressures exceed the strength of the matrix and grain bonds (Espinosa-Marzal and Scherer, 2010).

We also observed changes in the surface texture of all samples, consisting of grain loss, slaking and cracking. These changes in surface texture, along with the significant

reductions in UCS strength, were only detected in surface hardness measurements of sandstone samples within the laboratory tests. The field tests showed increased surface hardness, which may be interpreted as case hardening (Mol and Viles, 2012; Viles et al., 2011). In contrast, we recorded a significant reduction in UCS for field-based sandstone samples and no significant change in UCS for field siltstone. The inconsistency between observed decreases in UCS and constant or increasing surface hardness measurements indicates that our interpretation of rock strength from such surface hardness data does not capture the internal weakening of intact rock. Changes in the elasticity of rock, as captured via vibration frequency analysis, have been shown to better correlated with changes in brittle rock strength (Allison, 1990). This internal weakening is of critical importance to shallow rock slope failures, where block release of the incipient failure mass is contingent on brittle fracture through intact rock. As such, we suggest that the application of surface hardness measurements to understanding the influence of weathering on shallow rock slope failures may be limited and/or not appropriate in all situations.

5.5.3 Effect of weathering on failure style

The difference in grain sizes between the two sedimentary lithologies we tested appears to have a limited effect on the degree of strength loss, with both displaying similar reductions in strength. However, grain size may influence strain behaviour with sandstone samples recording no change in strain characteristics when compared to baseline tests, while siltstone displayed significant reductions relative to baseline tests. This difference in response may be due to the nature of the matrix of the siltstone. Fabre and Pellet (2006) highlight the link between observed deformation, cracking within an argillaceous rock matrix and grain sliding and rotation. The nature of the sandstone matrix may prevent these granular re-adjustments from occurring.

Our analysis indicates that a reduction in strength is linked to and manifest in a change in failure style. Weaker rocks display a more distributed multi-stage failure process reflected in their stress-strain behaviour and the resultant failure morphology (Observed

also in studies by Basu et al., 2009; Gupta and Seshagiri Rao, 2000). Multi-stage failures involve several stages of macro-scale fracture and strength loss until residual or total loss of strength occurs. These types of failure can temporally sustain high stress levels even after a peak stress level has been reached. It is only after sufficient post-peak strain has accumulated within the sample that subsequent failure event(s) occur. Weakening of the rock sample by weathering may lead to more diffuse micro-cracking, as seen in cyclic loading tests, which can be used as a proxy for environmental fluctuations and associated weathering processes, that eventually result in an increased number of macro-cracks (Cerfontaine and Collin, 2017). These distributed micro-cracks do not result in the same pattern of coalescence required for unstable 'run-away' macro-scale fracture, as normally predicted for a similar point on stress-strain curves (Eberhardt et al., 1998; Martin and Chandler, 1994). The failure events observed in the multi-failure stage failures instead may represent mini-coalescence events in weaker zones to form relatively smaller macro-scale fractures, which do not connect in the first instance.

5.5.4 Slope failure implications

We suggest that a change in failure style with strength loss over time (Figure 5.15) will determine the triggers required for failure and will hence dictate the timing of ultimate failure. Intact rock characterised by single stage brittle fracture likely requires a high magnitude loading event that will result in near instantaneous failures, as indicated by the unstable crack propagation threshold within Figure 5.15. As damage accumulates through time, the magnitude of environmental stresses required for fracture to occur decreases, but the frequency of such events will increase, resulting in a positive feedback. For weaker rock characterised by several stages of brittle failure, with each 'new' failure event and associated damage accumulation in the sample, the stress level required for further failure is decreased. For final failure to occur, only a low magnitude stress perturbation may be required (Figure 5.16). In the context of rock slope failure, this final stress perturbation may reflect stress-redistribution of the slope following progressive failure (e.g. Eberhardt et al., 2004a; Rosser et al., 2007; Stock et al., 2012),

environmental stress fluctuations (Collins and Stock, 2016; Gunzburger et al., 2005) or topographic stress concentrations within the slope (Brain et al., 2014). In such a scenario, even though topographic stress is not a control on the rate of weakening as we determined from our experimental datasets, it may therefore control the location of rock failure.

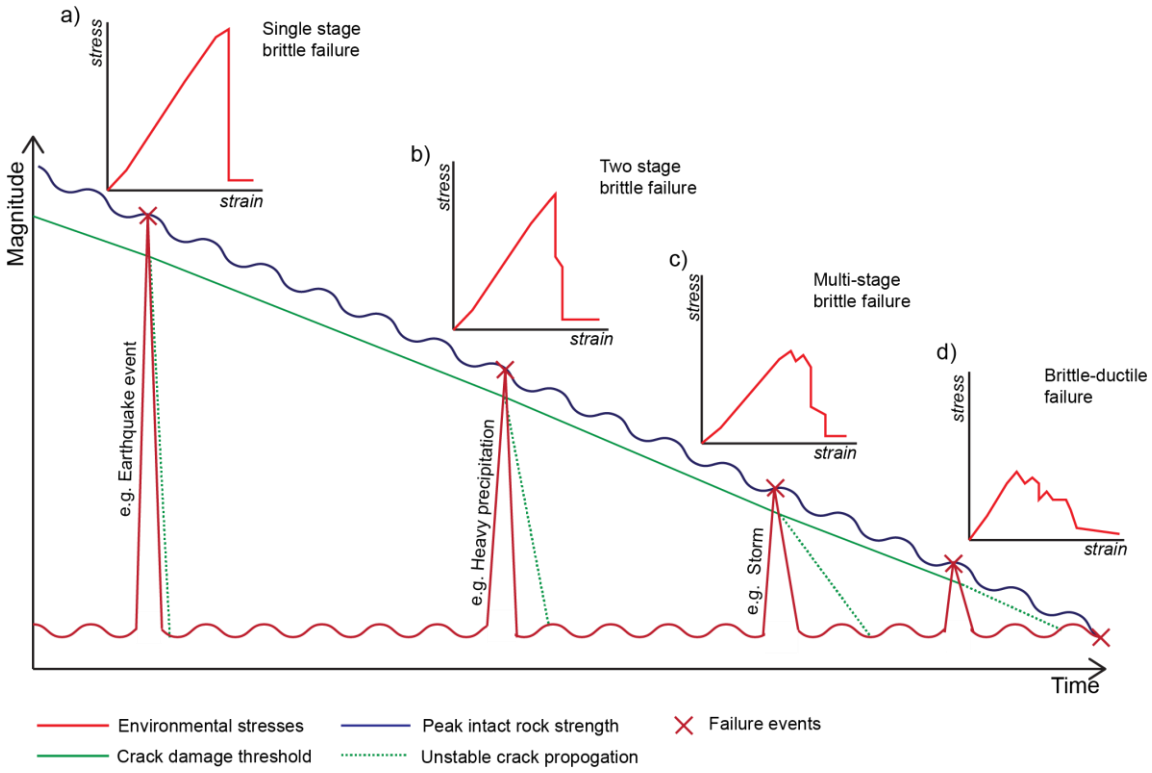

Figure 5.15: Conceptual diagram of the impact of incremental strength decrease over time in response to environmental conditions (modified from: Gunzburger et al., 2005). Over time, as rock strength decreases the failure style will transition from a purely brittle failure (a) to a brittle-ductile failure (d). Each stress-strain curve represents the type of failure style expected given the strength of the rock, with the dynamic loading events, such as earthquakes and storms representing the required stresses necessary for failure to occur.

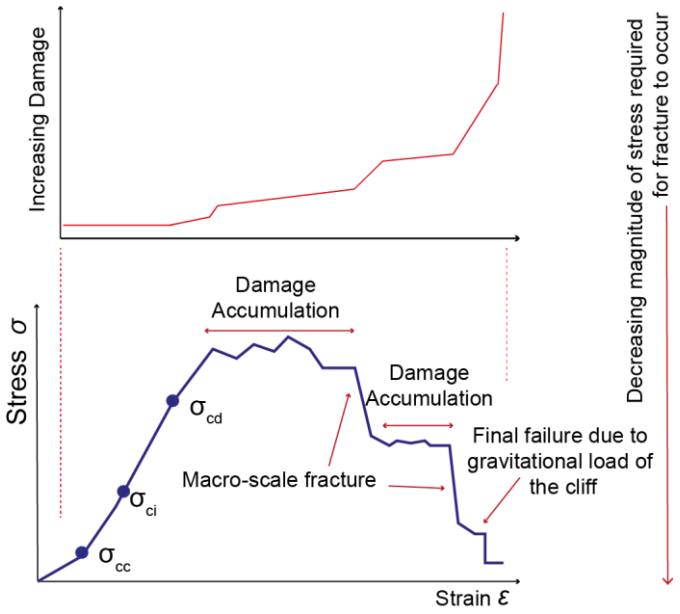

Figure 5.16: Conceptual stress-strain diagram of the stages and drivers of weathered brittle rock failure, displaying initial micro-crack initiation and propagation thresholds for intact rock (adapted from: Eberhardt et al., 1998). However, after the crack damage threshold (σ cd) is passed, the result in only partial runaway crack propagation within certain zones of the rock. For macro-scale fracture resulting in eventual final failure to occur, sustained stress and strain are required.

As final failure occurs, a distinct period of time after the initial damaging loading event (such as an earthquake or storm), this may explain the low observed correlations between environmental variables and failure (Lim et al., 2010; Rosser et al., 2007; Stock et al., 2012). This multi-stage failure history may be reflected in the resulting failure scar surface, with greater roughness coupled with surficial weathering provide an indication of failure history. Weathered broken rock bridges represent an initial failure event of the stress–strain graph, which has been followed by a long enough period of time for substantial surficial weathering (i.e. damage accumulation) to occur before final loss of strength (de Vilder et al., 2017). Additionally, pre-failure deformation may record several stages of macro-scale brittle failure, characterised by step-wise displacement through time. Observations of pre-failure deformation which do not result in hyperbolic acceleration towards failure may represent the lag between initial and final failure. The change in failure style may dictate the degree of discernible pre-failure deformation, with multi-failure events potentially displaying higher degrees of pre-failure deformation than

compared to single stage events as the period of time over which total loss of strength occurs is longer (Kromer et al., 2017; Petley et al., 2005).

5.6 Conclusion

We conducted a series of experiments on coarse- and fine-grained sedimentary rocks under constant uniaxial compressive stress to constrain the relationship between exposure to various environmental conditions, compressive stress and ultimate failure behaviour. Samples were modified to account for pre-existing micro-crack damage within the rock, as well as increased surface area and localised stress concentrations created by slope geometry. Our experimental dataset reveals:

- Weathering results in a significant reduction in intact rock strength.
- Compressive stresses of 2 MPa and 3.6 MPa neither enhance nor dampen the degree of weathering-induced strength loss. Alongside this, pre-existing damage and increased surface roughness also have no discernible influence on the magnitude of strength reduction resulting from weathering
- A disconnect between surface hardness and UCS measurements exists, limiting the applicability of using surficial measurements to understand the influence of weathering on brittle rock failure.
- Weathering not only results in a loss of strength, but in significant changes to failure style with weaker samples requiring several stages of macro-scale fracture before a total loss of strength is achieved.
- The magnitude of triggering events that result in brittle fracture, and hence frequency of such events, change as weathering induced strength degradation occurs. Weaker weathered samples may require several triggering events for ultimate rock failure to occur. The associated sequences of brittle fracture will be manifested in pre-failure deformation data.

This chapter addresses research objective 3. Samples were subjected to simulated topographic stress loading conditions and natural environmental processes. The constant vertical compressive stress had no significant influence on weathering intensity and as such does not control the rate of damage accumulation within intact rock. However, natural environmental conditions did result in significant strength reductions. Along with this decrease in strength associated changes in failure style occurred. This suggests that as a rock bridge weakens over time in response to natural environmental conditions, the mechanisms of failure changes. Weaker rock is likely to display a more complex sequence of fracture stages before ultimate failure occurs.

6 Discussion: Controls on intact rock fracture for rockfall release

6.1 Introduction

This thesis has investigated the controls on weathering-induced strength degradation required for fracture through rock bridges to allow rockfall release, with the aim of creating a mechanically correct model of rockfall detachment. These controls may dictate the spatial occurrence of intact rock fracture and timing, which interact to influence the nature and style of failure.

To assess this, each chapter within the PhD has primarily focussed on different spatial scales over which controls on weathering induced strength degradation act, with the mechanical implications for rockfall failure outlined within the discussion of each chapter. These mechanical implications are drawn together in this chapter to develop a new conceptual model of rockfall detachment. The spatial scales consider the near-surface of a rock slope (< 1 m), ranging from whole slope (10 m^2 – 100 m^2) to rock bridge (0.1 m^2 – 1 m^2) to micro-crack scales (1 x 10^{-4} m^2 - 10^{-3} m^2).

Chapter 3 characterised rockfall scar surfaces to provide information on the relative contributions of rock bridges, discontinuity release surfaces and weathering for rockfall release. Spatial and mechanical constraints at the scale of individual failures were established, via analysis of rock bridge attributes. The distribution and location of rock bridges within the wider slope inform the numerical modelling boundaries of Chapter 4.

Chapter 4 modelled the spatial distribution and concentration of stress and strain within the slope near surface, as a function of rock mass structure and slope topography. These results were contrasted with rockfall datasets to understand if areas of high stress dictate the spatial location of failure. Slope angle and the presence of overhangs dictate the modelled stress distribution and strain behaviour of the near-surface of a slope. However, the coincidence between slope angle, overhangs and rockfalls within real-

world datasets was limited, with only small overhang features correlated with increased rockfall activity.

Chapter 5 assessed controls on damage accumulation within rock over time, which had been subjected to representative ambient stress conditions and weathering conditions of a coastal rock cliff. This data allowed investigations of how these controls, such as pre-existing damage and modified geometries, influence damage accumulation within a rock and the associated changes to rock properties. Testing samples under representative ambient stress conditions allow the findings of the experiments to be upscaled to understand individual failure and whole slope. Weathering significantly alters rock strength, with weaker rocks characterised by post-peak strength with multiple stages of brittle failure before residual strength is achieved

Findings and observations from these three chapters form the basis for the conceptual mechanical model of rockfall detachment outlined in this chapter. The aim is to firstly explore the spatial controls on weathering induced strength degradation. Secondly, within the spatial assessment of weathering controls, the implications of these controls on rate and magnitude of weathering are examined. Finally, the spatial controls on rockfall detachment are analysed in conjunction with weathering induced changes to rock properties to understand the sequence(s) of failure required for ultimate rockfall failure.

6.2 Spatial controls on failure

The conceptual FEM models explored in Chapter 4 outline the importance of slope angle and micro-topography, as represented by overhangs, on near-surface stress and strain distribution, with the inclusion of discontinuities increasing the heterogeneity of modelled rock response. Yet, the results of the weathering experiments in Chapter 5 reveal that samples subjected to a constant vertical compressive stress, representative of overburden loading, are not significantly stronger or weaker than non-stressed control samples. This indicates that areas of concentrated stress and strain within the FEM

models of Chapter 4 do not necessarily represent areas of enhanced or dampened weathering.

Samples within the experiments of Chapter 5 were also modified to investigate if greater surface complexity, as created by topographic features such as overhangs or daylighting discontinuities, and the associated creation of both potential stress concentrations and greater surface exposure to weathering, resulted in significant differences in strength. These modified geometry samples were not significantly stronger or weaker than samples that had undergone no modification. Within the experimental set-up and conditions of Chapter 5, a constant applied vertical stress and sample modification had a negligible influence on strength degradation. Therefore, the distribution of stress and strain is purely a spatial control on failure rather than dictating the rate and magnitude of weathering induced strength degradation.

The linear increase in micro-crack density is assumed based on the lack of statistically significant differences in strength between the pre-damaged and unmodified samples in Chapter 5. The pre-damaged samples did not display elevated strength reduction relative to unmodified samples, suggesting that the existing micro-crack population within the samples did not change the rate of weathering. Based on these experimental observations, the rate of strength degradation, a proxy for weathering efficacy, does not therefore change through time in a manner that is observed in our tests. However, other studies (Viles et al., 2018; Warke, 2007) have observed increased rock disintegration in response to weathering tests for samples which have been ‘pre-stressed’ (damaged). Additionally, weathering experiments have also shown a decrease in weathering rate through time (e.g. Colman, 1981, Mushkin et al., 2014). The length of both the field and weathering experiments may have been of an insufficient duration to capture non-linear rates of strength change through time, and the experiments were designed to test absolute changes in strength rather than rates of change. As highlighted in Chapter 5, as a rock transitions from being dominated by cohesional strength to frictional strength, the influence of ambient gravitationally induced stress may become more important in

influencing the rates of weathering efficacy and associated strength degradation. Weathering experiments that document and record the transition of a material from cohesional to frictional dominated strength properties may be able to determine if a rate change in behaviour exists.

The influence of weathering on rock slope stability is also often viewed on longer time-scales than most weathering experiments are conducted over, including the experiments of Chapter 5 (Moses et al., 2014). Weathering is often viewed as controlling failure style (e.g. Durgin,1977), whereby the weathering grade as determined via ISRM (2015) classification indicates whether rocks are dominated by cohesional or frictional properties, as well as if they will fail in a brittle or ductile manner. Observations of the samples of Chapter 5 and of the rock mass at Boulby would results in classification of the rock as 'slightly weathered', even at the end of the weathering experiments. Even though significant reductions in strength have occurred, the broad scale weathering classification system does not accurately capture the resultant change in failure style over the timescale considered in this thesis and in response to the weathering mechanisms considered.

Regarding spatial controls on failure, the coincidence between slope topography, and hence stress distribution, with observed rockfalls in Chapter 4 was observed to be low. Other factors such as lithology (e.g. Lim et al., 2010), discontinuities (e.g. Moore et al., 2009) and progressive failure (e.g. Rosser et al., 2007) outlined in Chapter 4 may influence the spatial location of failure. Small scale overhang features (0.125 m^2) were correlated with increased rockfall activity in Chapter 4, with these overhang zones representing the migrating 'notch' of an upwardly-propagating sequence of rockfalls driven by progressive failure and stress re-distribution (Rosser et al., 2013)

Chapter 3 demonstrated that changes in rock bridge proportion were significantly correlated with subtle changes in lithology between the lower shale, upper shale and interbedded siltstone and sandstone units of the Boulby cliffs. Therefore, changes in rock mass structure (i.e. rock bridge proportion and discontinuity persistence) are correlated

with not only the wider geological setting but also local scale changes in lithology. This may be a function of mechanical stratigraphy within sedimentary systems, whereby joint spacing is a function of the thickness of lithological beds (e.g. Huang and Angelier, 1989; Ladeira and Price, 1981; Narr and Suppe, 1991). The joints are approximately vertical surfaces that are perpendicular to bedding, and as such do not include discontinuities such as bedding planes (Figure 6.1).

6.3 Controls on fracture propagation

The principles that control the propagation of joint surfaces can inform and may be comparable to the controls on, and the processes of fracture propagation, required for rockfall detachment. Joint propagation is controlled by changes in stiffness between lithologies, with fractures which initiate in areas of lower stiffness (i.e. lower Young's Modulus of Elasticity) and propagate towards areas of higher stiffness (i.e. higher Young's Modulus) resulting in fracture deflection or arrest (Figure 6.1) (Cooke and Underwood, 2001; Gudmundsson et al., 2010; Pollard and Aydin, 1988). Conversely, fractures which initiate in areas of higher stiffness can propagate through areas of lower stiffness with no such arrest of deflection (Figure 6.1) (Cooke and Underwood, 2001; Gudmundsson et al., 2010). The stiffness properties of the discontinuity itself, separating the materials, also influences the ability of a fracture to propagate (Cooke and Underwood, 2001). Therefore, the Young's Modulus of a rock is an important control on propagation of fracture surfaces, which is also a key input for theoretical equations of micro-crack growth (Anderson, 2005; Griffith, 1924, 1921; Irwin, 1957). These changes in material properties may explain the patterns of progressive failure that terminate at overhangs, which represent changes in lithologies (Rosser et al., 2013). Areas of limited change in the monthly and annual rockfall datasets of Chapter 4 are associated with 'blocky' sandstone layers (Figure 4.29), which may be areas of higher stiffness and therefore act as barriers for propagating fractures associated with rockfall release. As such, these stiffness contrasts may determine distances over which fractures can propagate both within a lithological layer and across multiple lithological layers.

Understanding the controls on fracture propagation is important for determining rockfall size, where the resultant failure may be a consequence of the eventual size and extent of the propagating failure surfaces, and their interactions with bedding planes and other such discontinuities. Analysis of rock bridge orientations with respect to the main scar surface in Chapter 3 indicated that rock bridges, and associated discontinuity surface, located perpendicular to the main scar surface were only present in smaller rockfalls (Figure 3.14). Larger rockfalls did not contain such orthogonal rock bridges, indicating that the fracture surface, which resulted in release of the rockfall block, was able to propagate across such cross-cutting discontinuity surfaces, rather than be deflected along or arrested at them. Smaller rockfalls may be the result of fracture propagation that deflects or arrests at rock bridges (Figure 6.2). Rockfall size, therefore, may reflect the ability of a fracture surface to propagate within a rock mass.

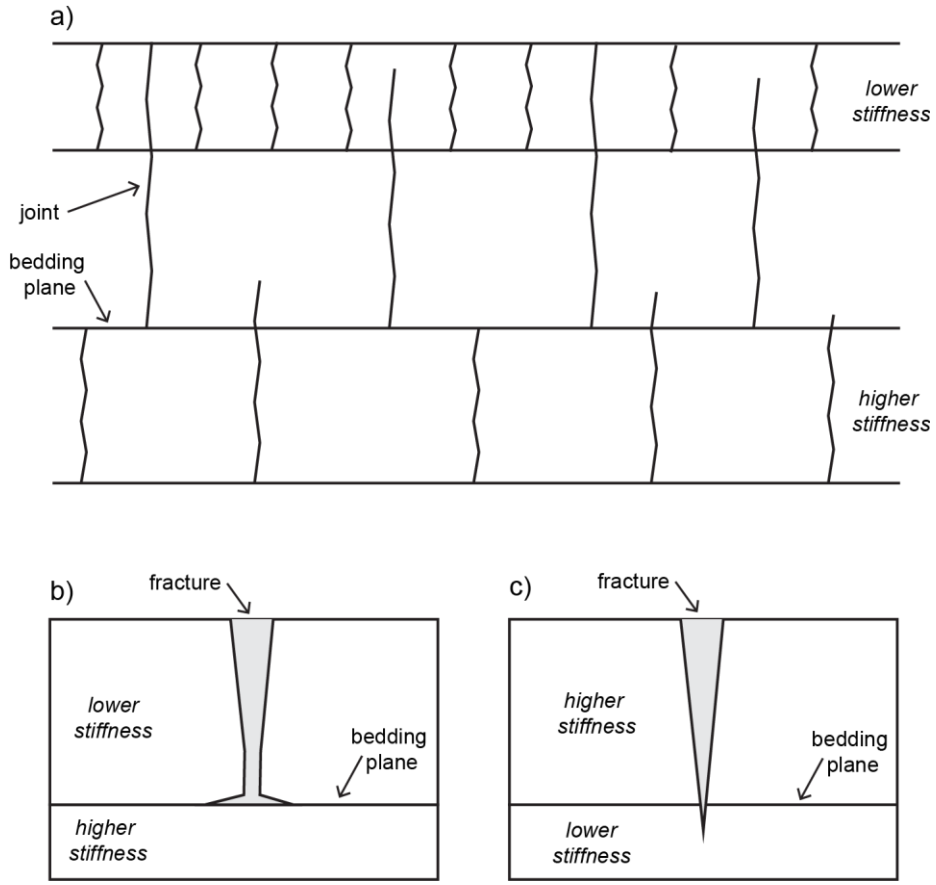

Figure 6.1: Schematic of fracture propagation or termination at bedding planes.
Bed thickness determines joint spacing, and the stiffness contrasts between layers determine if a fracture can propagate across a lithological layer. b) Termination of a fracture surface as fracture propagates from low to high stiffness material b) Fracture propagates across bedding plane into lower stiffness material (Modified from Cooke and Underwood, 2001)

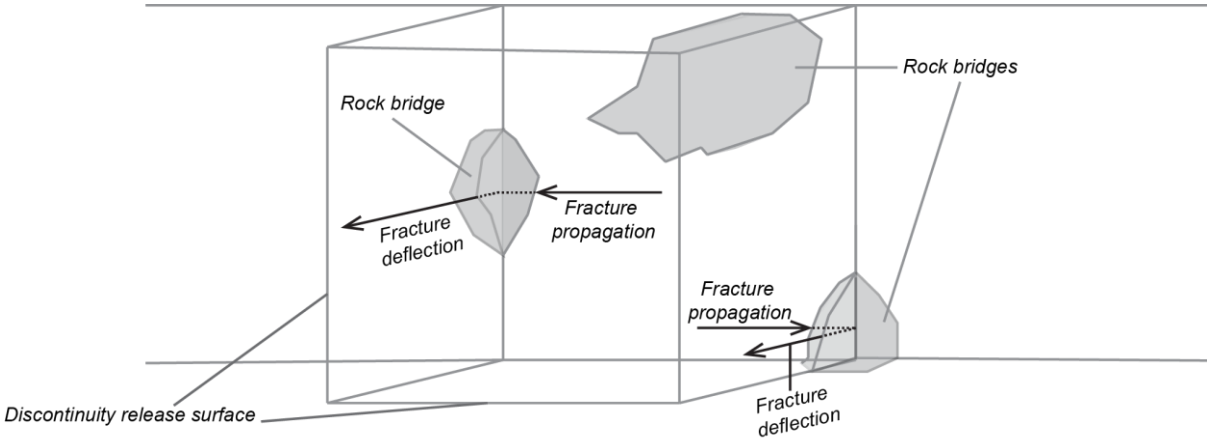

Figure 6.2: Conceptual model of rockfall failure, whereby propagating fractures deflect at rock bridges along cross-cutting discontinuities allowing block release to occur. This also results in the partial fracture of those rock bridges.

6.4 Implications of changes in rock properties

Chapter 5 outlined that as weathering occurred, rock properties changed. This included a reduction in stiffness of siltstone samples, as indicated by reductions in Young's Modulus relative to baseline (Table 5.6). Fractures that initiate and propagate within siltstone are likely unable to propagate through stiffer material. The sandstone, however, does not show an equivalent reduction in stiffness, though significant reductions in strength are observed (Table 5.6). Fractures which initiate and propagate here will propagate through and across materials of lower stiffness (Cooke and Underwood, 2001; Gudmundsson et al., 2010; Pollard and Aydin, 1988).

This suggests that even though strength is reducing for each rock type, UCS or other strength parameters cannot be used as the sole indicator of the style of rock failure, which requires stages of brittle fracturing. This also highlights the importance of lithology in controlling response of intact rock to weathering (Hall et al., 2012). The differences in Young's Modulus (i.e. stiffness) between the two rock types may be related to the nature of the matrix between grains, with the grains within siltstone potentially more able to slide and rotate in response to micro-cracking, accommodating increased strain (Fabre and Pellet, 2006). Changes to stiffness due to weathering within a lithological layer may also provide barriers to fracture propagation.

In the near-surface of steep slopes, confining stress is limited or non-existent, as reflected in the near-zero values of σ^3 (Figure 4.8). Therefore, the cohesional properties, rather than friction angle, are important for stability. Due to the brittle nature of rock mass in hard rock steep slopes, micro-cracking is an important but not sole form of cohesional strength loss (Martin, 1997). Reductions in cohesion in response to weathering may result in changes to failure mechanisms from compressional shear to extensional shear, independent of any changes in σ^1 and σ^3 (Figure 6.3a). Changes in friction angle result in failure occurring under lower normal and shear stress conditions, without any changes in σ^1 and σ^3 values (Figure 6.3b).

The modelled σ^1 and σ^3 values shown in Chapter 5 indicate that topography and rock mass structure interact to determine failure mechanisms, moving from either purely extensional, extensional-shear to compressional shear (Twiss and Moore, 1992). The ratio between σ^1 and σ^3 values determines whether fractures grow in extension or shear, with increases in confining pressure (σ^3 values) required for shear failure to occur (Diederichs, 2003; Leith et al., 2014a). Therefore, on a whole slope scale, topography and rock mass structure may dictate the nature of failure, and where weathering can result in changes to such failure behaviour.

The influence of topography and rock mass structure will dependent on the mechanical properties that control slope failures. For example, loss of cohesion for shallow failures in near-surface steep slopes may be important, while changes to friction angle become more important with greater confining pressure, which may be associated with deeper whole slope failures. This increase in confining pressure will result in macroscopic shear failure (Diederichs, 2003). The reduction in friction angle may also have a greater influence for shallow soil failures than brittle shallow rock failure, where the geometries of the soil failures are controlled by friction angle for sediments with and without cohesion (Milledge et al., 2014). Changes in material properties have also been shown to influence the development and form of larger-scale landforms (Koons et al., 2012).

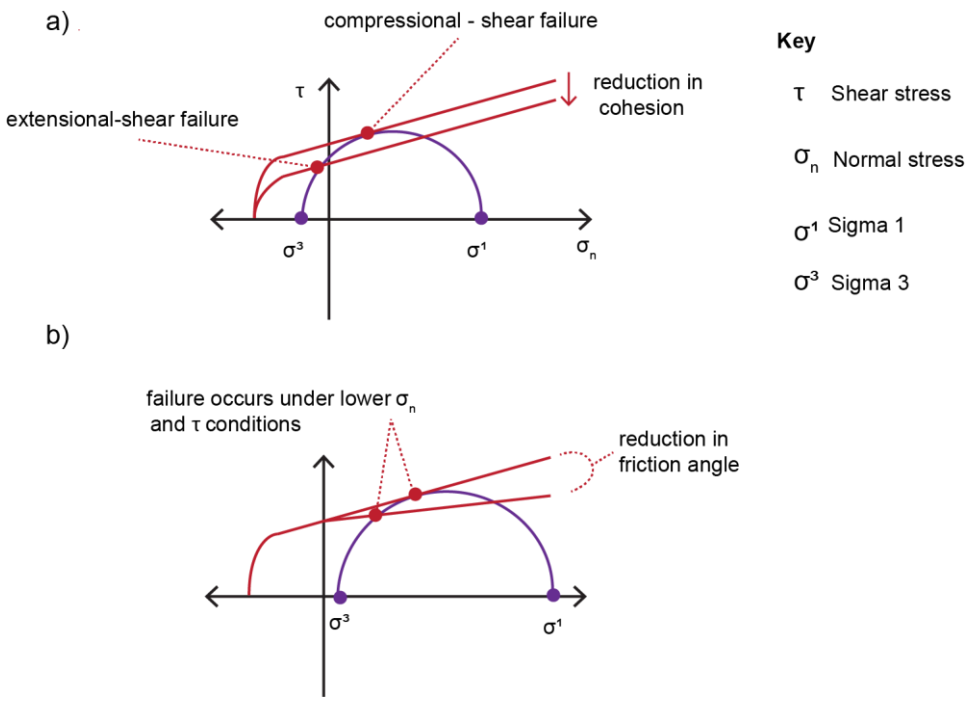

Figure 6.3: Schematic of the influence of weathering on Mohr-Coulomb failure criterion. a) Depending on the values of σ^1 and σ^3, reduction in cohesion may result in a change of failure mechanism. b) Changes in internal angle of friction angle results in failure occurring under lower normal and shear stress conditions, without any changes in σ^1 and σ^3 occurring.

6.5 Implications for individual rockfall failure

Rock bridge properties determine where weathering induced strength degradation is important for rockfall release, and where stress and strain are concentrated (Kemeny, 2005; Scavia, 1995). As outlined in Chapter 3, the proportion, location and distribution of rock bridges within a rockfall scar dictate the mechanics of failure. Rock bridge proportion determines the amount of intact rock required to break for rock block release to occur (Figure 3.10). The location of a rock bridge with respect to the main scar surface and rockfall centre of mass determine the stresses experienced by the rock bridge, and whether the rockfall is likely to fail in shear, tension or torsion (Figure 3.14 and Figure 3.15). As rockfall size increases, the number of rock bridges recorded within an individual rockfall scar increases (Figure 3.12). Therefore, for larger rockfalls to fail, fracture through multiple rock bridges is required, while for smaller rockfalls the stability is controlled by one critical rock bridge.

The detailed geotechnical characterisation within Chapter 5 shows that as these intact zones of rock weaken in response to weathering, the nature and style of failure will change, becoming more complex with multiple stages of brittle fracture (Figure 5.14). For rockfall failure, this multi-stage failure process may be represented as 'step-wise' fracture through multiple rock bridges within larger rockfalls, or partial fracturing through an individual rock bridge. Analysis of weathered rock bridge surfaces in Chapter 3 indicates that rock bridges can partially fracture, with sufficient time prior to final failure for surficial weathering and discolouration to occur (Figure 3.1 and Figure 3.10).

As two or more stages of brittle fracture are required for ultimate failure, this pattern of fracturing may result in a quasi-stable state (Leroueil, 2001). Final failure may occur once weathering processes have resulted in a critical concentration of micro-cracks, resulting in an acceleration towards failure (Main, 2000). This acceleration is associated with continued propagation of an incipient failure surface (Petley et al., 2002, 2005). The conceptual model outlined in Figure 5.16 illustrates this process, with each stage of brittle failure weakening the rock, so that the next stage of brittle fracturing requires a lower magnitude of stress to act as a trigger for failure.

As the magnitude of triggering events required for failure decreases, the frequency of such events will increase. This negative feedback results in acceleration towards failure. As the density of micro-cracks increases within a rock in response to weathering and external environmental triggers, a critical density threshold may be reached, where internal mechanisms rather than external triggers will drive the further growth and coalescence of micro-cracks resulting in the formation of a macro-scale fracture (Bieniawski, 1967; Eberhardt et al., 1998). On the scale of a whole slope, damage accumulation results in the failure of smaller rockfalls accompanied by increasing strain accumulation within a slope (Rosser et al., 2007). This process of smaller rockfalls continues until a certain threshold is passed resulting in a much larger final failure (Rosser et al., 2007).

For larger rockfalls (> 1 m²) that contain increased number of rock bridges (Figure 3.12), differential weathering between the rock bridges may result in initial fracture through the weakest rock bridge. The subsequent order of rock bridge fracture may be determined by the relative rate of weakening in each rock bridge. This does not preclude partial fracturing of individual rock bridges within larger failures from occurring. Therefore, the pattern of final failure may be more complex for larger rockfalls due to both the number of rock bridges, but also the influence of weathering on those rock bridges. The complexity of mechanical sequences of failure may be reflected in pre-failure deformation, which involve step-like changes in recorded displacement, indicative of discrete rock bridge fracture events (e.g. Carlà et al., 2017; Kromer et al., 2015; Kromer et al., 2017). Larger rockfalls are likely to display more variable and complex pre-failure deformation that requires careful interpretation to determine stability and time to final failure.

6.6 Conceptual model of rockfall detachment

The findings of this thesis reveal that as a rock slope weakens through time, the mechanics of rockfall detachment is likely to change. This section outlines and explores the end member scenarios of a conceptual model of the mechanics of rockfall detachment in relation to weathering induced strength degradation, and associated implications for observable pre-failure deformation and magnitude frequency characteristics of rockfall (Figure 6.4). For simplicity, this conceptual model assumes a single lithology and initial homogenous intact rock properties and rock bridge distribution across the slope. Within the model, micro-crack density increases linearly through time. Along with the linear increase in micro-cracks, the distribution of micro-cracks becomes more diffuse in a rock mass (Cerfontaine and Collin, 2017).

6.6.1 Unweathered rock slopes

In this scenario, the slope is freshly exposed comprising un-weathered (strong) rock, which is characterised by single stage brittle fracturing. Weathering induced micro-cracking is non-existent or negligible. Due to the strength of the rock, triggering mechanisms for failure likely require high-magnitude loading such as earthquakes or intense precipitation events (e.g. Iverson, 2000; Keefer, 1994; Keefer et al., 1987)

As rock properties are homogenous within this conceptual model there are no contrasts in stiffness across the slope. Due to the relatively high magnitude of stresses imposed on the slope by the triggering events, a subsequent higher magnitude of damage within the slope results in macro-scale fracture propagation (Scholz, 1968). Hypothetically, the homogenous material properties (i.e. no stiffness contrasts) results in fracture propagation across multiple rock bridges for a single trigger event, creating larger rockfalls. Small rockfalls may still occur, but their occurrence is dictated by the potential presence of cross-cutting discontinuities, which act as release surfaces both within the conceptual model, and within rock slopes in reality. The speed of the propagating fracture plane means that pre-failure deformation associated with rock bridge fracture, and subsequent strain accumulation may appear to be near-instantaneous.

In terms of characteristics of rockfall recorded across a rock slope, this pattern is likely dominated by episodic larger rockfalls or whole slope collapses. Smaller rockfalls are less frequent, as fracture arrest and deflection are unlikely to occur. Therefore, these stronger slopes may appear inactive due to the limited rockfall activity that may occur between high-magnitude events, yet failures are likely to be large and sudden, with little pre-failure deformation, and hence warning. Within this scenario, erosion and evolution of a rock slope is dominated by infrequent large rockfall events. Environmental and external triggers are directly correlated with failure, suggesting that if the frequency of these external triggers changes, so will the frequency of rockfall. However, increases in the frequency of these high-magnitude events will also increase damage within the slope, altering the subsequent failure behaviour. The theoretical magnitude-frequency

distribution of this conceptual model displays an inverse relationship often observed for real-world slopes (Dussauge et al., 2003; Guzzetti et al., 2002; Malamud et al., 2004). It is unlikely that the unweathered, freshly exposed rock slope within the model reflects any real-world slope as material can be weathered rapidly, with the sandstone samples in Chapter 5 displaying a significant reduction in strength after only a year of exposure to environmental processes.

6.6.2 Weathered rock slopes

In this scenario, weathering has resulted in increasingly heterogeneous material properties, which display multi-stage brittle failures. This is reflected in an increased density of micro-cracks within the rock mass

Due to the increased density of micro-cracks the threshold for initial failure is lower than un-weathered rock and may consist of external low-magnitude storm or rainfall events. As the damage within the rock mass accumulates, small perturbations in stress associated with external and internal triggers may result in further and ultimately final fracture and failure. The heterogeneity in material properties will likely create contrasts in stiffness properties within the slope, influencing propagation pathways. This may be linked to the diffuse distribution of micro-cracks, resulting in the formation of smaller macro-scale fractures, which represent 'mini-coalescence' events of micro-cracks (Cerfontaine and Collin, 2017). This is reflected in the multi-stage brittle failure behaviour of the weathering samples (Figure 5.14).

For both small and large rockfalls, as determined by the number of rock bridges within a scar, several stages of fracture propagation are required. Outlined below are four fracture patterns for different rockfall sizes and their associated rock bridge configuration, as determined from Figure 3.12:

- Small rockfalls (< 1 m² surface area) contain one rock bridge, which may display multiple stages of partial fracturing until final failure is achieved.

- Medium rockfalls (< 3.5 m² surface area) contain <5 rock bridges, where one main rock bridge dominates. The temporality of failure in this case will depend on the order of rock bridge fracture. It was hypothesised in Chapter 3 that the smaller 'peripheral' rock bridges may represent the partial fracture of larger rock bridges where propagating fractures have arrested or deflected along cross-cutting discontinuity surfaces achieving block release (Figure 6.2). If this partial fracturing occurred first, then the rock mass may be stable until further weakening allows fracturing of the main rock bridge to occur.
- However, if this main rock bridge is the first to fracture, the associated redistribution of stress may result in 'run-away' acceleration towards failure. The same mechanism of partial fracturing through peripheral rock bridges may still occur as for example B.
- Large rockfalls (3.5 m² > surface area) contain multiple rock bridges of similar size. Their fracture pattern is likely to be complex. They may occur where fracture propagation does not deflect to the surface along planes of weakness, potentially due to the absence of cross-cutting discontinuities, or the magnitude of a triggering event, creates stresses which are great enough for fracture propagation to initiate in stiffer intact rock and propagate for longer distances across multiple rock bridges. Partial fracturing of rock bridges may have occurred prior to this and/or complete fracture of some rock bridges within the incipient large rockfall could have occurred where the configuration of cross-cutting discontinuities did not provide release surfaces.

This variation in rockfall release scenarios may be reflected in the surface expression of deformation as seen in the monitoring observations of Carla et al., (2017) and Royan et al., (2014). Larger rockfalls are likely to display more variable deformation than smaller rockfalls, due to the increasing number of rock bridges within a rockfall scar.

Monitoring observations have revealed that external precipitation triggering events can initiate extended periods of increased and accelerated deformation indicating a critical

damage threshold has been reached in the rock, with previous observations showing that in some settings that this can accelerate to final failure within a week (Carlà et al., 2018; Kromer et al., 2017). The time-scales over which such deformation could be observed may vary depending on exact rock bridge attributes, with the amount of deformation and time over which such deformation occurred increasing for larger rockfalls (> 5 m^3 : Kromer et al., 2017), reflecting the breakage of multiple rock bridges.

Some monitoring studies have struggled to identify pre-failure deformation for smaller rockfalls (< 1 m^3 : Abellán et al., 2010; < 0.5 m^3 : Kromer et al., 2017), where fracturing may occur over timescales shorter than the monitoring interval or critical levels of damage have already accumulated within the singular rock bridge resulting in near instant failure (Abellán et al., 2010). Observed smaller periphery rockfalls around a larger failure mass may represent areas of rock release associated with partial fracturing of rock bridges within a larger incipient failure (Kromer et al., 2015; Rosser et al., 2007; Royan et al., 2015).

The FEM of Chapter 4 indicates that stress and strain values are dictated by slope angle, slope micro-topography (i.e. overhangs) and the presence of discontinuities. These interactions can create areas of greater volumetric strain and associated dilation, particularly at overhangs, with greater shear strain observed at concavities. Increased dilation may increase the potential for pre-failure deformation to be detected. Therefore, pre-failure deformation is not only dependent on rock bridge characteristics but also slope surface topography. The kinematic style of failure, such as toppling, sliding or wedge failure, is also shown to influence the degree of detectable displacement (Kromer et al., 2017; Rowe et al., 2017). Areas of toppling can be related to extensional and tensile failure mechanisms where greater dilation is possible (Wyllie and Mah, 2004). Conversely, areas such as concavities, may fail via sliding mechanisms where the heightened shear stress and strain allows the propagation of a shear failure surface. Sliding failures display less pre-failure deformation compared to toppling (Rowe et al., 2017).

The magnitude-frequency characteristics of rockfalls from the slope considered within this scenario are likely to be dominated by smaller rockfalls, due to shorter fracture propagation distances and peripheral rock bridge failure, which occur more frequently. Larger rockfalls may occur, where the absence of cross-cutting discontinuities prevents rockfall release. The magnitude-frequency distribution of rockfalls from the slope in this scenario reflect real-world data-sets, which are dominated by smaller, more frequent rockfalls (e.g. Barlow et al., 2012; Dussauge et al., 2003; Malamud et al., 2004). These rockfalls are less likely to be correlated to environmental conditions and occur in the apparent absence of triggers, with 'lags' between potential triggering events and ultimate failure (e.g. Leroueil, 2001; Matsuoka and Sakai, 1999; Rosser et al., 2007). This 'lag' effect may also be evident in a rock slope response to changing environmental conditions, where such environmental conditions act as the trigger for initial fracture events that eventually lead to final failure. Weathered rock slopes, therefore, adjust more slowly to new environmental conditions.

6.6.3 Transition between end-member scenarios

With increasing micro-crack density, more stages of brittle failure will occur and the magnitude of forcing required to trigger fracture will decrease. This may be accompanied by an increase in the frequency of smaller rockfalls. Potentially for two- to three-stage brittle failure stages, after an initial fracture event the incipient rockfall may remain stable for some time until another event of sufficient magnitude allows final failure to occur. In this case, pre-failure deformation will be characterised by short-events of macro-fracture, punctuated by longer periods of stability before sudden failure. Monitoring undertaken by Carla et al., (2017) revealed that out of nine deforming areas only five failed, while the other four areas showed considerable deformation but had not failed by the end of the study. These 'stable' areas where also larger than the failed sections, suggesting a link to the increasing amount of time required for such larger failures to occur. If another triggering event of a similar magnitude to the first fracture event were to occur, it is

unlikely that this would show acceleration towards failure comprising of multiple fracture events.

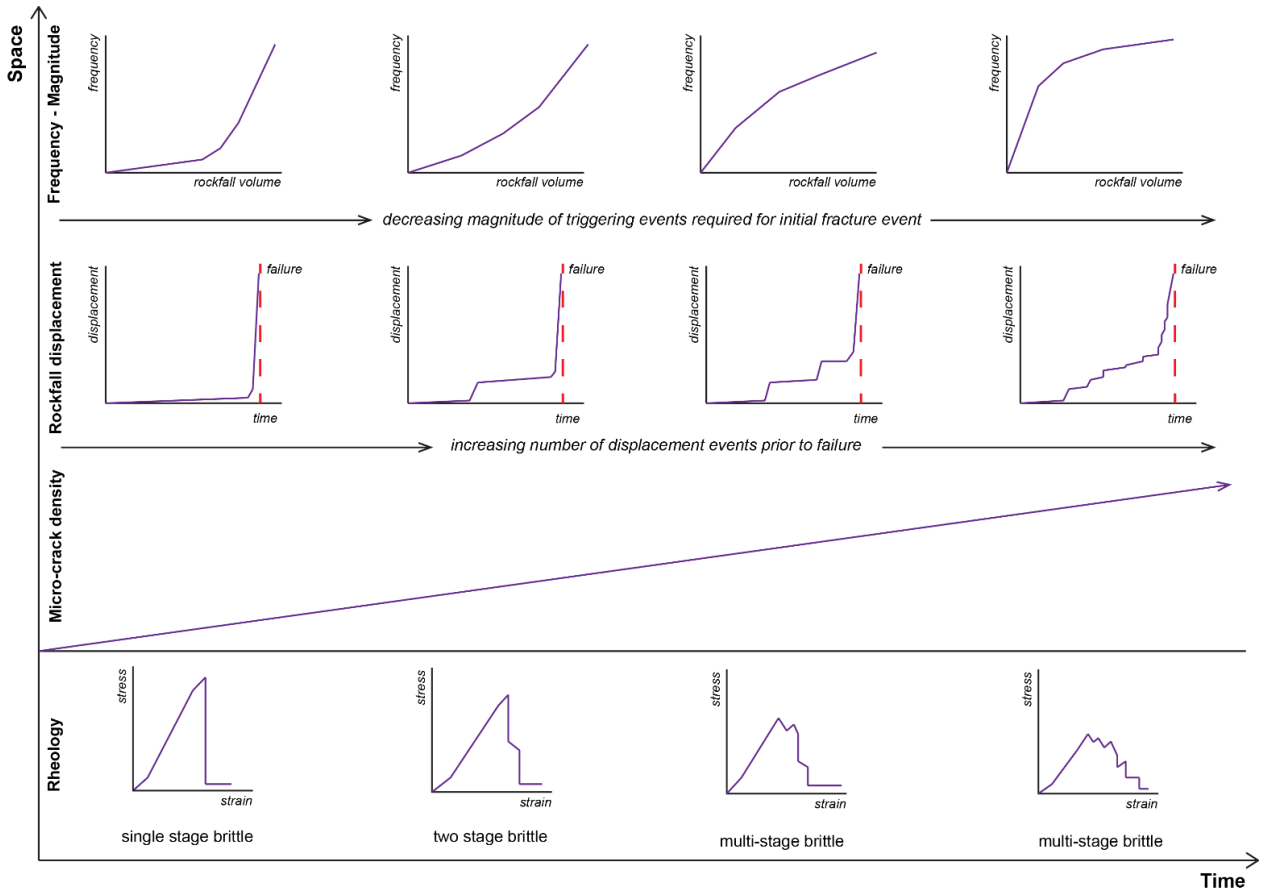

Figure 6.4: Conceptual model of the impact of rock weakening over time on rockfall mechanisms. Model consists of a single lithology slope with initial homogenous rock mass properties. As micro-crack density increases in response to weathering, changes in rock rheological behaviour occur. This increase in the number of stages of brittle fracture required for total failure, results in increased stages of rock bridge breakage required before rockfall failure, which are represented as displacement events in conceptual graphs of pre-failure deformation. The exact time and number of displacement events will be dependent on rockfall size. The magnitude of triggering events may be linked to fracture propagation lengths, so as the threshold for failure decreases, fractures will propagate a shorter distance resulting in smaller rock bridges.

6.6.4 Model implications

This conceptual model implies that the power-law relationships and associated exponents, which describe the magnitude –frequency characteristics of rockfall, and are likely to change over time (Dussauge-Peisser et al., 2002; Guzzetti et al., 2002; Malamud et al., 2004). The large standard deviations of calculated power-law exponents have been attributed to variable rock mass structure, lithology and physiographic setting (Barlow et al., 2012; Brunetti et al., 2009; Guzzetti et al., 2002). This variation could also record temporal components of changes to the rock mass properties, which are otherwise considered constant. The inclusion of more lithologies and their associated geo-mechanical properties within the conceptual model will also increase the complexity and variability of rockfall behaviour. Within this, areas of higher stress and strain, as dictated by slope topography and rock mass structure, may preferentially fail. As the magnitude-frequency distribution is not static through time, hazard and susceptibility assessments based on such distributions (Fell et al., 2008) also may need to evolve, potentially requiring ongoing characterisation and monitoring of rock slopes. Magnitude-frequency characteristics of a rock-slope are often a function of the monitoring interval over which rockfalls were observed (Williams et al., 2018). Stronger, less weathered rock slopes, where failure is more episodic, likely require larger monitoring intervals over time-spans equivalent to the return period of high magnitude event, in order to accurately capture the magnitude-frequency distribution of failures. Conversely, weathered rock slopes, which display smaller more frequent failures, likely require shorter monitoring intervals on the order of minutes to months, for accurate rockfall magnitude-frequency characterisation.

Additionally, as rock failure occurs, unweathered surfaces will be exposed, potentially ‘resetting’ the weathering induced damage within that area. Therefore, for an actively eroding rock slope, where this erosion occurs via discrete rockfall events, the spatial pattern and mechanical mode of failure may be a function of surface exposure time.

Adams et al., (2005) theorised that damage was greatest at the slope surface and decreased with increasing distance from slope surface into the rock mass. Surficial shallow rockfall activity may therefore remove the most damaged sections of the slope, exposing less damaged or pristine rock. Extrapolation of rockfall activity and erosion data suggests that the coastal cliffs at Boulby would completely re-surface within on average a 28 year period (Rosser et al., 2013). This feedback between rockfall activity, resultant surface exposure and weathering, regulates the frequency-magnitude characteristics of rockfalls, creating a similar distribution through time as the surface exposure ages will range from freshly exposed to 20+ years exposed. Understanding the time required for total surface 'resetting' may determine the time period over which monitoring can fully capture changes in the rockfall magnitude-frequency distribution of an individual slope. These surface ages will determine the degree of damage accumulation, and therefore the mode of mechanical detachment (Figure 6.4).

6.7 Summary

This chapter has assessed the spatial controls on weathering induced strength degradation, and more widely rockfall occurrence. This reveals that the stress distribution and strain behaviour does not determine areas of enhanced strength degradation and is not the dominant control on rockfall occurrence. The processes that control fracture propagation pathways through rock bridges may provide constraints on the spatial patterns of rockfalls, with the extent of the fully propagated fracture surface controlling the size of resultant rockfalls. Contrasts in rock properties influence the ability of a fracture surface to propagate, with the interplay between lithology and weathering resulting in greater heterogeneity of rock properties within a slope. This increased heterogeneity results in shorter fracture propagation distances, and therefore smaller rockfalls.

These changes in rock properties influence the mechanical mode of detachment of rockfall. As damage accumulates within a rock bridge, the stages of brittle fracture

required for complete failure of that rock bridge, or a sequence of rock bridges increases. Weathering induced strength degradation, results in a more prolonged failure sequence, with this increased variability and complexity of behaviour reflected in observations of pre-failure deformation. Subsequent interpretation of such data requires a careful and considered approach, due to the possibility of substantial 'lags' between an initial fracture event and ultimate failure.

Additionally, as a rockslope weathers and weakens over time, the rockfall magnitude frequency distribution will change as a function of the ability of fractures to propagate through rock. A freshly exposed slope that has undergone limited weathering, will likely display more episodic and larger rockfall, which can be directly correlated to external triggering events. In contrast, weathered rock slopes will be dominated by more frequent smaller rockfalls, which may occur in the absence of a discernible triggering event.

These changes in the frequency and size of rockfalls suggests that hazard and risk assessments, which incorporate magnitude-frequency distributions, should also change through time in response to the evolving strength of a rock slope. This also indicates that the mechanisms by which a rock slope, and more broadly landscapes, develop are also not static. The time-scales over which rock strength evolves needs further investigation but may be a function of the ability of rock-slope to 're-surface' by removing the near-surface damaged area of a rock slope via erosion. This 're-sets' the damage within a slope by exposing fresh rock. As such analysis of surface exposure age may be a proxy for weathering induced strength degradation and associated mechanisms of failure.

7 Conclusion

7.1 Evaluation of Aim

The overall aim of this thesis has been to explore the spatial and temporal controls on weathering induced strength degradation within a rock mass, and the associated implications for the mechanics of rockfall. This has been achieved through the four research objectives set and has resulted in the development of a new mechanical model of changes rock bridge breakage through time in response to weathering induced strength degradation. The stress distribution of a slope is not a dominant control on the temporality or spatial location of rockfall failure. Weathering results in significant intact rock strength degradation, with rock bridges within a slope determining where this strength degradation is important. Failure mechanisms are dependent on: the attributes of rock bridges, including their number and location within an individual failure; the location of an incipient failure mass with respect to surface micro-topography; and rock rheology, which changes with weathering.

7.2 Research Objectives

The conclusions of this study are presented in the context of the four research objectives, set out at the start of the thesis.

Characterise the failure surfaces of rockfall via morphological analysis to establish the relative contribution of intact rock fracture, discontinuity release surfaces and surficial weathering in rockfall failure.

A database of 657 rockfall scar surfaces was collated from rockfalls observed along a 200 m section of cliffs at Boulby, North Yorkshire UK. Detailed surface morphology of scar surfaces was captured using high resolution TLS and gigapixel photography. Rock bridge and weathering attributes of surfaces were forensically determined via automated classification of RGB pixel values.

Rock bridges account for 31% ±26% of an individual rockfall scar surface, with discontinuity release surfaces account for the remainder of scar surface area (Figure 3.10). Subtle differences in lithology and rock mass structure are significantly correlated with changes in rock bridge proportion. The number of rock bridges within a scar increases linearly with rockfall size, with larger rockfalls requiring fracture through multiple bridges before final failure can occur (Figure 3.12). Complexity of failure sequences therefore increases for larger rockfalls. The location of a rock bridge with respect to rockfall centre of mass and discontinuity release surfaces will determine the stresses experienced by the rock bridge, and influence failure mode (Figure 3.14 and Figure 3.15).

Surficial weathering extent varies widely for individual scars, with a mean weathering extent of 49.7% ±34.9% for scar surface area (Figure 3.10). Surficial weathering also occurs for already broken rock bridges surfaces (Figure 3.1), providing limits on the temporal sequence of rock bridge fracture within an individual failure. Weakening of rock bridges over time may be determined by the perimeter to area ratio of rock bridges, with larger ratio resulting in greater exposure to weathering processes and subsequent strength loss. The spatial and temporal sequence of failure which results in ultimate block release of a rockfall is a function of rock bridge attributes, including not only proportion but the number and location of rock bridges within an individual failure.

Model the interaction of micro-topography and rock mass structure in concentrating stress within the slope near surface (<1 m depth) and assess the coincidence, both in time and space, between rockfall and stress concentrations

Exploratory finite element modelling of 125 idealised 2D slope profiles assessed the influence of slope angle, overhang depth and discontinuity persistence on the near surface (< 1 m depth) stress distribution and strain behaviour of a rock slope. Slope geometries, rock and discontinuity properties were designed to be similar to the geometric and geotechnical properties of the cliffs at Boulby.

The baseline stress and strain distribution are determined by slope angle, with subtle changes in slope angle of 1° to 5° substantially altering these stress and strain values (Figure 4.8). The presence of overhangs and discontinuities result in deviations away from baseline (Figure 4.5 and Figure 4.14, respectively). Overhangs are characterised by lower stress and strain relative to baseline, with the concave areas between them display greater stress concentrations and higher strain values. This pattern is less clear for discontinuities, which are characterised by decreased stress and strain along their extent, with stress and strain concentrated at rock bridges. Increases in overhang depth amplify both the effect of overhangs and discontinuities. Changes in discontinuity persistence have limited impact on stress and strain distribution. Variations to these generalised and simplified observations exist and are often dependent on slope angle.

Coincidence between overhangs and slope angle with observed rockfalls at Boulby were limited. Only small overhang features are correlated with increased rockfall activity, which potentially reflects the upward propagation of rockfalls (Table 4.4). However, at larger scales rockfall fail equally in concave and overhang zones (Table 4.5), indicating that the distribution of stress and strain as dictated by topography and rock mass structure is not the main control on spatial patterns of failure. Progressive failure dynamics, weathering and lithology may also explain these patterns. Failure mechanisms, however maybe related to overhang locations, with failure at overhangs likely to occur via extensional-shear mechanisms, while for concavities failures occur by compressional-shear mechanisms.

Measure the degree of strength degradation for a rock subjected to simulated topographic stress loading conditions and natural environmental processes.

A series of weathering experiments were conducted, where sedimentary rock samples were placed under a constant vertical compressive stress, applied via novel experimental setups using front loading oedometers and lever systems. Samples were also modified to understand the influence of existing micro-crack damage and local slope geometry on

weathering intensity. 64 samples were subjected to either laboratory based intensive saltwater wetting and drying or field based natural environmental conditions. Detailed geotechnical characterisation of rock stress-strain behaviour was determined via UCS testing. This allowed analysis of rock strength and failure style changes due to weathering to be undertaken.

This analysis revealed that weathering results in a significant reduction in intact rock strength. However, no significant relationship exists between weathering and compressive stress representative of gravitationally induced ambient stress conditions. Compressive stress does not result in enhanced weathering or dampened weathering and is therefore not a control on the spatial intensity of weathering. Strain data indicates that stresses within the experiments are of a sufficient enough magnitude to counteract the compressive stress. Sample modifications also not a significant control on weathering induced strength degradation.

The loss of strength results in changes to failure style, whereby weaker samples display multiple stages of brittle failure before residual strength is reached. These changes in the mechanisms of failure will change the surficial expression of pre-failure deformation, with implications for the interpretation of monitoring data. Alongside this, the magnitude of triggering stresses required to promote ultimate and final rock failure will also change as the rock weakens.

Develop a new conceptual rockfall failure model, based on mechanically correct principles of rockfall evolution.

The conceptual model was based on the integration of findings from Research Objectives 1, 2, and 3. Rockfall detachment is a function of rock bridge attributes, including their proportion and number within an individual failure alongside their strength and rheological characteristics.

Variations in rock properties within a slope will control fracture propagation behaviour, influencing the number of rock bridges a propagating failure surface can fracture through,

and therefore, in conjunction with cross-cutting discontinuities, controls the magnitude of resultant failures. Weathering induced changes in rock properties result in changes to failure style. Greater weathering induced strength degradation within the slope is likely to result in increased 'heterogeneity' of rock properties, creating more 'stiffness' barriers to propagating rockfall failure surfaces, and potentially resulting in smaller rockfalls. As the magnitude of stresses required for fracturing is reduced, these smaller rockfalls are also likely to be more frequent. Weaker weathered rock is likely to display a more complicated failure sequence requiring multiple stages of brittle failure within a rock bridge or across several rock bridges, with this complexity reflected in pre-failure deformation data. In this scenario, the time between initial fracture event and final ultimate failure may be prolonged.

Over time, the patterns of pre-failure deformation and the magnitude-frequency characteristics of rockfalls will change in response to weathering. Removal of weathered material via rockfall, and subsequent exposure of a fresh surface may 'reset' the damage within the rock, and therefore the nature of rockfall detachment.

7.3 Recommendations for future research

To build upon and extend the findings of this study, the recommendations for future research are outlined below.

Structural controls on rock bridge attributes

As the location and size of rock bridges are the end result of a joint's inability to continue further propagation, a greater understanding of the conditions under which joints form and propagate may provide insights into the associated rock bridge characteristics. For example, more localised topographic unloading stresses may create relatively small and diffuse rock bridges within a rock mass, while regional and higher stress tectonic conditions may create larger, but fewer rock bridges within a rock mass. This potentially influences the size of possible failures from a slope.

Additionally, the size of rock bridges and their perimeter to area ratio may determine weathering exposure and influence the rate of rock bridge weakening. A higher ratio created by more frequent but smaller rock bridges in a slope may allow strength degradation to occur at faster rate than for slopes with a low ratio comprised of larger but less frequent rock bridges. Further field and laboratory investigation, potentially via analogue models, is required to understand the effect of increased surface area at the discontinuity/rock bridge tip on rock strength degradation. This may hold implications for the timing of rockfall.

Integration of geotechnical testing and 4-D remote sensing monitoring.

As outlined in the conceptual model, the nature of pre-failure deformation may be a function of rock strength degradation. However, this needs 'ground-truthing' via the geotechnical characterisation of rock strength for rock slopes that are actively being monitored. This will allow the assessment of how patterns of pre-failure deformation vary in response to changes, in not only rock strength but also failure style. The integration of remote-sensing data with laboratory testing may also be able to provide an assessment of surfaces exposure age, which can potentially be used as a proxy or predictor for the sequences and associated timing of rockfalls.

The integration of high resolution photography with 4-D terrestrial laser scanning may also allow for photographic documentation of rock bridge fracture and the sequential development of a rockfall scar, via the failure of periphery material, recorded over the same intervals as the monitoring data. This would allow a greater investigation of the links between rock bridge breakage and the surface expression of such deformation.

Influence of rock properties, with specific reference to lithology, on fracture propagation pathways

The size of failures is in part dependent on the extent of fracture propagation through rock bridges in a rock mass. Fracture propagation is often halted by changes in the elasticity of rock between different lithological units (Pollard and Aydin, 1988).

Geotechnical characterisation in Chapter 5 indicates that alongside weathering induced strength degradation, changes to elasticity and strain behaviour can occur. These changes are however lithology dependent, with the Siltstone samples displaying reductions in elasticity in contrast to the constant elasticity and strain behaviour of the Sandstone samples, though both samples displayed significant reductions in strength.

This implies that it is not only the strength of the rock that is an important control on stability, but also other properties such as its ability to deform elastically. Further characterisation of the effect of weathering on rock properties for varying rock types, may be able to explain the inferred fracture propagation pathways and the resultant observed failures sizes. This also holds implications for the size of possible failures from a slope, particularly for interbedded sedimentary sequences.

8 Appendix A: Published Manuscripts

Appendix A1: Forensic Analysis of Rockfall Scars (Geomorphology, 2017)

de Vilder, S.J., Rosser, N.J., and Brain, M.J., 2017. Forensic analysis of rockfall scars. Geomorphology. 295. 202-214

In manuscript format and available at: http://dro.dur.ac.uk/22210/

Forensic analysis of rockfall scars

de Vilder, S.J.[1]*, Rosser, N.J.[1], Brain, M.J.[1]

[1]Department of Geography, Durham University, Lower Mountjoy, South Road, Durham DH1 3LE UK

*Corresponding author: s.j.de-vilder@durham.ac.uk

Keywords: Rock bridges, Failure mechanisms, Rock mass strength, Discontinuity persistence, Rockslope failures, Progressive failure.

Abstract:

We characterise and analyse the detachment (scar) surfaces of rockfalls to understand the mechanisms that underpin their failure. Rockfall scars are variously weathered and comprised of both discontinuity release surfaces and surfaces indicative of fracturing through zones of previously intact rock, known as rock bridges. The presence of rock bridges and pre-existing discontinuities is challenging to quantify due to the difficulty in determining discontinuity persistence below the surface of a rock slope. Rock bridges form an important control in holding blocks onto rockslopes, with their frequency, extent and location commonly modelled from the surface exposure of daylighting discontinuities. We explore an alternative approach to assessing their role, by characterising failure scars. We analysed a database of multiple rockfall scar surfaces detailing the areal extent, shape, and location of broken rock bridges and weathered surfaces. Terrestrial laser scanning and gigapixel imagery were combined to record the detailed texture and surface morphology. From this, scar surfaces were mapped via automated classification based on RGB pixel values.

Our analysis of the resulting data from scars on the North Yorkshire coast (UK) indicates a wide variation in both weathering and rock bridge properties, controlled by lithology and associated rock mass structure. Importantly, the proportion of rock bridges in a rockfall failure surface does not increase with failure size. Rather larger failures display fracturing through multiple rock bridges, and in contrast smaller failures fracture occurs only through a single critical rock bridge. This holds implications for how failure mechanism changes with rockfall size and shape. Additionally, the location of rock bridges with respect to the geometry of an incipient rockfall is shown to determine failure mode. Weathering can occur both along discontinuity surfaces and previously broken rock bridges, indicating the sequential stages of progressively detaching rockfall. Our findings have wider implications for hazard assessment where rock slope stability is dependent on the nature of rock bridges, how this is accounted for in slope stability modelling, and the implications of rock bridges on long-term rock slope evolution.

Introduction

The scar left behind after a rockfall from a rock face, commonly comprised of exposed joint surfaces separated by zones of broken intact rock termed *rock bridges*, holds significant insights into the conditions prior to failure, and the mechanics of that failure. Despite this, the analysis of failure scars has been largely restricted to detailed post-failure analysis of single, commonly large, rockfall or rockslides, rather than analysis of an inventory of multiple events (e.g. Frayssines and Hantz, 2006; Paronuzzi and Sera, 2009; Sturzenegger and Stead, 2012). To gain insight into the influence of rock structure on stability, failure mechanisms are commonly inferred from the back analysis of stability based upon the wider slopes' rock mass strength (RMS), which is estimated from the combined influence of pre-existing discontinuities, intact rock strength, and the degree of weathering (Barton, 1974; Hoek and Brown, 1997; Jennings, 1970; Selby, 1980). The control of intact rock strength is most significant at rock bridges, as they form the attachment points holding a failing block to the rock mass (Jennings, 1970) (Figure 1a). Failure is known to often occur as a complex, time-dependent interaction between shearing along discontinuities and progressive fracturing through rock bridges, termed 'step-path' failure (Brideau et al., 2009; Jennings, 1970; Scavia, 1995).

Structural assessment of stability is routinely undertaken through field investigation by direct observation (e.g. Priest, 1993), remote sensing (e.g. Dunning et al., 2009; Sturzenegger and Stead, 2009), geophysical survey (e.g. Clarke and Burbank, 2011), or intrusive ground investigations such as borehole logging. However, characterising the persistence of discontinuities through a potentially unstable rock slope remains challenging. As such, many studies have assumed that discontinuities are fully persistent and the resulting stability analysis employs a purely kinematic analysis of failure (e.g. Goodman and Shi, 1985; Wyllie and Mah, 2004). Importantly however, rock bridges influence overall slope stability, and experiments with limit equilibrium modelling shows even a single-digit percentage presence of rock bridges as a proportion of total discontinuity length within a slope will substantially increase the overall factor of safety

(Frayssines and Hantz, 2009; Jennings, 1970). Field data from previous failures suggests a wide range in a rock bridge prevalence that is inevitably site specific, including very small percentages (0.2% to 45% as reported by: Tuckey and Stead, 2016 and references therein). In addition, prior to failure the slope can become weakened via a complex suite of weathering processes (Viles, 2013a), which alter the mechanical properties of exposed discontinuities, already broken rock bridges and those, which may break in future.

The identification and attributes of significant intact rock bridges is poorly constrained in field studies, due to the difficulty of assessing their presence within the rock mass. Forensic analysis of a rockfall scar provides the most direct assessment of their role within a rockfall event (Figure 1b). However, few studies have fully characterised rockfall scars, with many focussed on specific analysis at single sites. This, combined with the wide range of reported rock bridge presence and only limited and disparate assessment of general characteristics between sites, we argue provides insufficient evidence to fully constrain the role of rock bridges in controlling rockfall (e.g. Frayssines and Hantz, 2006; Lévy et al., 2010; Paronuzzi et al., 2016).

A broader assessment, and detailed analysis of both rock bridges and other scar attributes can be used to infer the nature of stresses at the time of failure (e.g. Paronuzzi et al., 2016; Paronuzzi and Sera, 2009), subsequent failure mode (Bonilla-Sierra et al., 2015; Stock et al., 2011), the sequence of rock bridge breakage (Stock et al., 2012), and the prevalence of weathering, and hence relative age of discontinuities and rock bridge breakage. This has important implications for hazard assessment of individual slopes (Fell et al., 2008), and also for how rock strength and structure influence longer-term landform change (Clarke and Burbank, 2010; Koons et al., 2012).

To address this, we present analysis of a rockfall scar database consisting of 657 individual rockfalls, which range in surface area from 0.1 m² to 27 m². Our aim is to characterise rock bridges within individual rockfall scars in this inventory in order to understand how they determine the type, mode and location of failure.

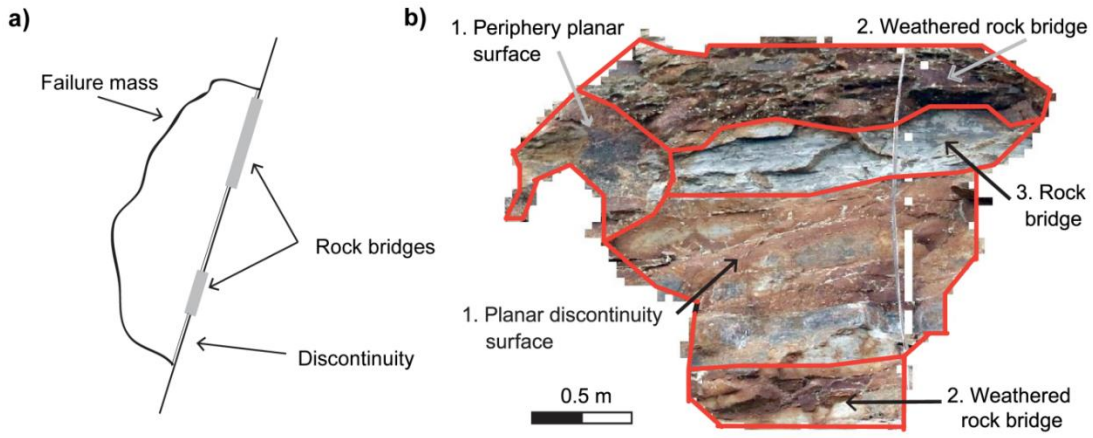

Figure 1: a) Simplified profile view of a rockfall held to a rockslope by rock bridges and a pre-existing yet not fully formed discontinuity. The incipient rockfall requires the rock bridges separating the discontinuities to be broken before failure can occur. b) Example high resolution photograph of a siltstone rockfall scar, from North Yorkshire coastal cliffs, U.K. The scar contains discontinuities of varying persistence, plus three separate broken rock bridges that have been variously weathered, as indicated by the surface colour. Analysis of the age of the features, as indicated by their weathering, suggests the order of failure, with the discontinuity surfaces forming first, before fracturing and weathering of rock bridges, and the final fracture of a freshly exposed rock bridge.

Study Site

We monitored a 200 m section of near-vertical cliffs at Staithes, North Yorkshire, UK over a 13-month period to document and characterise rockfall activity (Figure 2). The rock portion of the cliffs is ~60 m in height, and located on a storm-dominated macro-tidal coastal environment. The 200 m survey section contains a lower shale unit (~10 m high, extending from the cliff toe at mean high water level), an upper shale unit (~32 m high) and an interbedded siltstone and sandstone unit (~12 m high), capped by a glacial till (Figure 2c). These form part the of the Lower Jurassic Redcar Mudstone and Staithes

Sandstone formations (Rawson and Wright, 2000). All units display a bedding dip of 2° to the south-east, which is broadly orthogonal to the northern aspect of the cliff face, and a complex discontinuity pattern, which varies in orientation and persistence between the interbedded layers in each major rock type. From field mapping, the dark blue-grey lower shale unit is slightly weathered with some surficial algal cover, is moderately strong to strong, and has indistinct bedding with iron-stone bands throughout, as well as a widely spaced joint pattern of varying persistence (classification based on ISRM, 2015). The upper shale unit is similar with a dark blue-grey colouring, slightly weathered, is indistinctly bedded with ironstone bands, and is moderately strong to strong. However, its joint pattern shows a greater variance in spacing. The interbedded siltstones and sandstones are comprised of gradational beds of silt and sand, which can be up to 3 m in thickness, and display a widely spaced (~2 m) 'blocky' joint pattern with narrow to widely dilated joints. It is slightly weathered, is light blue-grey, and moderately strong to strong.

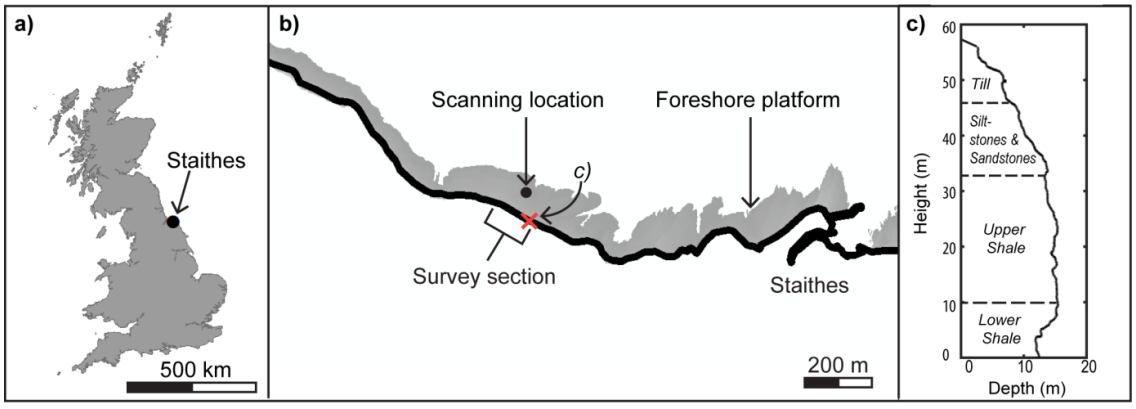

Figure 2: a) Location of Staithes, North Yorkshire, UK. b) Map view of survey section and scanning location at Staithes. The location of the cliff cross-profile section presented in c)., is indicated by the cross. c) Typical cliff and lithological profile of the survey section.

Methods

Overview of approach

Understanding the role of rock bridges and weathering in controlling failure behaviour requires complete characterisation of scar surface attributes. Both high resolution imagery and 3D models of the rockfall scars derived from pre- and post-failure topography are required to create and collate the scar database. From this, we undertook detailed analysis of the rockfall scar texture, structure and colour to quantify the properties of broken rock bridges and conversely discontinuities. This involves not only understanding the proportion of each element within an individual failure surface, but also their distribution, orientation and location with respect to the overall rockfall scar. Given the near-vertical cliff face and the typical nature of rockfall on these cliffs (see: Rosser et al., 2013), we assume that blocks delimited by pre-existing discontinuities alone must fall instantly in response to rock bridge failure in an adjacent supporting block and so are indistinguishable from rockfall controlled by rock bridges.

Firstly, we define the areal proportion of rock bridges (*%rb*) and weathered surfaces (*%w*) within each individual rockfall scar as a percentage of the total scar surface area, and proportion of weathered rock bridges (*%wrb*) as a percentage of individual rock bridge area. Respectively, these characteristics control slope stability (Jennings, 1970), indicate the exposure to environmental processes (Viles, 2013a), and places limits on the temporal order of failure (Stock et al., 2011). Secondly, we constrain if fracturing through rock bridges is either uniformly distributed across the rockfall scar, or is more locally concentrated. The distribution of rock bridges determines the location, direction and magnitude of stress concentration at each attachment point that supported the rockfall prior to release. Thirdly, we determine the locations of rock bridges with respect to the critical slip path, which influences the stress required for failure along this orientation (Tuckey and Stead, 2016). Fourthly, we analyse the location of a rock bridge within a rockfall scar relative to its centre of mass, which represents the location about which forces act and rotation occurs (Hibbeler, 2010). This places controls on failure mode,

with simple moments indicating if failure was most likely in tension or shear (Bonilla-Sierra et al., 2015; Stock et al., 2011).

Rockfall inventory & descriptors

We collected repeat terrestrial laser scanning (TLS) surveys of a 200 m section of coast on an approximately monthly basis over a 15 month period (June 2015 to September 2016) (Figure 2). A Riegl VZ -1000 laser scanner was consistently positioned ~100 m from the cliff toe to collect 3D point clouds with spacing of 0.01 m to 0.02 m. From this, we undertook 2.5D change detection of the sequential cliff surfaces using the approach detailed in Rosser et al. (2005), which assumes that the cliff face can be approximated to a 2D planar surface. Triangular irregular network (TIN) models were created of the pre- and post-failure topography and combined to form a 3D rockfall model, from which we calculated centre of the mass, volume and dimensions, assuming a uniform rock density.

We captured high resolution photography to provide information on surface texture, discoloration due to weathering and context for interpreting the 3D scan data. We collated gigapixel panoramic images of the cliff face on an approximately monthly basis over 13 months (August 2015 to September 2016) from the same foreshore position as the TLS (Figure 2). We used a 50 MP Canon EOS 5DS R camera with a 300 mm telephoto lens, in conjunction with a Gigapan Epic Pro mount. The individual photos were stitched into one panoramic image (8,688 by 5,792 pixels), achieving an on-cliff pixel resolution of 0.001 m to 0.002 m (Figure 3). We manually adjusted aperture, shutter speed and ISO depending on conditions to capture sharp, high-quality images.

Each panoramic image was overlaid on the DEM collected in the same month. We geo-referenced the image using a spline transformation with at least 200 control points. Rockfall scars were extracted from the Gigapan images using the rockfall locations extent from the change measured using the TLS data comparison. Rockfall scar images

that had undergone distortion or warping of pixels during geo-referencing were manually deleted from the database.

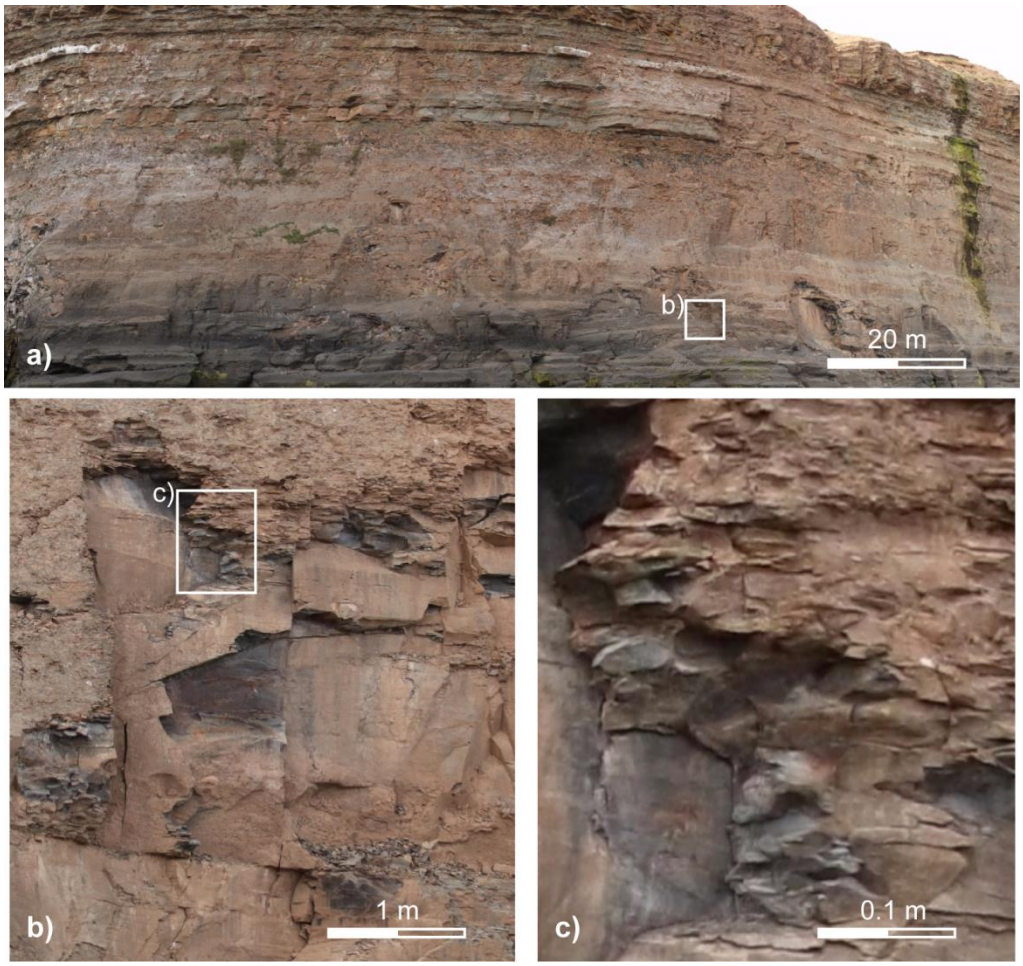

Figure 3: a) Panoramic gigapixel image of the monitored cliff section. b) Close-up of a rockfall scar. c) Close-up of a freshly broken rock bridge.

Data Processing

Over the survey period we identified a total of 657 rockfall scars with > 0.1 m² surface area. We consider it unlikely that failures smaller than 0.1 m² are controlled to the same degree by the interaction of discontinuity release surfaces and rock bridges due to large discontinuity spacing (> 2 m) and the relatively high strength of the cliff rock as compared to small rockfall volume (mass), and so these were not included in the analysis.

We automated the classification of rockfall scar features to avoid the subjectivity associated with manual classification. This automated process involved a routine to classify areas of fracture through rock bridges within the scar surface imagery. Inspection of the imagery revealed that broken rock bridges in rockfall scars on these cliffs are characterised by rough surfaces with micro-topography comprised of small (cm – scale) planar segments separated by small (10^{-1} - 10^{1} cm) linear edges, as compared to the smooth and planar pre-existing discontinuity surfaces. High numbers of contiguous small segments and edges represent the remnants of failed rock bridges in the scar surface. We also undertook automated colour classification to identify discoloured surfaces indicative of weathering.

Edge Detection

To discretize the scar surface into zones of broken rock bridges and pre-existing discontinuities, we developed a method to delimit areas of similar texture within the scar. We employed an automated image classification technique, based upon the RGB values in the high-resolution optical imagery, adapting an approach used for petrographic grain boundary detection, developed by Li et al. (2008). This involves four stages outlined in Figure 4, namely: edge detection, noise reduction, vectorisation and density classification. Edges were detected by the contrast of light to dark tones in pixel values, indicative of shadowing created by rough surfaces (Figure 4a). To enhance contrast, images were converted to grey-scale and smoothed by obtaining and applying a median pixel value over a specified area to reduce small scale noise (Figure 4b). As fractures are likely to have linear features and be continuous within patches, pixel contrasts less than the smoothing area were considered noise. The range in pixel values was calculated over a kernel size of 12 by 12 pixels or 0.018 m by 0.018 m, which retained resolution but remained insensitive to gradual shifts in tone and/or colour due to natural lithological or weathering variations (Figure 4c). This kernel highlighted only abrupt changes in pixel values, and as such identified those areas more related to fracturing of

intact rock. As an individual rockfall scar assessment of relative pixel value range, this approach is insensitive to larger scale (e.g. month to month) variations in ambient colour, and lighting. The pixel value range was converted into a binary using Otsu's (1979) thresholding algorithm, allowing classification of the scar surface into zones of 'non-edges' and 'edges' (Figure 4d). As this was a relative threshold value set via cluster analysis of grey-scale pixel histogram rather than a pre-determined absolute value – it allowed areas of relatively higher pixel contrast to be separated from areas of relatively lower pixel contrast for each rockfall scar. As a second stage of noise reduction, fracture zones < 0.002 m in length were omitted and those with tips within a 0.01 m area were conjugated to form a continuous single 2D zone feature (Figure 4e). Zones of fracture edges were converted into polylines using a centre-line vectorisation, whereby proximal collinear edges within 0.0225 m were merged (Figure 4f). The line features allowed densities of fractures to be obtained using a kernel with radius of 0.25 m (Silverman, 1986), which retained detail whilst simplifying small-scale noise (Figure 4g). This produced coherent zones, which described low to high edge densities across the rockfall scar surface (Figure 5). Areas of higher density indicated fracturing through a broken rock bridge (Figure 4h), verified by visual comparison of a subsample of the classified inventory.

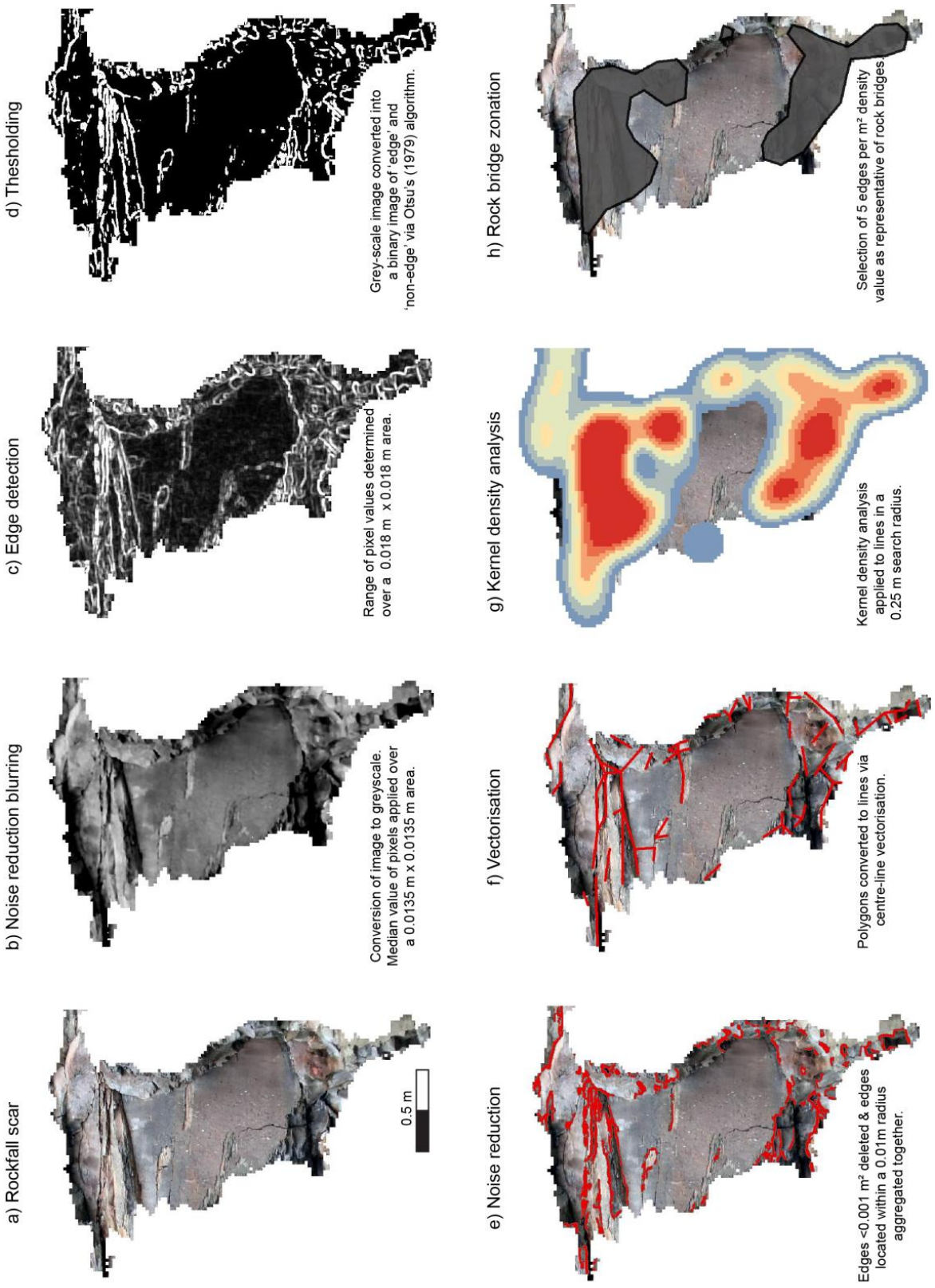

Figure 4: Detailed stages of edge detection from the original image (a), through initial noise reduction (b), to edge detection algorithms(c-d), further noise reduction (e), and density analysis of edges (f-h).

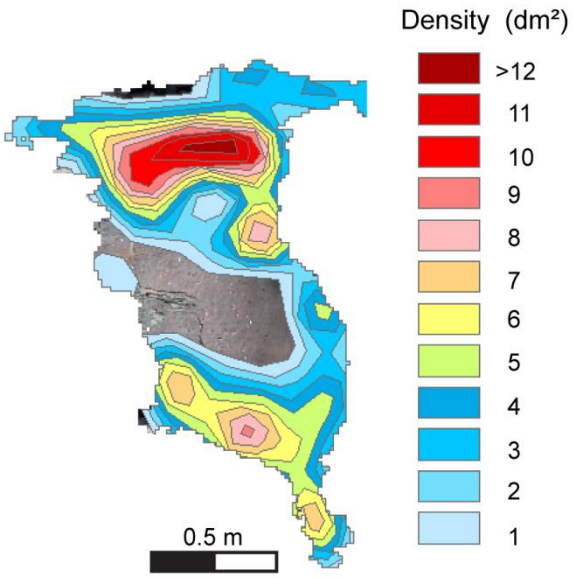

Figure 5: Density classes derived from kernel density analysis of edges within rockfall scars. Density increases from 1 edge per m² to ≥12 edges per m² within this rockfall, though densities >15 edges per m² occur within the database. The incremental density value is simplified as *dm².*

Rock bridge determination

Based upon the density of features derived using the image classification, a threshold that identifies a 'rock bridge' from other areas is needed. To determine the edge density range over which features are classified as rock bridges we analysed a subset of the rockfall database, which consisted of a random sample of 163 rockfall scars > 0.1 m² recorded between the two monitoring intervals of 25/11/2015 and 26/01/2016, This sub sample contained a wide range of rockfall sizes and respective lithologies. Individual rock bridge areas were derived from incrementally increasing density values between 1 - 15 edges per m² (*dm²*). Mean, median, interquartile range and the number of observations of individual rock bridges (*rb_count)* for each *dm²* value were determined to evaluate the success of the classification (Figure 6). The *rb_count* within a scar peaks at density values of five *dm²* before decreasing. At lower *dm²* rock bridges are conjoined, resulting in a lower number of observations, before features become separated into several

individual rock bridges when using higher *dm²* (Figure 5). Above five *dm²* the numbers of observations decrease as some areas no longer contain enough features to be classified as a rock bridge by the kernel density analysis.

The mean, median and interquartile range of individual rock bridge areas decreases with increasing *dm²*. On the basis of this, and in consideration with the peak *rb_count*, we selected a density of five *dm²* for classification. Visual assessments of (>50) rockfalls scars confirmed that this was a 'best-fit' for areas of dense fracturing. Additionally, we calibrated this method with manual mapping of a subsample of 15 rockfall scars, which derived descriptive statistics comparable to and within the margin of error of each (Table 1). Visual comparison reveals that the relative location and proportion of rock bridges predicted by both methods are comparable(S.J. de Vilder et al., 2017).

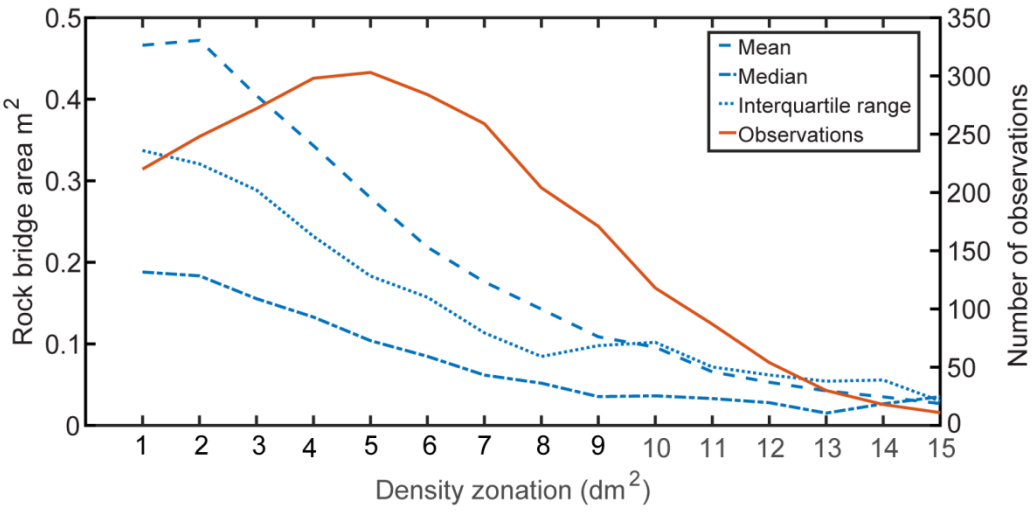

Figure 6: Descriptive values of rock bridge area recorded from different density values. These densities are determined from kernel density analysis of edges recorded within rockfall scars. They increase from 1 *dm²* to ≥15 *dm².*

Table 1: Descriptive statistical comparison between automatic and manual classification of the rock bridge scar surface area.

	Mean (m^2)	Std.dev. (m^2)	Median (m^2)	Margin of error (99% confidence) *	Count
Automatic Classification	0.318	0.499	0.102	0.100	74
Manual Classification	0.191	0.283	0.100	0.157	64

*Due to differences in sample size a *z (99%)* and *t (99%)* confidence interval were used for the automatic (n >30) and manual methods (n <30) respectively.

Weathering surface classification

We classified rockfall scars into categories to constrain the role of weathering-controlled strength degradation along discontinuities, and within rock bridge fracture (Viles, 2013a). Classification was based on RGB pixel values to represent the intensity of rock weathering relative to virgin rock (Figure 7a). We manually chose characteristic RGB histogram ranges, consisting of 25 RGB samples selected to cover a wide range of different surfaces and lithologies exposed upon the cliff. These 25 samples were further classified into five categories determined via histogram evaluation and visual assessment as: unweathered, shadow, biologically weathered, slightly weathered/till covered and moderately weathered. The glacial till that caps the cliff (Figure 2) and drape debris over the cliff face making the distinction between the till cover and slightly weathered surfaces at times ambiguous. Biologically weathered surfaces contain a coating of green algae and are often present on rockfall scars within the tidal inundation zone at the base of the cliff. To characterise the broader pattern of weathering within rockfall scars, we selected the dominant weathering types (Figure 7c). As part of this broad assessment, moderately weathered, slightly weathered/till covering and biologically weathered surfaces were combined and simplified to create a single weathered category.

We calibrated this automatic method with a manually mapped database. Comparison of descriptive statistics for 15 rockfall scars (Table 2), reveal that the mean and median

values are comparable and within the calculated margin of error. Visual assessment of automated results is comparable to the hand mapped interpretations (S.J. de Vilder et al., 2017)

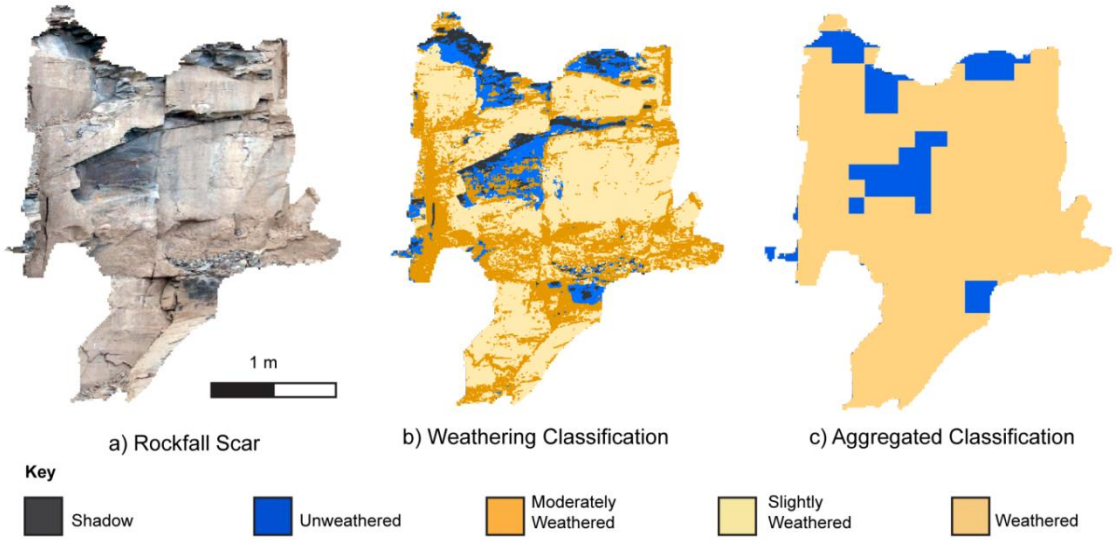

Figure 7: Automated weathering surface classification of rockfall scar surface (a) into a detailed 5 category classification of individual pixels (b) and a broader classification of 3 categories based on a 100 by 100 pixel area (c). Categories are outlined in the key.

Table 2. Descriptive statistical comparison between automatic and manual classification of the weathered scar surface area.

	Mean (m^2)	Std.dev. (m^2)	Median (m^2)	Margin of error (99% confidence) *	Count
Automatic Classification	0.264	1.044	0.025	0.212	148
Manual Classification	0.237	0.351	0.089	0.194	82

* Due to differences in sample size a *z (99%)* and *t (99%)* confidence interval were used for the automatic ($n > 30$) and manual methods ($n < 30$) respectively.

Results and Interpretation

Rockfall characteristics

Rockfall scars in the database (n = 657) had a mean surface area of 0.652 m² (Table 3), with 13% of rockfall scars having a surface area > 1 m². We use scar surface area as a metric for rockfall size, as it provides a consistent comparison with *%rb* and *%w* and has positive linear relationship with measured rockfall volume (*r =0.927, p = -0.033*). Rockfalls are distributed from across the cliff face, with the highest concentration observed in the shale units (54% in the upper shale and 28% in the lower shale). Fewer interbedded siltstone and sandstone rockfalls are captured due to their location within the cliff face. These events were commonly discarded due to pixel distortion as a result of both the relative steep angle of data capture and nature of 'stretching' the panoramic image over the protruding sandstone and siltstone beds..

Table 3: Characteristics of rockfall volume, area and simple geometric variables within the database.

	Area (m²)	Volume (m³)	Width (m)	Height (m)	Depth (m)
Mean	0.652	0.236	1.076	0.893	0.652
Median	0.233	0.043	0.760	0.660	0.494
Std.dev.	1.534	1.208	0.971	0.722	0.547
Min	0.100	0.010	0.260	0.083	0.175
Max	26.912	27.003	9.560	6.160	3.956
Range	26.812	26.993	9.300	6.077	3.781

Rockfall scar characteristics

Rock bridge and weathering proportions

The distribution of *%rb* displays a wide range in values with a skewness of 0.4, and peak in observations for < 2 *%rb* (Figure 8a). This includes rockfalls with no rock bridges, which account for 20% for rockfalls within the database. Such rockfall are predominately

< 0.2 m² with a maximum scar surface area of 1.66 m² (Figure 9). Excluding this subset, *%rb* values are normally distributed with a wide range in values from 0% to 97.6%, and a mean value of 31% ± 26% and a median of 29% (Figure 8a and Table. 4). Individual rockfall scars therefore display a large range in the proportion of their surface that comprises broken rock bridges.

To understand what drives this large range in *%rb* values, we assessed rockfall volume and lithological differences. Rockfall scar area showed no correlation with *%rb* ($r = -0.122$, $p = 0.006$), with a wide scatter in *%rb*. Comparison of descriptive statistics between the three lithologies revealed a 10*%rb* difference by rock type (Table 4). The lower shale displayed the lowest *%rb* (26.7%) and interbedded siltstones and sandstones displayed the highest (*%rb* = 34.7%). A similar pattern is observed for the median values of *%rb*. Analysis of variance indicates that the lower shale unit had a statistically-significant ($p = 0.01$) lower mean *%rb* than that of the upper shale and siltstone/sandstone units. Therefore, *%rb* varies as a function of lithology but not with increasing rockfall size. The different lithological units, and their associated rock mass structure, can be considered a critical influence on the prevalence of rock bridge proportion within the scars (and therefore rockfalls) that each unit generates.

%w has a bimodal distribution whereby rockfalls are generally characterised by either <4 *%w*, or more strongly at values of >98 *%w* surface weathering (Figure 8b). There is a wide but consistent range in values between these two end members, which generates a mean value of 49.7 % ± 34.9%, and a median of 48.9%. Surfaces with >98 *%w* correspond to the peak in values for <2*%rb,* suggesting that rockfalls with nearly 100*%w* contain 0*%rb*. However, as the peak is larger for *%rb*, some of these scar surfaces with no rock bridges must have been partly unweathered prior to failure. This suggests that *%w* is not solely related to discontinuity occurrence within the rockfall scar, and as such must be related to weathering of already broken rock bridges. The wide range in values also indicates that discontinuity connectivity within the rock mass influences the distribution of weathering across the scar surface prior to failure.

%wrb has a similar bimodal distribution to %w with rock bridges strongly >98*%wrb* or <20 *%wrb,* and a wide consistent range in values (Figure 8c). *%wrb* has a mean value of 43.51% ±35.19%, and a median value of 35.5%. Most rock bridges however are only partly weathered, with 79.95% of all rock bridges containing <50*%wrb*, and *%wrb* overall accounts for 12.99% of total rock bridge area. This may be a function of the areal aggregation during classification and the ambiguity of classifying till covered/slightly weathered surfaces (Figure 7), introducing an element of uncertainty in this result. As such, we suggest that the broad pattern of these results rather than the exact *%wrb* value is more important. The result implies that some rock bridges within the rock mass have been either partially or completely fractured before final failure of the rockfall, and these fractured surfaces have been exposed for a significant period of time for surficial weathering and discolouration to take place.

Table 4: Descriptive statistics for *%rb* based on geology

	Mean	Std.dev.	Median	Max	Min	Count
All	30.8	25.8	28.9	97.6	0	657
Lower Shale	26.2	26.7	20.3	97.6	0	184
Upper Shale	31.9	25.1	31.2	95.3	0	356
Siltstone/Sandstone	34.7	25.9	36.2	93	0	117

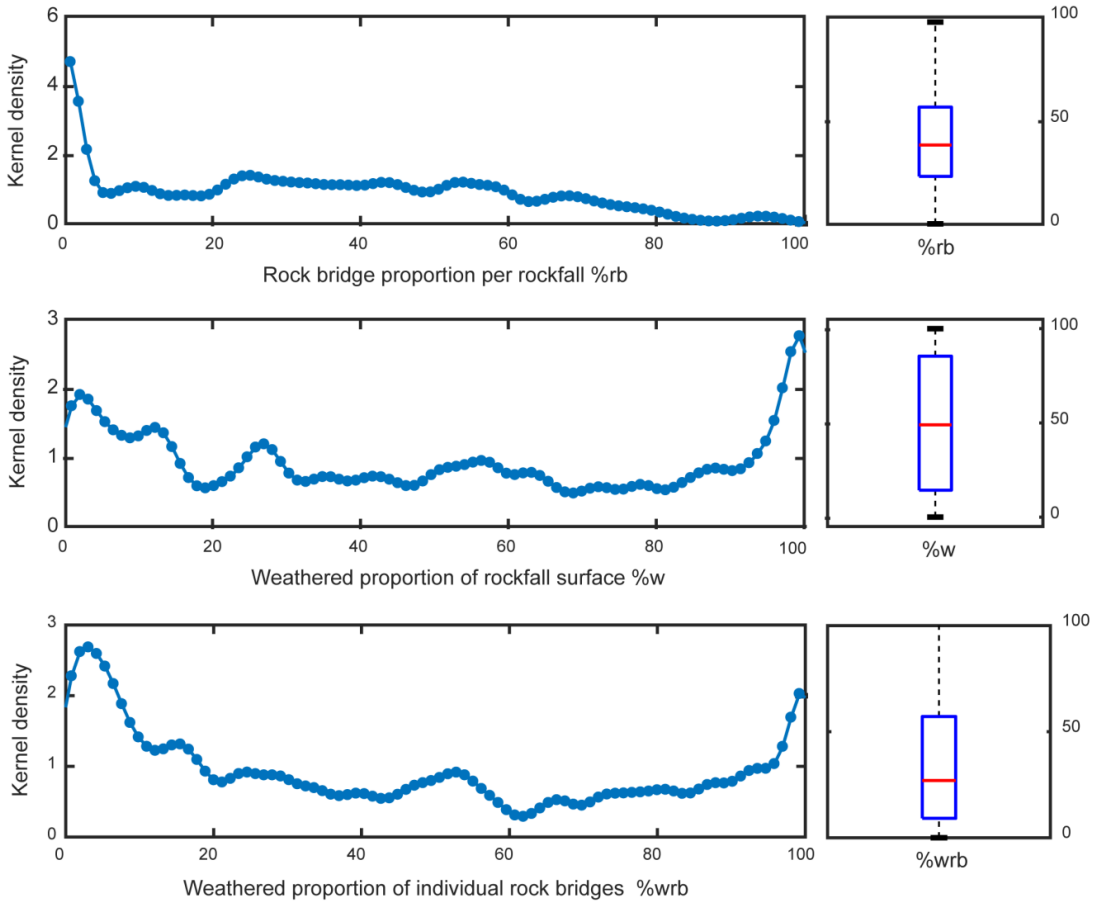

Figure 8: Histograms and box plots of a) *%rb* and b) *%w* and c) *%wrb*.

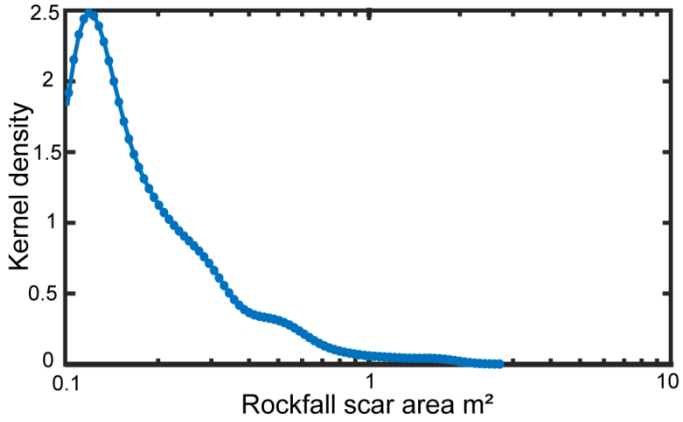

Figure 9: Kernel density plot of the area distribution of rockfall scars recorded with no rock bridges.

Rock bridge distribution

Rockfalls have a median value of one rock bridge per scar, with a mean value of 1.8 ± 2.2. The number of rock bridges per scar has a significant positive linear correlation with increasing rockfall scar area (r = 0.928; Figure 10a). This demonstrates that larger rockfalls contain more individual rock bridges, as opposed to larger rockfalls purely being larger versions of their smaller counterparts. Mechanically, larger rockfalls may therefore behave and fail in a manner quite different to smaller rockfall, and so may be sensitive to a different set of conditions, controls or thresholds on failure. Around 0.5 m² scar surface area, rockfalls tend to contain ≥2 rock bridges, with the trend indicating that rockfalls with 1 m² surface area are most likely to contain two or more rock bridges. This indicates that, in broad terms for every 0.5 - 1 m² of increasing rockfall scar surface area, there is one additional rock bridge holding the block to the rock face. Individual rock bridge area is predominantly measured to be *c*. 0.1 m² (Figure 10). A 0.5 m² rockfall surface area that contains a 0.1 m² rock bridge adheres to the mean *%rb* estimate.

Within each rockfall scar, we examined the areal extent of the individual rock bridge(s) (Figure 10b). We compared the relative area of the largest rock bridge within the scar to all the other rock bridges within the same scar. Our analysis identifies that for rockfalls with <5 rock bridges, one main rock bridge dominates the scar surface, with smaller peripheral bridges. As the number of rock bridges increases the dominance of a single bridge decreases, as the fraction of the scar rock bridge area occupied by the largest rock bridge as compared to all other rock bridges reduces. This suggests that for larger rockfalls with > 5 rock bridges in the inventory, rock bridges tend to be of a similar surface area. Conceptually, and assuming a homogenous rock mass structure, as the failure scar surface area grows it incorporates more rock bridges. With increasing rockfall volume, fractured rock is distributed across multiple bridges of similar size, rather than concentrated in one primary rock bridge. By implication the perimeter to area ratio of rock bridges changes with rockfall volume, which exposes a greater area of the supporting rock bridges to be exposed to weathering within the rock mass.

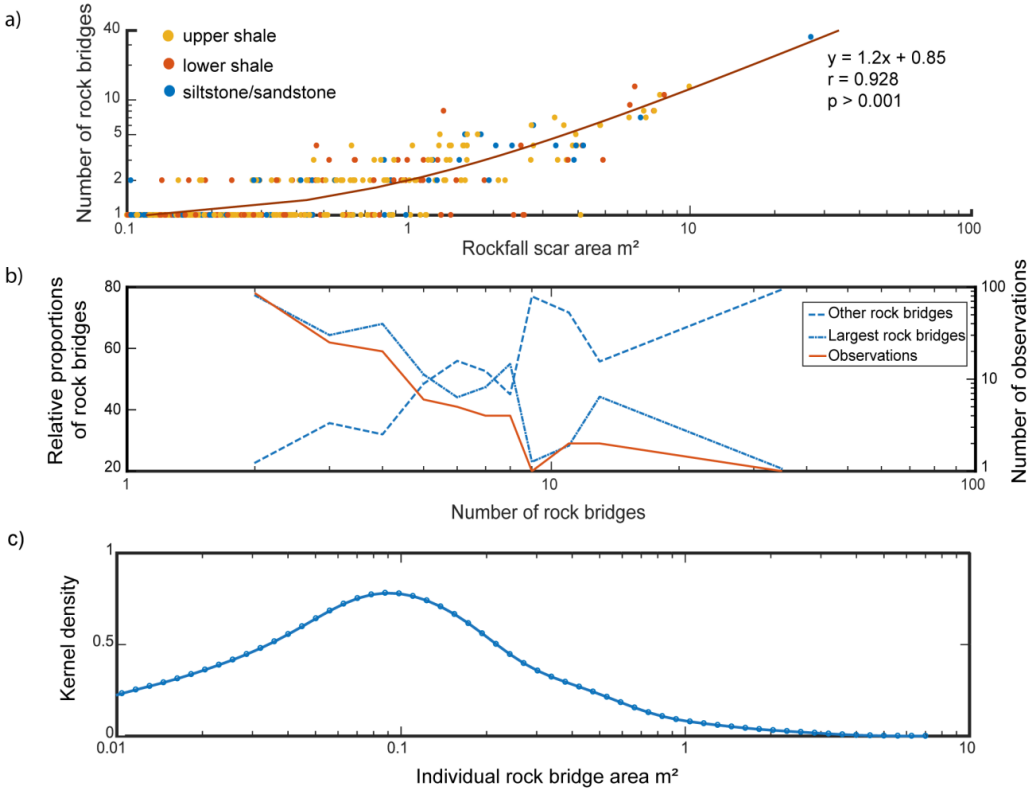

Figure 10: a) Scatter plot displaying a positive linear trend between number of rock bridges per scar and rockfall scar area. b) Mean values of the relative proportion of the largest rock bridge within an individual scar compared with the proportion of all other rock bridges within an individual scar. For example, if a rockfall scar contains two rock bridges, the largest accounts for 80% of rock bridge area while the other accounts for only 20 %. The number of observations for the calculation of mean values is plotted on the right axis and descreases with increasing rock bridges. c) Kernel density plot of individual rock bridge area distribution, displaying that most rock bridges are 0.1 m².

Rock bridge orientation

We assessed the orientation of rock bridges with respect to rock bridge planarity relative to the main failure surface. We compared the mean slope and aspect (derived from the cliff face surface topography model) of the rock bridges with that of the overall aspect

and slope of the scar surface (Fig 11a). Slope and aspect are comparable to the dip and dip direction, respectively, of a discontinuity given the projection of the cliff face data employed here. Scar aspect was measured relative to cliff normal (Figure 2b) and as such represents deviations from the cliff face aspect. From this we derived a mean aspect value of 173.7° ± 53.1°, indicating that the most rockfall scars are oriented approximately parallel to the cliff face.

We define rock bridges as co-planar with the main failure surface, if both slope and aspect are ≤15° from scar surface orientation. Due to the relatively small failure size and based on field observation, we assumed rockfalls scar surfaces contained one main planar failure surface, and therefore co-planar rock bridges are also in-plane with this surface. We define rock bridge deviations in slope and aspect of >15° as non-planar. Our definition of non-planar bridges does not necessarily distinguish in-plane rock bridges along intersecting joints from out-of-plane rock bridges located between discontinuities of differing orientations. 69.5% of rock bridges were defined as predominately co-planar, with 30.5% predominantly non-planar. Rockfalls that contain both non-planar and co-planar rock bridges account for 14.8% of events in the inventory. For these rockfalls, scars are dominated by co-planar rock bridges (97%), with non-planar rock bridges forming only a minor component of the total scar. Therefore, nearly all rockfalls which contained both non-planar and co-planar bridges were accounted for within the 69.5 % of rock bridges which are predominately co-planar. This suggests that lateral release surfaces related to discontinuities striking perpendicular to the cliff face contain fewer rock bridges. Assessment of mean *%rb* between co-planar and non-planar rock bridges reveals that non-planar rock bridges show a higher proportion (51.1*%rb*) compared to co-planar (35.4*%rb*) (Figure 11b). Analysis of variance indicates that this difference is statistically significant ($p > 0.001$), so although non-planar rock bridges are less prevalent in our dataset, when they are recorded, their *%rb* is normally higher. Analysis of the distribution of co-planar versus non-planar rock bridges shows that (larger) rockfalls with multiple rock bridges are less likely to contain non-planar rock

bridges (Figure 11c). Therefore, non-planar rock bridges are limited to smaller rockfalls, which as identified previously, tend to contain only one rock bridge. These smaller rockfalls are more likely to be associated with discontinuity surfaces, which comprise rock bridges, whereas the larger rockfalls have fractured both through and across discontinuities.

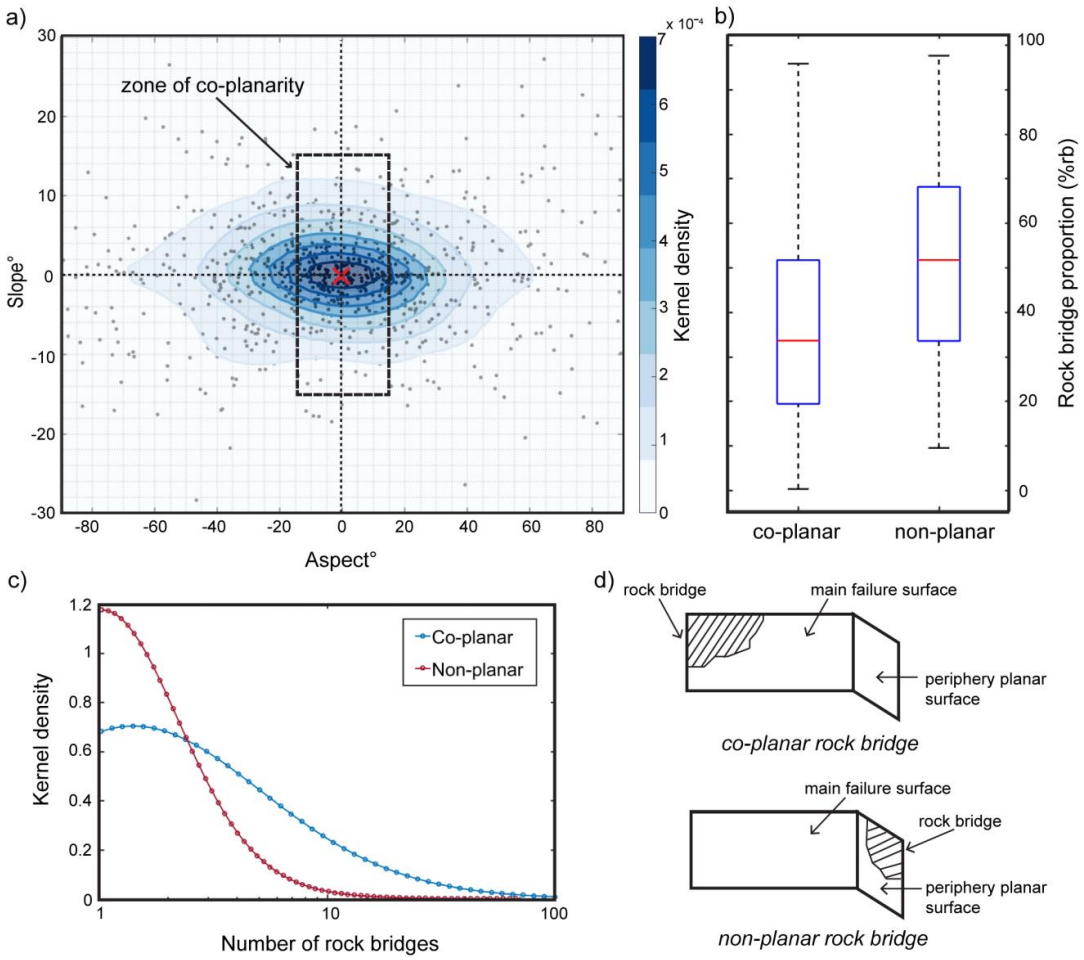

Figure 11: a) Kernel density plot displaying the difference in mean slope and mean aspect between rock bridge and the rockfall scar surface. Co-planarity defined as change in slope & aspect of < 15 °. b) Box plot displaying difference in *% rb* between co-planar and non-planar rock bridges. c) Kernel density plot of the number of rock bridges for either co-planar or non-planar rock bridges. d) Conceptual end-member examples of co-planar and non-planar rock bridges.

Rock bridge location

We normalise the coordinates of the position of the centre of the rock bridge relative to the coordinates of the 3D centre of mass projected back onto the cliff face for each rockfall. The centre of the rockfall is located at coordinates {1,1}, and rock bridge positions are displayed relative to this point (Figure 12). The highest density of rock bridges is generally located just above the rockfall centre of mass. Overall, more rock bridges are located above the rockfall centre of mass (52.4%), as opposed to below (47.6%), although this distinction is not clear. Rock bridges are however clustered around the projection of the rockfall centre of mass onto the cliff, with a decreasing density in bridge position with increasing radial distance relative to the scar extent. Rock bridges are broadly represented in all areas of the rockfall scar, except on the very periphery. Rock bridges therefore may not define the perimeter of the rockfall, but rather support a mass of which the extent is defined by the rock mass structure.

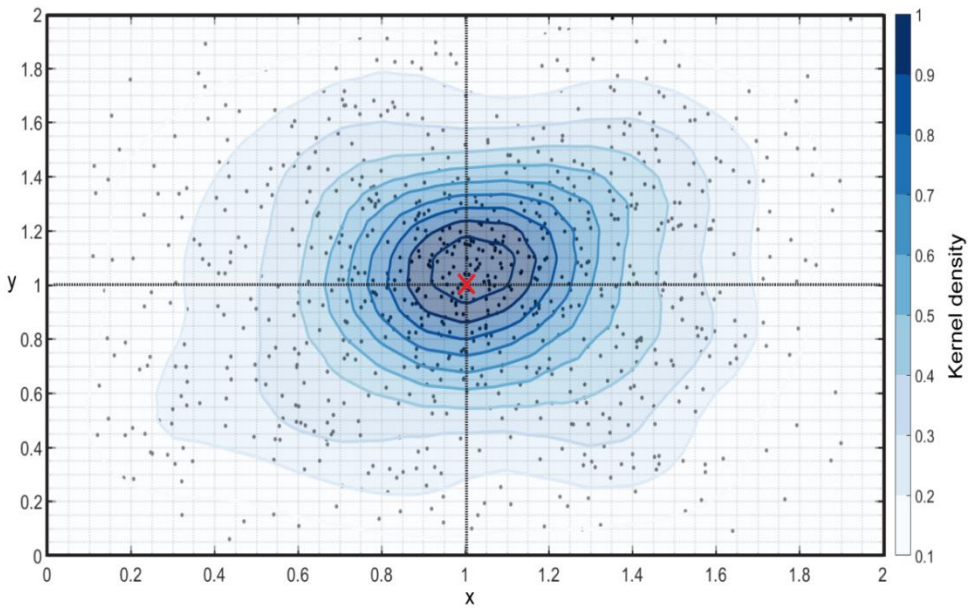

Figure 12: Kernel density plot of rock bridge centres normalised to the rockfall centre of mass. The rockfall centre is located at the x of 1, 1- with y values < 1 located below the rockfall centre and y values > 1 located above the rockfall centre.

Discussion

Rock bridge role in failure

Our results demonstrate that a wide range of *%rb* is possible within failures from the same rock type and structure. This holds across a range of rockfall sizes but varies with source rock lithology. The mean *%rb* value of 31% ±26% is higher than previously reported for other rockfall scar analysis case studies, which invariably focus on larger volume events, often in more competent or massively jointed rock. Previous studies, comprising of individually mapped rockfall scars, displayed a range of 0.2% to 26% (Frayssines and Hantz, 2006; Lévy et al., 2010; Paronuzzi et al., 2016; Paronuzzi and Sera, 2009; Stock et al., 2012, 2011). Estimates obtained from discontinuity persistence mapping and back analysis modelling display a larger range of 1% to 45% (Elmo et al., 2011; Gischig et al., 2011; Grøneng et al., 2009; Karami et al., 2007; Matasci et al., 2015; Sturzenegger and Stead, 2012; Tuckey and Stead, 2016). All of these estimates, including our dataset, display a six order of magnitude range in rockfall size (from 0.01 m^3 to 10,000 m^3) and consider various rock types.

We suggest that the large recorded variance in *%rb,* which we report here, is due to the spatial distribution of rock bridges within the slope, as determined by the persistence and spacing of discontinuities within the rock mass (Tuckey and Stead, 2016). To account for this variance, robust sensitivity analysis within modelling to determine failure susceptibility is needed. Through analysis of rockfall scars from the three rock types considered here, it is evident that lithology is an important control on rock mass strength in defining the nature of rock bridges, and even subtle changes in rock mass structure between the three lithological units results in significant *%rb* differences. This indicates that not only the wider geology, but also the local scale lithology changes control rock mass characteristics that are important controls in releasing blocks as rockfall. Joint density, a proxy for joint spacing, varies with bed thickness (e.g. Huang and Angelier, 1989; Ladeira and Price, 1981; Narr and Suppe, 1991), indicating that within interbedded

sedimentary sequences rock bridge characteristics will vary as function of mechanical stratigraphy.

The distribution of these rock bridges influences the stress within the incipient failing mass, determining its eventual failure mode (Bonilla-Sierra et al., 2015; Stock et al., 2011). Our dataset demonstrates that most rockfalls in our inventory will contain a singular rock bridge, which may be located throughout the scar, except on its periphery, with an approximately equal location probability above or below the rockfall centre of mass. Bonilla-Sierra et al., (2015) modelled rock bridge location in relation to a translational failure. Higher concentrations of tensile cracking were associated with rock bridges located at the top of the failure surface, a steeper slope angle and a lower centre of mass. When the rock bridge is located above the centre of mass, and assuming simplified geometry, the force acting on the failure mass generates a bending moment that results in greater tensile cracking and associated rotation (Hibbeler, 2010). Conversely, shear cracking was associated with a more shallow failure surface and rock bridges located in the centre or lower parts of failure (Bonilla-Sierra et al., 2015). Using a similar simplification, we suggest that rockfalls with rock bridges located above the centre of mass likely fail predominantly in tension, while rockfalls with rock bridges in line with or below centre of mass are likely to predominantly fail in shear (Figure 13). The degree of deviation of rock bridge location from the rockfall centre needed to generate sufficient bending moment and associated tensile failure is unknown. Further modelling would reveal if even slight deviations in rock bridge location results in an imbalance of forces, affecting those acting on a failing block and resulting in a change to the dominant failure mode.

Additionally, rock bridges that are non-planar to the main failure surface or located to the side of the centre of mass introduce an element of twisting or torsion into the mechanical analysis, which is rarely considered within the 2-dimensional analysis of slope failure mechanics (e.g. Wyllie and Mah, 2004), but is standard practice for structural engineering (e.g. Hibbeler, 2010). These require a fully 3D approach to account for

dilation and rotation of blocks within the rock mass. Analysis of the stresses experienced by the rock bridges will determine which strength characteristics, such as tensile or shear, are most important for stability. We show here that with increasing rockfall size, more rock bridges are likely to be incorporated into the eventual failure surface. This increases the complexity of the forces acting on the incipient failure mass due to their multiple attachment points to the slope. This also highlights the potential for the sequential failure of one rock bridge at a time, and the subsequent transfer of and changes in the nature of stress on remaining intact bridges.

Our results show that smaller rockfalls containing <5 rock bridges are commonly dominated by one large main rock bridge, which dictates the potential for failure and release. The mechanical and compositional characteristics of this main bridge will determine its strength, and the magnitude and trajectory of stress required for failure to occur. Within a heterogeneous (sedimentary) lithology, small scale (10^{-3} m to 10^{0} m) intrinsic flaws such as, micro-cracks, grain boundaries and sedimentary structures, such as ripples or concretions may predispose the rock bridge to failure by forming initiation points for micro- and macro- crack propagation (Kranz, 1983; McConaughy and Engelder, 2001; Pollard and Aydin, 1988). As such, the temporal behaviour of these smaller rockfalls may be difficult to predict.

As a failure develops, it remains unclear how the failure responds to, accommodates and incorporates smaller peripheral rock bridges, or includes the partial failure of larger rock bridge located on the edge of failure scar. In the case of a partial failure of a larger rock bridge, questions concerning controls on termination of fracture within that rock bridge and the impact on the dimensions of the failure mass are raised. This point of termination may be determined by intersecting cliff perpendicular discontinuities or non-persistent bedding, whereby fracture propagation deflects and stops at these boundaries due to changes in the near–field stresses experienced by the propagating crack tip, influenced by changes in lithological composition and mechanical interactions with discontinuities (Pollard and Aydin, 1988; Scavia, 1990). Therefore, discontinuity spacing may control

rockfall geometry and the amount of partial and complete fracturing required through rock bridges contained within the incipient failure mass.

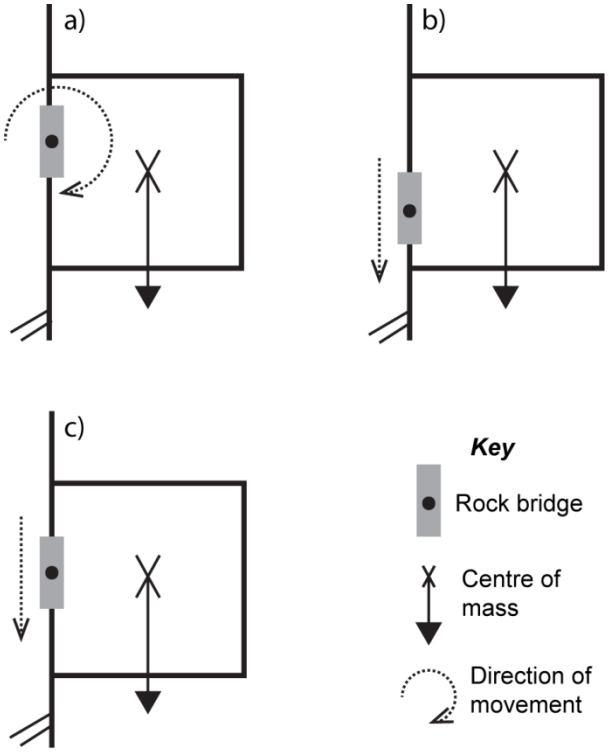

Figure 13: Conceptual model of rock bridge attachment points and potential failure directions. a) Rock bridges located above centre of mass may result in outward rotation of the incipient rockfall block and associated tensile failure. b) & c) Rock bridges located below centre of mass may fail in shear due to downward forces acting on the rock bridges.

Implications for progressive failure

For larger rockfalls, fracturing through each of the multiple rock bridges is required. The order through time in which rock bridges fracture remains poorly constrained but is likely to be complex. This order must have important implications for progressive failure and stress redistribution within the incipient scar (Eberhardt et al., 2004a; Kemeny, 2003; Stead et al., 2006). For instance, the fracture of minor rock bridges may result in

significant enough changes to stress distribution to create instability, or it may only be the fracture of larger bridges that are the catalyst for acceleration towards final failure and block release. Fracturing may represent or may drive pre-failure deformation (e.g. Rosser et al, 2007; Kromer et al., 2015) whereby observed surface deformation may be a manifestation of fracturing of rock bridges within the rock mass. Our analysis of *%wrb* distribution has indicated that substantial weathering of fractured rock bridges can occur before final failure, suggesting that pre-failure deformation may not always result in a sudden acceleration towards failure and may evolve over a period sufficiently long enough for weathering to take hold. In these circumstances the redistribution of stress may result in a new prolonged (quasi-)equilibrium state (Leroueil, 2001). Modelling of progressive failure may help understand this temporal pattern by accounting for the distribution of fracturing and stress between these multiple rock bridges (Stead et al., 2006).

Rockfall failure is commonly poorly correlated with environmental conditions and can occur entirely independently of environmental triggers (Lim et al., 2010; Rosser et al., 2007). However, smaller rockfalls (< 0.1 m^3) can be more successfully correlated to, for example, mean air temperature and wind velocity (Lim et al., 2010). These correlations may exist for small rockfalls that display no rock bridges, and as such require no fracturing through intact rock to instigate release. For rockfalls with rock bridges, some form of rock strength weakening is needed for failure to occur at low magnitude environmental stress triggers that are otherwise insufficient to fracture intact rock (Gunzburger et al., 2005). This weakening is likely to be driven by processes such as weathering or stress redistribution as described here (Collins and Stock, 2016; Gunzburger et al., 2005; Viles, 2013a). These processes can create stress fluctuations within the slope that drive the development and coalescence of micro-cracks, eventually reducing the strength of rock to the point of failure(Attewell and Farmer, 1973; Cruden, 1974; Stock et al., 2012).

Our analysis shows that the rockfalls considered here display a wide range of exposure to weathering prior to failure, as represented by the variation in *%w* and *%wrb*. However, not all discontinuity surfaces may be weathered, with the prevalence determined by the connectivity of the discontinuity sets and the intensity and efficacy of environmental conditions acting on and within the slope. The relationship between this exposure and connectivity influences weakening within the slope (Gischig et al., 2011; Viles, 2013). Weathering at the interface between a rock bridge and a discontinuity, known as the crack tip, where stress is concentrated, is an important control on weakening and fracture propagation (Collins and Stock, 2016). The rock bridge perimeter to rock bridge area ratio must to some extent dictate this rate of weakening of rock bridges. For example, two slopes with the same overall rock bridge proportion may weaken at different rates depending on rock bridge size, shape, area and distribution. A slope that contains smaller but more abundant rock bridges may weaken at a faster rate due to high perimeter to area ratio.

As attachment points to the slope, rock bridges represent zones of stress concentration. Recent research has shown a complex relationship between weathering and stress prior to failure, which suggests that stress concentrations may either enhance or dampen the efficiency of weathering events (Brain et al., 2014; Bruthans et al., 2014). Understanding the stress regime that rock bridges experience can determine their temporal and spatial response to weakening (Kemeny, 2003). Micro-cracks may be preferentially oriented with respect to the applied stress (Brain et al., 2014), impacting overall strength. For example, mode 1 cracking will reduce tensile intact rock strength. The models presented by Scavia and Castelli (1996) indicate that fracture propagation is dependent on rock bridge size, with larger rock bridges requiring tensile σ_3 conditions - the minimum principal stress, for fracture to occur. Defining rock bridge proportion and distribution, along with failure mode, is critical for assessing the failure stress regime. The exact nature of feedbacks between weakening, the stress regime and individual failures, and how these interactions drive the propagation of further failure requires detailed

quantification. These interactions affect the timing of rockfall failure, which holds implications for the frequency and magnitude of rockfall activity, a critical input of hazard assessments (Fell et al., 2008) and slope erosion rate calculations (Barlow et al., 2012; Dussauge et al., 2003; Malamud et al., 2004).

Influence on rock mass strength

We observe that while most rock bridges are co-planar to the main failure surface, ~30% are not. These non-planar rock bridges may represent fracturing through intact rock along discontinuity sets, or the partial fracturing of peripheral rock bridges co-planar to the failure surface. Non-planar rock bridges are largely absent from larger rockfalls, suggesting that they are representative of partial fracturing through peripheral rock bridges, or that they have been subsumed into the failed mass and so are not visible within our analysis. This indicates that most rock bridges are located co-planar to the main failure surface, which in this instance is cliff parallel. The prevalence of rock bridges along cliff parallel discontinuities may be related to the conditions of joint formation. These cliff-parallel joints may be formed in response to local scale topographic stress and slope curvature (Gerber and Schiedegger, 1969; Martel, 2017). It is unlikely that these discontinuities represent large scale sheeting joints, like those observed in the granitic rocks of Yosemite valley, due to the lower magnitude of overburden stress and weaker lithologic characteristics of the rocks considered here (Martel, 2017). We however assume that smaller scale topographic stresses may generate smaller scale fracturing comparable in form if not scale.

These localised topographic stresses may result in an intermittent smaller-scale joint propagation. Additionally, as joint density increases within a rock mass, the interactions between the individual joints inhibit each other's expansion (Pollard and Aydin, 1988), by changing the stress intensity factor of the propagating crack tip of a joint (Scavia, 1990). This results in less persistent but higher density jointing with a greater prevalence

of rock bridges, distributed in distinct zones within the slope. In contrast, intersecting joints, which may have been formed by larger regional scale stresses associated with tectonics and uplift, may be more persistent separated by larger rock bridges (Brideau et al., 2009; Tuckey and Stead, 2016). Our analysis reveals that non-planar bridges account for a higher proportion of scar surface area. Therefore, the spatial prevalence and pattern of rock bridges within a slope is related to its rock mass strength characteristics as determined by joint type. The propagation and persistence of joints in turn is influenced by lithology (Pollard and Aydin, 1988). Defining the conditions of joint formation and their resulting characteristics will enhance our understanding of rock mass strength (Moore et al., 2009). Consequently, this has implications for slope evolution, with numerous studies outlining the influence of rock mass strength on differential slope forms (Augustinus, 1992; Moore et al., 2009; Selby, 1982). Understanding the intrinsic properties of rock mass strength, as represented by rock bridges, discontinuities and weathering, will better inform the parameters of larger scale landscape evolution models (Moore et al., 2009).

6. Conclusions

We present the first large scale database of rock bridge and rockfall scar weathering characteristics (0.1 m² to 27 m²). Our analysis reveals:

- Rock bridges account for 31% ±26% of failure scar surface area. The wide range in *%rb* is related to subtle changes in lithology and rock mass structure.
- Failure mode is dependent on the imbalance of mass created by the deviation between the rockfall centre and rock bridge attachment point. This point may be subjected to tensile, shear and torsional stresses, which influences the parameter of strength critical for stability. 3D modelling is required to provide a comprehensive slope stability analysis.

- The number of rock bridges within a scar, and associated failure complexity, increase linearly with rockfall size. The majority of rockfalls are dominated by one main rock bridge, which is critical for maintaining stability. For larger rockfalls to fail, progressive failure and fracturing is likely required through multiple rock bridges. Through time the stress applied to each rock bridge may change as it tends towards being the next in sequence to fail.
- Rock bridges must have been weakened prior to failure, with the rock bridge perimeter to area ratio determining weathering exposure at the discontinuity/rock bridge boundary. Not only is rock bridge proportion a control on stability, but other rock bridge attributes are important to provide a full explanation of the spatial and temporal occurrence of failure.
- Rock bridges provide controls on the mode, spatial pattern, and temporal behaviour of failure, which influences slope stability as a whole.

Acknowledgements

The authors gratefully acknowledge the continued support for this research from ICL Fertilizers (UK) Ltd. We also thank Sam Waugh, Emma Vann Jones, Heather Bell, Simon Varley and Zuzanna Swirad for help with the collection of field data.

Appendix A2: Forensic Rockfall Scar Analysis: Development of a mechanically correct model of rockfall failure (3rd NASL conference proceedings)

de Vilder, S.J., Rosser, N.J., Brain, M.J., and Vann Jones, E.C., 2017. Forensic rockfall scar analysis: development of a mechanically correct model of rockfall failure. In: 3rd North American Symposium on Landslides. 829-839

Forensic rockfall scar analysis: Development of a mechanically correct model of rockfall failure

de Vilder, S.J., s.j.de-vilder@durham.ac.uk, Rosser, N.J., n.j.rosser@durham.ac.uk, Brain, M.J., matthew.brain@durham.ac.uk, Vann Jones (nee Norman), E.C., e.c.vann-jones@durham.ac.uk

Department of Geography, Durham University, Durham, DH1 3LE, United Kingdom

ABSTRACT: The mechanical controls on small (< 10 m³), individual rockfall in jointed rock masses are not well constrained. We use forensic analysis of rockfall detachment surfaces (scars) which display fractured surfaces broken through intact rock, termed rock bridges as well as pre-existing discontinuities, to understand failure mechanisms. The relative significance of intact rock fracture versus release along pre-existing surfaces in stability has not been thoroughly investigated using field data. The relative role of each of these components determines where weakening, is important in controlling the nature and timing of rockfall. This is vital for defining mechanically accurate models of failure.

An initial inventory of rockfall scars from coastal rock cliffs was captured using high-resolution gigapixel imaging and terrestrial laser scanning to determine these relationships. Fracture mapping, planar surface identification, and weathering classification were undertaken to identify similarities in the mechanical controls on failure. Preliminary analysis reveals that even small rockfall display a multi-stage failure history, whereby final failure occurs through fracture of a single unweathered rock-bridge. Intact rock breakage accounts for 22 ±12% of the full scar surface. The rock bridges are commonly clustered at the scar crest or base, while planar pre-existing joint surfaces dominate the scar center. This suggests that although cantilevered, most rockfalls in this inventory are more likely to fail through tension. We consider volumetric and lithologic controls on failure mode, and consider the wider potential of this approach.

INTRODUCTION

Rockfall scars contain valuable information that describes the controls on failure mode. Scars are commonly characterized by a combination of discontinuity surfaces of varying persistence and zones of relatively fresh fracturing through previously intact rock, with both being subjected to varying degrees of weathering (Fig. 1). These zones of fractured intact rock are referred to as rock bridges throughout this paper. Previous research has shown that failure occurs through progressive fracturing of intact rock bridges, in a process termed step-path failure (Jennings, 1970; Scavia, 1995; Eberhardt et al., 2004; Kemeny, 2005; Brideau et al., 2009). A wide variety of research has been conducted to understand the kinematics, rock mass characteristics and driving forces of failure, yet few studies have tried to link this understanding to evidence recorded in the remaining rockfall scar, and in

particular the role of intact rock fracture that may be suitable for verifying slope stability model assumptions. Rock bridges contribute substantially to the stability of a slope (Scavia, 1990; Frayssines & Hantz, 2009; Paronuzzi & Sera, 2009; Paronuzzi et al., 2016), with various modelling studies highlighting that scars that display 0.1% of breakage through rock across the failure surface greatly increases the overall factor of safety (Jennings, 1970; Frayssines & Hantz, 2009; Elmo et al., 2011). Therefore, the prevalence of rock bridges within failure surfaces must be an important control on stability. Conceptually, the location and distribution of rock bridges within a scar is suggested to control failure mode (Stock et al., 2011; Tuckey & Stead, 2016). As these zones are critical for stability, rock bridge weakening driven by weathering or stress changes due to progressive failure, can be a temporal constraint on failure (Eberhardt et al., 2004; Gischig et al., 2011; Viles, 2013). It is vital to properly understand the presence, characteristics and role of these zones in order to construct mechanically correct models of rockfalls.

Few studies have mapped rockfall scars to examine their characteristics in detail, and these studies have been limited to single event cases –notably studies of large scale rockfalls (10 m^3 to 10,000 m^3) (Paronuzzi & Sera, 2009; Lévy et al., 2010; Stock et al., 2011; Stock et al., 2012; Paronuzzi et al., 2016) or small inventories of similar scale rockfalls (Frayssines & Hantz, 2006). These studies display percentage estimates of rock bridge area within the total failure surface, which range from 0.2% to 30% and contain qualitative information regarding the other scar characteristics. Discontinuity persistence has also been used to predict the presence of rock bridges within jointed rock masses and provides percentage estimates of length of intact rock along a particular discontinuity set (Sturzenegger & Stead, 2012; Grøneng et al., 2009; Matasci et al., 2015; Tuckey & Stead, 2016; Karami et al., 2007).

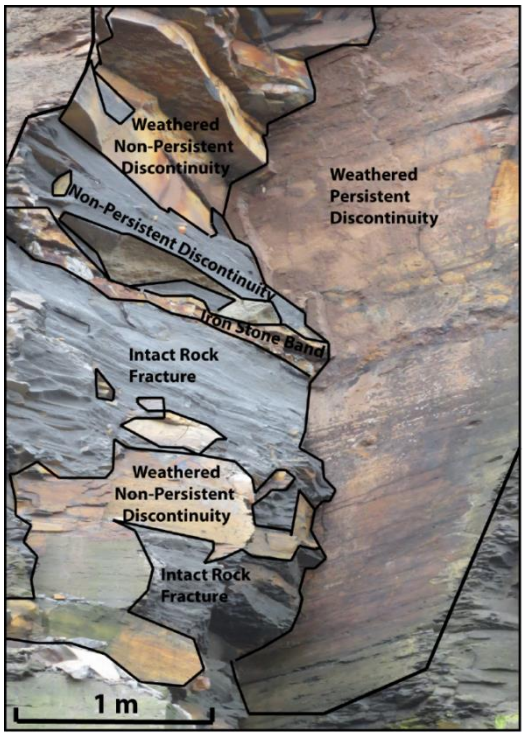

Figure 1. Photograph of a recent rockfall scar from the Staithes coastline. This shale scar displays weathered discontinuities of varying persistence, unweathered discontinuity surfaces, and fresh breakage of intact rock.

These estimates display rock bridge proportions of 1 % to 5 %. Modelling studies using discrete fracture networks (DFN's) have shown via back analysis that rock bridges often account for 3 % to 45 % of a final failure surface (Elmo et al., 2007; Karami et al., 2007; Moffit et al., 2007; Elmo et al., 2011; Gischig et al,. 2011a), with the higher percentage in fracturing due to some discontinuity sets having a much higher proportion of intact rock along their length than other discontinuity sets.

However, most of these studies provide little or only qualitative information on the exact details of rock bridges, discontinuity surfaces or weathering within rockfall scars, and their relative significance. This includes their location within the scar, and

their size and distribution. The variation in weathering has not been quantified or linked to factors including joint continuity or intact rock strength degradation. As Stock et al. (2011) and Bonilla-Sierra et al. (2015) infer, the location of a rock bridge is important for understanding if rockfall fails in tension or shear, as they can form a pivot point about which the failing rock block is able to potentially rotate and fail in tension (Fig. 2). Therefore, not only does the proportion of intact rock fracture and discontinuity surfaces need to be defined, their characteristics are also important controls on failure.

This paper presents the results of forensic analysis using an inventory of rockfall scars observed using high resolution 3D scanning and imaging along the coastal cliffs of Staithes, North Yorkshire, UK. This database is examined to consider how the characteristics of weathering, rock bridges and planar joint surfaces can be used to infer controls on rockfall failure.

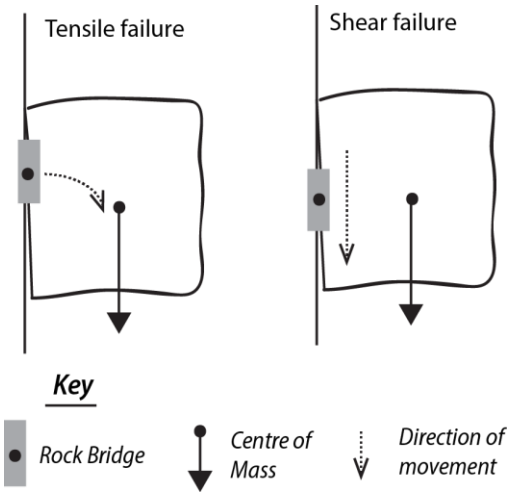

Figure 2: Rock bridge location may determine failure mode via influencing the balance of mass within an incipient rockfall failure. Tensile failure may occur when the rock bridge location deviates from the center of mass, creating a mass imbalance and the potential for rotation. Conversely, shear failure occurs when the rock bridge and rockfall center of mass are balanced.

STUDY SITE

Rockfall scars were recorded from a 200 m long section of coastal cliffs located between Staithes and Boulby, as shown in Figure 3. The cliffs are near vertical and up to 60 m in height, with a wide shore platform which extends >300 m seawards at low tides. This is a storm-dominated coastline, which experiences a semi-diurnal tide of c. 6 m. The cliffs are comprised of a lower and upper shale unit, and an interbedded siltstones and sandstones unit, which form part of the Lower Jurassic Redcar Mudstone and Staithes Sandstone formations, and are all capped by a layer of glacial till (Rawson and Wright, 2000). All these layers display a bedding dip of 2° to the south east, and a complex discontinuity pattern which varies in persistence between the different rock type exposures. The lower shale unit is characterized by widely spaced persistent joints, and has a surface covering of algae as it sits within the tidal range zone. In contrast the upper shale unit displays a less persistent joint pattern, and in places the rock mass appears to be massively jointed. The interbedded siltstone and sandstones comprise beds of up to 3 m in thickness, which displays a blocky weathered discontinuity pattern with dilated joints. Norman (2012) showed that of the rockfalls recorded along this section of cliff over a 2 year period, 60 % of net eroded volume was related to rockfalls between 0.1 m^3 and 10 m^3, accounting for >20 % of rockfalls recorded. Rockfalls of this size are important for coastal erosion and retreat.

Previous research along this coast has also shown that rockfalls occur across the whole cliff face, not just within the wave inundation zone, with higher numbers of failures concentrated in certain lithological layers (such as the interbedded siltstones

& sandstones) as well as at the boundaries between layers (Lim et al., 2010; Rosser et al., 2013). The different lithological units in part control rockfall geometry, which indicates that the rock mass structure and jointing patterns of the cliff face determine failure volume and shape (Lim et al., 2010). However, pure kinematic failure – without any fracturing through rock bridges, is not a dominant failure mechanism along these cliffs, with many rockfall scars, such as seen in Figure 1, displaying rock bridges in combination with discontinuity release surfaces (Rosser et al., 2013).

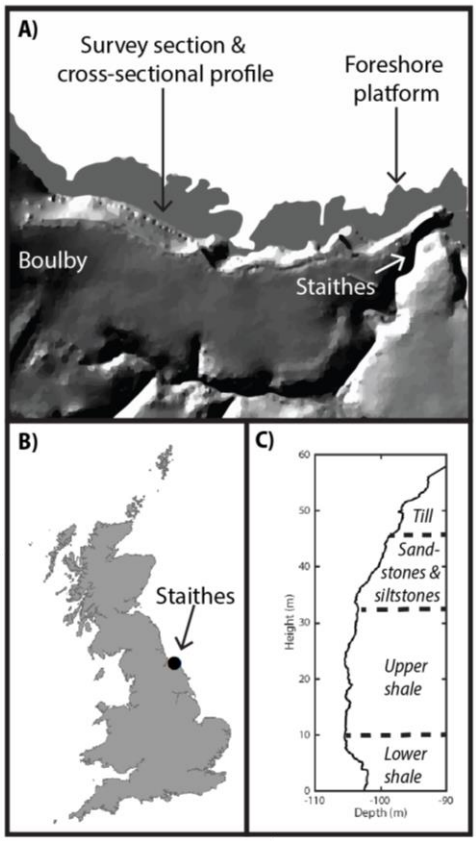

Figure 3. A) Location of the 100 m survey section between Boulby and Staithes. B) Location of Staithes along the North Yorkshire coast, UK. C) Cross-section profile displaying the different lithological layers present within the survey section.

METHODS

Data Collection

3D point clouds were captured monthly using a Reigl VZ – 1000 terrestrial laser scanner (TLS). The scans were collected from one scan positon located at a distance of 100 m from the cliff toe, and the resulting point clouds covered a 200 m long section of cliff, with a 0.01 m to 0.02 m point spacing. Change detection was undertaken on the sequential scans using the methodologies outlined in Rosser et al. (2005), and provided the locations of rockfalls and their characteristics within the scan area.

To provide textural and color information of the rockfall scar surfaces, Gigapixel photographic imagery was collected. A Gigapan Epic Pro was used in conjunction with a 50MP Canon EOS 5DS R and a 300 mm telephoto lens to capture multiple images of the cliff face (c. 150 individual photographs). Associated Gigapan Stitch software was used to sequence and stitch the photos into one resulting gigapixel panoramic image, with an average file size of 4 GB. The photographs were collected from the same position as the TLS, with each individual photograph achieving an on cliff pixel resolution of 1 mm to 2 mm. Aperture, shutter speed and ISO were manually adjusted to allow for sharp high-quality images to be captured.

The panoramic pictures were geo-referenced onto the DEM model of the cliff face derived from the 3D point clouds, using a spline transformation in ArcMap 10.2. This required the manual selection of >200 control points to allow the 2D image to be stretched into place over the 3D DEM. From this, the resulting rockfall scars were ‘clipped’ from the panoramic photograph using the rockfall locations determined from change detection (Fig. 4). Obtaining both high-resolution point clouds and imagery allows the fine scale detail of the shape of the rockfall scars themselves (in terms of point cloud change detection) and the texture of fracturing (on scales greater than

2 mm) within the rockfall scar as well as subtle color differentiation.

Rockfall Scar Mapping

Fifteen rockfall scars were chosen to form the preliminary database considered here. These rockfalls were chosen to cover a range of volumes (from 0.02 m^3 to 27 m^3) and the three dominant exposed lithologies (lower shale, upper shale, and interbedded siltstones & sandstones) present within this section of cliff (Fig. 3). The features of the rockfall scars were mapped and separated into three categories; fractures/edges, planar surfaces, and weathered surfaces. Edges are representative of fracturing through intact rock and as such form a component part of a broken rock bridge. Mapping allows qualitatively determined zones of high - concentrations of edges to be defined. These high concentrations are representative of broken rock bridges (Fig. 5a.). Rock bridge proportion is calculated as a percentage of the total scar surface area, and herein referred to as *% rb*. A planar surface was considered indicative of pre-existing (pre-failure) joints and bedding faces, with a 'smooth' texture and limited fracturing evident.

Each individual planar surface within a rockfall scar was mapped, with the number of planar surfaces per scar, their total area and location within the rockfall scar noted (Fig. 5b.). Their orientation and resulting geometry (i.e. wedge or planar shaped) was also recorded. Weathering classification was based on color differential relative to the overall cliff face, with the total area of weathered surfaces, and their location recorded within the scar (Fig. 5c.). Both planar surface (*% ps*) and weathered proportions (*% w*) were also calculated as percentages of total failure surface.Table 1 presents the information recorded from each of the rockfall scars. From this information for each rockfall scar, an interpretation of failure sequence and associated controls was constructed, as displayed in Figure 5d. This example rockfall scar will be used to illustrate how an interpretation was undertaken. This failure scar is comprised of multiple rock bridges and discontinuity surfaces which display a varying degree of weathering and have subsequently been separated into three stages of failure. The weathered planar surface (Fig. 5d - 1.) forms the majority of the rockfall scar with a planar surface on the periphery. Fracturing has occurred through two rock bridges located at the base and top of scar (Fig. 5d - 2.). As these two zones are weathered, it is hypothesized that this fracturing occurred before final failure. Final failure occurred after fracturing through an unweathered rock bridge (Fig. 5d - 3.) located at the top of the scar. The time between failure of the first and last rock bridge is unknown but must have been substantial enough to allow for significant weathering of the fractured surface.

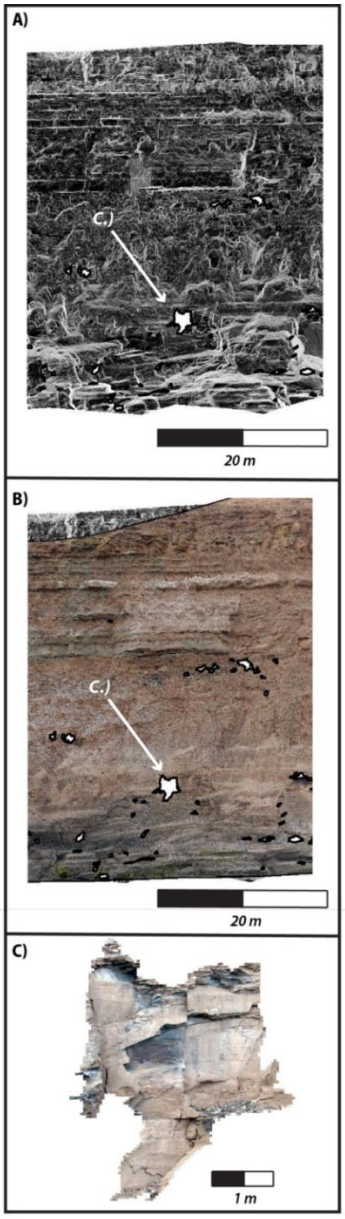

Figure 4. A) DEM of the scan area, display rockfalls greater than > 0.1 m². B) DEM with gigapixel panoramic image stretched onto it. C) The rockfall 'clipped' out of the gigapixel image using the DEM derived rockfall locations and geometries.

.

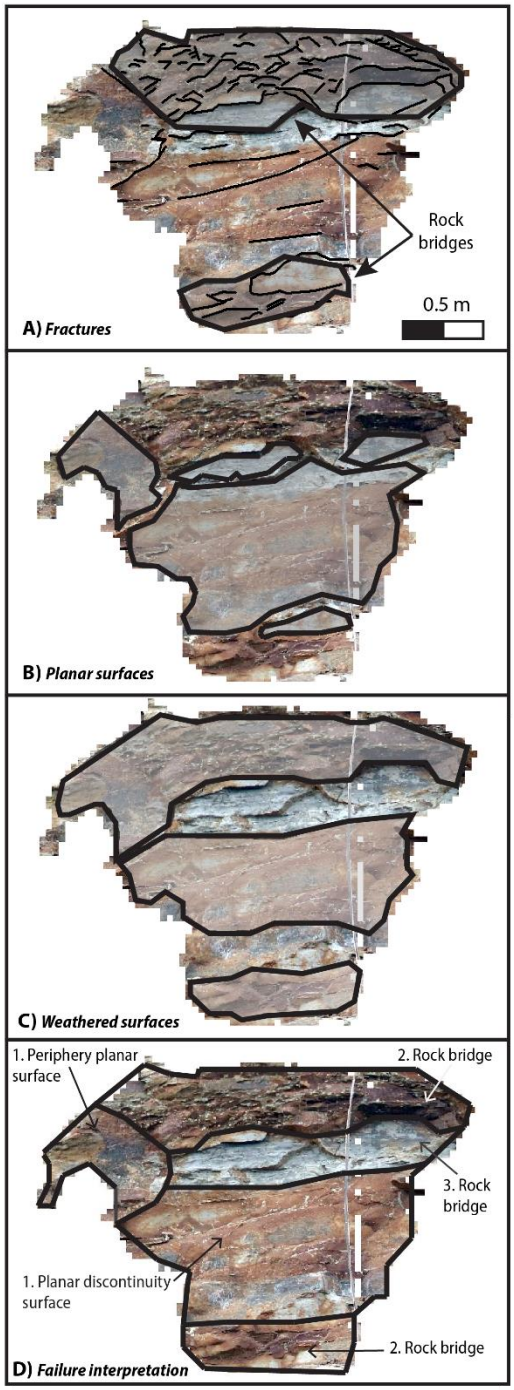

Figure 5. A) Mapped edges with fracture zones B) Mapped planar surfaces, C) Mapped weathered surfaces and D) Interpretation of failure mechanisms in rockfall scar, with the numbers (1 to 3) representing the stages of failure.

DATABASE ANALYSIS

Proportion of rock bridges & discontinuity faces

The proportion of rock bridges (*% rb*), planar surfaces (*% ps*) and weathering (*% w*) was calculated from the database (Table 2). Rock bridges account for approximately 20% of failure surface area, but can range from 7% up to nearly half of the failure surface. Planar discontinuity surfaces found within the rockfall scar account for 50% of failure area on average, and also display a wide range from 30% to 75% of failure surface. Weathered surfaces account for 40% of rockfall scar area, and show the largest range, with weathering occurring both along discontinuity faces as well as previously failed rock bridges. This can be determined from comparing the location of weathering with those of rock bridges and planar surfaces in Table 1, as well as from the interpretation of failure sequence (see: Fig. 5d). The *% rb* values are higher than previously observed in rockfall scars, with a previous range of 0.2% to 26%, with a mean of 4% and standard deviation of 7% (Frayssines & Hantz, 2006; Paronuzzi & Sera, 2009; Lévy et al,. 2010; Stock et al., 2011; Paronuzzi et al., 2016). This may be due to differences in mapping rock bridge areas, with previous studies characterization on color and texture with unweathered surfaces defined as rock bridges. As shown in Figure 5d, rock bridges can be broken through, and weathered, before final failure of the rockfall. As a result, it may be that the *% rb* within a slope has been underestimated. This dataset ($n = 15$) along with previously published studies ($n = 17$) represent a wide range of lithologic and rock mass strength settings generating rockfalls that display 6 orders of magnitude difference in volume (from 0.02 m³ to 10,000 m³). This variation may result in different rockfall scar characteristics.

Rock bridge characteristics

The number of planar surfaces and rock bridges increase with increasing rockfall scar surface area (see Fig. 6a). This linear relationship indicates that for approximately 1 m² area of a failure surface there is at least 1 rock bridge, with an average area of c. 0.2 m². Analysis of individual rock bridge area confirms this relationship (Fig. 6b) This empirical estimate could be extrapolated to the whole slope, and this number used to feed into discrete fracture network (DFN) models of slope stability (Moffit et al., 2007; Elmo et al., 2011; Tuckey and Stead, 2016). However, no information is provided on the location of these rock bridges with respect to discontinuity surfaces, or failure scar geometry. The percentage of rock bridges along a particular discontinuity set can control failure evolution, especially if the orientation of that set is critical for global stability of the slope (Elmo et al., 2011; Gischig et al., 2011a; Stead & Wolter, 2015; Tuckey & Stead, 2016).

An increase in the number of rock bridges also means that for failure to occur, for larger rockfalls fracturing through multiple intact rock bridges is required. Figure 7 illustrates this increasing complexity of failure history for rockfall of increasing size. Nearly all of the rockfalls, irrespective of volume, displayed a multi-stage failure history (Table 1). As the example rockfall scar in Figure 5 shows, the temporal evolution of these scars is complex as the rockfall appears to have stabilized between the first fracture through a rock bridge and the final rock bridge failure, long enough for surface weathering to occur. Further investigation of failure sequence may provide useful information on the role of damage accumulation through time within a rockslope.

Table 1: Rockfall scar database of 15 rockfall scars containing information relating to rock bridges, planar joint surfaces and weathering.

ID	Date	Area (m^2)	Vol (m^3)	Lithology	Rock bridge proportion (*% rb*)	No. of rock bridge zones	Rock bridge location*	Planar surface proportion (*% ps*)	No. of planar surfaces	Planar surface location*	Weathered Proportion (*% w*)	Weathered Location*	Shape
1***	Mar-16	0.11	0.02	Lower Shale	18	1	T (LS)	64	1	T, M, B	0	NA	Planar
2	Mar-16	0.11	0.03	Upper Shale	36	2	T, B	57	4	M	38	M	Wedge
3	Mar-16	0.15	0.02	Siltstone	7	1	M	76	5	T, M, B	80	T, M, B	Wedge
4	Mar-16	0.15	0.03	Lower Shale	13	1	T,M (LS&RS), B	53	4	M	39	B (LS)	Planar
5	Mar-16	0.43	0.11	Lower Shale	21	1	M (LS)	58	5	M (RS)	30	M (LS)	Arch
6	Mar-16	0.45	0.07	Siltstone	7	2	NA	67	1	T, M, B	56	T, B	Planar
7**	Mar-16	0.88	0.52	Lower Shale	14	2	M	48	4	T, M (LS & RS), B	20	T, M (LS & RS), B	Wedge
8	Aug-15	1.01	0.2	Lower Shale	13	2	T, B	73	3	T, M, B	85	T, M, B	Planar
9	Jan-16	1.81	0.35	Siltstone	43	3	T, B	29	5	T, M	66	T, M, B	Planar
10	Oct-15	2.56	1.24	Lower Shale	8	3	M	55	3	M, B	6	T, B	Wedge
11***	Aug-15	3.34	1.07	Siltstone	.42	2	T, B	51	5	M	65	T, M, B	Planar
12	Nov-15	4.09	2.12	Upper Shale	39	3	M (LS), B (LS)	47	1	M (RS)	19	M	Planar
13	Aug-15	4.8	2.01	Upper Shale	35	2	T, B	44	9	M	13	T	Planar
14***	Aug-15	6.37	3.04	Lower Shale	18	9	T, M	44	14	M (LS)	4	T, M (LS)	Arch
15	Jan-16	26.9	27	Siltstone	19	30	T, B	32	32	M & B	45	T, B	Planar

* Location abbreviations: T = top, M= middle, B = base, LS = left side, RS = right side.

** Rockfall displayed in Figure 4*** Rockfalls displayed in Figure 6.

Table 2: Descriptive statistics of the proportion of each element within a rockfall scar.

	Mean	Standard Deviation	Min	Max
Rock bridge proportion (*% rb*)	22.15	12.76	6.67	43.09
Planar surface proportion (*% ps*)	53.09	13.06	28.95	76
Weathered proportion (*% w*)	37.77	26.93	0	85.15

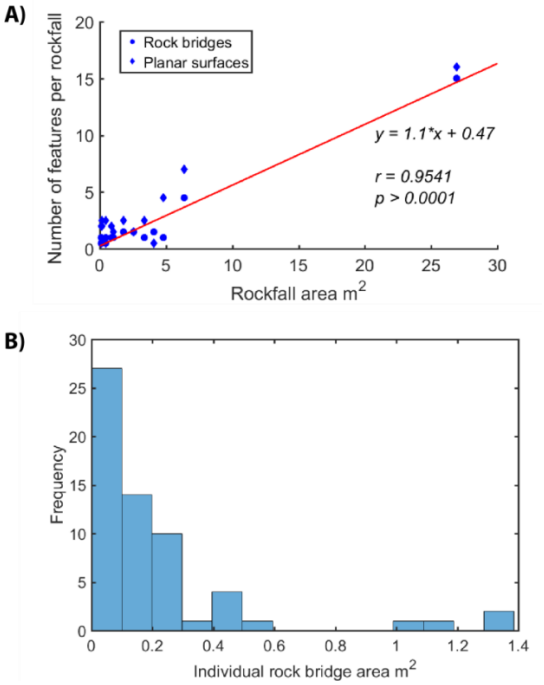

Figure 6. A) Scatter plot showing as rockfall size increases the number of rock bridges and planar surfaces (i.e. joint faces) also increases. B) Histogram of individual rock bridge area, with most rock bridges ≤ 0.3 m².

Rock bridge location

Analysis of fracture zone locations reveals that rock bridges are mainly located at either the top or base of rockfall scars. The few cases in which rock bridges are located in the middle of the scar are associated with wedge shaped failures (Table 1), whereby rock bridges are located at the intersection of the discontinuities forming the wedge. The reverse pattern is observed for planar surfaces, with most flat scar surfaces located in the middle of the footprint.

Therefore, rockfalls from these cliffs are suspended or 'hang' from the rock slope prior to failure. This has implications for failure mode as Stock et al. (2011) inferred in their case-study of rockfalls in Yosemite, USA.

Modelling has shown that greater tensile cracking is associated with rock bridges located at the top of failure surface, while shear cracking is associated with rock bridges located in the center or lower parts of the failure surface (Bonilla-Sierra et al., 2015). The amount and distribution of tensile or shear cracking is dependent on the center of gravity of a failing mass, the depth of the failure surface, and the moment generated prior to release. In this case, tensile-associated flexural or rotational failures are likely to be the dominant mode of failure, unless a wedge shape failure mode is predominant (Paronuzzi & Sera, 2009; Paronuzzi et al., 2016).

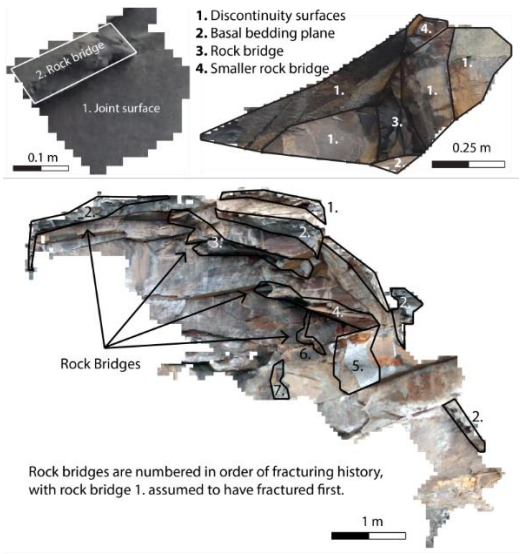

Figure 7: Three rockfall scars and their interpretations are presented. With increasing area, the number of rock bridges and discontinuity surfaces increases, as does the stages required for failure.

Need for a larger database

All of these observations and their implications are based on a dataset of *n = 15*, and combining with previously published data this in total consists of 32 rockfalls for which rockfall scar analysis has been undertaken. As stated earlier, these 32 rockfalls consist of a wide variation in rock mass structure, lithology (i.e. granite, limestone, siltstone, and shale), and volume (0.02 m³ to 10,000 m³). To determine the appropriate sample size for this database of rockfalls recorded along the North Yorkshire coastline, the sample needed for accurate representation of rockfall area and volume, plus rock bridge area, planar surface area and weathered surface area within the rockfall scar were determined. These attributes were chosen as they are the key variables from which *% rb*, *% ps*, and *% w* are calculated, and therefore will affect the statistical distribution and significance of these values. For example, a margin of error of 0.25 m² (as defined in Table 3) for the mean rock bridge area of 0.81 m (using the mean rockfall area), will generate a variance in *% rb* from 16 % to 30 % ,with a range just greater than that of the expected standard deviation from mean *% rb* (Table 2). The use of the same margin of error for planar and weathered surfaces generated similar results. Table 3 outlines that a sample size of greater than 100 rockfall scars is needed for 90 % degree of confidence in results, while to achieve a 99 % degree of confidence in the mean value of the population 200 to a 1000 rockfall scars are required using the given margin of errors. As such, the relationships and values determined earlier in this paper have to be treated with caution.

This small sample size does not allow the whole population of rockfall scars to be accurately characterized, nor does it allow for the role of lithology, area or slope geometry to be determined. Determination of these sample sizes (Table 3) does not also take into account that the cliffs are composed of three lithologies and their associated structure. Thus, to ascertain if there are statistically significant differences between the different rock masses a much larger database is need. On the whole, to obtain statistically significant values of the characteristics of rock bridges for empirical inputs into slope stability models, analysis of a larger database of rockfall scars is required. More information is needed about rockfall geometry, failure depth and slope angle to allow for the classification of failure mode and controls on rockfall failure to be established.

Table 3. Sample size determination of rockfall area and scar characteristics.

	Area (m²)	Rock bridge area (m²)	Planar Surface area (m²)	Weathered surface area (m²)
Margin of error	*1*	*0.25*	*0.25*	*0.25*
90% (z0.05)	115.24	70.33	187.23	385.65
95% (z0.025)	163.60	99.84	265.80	547.49
99% (z0.005)	282.59	172.47	459.12	945.71

FUTURE WORK

The creation of larger more comprehensive rockfall scar database (> 300 rockfall scars) requires a different methodological approach. The mapping by hand of a such a large number of rockfall scars is time-consuming and inefficient, plus allows for qualitative judgement calls on what constitutes a rock bridge, and weathered surface. A semi-automatic classification approach of forensic scar analysis of both rock bridges (and thus discontinuity faces) and weathered surfaces are needed. The next

stage of this project will be the development of these methods and analysis of the subsequent rockfall scar database. It is proposed that for mapping of fractures and texture of the rockfall scar surface, edge detection based on the classification of pixel value range will be used (based upon Li et al., 2008). In this method, edges are determined as areas where there is a significant contrast in pixel values across a specified distance. From the 'edge' maps, zones of higher density will be classified as rock bridges. Automatic weathering classification will be based on pre-defined color pixel values and ranges, which is then applied to the whole dataset, in order to ensure consistency. In addition to these two methods, information on rockfall geometry and associated center of gravity, along with failure slope angle will be used to assess and test models of the dominant failure mode for these rockfalls. Information about failure surface orientation with respect to rock bridge location will ascertain which discontinuity sets and associated rock bridges are critical for slope stability. This database will enable statistically significant relationships concerning rock bridge and weathering proportion within failure to be determined, as well as the contributions of both to failure mode and stresses acting on the slope. It will provide increased information about controls on rockfall evolution and failure.

CONCLUSIONS

This paper presents an initial database of 15 rockfall scars observed and analyzed along the coastal cliffs of North Yorkshire. Mapping of the scars has allowed the proportion and characteristics of rock bridges, discontinuities and weathering to be determined. Analysis of this information has revealed:

Rock bridges account for approximately 22 % ±12% of rockfall scar area, and weathered surfaces account for 40 % ±26 %

The number of rock bridges and discontinuity faces (i.e. joints or bedding) increases linearly with increasing rockfall area, and hence volume. This implies that on average, for every 1 m² of rockfall failure area there is 1 rock bridge.

Nearly all rockfall display multi-stage failure histories, whereby prior to final failure several stages of fracturing can occur through intact rock bridges. The scale of complexity of rockfall scar surfaces increases with rockfall volume.

Rock bridges are predominately located at the top and/or base of the scar, with this location possibly an important control on mode of failure, and the associated strength parameter critical for stability.

The analysis of the samples in this study (and all other previous rockfall scar case-studies) is small, yet covers a wide range of variables such as rockfall volume, lithology and rock mass characteristics. In addition, the relationships derived are largely qualitative. Statistical analysis has shown that to have a greater degree of confidence (> 99%) in the results and relationships determined from them, a database of greater than 300 rockfall scars is needed.

Acknowledgements

Ongoing support for this research is provided by ICL Fertilizers (UK) Ltd.

REFERENCES

Bonilla-Sierra, V., Scholtès, L., Victor, F., and Elmouttie, M., 2015, DEM analysis of rock bridges and the contribution to rock slope stability in the case of translational sliding failures: International Journal Rock Mechanics Mining Sciences, Vol. 80, pp.67–78.

Brideau, M., Yan, M., and Stead, D., 2009, The role of tectonic damage and brittle rock fracture in the development of large rock slope failures:

Geomorphology, Vol. 103, pp.30–49.

Eberhardt, E., Stead, D., and Coggan, J.S., 2004, Numerical analysis of initiation and progressive failure in natural rock slopes-The 1991 Randa rockslide: International Journal Rock Mechanics Mining Sciences, Vol. 41, pp.69–87.

Elmo, D., Clayton, C., Rogers, S., Beddoes, R., and Greer, S., 2011, Numerical Simulations of Potential Rock Bridge Failure within a Naturally Fractured Rock Mass. In: Eberhardt, E. and Stead, D. (Editors), Slope Stability 2011: International symposium on rock slope stability in open pit mining and civil engineering, Vancouver, Canada, pp 1–13.

Elmo, D., Yan, M., Stead, D., and Rogers, S.F., 2007, The importance of intact rock bridges in the stability of high rock slopes - towards a quantitative investigation using an integrated numerical modelling; discrete fracture network approach. In: Potvin, Y. (Editor), Slope Stability 2007 : Proceedings of the 2007 International symposium on rock slope stability in open pit mining and civil engineering, Perth, Australia, pp 253–266.

Frayssines, M., and Hantz, D., 2006, Failure mechanisms and triggering factors in calcareous cliffs of the Subalpine Ranges (French Alps): Engineering Geology, Vol. 86, pp. 256–270.

Frayssines, M., and Hantz, D., 2009, Modelling and back-analysing failures in steep limestone cliffs: International Journal Rock Mechanics Mining Sciences, Vol. 46, pp. 1115–1123.

Gischig, V., Amann, F., Moore, J.R., Loew, S., Eisenbeiss, H., and Stempfhuber, W., 2011a, Composite rock slope kinematics at the current Randa instability, Switzerland, based on remote sensing and numerical modeling: Engineering Geology, Vol. 118, pp. 37–53.

Gischig, V., Moore, J.R., Evans, K., Amann, F., and Loew, S. 2011b, Thermomechanical forcing of deep rock slope deformation : 1. Conceptual study of a simplified slope: Journal Geophysical Research, Vol. 116, No.F04010, pp. 1-18.

Grøneng, G., Nilsen, B., and Sandven, R., 2009, Shear strength estimation forAknes sliding area in western Norway: International Journal Rock Mechanics Mining Sciences, Vol. 46, pp. 479–488.

Jennings,J.E., 1970, A mathematical theory for the calculation of the stability of open cast mines. In: Van Rensburg, P. (Editor), Planning open pit mines: Proceedings of the Symposium on the Theoritical background to the planning of open pit mines with special reference to slope stability, Johannesburg, South Africa, pp 87–102.

Karami, A., Greer, S., and Beddoes, R., 2007, Numerical assessment of step-path failure of northwest wall of A154 Pit, Diavik Diamond Mines. In: Potvin, Y. (Editor), Slope Stability 2007 : Proceedings of the 2007 International symposium on rock slope stability in open pit mining and civil engineering, Perth, Australia, pp 293–305

Kemeny, J., 2005, Time-dependent drift degradation due to the progressive failure of rock bridges along discontinuities: International Journal of Rock Mechanics and Mining Sciences: Vol.42, pp.35–46.

Lévy. C., Baillet, L., Jongmans, D., Mourot, P., and Hantz, D., 2010, Dynamic response of the Chamousset rock column (Western Alps, France): Journal Geophysical Research, Vol. 115, No.F04043, pp.1–13.

Li, Y., Onasch, C.M., and Guo, Y., 2008, GIS-based detection of grain boundaries: Journal Structural Geology, Vol. 30, pp.431–443.

Lim, M., Rosser, N.J., Allison, R.J., and Petley, D.N., 2010, Erosional processes in the hard rock coastal cliffs at Staithes, North Yorkshire: Geomorphology, Vol. 114, pp.12–21.

Matasci, B., Jaboyedoff, M., Loye, A., Pedrazzini, A., Derron, M.H., and Pedrozzi, G., 2015, Impacts of fracturing patterns on the rockfall susceptibility and erosion rate of stratified limestone: Geomorphology, Vol. 241, pp.83–97.

Moffit, K., Rogers, S., and Beddoes, R., 2007, Analysis of slope stability in strong, fractured rock at the Diavik Diamond Mine, NWT. In: Eberhardt, E. Stead, D. and Morrison, T. (Editors), Rock Mechanics: Meeting Society's challenges and Demands, Proceedings of the 1st Canada-US Rock Mechanics Symposium, Vancouver, Canada, pp 1245–1250

Norman, E.C., 2012, Microseismic monitoring of the controls on coastal rock cliff erosion. Unpublished Ph.D. Thesis, Department of Geography, Durham, Durham University, U.K., 259 p.

Paronuzzi, P., and Sera, W., 2009, Stress state analysis of a collapsed overhanging rock slab : A

case study: Engineering Geology, Vol. 108, pp.65–75.

Paronuzzi, P., Bolla, A., and Rigo, E., 2016, 3D Stress – Strain Analysis of a Failed Limestone Wedge Influenced by an Intact Rock Bridge: Rock Mechanics Rock Engineering, Vol. 49, pp.3223–3242.

Rawson, P.F., and Wright, J.K., 2000, The Yorkshire Coast - 3rd edition: Geologists'Association, London, U.K., 130 p.

Rosser, N.J., Brain, M.J., Petley, D.N., Lim, M., and Norman, E.C., 2013, Coastline retreat via progressive failure of rocky coastal cliffs: Geology, Vol. 41, pp. 939–942.

Rosser, N.J., Petley, D.N., Lim, M., Dunning, S.A., and Allison, R.J., 2005, Terrestrial laser scanning for monitoring the process of hard rock coastal cliff erosion: Quarterly Journal Engineering Geology Hydrogeology, Vol. 38, pp. 363–375.

Scavia, C., 1990, Fracture mechanics approach to stability analysis of rock slopes: Engineering Fracture Mechanics, Vol. 35, pp. 899–910.

Scavia, C., 1995, A method for the study of crack propagation in rock structures: Geotechnique, Vol. 45, pp.447–463.

Stead, D., and Wolter, A., 2015, A critical review of rock slope failure mechanisms : The importance of structural geology: Journal Structural Geology, Vol. 74, pp.1–23.

Stock, G.M., Bawden, G.W., Green, J.K., Hanson, E., Downing, G., Collins, B.D., Bond, S., and Leslar, M., 2011, High-resolution three-dimensional imaging and analysis of rock falls in Yosemite Valley, California: Geosphere, Vol. 7, pp.573–581.

Stock, G.M., Martel, S.J., Collins, B.D., and Harp, E.L., 2012, Progressive failure of sheeted rock slopes: the 2009-2010 Rhombus Wall rock falls in Yosemite Valley, California, USA: Earth Surface Processes and Landforms, Vol. 37, pp. 546–561.

Sturzenegger, M., and Stead, D., 2012, The Palliser Rockslide, Canadian Rocky Mountains : Characterization and modeling of a stepped failure surface: Geomorphology, Vol. 138, pp.145–161.

Tuckey, Z., and Stead, D., 2016, Improvements to fi eld and remote sensing methods for mapping discontinuity persistence and intact rock bridges in rock slopes: Engineering Geology, Vol. 208, pp. 136–153.

Viles, H.A., 2013, Linking weathering and rock slope instability: non-linear perspectives: Earth Surface Processes Landforms, Vol. 38, pp. 62–70.

9 Appendix B: Weathering Experiment Datasets

Appendix B1: Monitoring descriptions for test WD1 . Blank spaces in the table indicate that no surficial changes were recorded in that week's monitoring. The final description presents a complete description of the cores for comparison with the initial descriptions.

Week	Initial	1	2	3	4	5	6	7	8	9	10	11	12	13	Final
Load 1 (11C)	Light grey brown. No visible cracks.		Medium grey brown. Small grains at base of container.					Minor iron leaching appears.	Increase in iron leaching.						Medium grey brown. No visible cracks, though grain-size cavities are present throughout core .
Control 1 (11A)	Light grey brown. No visible cracks.		Medium grey brown. Small grains at base of container.												Medium grey brown, with some minor orange mottling (due to individual grains). No visible cracks, though grain-size cavities are present throughout core.
Load 2 (15A)	Light grey brown. Large vertical (30mm long) crack on side, with large cavity at base (10mm x 20mm).		Medium grey brown. Small grains at base of container. No change in large crack.				Some iron leaching around base of container.		Appearance of small (3 - 5 mm) sub-horizontal crack at base of core.						Light grey brown. Large vertical crack (50 mm long, 20 mm wide), with large cavity at base (30 mm x 20 mm). Grain sized cavities throughout core.
Control 2 (12A)	Light grey brown. Cracking and cavity on side of core (20mm x 20mm)		Dark grey brown. Small grains at base of container. No change in large crack.												Brown with very minor orange tinge. Large crack and cavity on side (20 mm x 20mm). No visible cracks through grain sized cavities are present throughout core.
Load 3 (18A)	Light grey brown. No visible cracks.		Light grey brown. Small grains at base of container. Minor iron leaching.	Increase in iron leaching	Significant increase in iron leaching		Increase in iron leaching - base of sample is stained dark orange.								Light grey brown, with gradational orange staining at the base of core. No visible cracks through grain sized cavities are present throughout core.
Control 3 (18B)	Light grey brown. No visible cracks.		Light grey brown. Small grains at base of container.						Reddish brown appearance of top half of core.						Medium grey brown. No visible cracks, two large grain size cavities on top of core.
Load 4 (15B)	Light grey brown. No visible cracks.		Dark grey brown. Small grains at base of container. Minor iron leaching.	Increase in iron leaching											Medium grey brown, stained orange at base. No visible cracks through grain sized cavities are present throughout core.
Control 4 (4C)	Light grey brown, with orange mottling. No visible cracks		Dark grey. Small grains at base of container.					Reddish brown appearance of top half							Light grey, mottled orange brown. No visible cracks through grain sized cavities are present throughout core.

Appendix B2: Monitoring descriptions for test WD2. Blank spaces in the table indicate that no surficial changes were recorded in that week's monitoring. The final description presents a complete description of the cores for comparison with the initial descriptions.

Week	Initial	1	2	3	4	5	6	7	8	9	10	11	12	13	Final
Load 1 (19D)	Light grey-brown. Medium to coarse grained. Large irregular cavity (40 mm x 15 mm) at base of core	Small grains at base of container.			Very minor iron staining at base of core?					Minor iron staining at base of core					Dark grey brown. Minor crumbling at top of core around notches. Very minor iron staining around base rim of core. Large irregular cavity (40 mm x 15 mm) at base of core
Control 1 (19C)	Light grey-brown, mottled an orange brown at base of core. Fine to medium grained. No visible cracks	Small grains at base of container.													Dark grey brown, mottled orange at base. Crumbling at top of core on all sides. Salt crystallised on top.
Load 2 (7A)	Light grey brown. Fine to medium grained. Cavity (25 x 10 mm) at base of core.	Small grains at base of container.	Some very minor iron staining	Minor iron staining			Major iron staining								Dark grey brown. Minor iron staining along base rim of core. Cavity at base of core (25 x 10 mm)
Control 2 (9J)	Light grey brown. Fine to medium grained, with minor coarse grains. Minor cavity at base of core (15 x 5 mm)	Small grains at base of container.					Minor iron staining			Major iron staining		Iron staining on the base of core			Dark grey brown mottled light grey brown. Crumbling at top of core. Minor iron staining along base rim of core. Coarse grains appear to have been plucked out of surface of core
Load 3 (19A)	Very light grey brown. Fine to coarse grained. Minor cavities at top and base of core (both 10 x 10 mm)	Small grains at base of container.	Minor iron staining				Major iron staining					Iron staining on the base of core			Dark grey brown. Minor iron staining along base rim of core. Minor cavity at base of core (30 mm x 10 mm) and top of core (15 x 10 mm).
Control 3 (19B)	Very light grey brown. Fine to coarse grained. Minor cavity at base (5 x 5mm)	Small grains at base of container.													Dark grey brown. Minor crumbling at top and base of core. Minor cavity at base of core (10 x 5 mm)
Load 4 (6B)	Light grey brown. Fine to medium grained. No visible cracks	Small grains at base of container.	Minor iron staining				Major iron staining					Iron staining on the base of core			Dark brown grey. Minor iron staining along base rim of core. No visible cracks
Control 4 (6A)	Light grey brown. Fine to medium grained. No visible cracks	Small grains at base of container.													Dark brown grey. Crumbling at top of core. Mudstone seams appear to have been removed, now with indentations of 5 mm deep.

Appendix B3: Monitoring descriptions for test WD3. Blank spaces in the table indicate that no surficial changes were recorded in that week's monitoring. The final description presents a complete description of the cores for comparison with the initial descriptions.

Week	Initial	1	2	3	4	5	6	7	8	9	10	11	12	Final
Load 1 (21C)	Light grey blue. Finely banded. No visible cracks			Minor iron staining. 2 x sub-horizontal stepped cracks in mid core (20 mm long). Minor grains.							Increase in iron staining		Minor grains associated with slaking	Light grey blue mottle orange brown. No visible cracks
Control 1 (21B)	Light grey blue with minor orange brown mottling at top of core. Finely banded. No visible cracks			Sub-horizontal stepped crack (30 mm long) in mid core. Minor grains at base of container				2 x sub-horizontal stepped en-echelon cracks in mid core (20 mm long)						Light grey blue mottled grey orange. 2 x sub-horizontal (en-echelon) cracks in mid core (20 - 35 mm long)
Load 2 (20I)	Light grey brown, with minor grey blue streaks. No visible cracks			Minor iron staining. Substantial amount of grains at base of container				Numerous sub-vertical cracks on surface related to slaking (5 - 20 mm long)	Large slaking event. 'Slab' (10 mm wide, 2 mm deep, 25 mm long) removed from core	Increase in slaking	Appearance of incipient large 'slake'		Increase in slaking (?)	Grey brown, reddish staining at base. Grain sized cavities due to slaking. A 45° crack at top of core (20mm long, 2 mm aperture)
Control 2 (20A)	Light grey brown. No visible cracks			Substantial amount of grains at base of container	Minor iron staining at base of cont. (?)			Minor amounts of iron staining at base. Sub-horizontal, arch shaped crack in mid core (20 mm))	Minor slaking event. 'Slab' (10 mm long, 5 mm wide, 2 mm deep). Shallow cracks at top and in mid core.	Increase in slaking. Large pieces removed from top of core (?)	Increase in slaking			Light grey brown, reddish brown staining at base. Large cavity at base (20 mm long, 5 mm high, 5 mm deep). Grain sized cavities due to slaking
Load 3 (22A)	Light grey blue, with minor orange mottling. Edge (20 mm long, 2mm deep) missing from base of core. Finely banded			Minor iron staining and minor grains at base of container	Substantial iron staining			Numerous (>20) small (5 -10 mm long) sub-vertical cracks within core related to slaking. Large 'chunks at base of core	Increase in slaking	Increase in slaking	Increase in slaking			Dark grey blue mottled orange. Grain sized cavities due to slaking - has a striped appearance. 2 x 45 ° cracks at top of core (20 mm - 10 mm long, 1 mm aperture)
Control 3 (20H)	Light grey brown. No visible cracks. Minor indents (1 x 1 mm) on outside of core			Minor grains at base of container				Increased slaking		Increase in slaking	Increase in slaking			Grey brown. No visible cracks but grain sized cavities due to slaking
Load 4 (20E)	Light grey bluish brown. Minor cavity at base of core (2 mm deep, 1 mm high, 5 mm wide)			Minor iron staining and minor grains at base of container				Sub-vertical cracks (x 3) (10 mm long) related to slaking	Increase in slaking	Increase in slaking	Increase in slaking			Grey brown with minor orange mottling. Grain sized cavities due to slaking. Small cavity y at base and in mid core (5x 10 x2 mm)
Control 4 (20G)	Light grey brown. Minor cavities (x 3) present on surface of core (5 x 2 x 2 mm)			Substantial amount of grains at base of container					Increase in slaking	Increase in slaking	Increase in slaking			Grey brown. No visible cracks but grain sized cavities due to slaking

Appendix B4: Monitoring descriptions for test WD4. Blank spaces in the table indicate that no surficial changes were recorded in that week's monitoring. The final description presents a complete description of the cores for comparison with the initial descriptions.

Week	Initial	1	2	3	4	5	6	7	8	9	10	11	12	Final
Load 1 (20C)	Light grey brown. Finely banded. No visible cracks		Slaking in container - 1 large slake. Arch shaped crack by notch (5 mm long).		Minor iron staining									Dark grey brown. Minor cavities in top half of core (2 - 5 mm wide, 2 mm aperture, 2 mm deep)
Control 1 (20F)	Light grey brown. Finely banded. Minor cavities on core surface (1 mm wide, <1 mm deep, 2 mm long)		Slaking in container.		Minor iron staining									Dark grey brown. Small minor cavities throughout core (2 - 5 mm wide, <2 mm wide, 2 mm deep)
Load 2 (18C)	Light grey brown, horizontally finely banded. No visible cracks.		Slaking in container. Minor iron staining.	Major iron staining										Dark grey brown. Finely banded. No visible cracks.
Control 2 (20D)	Light grey brown. Finely banded. No visible cracks		Slaking in container.	Minor iron staining - may be related to grain colour	Large slaking event.								Minor increase in slaking	Dark grey brown. Minor surficial flakes (2 x 5 mm) on surface of core. Sub-horizontal crack (50 mm long, <1 mm aperture), and sub-horizontal crack (20 mm long, < 1 mm aperture) at top of core. Incipient large flake (20 x 20 mm, 2mm deep).
Load 3 (20K)	Light grey brown. Finely banded. Cavity (2 mm wide, 1 mm deep, 10 mm long) in mid core by notch.		Slaking in container. Minor iron staining.	Major iron staining										Dark grey brown, minor incipient surficial flake in mid core (10 mm high, 5 mm wide, 1 mm deep). Large cavity on lower core (20 mm long, 2 mm wide, 5 mm deep)
Control 3 (20B)	Light grey brown. Finely banded. Minor cavities on core surface (1 mm wide, <1 mm deep, 2 mm long)		Slaking in container. Minor iron staining.	Minor iron staining.										Dark grey brown, with orange brown staining at base of core. Minor cavities in top half of core (2 -5 mm wide, < 2 mm aperture, 2 mm deep).
Load 4 (18F)	Light grey brown, horizontally finely banded. No visible cracks.		Minor iron staining (?)	Major iron staining										Dark grey brown. Finely banded. No visible cracks.
Control 4 (18D)	Light grey brown, horizontally finely banded. No visible cracks.		Minor iron staining.											Dark grey brown. Finely banded. 2 x sub-horizontal stepped cracks at top of core (20 mm long, <1 mm aperture).

Appendix B5: Monitoring descriptions for Field experiment. Blank spaces in the table indicate that no surficial changes were recorded in that week's monitoring.

Test	Rock Type	Variables*	Sample		22/08/2016	20/09/2016	19/10/2016	17/11/2016	09/12/2016	20/01/2017	03/03/2017	10/04/2017	19/05/2017	22/06/2017	07/08/2017	30/08/2017
Stressed	Catcastle Buff Sandstone	N	1	19B	Grey brown. No visible cracks.	Minor grains at base of sample.				Minor iron staining?						
		N	2	19A	Grey brown, mottled light grey brown. No visible cracks.	Small flaking event - 2 mm wide flake.										
		P	3	5C	Grey brown, mottled light grey brown. No visible cracks.		Minor iron staining?								>Grain sized cavities due to slaking	
		P,N	4	12C	Grey brown, mottled light grey brown. No visible cracks.	Minor grains at base of sample.										>Grain sized cavities due to slaking
			5	20A	Grey brown, mottled light grey brown. No visible cracks.	Minor iron staining?								Minor grains at base of sample		
			6	11B	Light grey brown. No visible cracks.			Minor iron staining?								
		P,N	7	14A	Light grey brown. No visible cracks.	Minor grains at base of sample. Minor iron staining?								Minor grains at base of sample		
		P	8	13A	Light grey brown. No visible cracks.	Minor grains at base of sample.					20 mm sub-horizontal crack at base of core.			Minor grains at base of sample		
	Skinningrove Siltstone	N	9	12D	Light grey blue. No visible cracks.	Minor grains at base of sample.	Very minor iron staining?						Core is powdery to touch. Major grains at base of sample.		Major grains at base of container.	
			10	13F	Light grey blue. No visible cracks.								Core is powdery to touch. Major grains at base of sample.			
			11	19C	Light grey blue. No visible cracks.	Minor iron staining?						Core is powdery to touch.	Slaking on core surface.	Major grains at base of sample.		
			12	20B	Light grey blue. No visible cracks.	Minor iron staining?						Core is powdery to touch.		Major grains at base of sample.		
		N	13	12C	Light grey blue. No visible cracks.	Minor grains at base of sample	Minor iron staining?					Core is powdery to touch.	>Grain sized cavities due to slaking	Major grains at base of sample.		
			14	19A	Light grey blue. No visible cracks.	Minor iron staining?						Core is powdery to touch.	>Grain sized cavities due to slaking	Major grains at base of sample. Grains are wet & appear in 'clumps' on core.		
		N	15	13B	Light grey blue. No visible cracks.		Minor iron staining?					Core is powdery to touch.	>Grain sized cavities due to slaking	Major grains at base of sample.		
			16	11C	Light grey blue. No visible cracks.	Minor iron staining?						Core is powdery to touch.	>Grain sized cavities due to slaking	Major grains at base of sample.		
Control	Catcastle Buff Sandstone	N	17	20B	Light grey brown. No visible cracks.	Minor grains at base of sample.										
		N	18	5A	Grey brown, mottled light grey brown. No visible cracks.											
			19	20C	Light grey brown. No visible cracks.											
			20	16A	Light grey brown. No visible cracks.											
		P	21	13C	Light grey brown. No visible cracks.											
		P	22	9A	Light grey brown. No visible cracks.											
		P,N	23	4C	Very light grey brown. No visible cracks.											
		P,N	24	12B	Grey brown. No visible cracks.											
	Skinningrove Siltstone		25	7E	Grey blue. 10 mm long crack at top of core.	5 mm sub-horizontal crack in mid core.		5 mm sub-vertical crack at top of core		25 mm sub-horizontal stepped crack at top of core.		Core is powdery to touch.	Minor grains at base.	Major grains at base of sample.		
		N	26	11B	Light grey blue. Cavities at both base and top of core.							Core is powdery to touch.		Major grains at base of sample.		
		N	27	13D	Light grey blue. No visible cracks.							Core is powdery to touch.		Major grains at base of sample.		
			28	13C	Light grey blue. Hairline cracks (approx. 5 mm long) at base.					30 mm sub-horizontal arc shaped crack at top of core.			Minor grains at base.	Major grains at base of sample.		
		N	29	20A	Light grey blue. Cavity at base.											
			30	18A	Light brown, banded. No visible cracks.							Core is powdery to touch.		Major grains at base of sample.		
		N	31	18E	Light brown, banded. No visible cracks.							Core is powdery to touch.		Major grains at base of sample.		
			32	19B	Light grey blue. No visible cracks.			20 mm sub-horizontal crack at top of core.		3 x 20 mm sub-vertical stepped cracks at top of core		Core is powdery to touch.	Minor grains at base.	Major grains at base of sample. Grains are wet and appear in 'clumps' on side of core. FAILED		

*P = preloaded, N = notched.

Appendix B6: Observations of weight change in samples for laboratory Sandstone (WD1 & WD2) tests.

Sample	Pre-Test (Dry) (g)	Post Test (Wet)(g)	Post Test (Dry)(g)	Difference (g)	Difference %
Load 1 (11C)	416.12	423.96	421.13	-5.01	1.203979621
Control 1 (11A)	415.61	426.56	423.13	-7.52	1.80938861
Load 2 (15A)	422.23	431.05	428.43	-6.2	1.468394003
Control 2 (12A)	423.54	435.28	431.18	-7.64	1.803843793
Load 3 (18A)	402	418.01	416.41	-14.41	3.584577114
Control 3 (18B)	407.55	423.4	419.43	-11.88	2.914979757
Load 4 (15B)	412.62	423.03	419.4	-6.78	1.643158354
Control 4 (4C)	411.6	424.49	420.11	-8.51	2.067541302

Sample	Pre-Test (Dry) (g)	Post Test (Wet)(g)	Post Test (Dry)(g)	Difference (g)	Difference %
Load 1 (19D)	400.06	411.99	408.08	-8.02	2.004699295
Control 1 (19C)	415.18	421.61	419.1	-3.92	0.944168794
Load 2 (7A)	402.48	411.03	408.12	-5.64	1.401311866
Control 2 (9J)	403.14	411.4	408.58	-5.44	1.349407154
Load 3 (19A)	399.11	411.37	407.68	-8.57	2.147277693
Control 3 (19B)	395.12	406.71	402.42	-7.3	1.847539988
Load 4 (6B)	413.14	422.32	419.16	-6.02	1.457133175
Control 4 (6A)	416.99	421.43	418.84	-1.85	0.443655723

Appendix B7: Observations of weight change in samples for laboratory siltstone (WD3 & WD4) tests.

Sample	Pre-Test (Dry) (g)	Post Test (Wet)(g)	Post Test (Dry)(g)	Difference (g)	Difference %
Load 1 (21C)	447.95	455.36	451.67	3.72	-0.8304498
Control 1 (21B)	443.91	452.86	449.32	5.41	1.2187155
Load 2 (20I)	377.65	405.44	395.77	18.12	4.7980935
Control 2 (20A)	379.62	404.37	394.74	15.12	3.9829303
Load 3 (22A)		410.82	401.68	401.68	
Control 3 (20H)	380.3	408.52	399.28	18.98	4.9907967
Load 4 (20E)	363.24	391.83	381.45	18.21	5.0132144
Control 4 (20G)	383.39	410.3	401.96	18.57	4.8436318

Sample	Pre-Test (Dry) (g)	Post Test (Wet)(g)	Post Test (Dry)(g)	Difference (g)	Difference %
Load 1 (20C)	374.32	402.13	394.71	20.39	5.447210943
Control 1 (20F)	357.2	392.91	385.99	28.79	8.059910414
Load 2 (18C)	370.16	389.93	382	11.84	3.198616814
Control 2 (20D)	354.93	382.11	373.61	18.68	5.263009608
Load 3 (20K)	363.49	398.66	389.33	25.84	7.108861317
Control 3 (20B)	355.09	396.46	388.41	33.32	9.383536568
Load 4 (18F)	367.33	388.01	379.73	12.4	3.375711213
Control 4 (18D)	365.24	399.43	391.71	26.47	7.247289454

Appendix B8: Observations of weight change in samples for Field test.

Sample	Pre-Test (Dry) (g)	Post Test (Dry)(g)	Difference (g)	Difference %
19B	399.96	423.06	-23.1	5.775577558
19A	405.3	423.18	-17.88	4.411547002
5C	387.7	388.63	-0.93	0.239876193
12C	431.29	427.95	3.34	-0.774420923
20A	413.47	416.52	-3.05	0.737659322
11B	416.2	418.61	-2.41	0.579048534
14A	409.16	409.18	-0.02	0.004888063
13A	407.1	410.95	-3.85	0.945713584
12D	414.35	407.63	6.72	-1.621817304
13F	430.69	429.87	0.82	-0.190392161
19C	401.06	384.25	16.81	-4.191392809
20B	446.48	448.94	-2.46	0.550976528
12C	415.89	408.85	7.04	-1.692755296
19A	400.99	382.82	18.17	-4.531285069
13B	420.69	413.21	7.48	-1.778031329
11C	372.54	362.74	9.8	-2.630590004
20B	446.48	409.26	37.22	-8.336319656
5A	422.71	416.97	5.74	-1.357904947
20C	426.96	402.75	24.21	-5.670320405
16A	405.5	405.8	-0.3	0.073982737
13C	412.1	412.34	-0.24	0.058238292
9A	414.56	412.04	2.52	-0.607873408
4C	410	391.2	18.8	-4.585365854
12B	436.11	430.17	5.94	-1.362041687
7E	321.57	295.79	25.78	-8.016917001
11B	379.38	383.87	-4.49	1.183509937
13D	414.24	403.01	11.23	-2.710988799
13C	401.06	422.31	-21.25	5.298459083
20A	438.92	434.32	4.6	-1.048026975
18A	367.7	348.22	19.48	-5.297797117
18E	371.54	353.14	18.4	-4.952360446
19B	401.02	na	na	na

.

Appendix B9: Photographs taken during Monitoring of WD1.

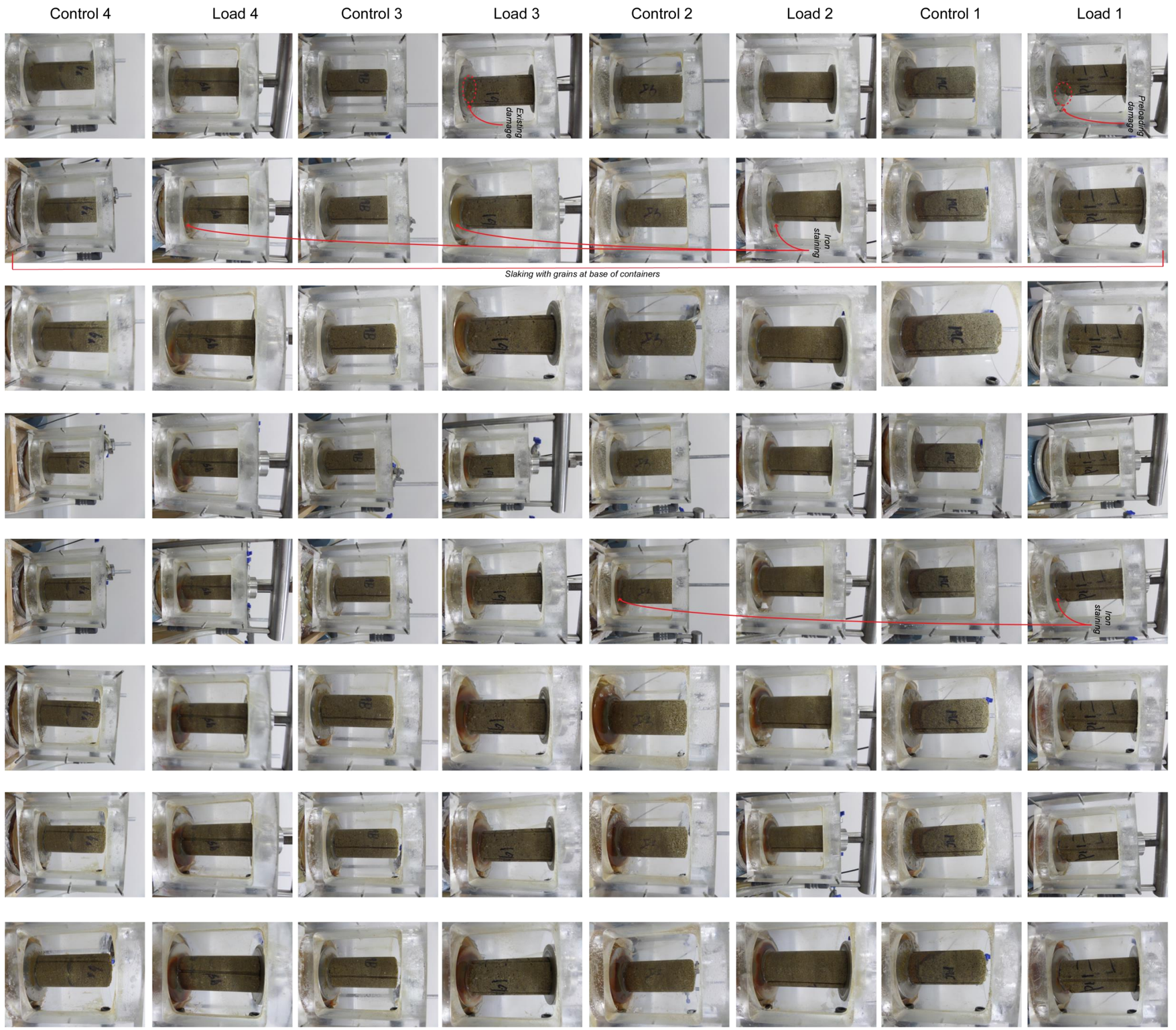

Appendix B10: Photographs taken during Monitoring of WD2.

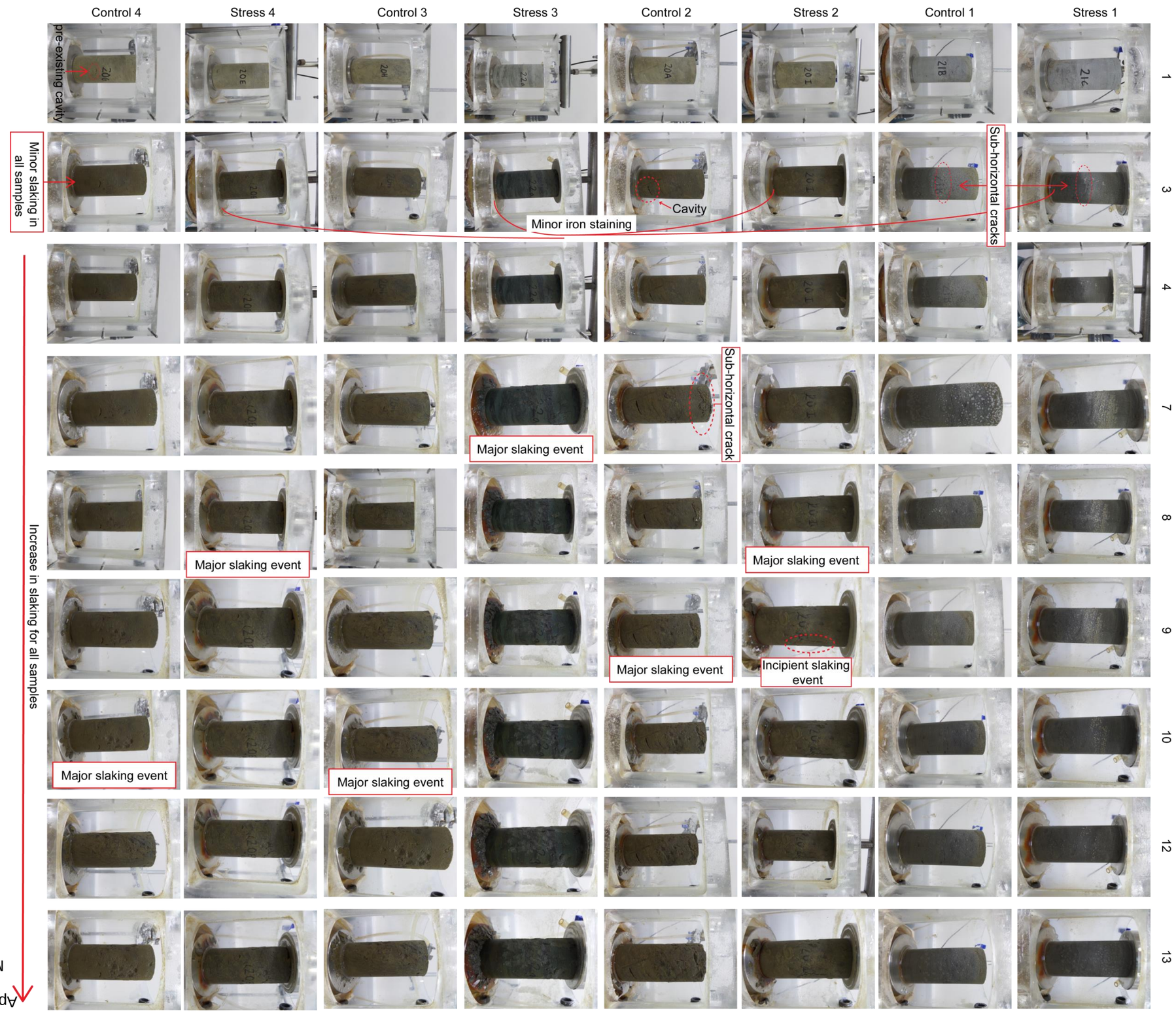

Appendix B11: Photographs taken during Monitoring of WD3.

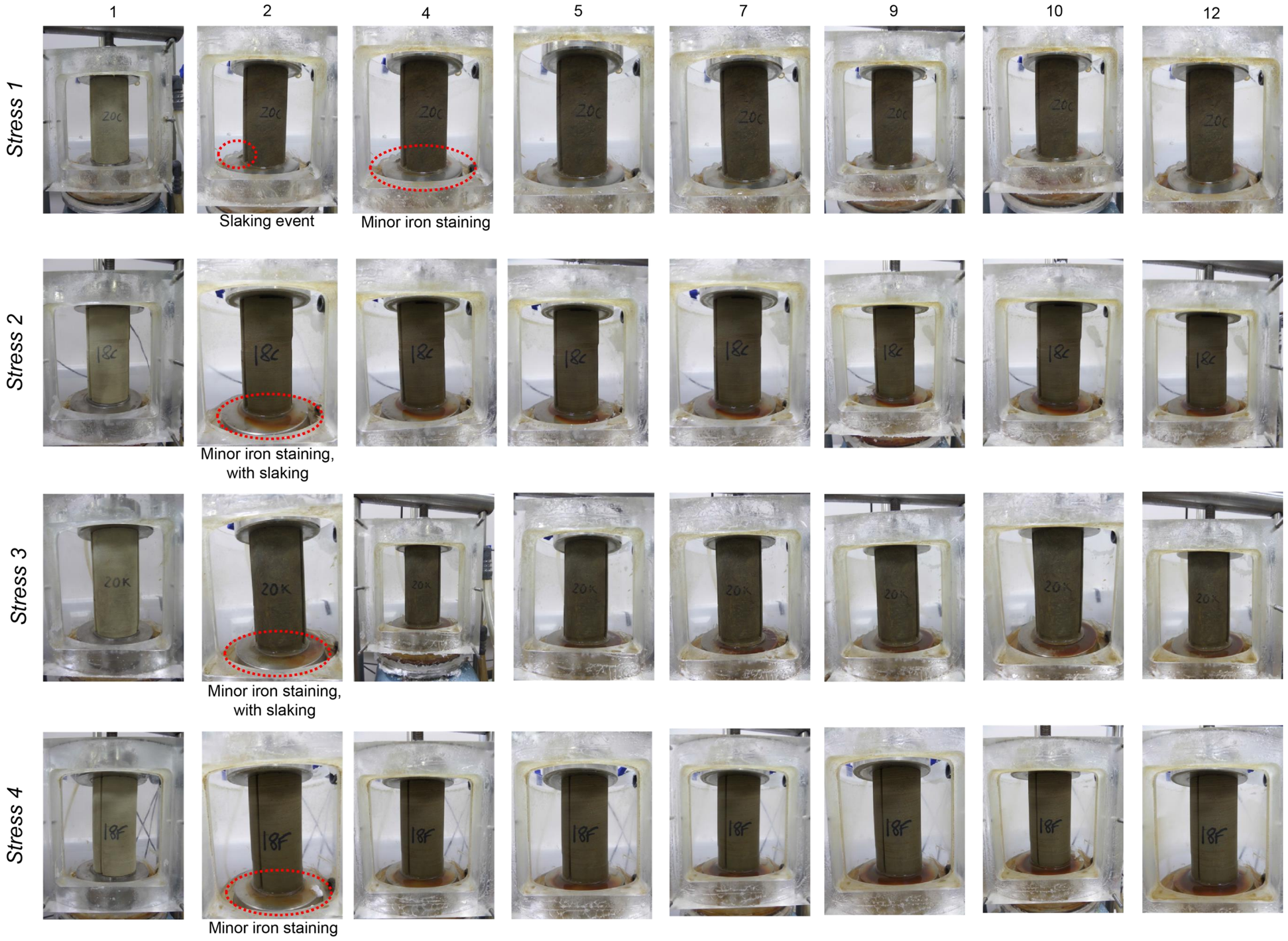

Appendix B12: Photographs taken during Monitoring of WD4 Stress Samples.

Appendix B13: Baseline UCS values for Skinningrove Siltstone and Catcastle Buff Sandstone.

Sample	Maximum Axial Stress (MPa)	Axial Strain at Failure (%)	Young's Modulus (GPA)	Failure Style	Bulk Density (g cm^{-3})	Axial Strain at Failure (Transducer 1) (%)	Axial Strain at Failure (Transducer 2) (%)	Radial Strain (%)
4A	27.82	1.4041	8.328432	1	2.2	NA	0.3776	-0.6174
4B	25.59	1.449	8.972875	2	2.2	NA	0.355	-0.287
4E	28.77	1.436	8.800227	1	2.2	0.3972	0.4276	-0.6383
4G	27.09	1.4007	10.96903	1	2.2	0.3705	0.3802	-0.5118
4J	31.03	1.5417	10.63124	1	2.16	0.4135	0.4631	0.4494
11E	35.52	1.5392	13.22426	1	2.2	0.2982	0.464	-0.6032
11B	35.52	1.5808	13.31726	1	2.24	0.3182	0.3723	-0.6211
13E	36.60	1.3956	NA	2	2.39	0.574	0.0072	-0.9637
23A	40.10	1.5444	6.6437	3	2.51	0.297	0.3023	NA
24A	34.67	1.5021	4.154	3	2.5	0.3323	0.2742	NA
24B	39.65	1.3773	NA	2	2.48	0.2157	0.6984	NA
24C	47.48	1.4805	4.87625	2	2.49	0.1671	0.9848	NA

Sample	Maximum Axial Stress (Mpa)	Axial Strain at Failure (%)	Young's Modulus (GPA)	Failure Style	Bulk Density (g cm^{-3})	Axial Strain at Failure (Transducer 1) (%)	Axial Strain at Failure (Transducer 2) (%)	Radial Strain
3A	56.40	1.2065	6.143	1	2.35	0.076	0.116	-0.089
2B	59.36	1.21	5.5742	1	2.36	0.1012	0.1207	-0.216
2C	42.63	1.1274	5.5224	2	2.36	0.005	0.215	-0.285
2A	60.02	1.2352	6.3811	1	2.36	0.172	0.096	-0.187
1E	62.86	1.3818	4.6513	1	2.44	0.195	0.077	-0.435
4A	47.03	1.1669	4.5825	1	2.36	0.081	0.191	-0.042
7B	57.75	1.302	6.1753	1	2.44	0.076	0.148	-0.352
1D	52.34	1.208	6.1813	1	2.42	0.179	0.092	-0.213
8A	46.06	1.2871	4.208	1	2.4	0.118	0.134	-0.366
21A	64.28	1.2913	6.75625	1	2.48	0.1649	0.4774	NA
22B	63.86	1.3205	6.431	1	2.38	0.1164	0.3967	NA

10 References

Abellán, A., Calvet, J., Vilaplana, J.M., Blanchard, J., 2010. Detection and spatial prediction of rockfalls by means of terrestrial laser scanner monitoring. Geomorphology 119, 162–171. https://doi.org/10.1016/j.geomorph.2010.03.016

Abellan, A., Oppikofer, T., Jaboyedoff, M., Rosser, N.J., Lim, M., Lato, M.J., 2014. Terrestrial laser scanning of rock slope instabilities. Earth Surf. Process. Landforms 39, 80–97. https://doi.org/10.1002/esp.3493

Abellán, a., Jaboyedoff, M., Oppikofer, T., Vilaplana, J.M., 2009. Detection of millimetric deformation using a terrestrial laser scanner: experiment and application to a rockfall event. Nat. Hazards Earth Syst. Sci. 9, 365–372. https://doi.org/10.5194/nhess-9-365-2009

Adams, P.N., Storlazzi, C.D., Anderson, R.S., 2005. Nearshore wave-induced cyclical flexing of sea cliffs. J. Geophys. Res. Earth Surf. 110, 1–19. https://doi.org/10.1029/2004JF000217

Aldred, J., Eppes, M.C., Aquino, K., Deal, R., Garbini, J., Swami, S., Tuttle, A., Xanthos, G., 2016. The influence of solar-induced thermal stresses on the mechanical weathering of rocks in humid mid-latitudes. Earth Surf. Process. Landforms 41, 603–614. https://doi.org/10.1002/esp.3849

Allison, R.J., 1990. Developments in a non-destructive method of determining rock strength. Earth Surf. Process. Landforms 15, 571–577.

Amato, J.D., Hantz, D., Guerin, A., Jaboyedoff, M., Baillet, L., Mariscal, A., 2016. Influence of meteorological factors on rockfall occurrence in a middle mountain limestone cliff. Nat. Hazards Earth Syst. Sci. 16, 719–735. https://doi.org/10.5194/nhess-16-719-2016

Amitrano, D., 2005. Seismic precursory patterns before a cliff collapse and critical point phenomena. Geophys. Res. Lett. 32. https://doi.org/10.1029/2004GL022270

Anderson, T.L., 2005. Fracture Mechanics: Fundamentals and Applications, 3rd ed. CRC Press, Florida.

ASTM D5453-08, 2008. Standard practices for preparing rock core as cylindrical test specimens and verifying conformance to dimensional and shape tolerances. Astm. https://doi.org/10.1520/D4543-08.

ASTM D7012-14, 2014. Standard test methods for compressive strength and elastic moduli of intact rock core specimens under varying states of stress and temperature. ASTM International, West Conshohocken, PA.

Atkinson, B.K., 1984. Subcritical crack growth in geological materials. J. Geophys. Res. 89, 4077–4114. https://doi.org/10.1029/JB089iB06p04077

Attewell, P.B.B., Farmer, I.W.W., 1973. Fatigue behaviour of rock. Int. J. Rock Mech. Min. Sci. 10, 1–9. https://doi.org/10.1016/0148-9062(73)90055-7

Augustinus, P.C., 1992. The influence of rock mass strength on glacial valley cross-profile morphometry: A case study from the Southern Alps, New Zealand. Earth Surf. Process. Landforms 17, 39–51.

Bachmann, D., Bouissou, S., Chemenda, A., 2006. Influence of large scale topography on gravitational rock mass movements: New insights from physical modeling. Geophys. Res. Lett. 33, 1–4. https://doi.org/10.1029/2006GL028028

Bachmann, D., Bouissou, S., Chemenda, A., 2004. Influence of weathering and pre-

existing large scale fractures on gravitational slope failure: insights from 3-D physical modelling. Nat. Hazards Earth Syst. Sci. 4, 711–717. https://doi.org/10.5194/nhess-4-711-2004

Bahat, D., Grossenbacher, K., Karasaki, K., 1999. Mechanism of exfoliation joint formation in granitic rocks, Yosemite National Park. J. Struct. Geol. 21, 85–96.

Barla, G., Barla, M., Debernardi, D., 2010. New triaxial apparatus for rocks. Rock Mech. Rock Eng. 43, 225–230. https://doi.org/10.1007/s00603-009-0076-7

Barlow, J., Lim, M., Rosser, N., Petley, D., Brain, M., Norman, E., Geer, M., 2012. Modeling cliff erosion using negative power law scaling of rockfalls. Geomorphology 139–140, 416–424. https://doi.org/10.1016/j.geomorph.2011.11.006

Barton, N., 1974. Estimating the shear strength of rock joints, in: Proceedings of the 3rd Congress of International Society of Rock Mechancis. Advances in Rock Mechanics. Denver, pp. 219–220.

Barton, N., Lien, R., Lunde, J., 1974. Engineering classification of rock masses for the design of tunnel support. Rock Mech. 6, 189–236. https://doi.org/10.1007/BF01239496

Basu, A., Celestino, T.B., Bortolucci, A.A., 2009. Evaluation of rock mechanical behaviors under uniaxial compression with reference to assessed weathering grades. Rock Mech. Rock Eng. 42, 73–93. https://doi.org/10.1007/s00603-008-0170-2

BGS, 2017. Geology of Britain [WWW Document]. URL http://mapapps.bgs.ac.uk/geologyofbritain/home.html (accessed 11.24.17).

Bieniawski, Z.T., 1967. Mechanism of brittle fracture of rock. Part I - Theory of the fracture process. Int. J. Rock Mech. Min. Sci. 4, 395–406.

Bjerrum, L., 1967. Progressive failure in slopes of overconsolidated plastic clay and clay shales. J. Soil Mech. Found. Div. 93, 1–49.

Bonilla-Sierra, V., Scholtès, L., Victor, F., Elmouttie, M., 2015. DEM analysis of rock bridges and the contribution to rock slope stability in the case of translational sliding failures. Int. J. Rock Mech. Min. Sci. 80, 67–78. https://doi.org/10.1016/j.ijrmms.2015.09.008

Borrelli, L., Greco, R., Gulla, G., 2007. Weathering grade of rock masses as a predisposing factor to slope instabilities: Reconnaissance and control procedures. Geomorphology 87, 158–175. https://doi.org/10.1016/j.geomorph.2006.03.031

Brace, W.F., Paulding, B.W., Scholz, C., 1966. Dilatancy in the fracture of crystalline rocks. J. Geophys. Res. 71, 3939–3953. https://doi.org/10.1029/JZ071i016p03939

Brain, M.J., Rosser, N.J., Norman, E.C., Petley, D.N., 2014. Are microseismic ground displacements a significant geomorphic agent? Geomorphology 207, 161–173. https://doi.org/10.1016/j.geomorph.2013.11.002

Brideau, M.A., Pedrazzini, A., Stead, D., Froese, C., Jaboyedoff, M., van Zeyl, D., 2011. Three-dimensional slope stability analysis of South Peak, Crowsnest Pass, Alberta, Canada. Landslides 8, 139–158. https://doi.org/10.1007/s10346-010-0242-8

Brideau, M.A., Stead, D., 2010. Controls on block toppling using a three-dimensional distinct element approach. Rock Mech. Rock Eng. 43, 241–260. https://doi.org/10.1007/s00603-009-0052-2

Brideau, M., Yan, M., Stead, D., 2009. The role of tectonic damage and brittle rock fracture in the development of large rock slope failures. Geomorphology 103, 30–49. https://doi.org/10.1016/j.geomorph.2008.04.010

Brunetti, M., Guzzetti, F., Rossi, M., 2009. Probability distributions of landslide volumes. Nonlinear Process. Geophys. 16, 179–188. https://doi.org/10.5194/npg-16-179-2009

Bruthans, J., Filippi, M., Schweigstillová, J., Řihošek, J., 2016. Quantitative study of a rapidly weathering overhang developed in an artificially wetted sandstone cliff. Earth Surf. Process. Landforms 723, 711–723. https://doi.org/10.1002/esp.4016

Bruthans, J., Soukup, J., Vaculikova, J., Filippi, M., Schweigstillova, J., Mayo, A.L., Masin, D., Kletetschka, G., Rihosek, J., 2014. Sandstone landforms shaped by negative feedback between stress and erosion. Nat. Geosci. 7, 597–601.

Cai, M., Kaiser, P.K., Uno, H., Tasaka, Y., Minami, M., 2004. Estimation of rock mass deformation modulus and strength of jointed hard rock masses using the GSI system. Int. J. Rock Mech. Min. Sci. 41, 3–19. https://doi.org/10.1016/S1365-1609(03)00025-X

Carlà, T., Farina, P., Intrieri, E., Botsialas, K., Casagli, N., 2017. On the monitoring and early-warning of brittle slope failures in hard rock masses: Examples from an open-pit mine. Eng. Geol. 228, 71–81. https://doi.org/10.1016/j.enggeo.2017.08.007

Carlà, T., Farina, P., Intrieri, E., Ketizmen, H., Casagli, N., 2018. Integration of ground-based radar and satellite InSAR data for the analysis of an unexpected slope failure in an open-pit mine. Eng. Geol. 235, 39–52. https://doi.org/10.1016/j.enggeo.2018.01.021

Cerfontaine, B., Collin, F., 2017. Cyclic and Fatigue Behaviour of Rock Materials: Review, Interpretation and Research Perspectives. Rock Mech. Rock Eng. 51, 1–24. https://doi.org/10.1007/s00603-017-1337-5

Clarke, B.A., Burbank, D.W., 2011. Quantifying bedrock-fracture patterns within the shallow subsurface: Implications for rock mass strength, bedrock landslides, and erodibility. J. Geophys. Res. Earth Surf. 116. https://doi.org/10.1029/2011JF001987

Clarke, B.A., Burbank, D.W., 2010. Bedrock fracturing, threshold hillslopes, and limits to the magnitude of bedrock landslides. Earth Planet. Sci. Lett. 297, 577–586. https://doi.org/10.1016/j.epsl.2010.07.011

Collins, B.D., Stock, G.M., 2016. Rockfall triggering by cyclic thermal stressing of exfoliation fractures. Nat. Geosci. 9, 395–400. https://doi.org/10.1038/NGEO2686

Collins, B.D., Stock, G.M., Eppes, M.-C., Lewis, S.W., Corbett, S.C., Smith, J.B., 2018. Thermal influences on spontaneous rock dome exfoliation. Nat. Commun. 9, 762. https://doi.org/10.1038/s41467-017-02728-1

Colman, S.M., 1981. Rock weathering rates as a function of time. Quarternary Research. 15, 250-264.

Cook, R.D., 1995. Finite Element Modeling for Stress Analysis. John Wiley & Sons.

Cooke, M.L., Underwood, C.A., 2001. Fracture termination and step-over at bedding interfaces due to frictional slip and interface opening. J. Struct. Geol. 23, 223–238. https://doi.org/10.1016/S0191-8141(00)00092-4

Coombes, M.A., Feal-Pérez, A., Naylor, L.A., Wilhelm, K., 2013. A non-destructive tool for detecting changes in the hardness of engineering materials: Application of the Equotip durometer in the coastal zone. Eng. Geol. 167, 14–19. https://doi.org/10.1016/j.enggeo.2013.10.003

Crosta, G.B., Agliardi, F., 2003. Failure forecast for large rock slides by surface displacement measurements. Can. Geotech. J. 40, 176–191. https://doi.org/10.1139/t02-085

Cruden, D.M., 1974. The static fatigue of brittle rock under uniaxial compression. Int. J. Rock Mech. Min. Sci. Geomech. 11, 67–73.

de Vilder, S.J., Rosser, N.J., Brain, M.J., 2017. Forensic analysis of rockfall scars. Geomorphology 295, 202–214. https://doi.org/10.1016/j.geomorph.2017.07.005

de Vilder, S.J., Rosser, N.J., Brain, M.J., Vann Jones, E.. C., 2017. Forensic rockfall scar analysis: Development of a mechanically correct model of rockfall failure. 3rd North Am. Symp. Landslides 829–839.

Dewez, T.J.B., Rohmer, J., Regard, V., Cnudde, C., 2013. Probabilistic coastal cliff collapse hazard from repeated terrestrial laser surveys : case study from Mesnil Val (Normandy , northern France). J. Coast. Res. 702–707. https://doi.org/10.2112/SI65-119.1

Diederichs, M.S., 2003. Manuel Rocha Medal Recipient Rock Fracture and Collapse Under Low Confinement Conditions. Rock Mech. Rock Eng. 36, 339–381. https://doi.org/10.1007/s00603-003-0015-y

Dunning, J.D., Huf, W.L., 1983. The effects of aqueous chemical environments on crack and hydraulic fracture propagation and morphologies. J. Geophys. Res. 88, 6491–6499.

Dunning, S.A., Massey, C.I., Rosser, N.J., 2009. Structural and geomorphological features of landslides in the Bhutan Himalaya derived from Terrestrial Laser Scanning. Geomorphology 103, 17–29. https://doi.org/10.1016/j.geomorph.2008.04.013

Duperret, A., Taibi, S., Mortimore, R.N., Daigneault, M., 2005. Effect of groundwater and sea weathering cycles on the strength of chalk rock from unstable coastal cliffs of NW France. Eng. Geol. 78, 321–343. https://doi.org/10.1016/j.enggeo.2005.01.004

Durgin, P.B., 1977. Landslides and the weathering of granitic rocks. Geol. Soc. Am. 3, 127–131.

Dussauge-Peisser, C., Helmstetter, A., Grasso, J.R., Hantz, D., Desvarreux, P., Jeannin, M., Giraud, A., 2002. Probabilistic approach to rock fall hazard assessment: potential of historical data analysis. Nat. Hazards Earth Syst. Sci. 2, 15–26. https://doi.org/10.5194/nhess-2-15-2002

Dussauge, C., Grasso, J.-R., Helmstetter, A., 2003. Statistical analysis of rockfall volume distributions: Implications for rockfall dynamics. J. Geophys. Res. (Solid Earth) 108. https://doi.org/10.1029/2001JB000650

Eberhardt, E., Stead, D., Coggan, J.S., 2004a. Numerical analysis of initiation and progressive failure in natural rock slopes—the 1991 Randa rockslide. Int. J. Rock Mech. Min. Sci. 41, 69–87. https://doi.org/10.1016/S1365-1609(03)00076-5

Eberhardt, E., Stead, D., Karami, A., Coggan, J., 2004b. Numerical analysis of brittle fracture propagation and step-path failure in massive rock slopes. Can. Geotech. Conf. 1–8.

Eberhardt, E., Stead, D., Stimpson, B., 1999. Quantifying progressive pre-peak brittle fracture damage in rock during uniaxial compression. Int. J. Rock Mech. Min. Sci. 36, 361–380.

Eberhardt, E., Stead, D., Stimpson, B., Read, R.S., 1998. Identifying crack initiation and propagation thresholds in brittle rock. Can. Geotech. J. 35, 222–233.

Eberhardt, E., Stimpson, B., Stead, D., 1999. Effects of Grain Size on the Initiation and Propagation Thresholds of Stress-induced Brittle Fractures. Rock Mech. Rock Eng. 32, 81–99.

Einstein, H.H., Baecher, G.B., 1983. Probabilistic and statistical methods in engineering geology. Rock Mech. Rock Eng. 16, 39–72. https://doi.org/10.1007/BF01030217

Einstein, H.H., Veneziano, D., Baecher, G.B., O'Reilly, K.J., 1983. The effect of discontinuity persistance on rock slope stability. Int. J. Rock Mech. Min. Sci. 20, 227–236.

Einstein, H.H., Veneziano, D., Baecher, G.B., O'Reilly, K.J., 1983. The effect of discontinuity persistence on rock slope stability. Int. J. Rock Mech. Min. Sci. 20, 227–236. https://doi.org/10.1016/0148-9062(83)90003-7

Eitel, J.U.H., Hofle, B., Vierling, L.A., Abellan, A., Asner, G.P., Deems, J.S., Glennie, C.L., Joerg, P.C., LeWinter, A.L., Magney, T.S., Mandlburger, G., Morton, D.C., Muller, J., Vierling, K.T., 2016. Beyond 3-D: The new spectrum of lidar applications for earth and ecological sciences. Remote Sens. Environ. 186, 372–392. https://doi.org/10.1016/j.rse.2016.08.018

Elmo, D., Clayton, C., Rogers, S., Beddoes, R., Greer, S., 2011. Numerical Simulations of potential rock bridge failure within a naturally fractured rock mass, in: Proceedings International Symposium on Rock Slope Stability in Open Pit Mining and Civil Engineering (Slope Stability 2011). pp. 18–21.

Elmo, D., Yan, M., Stead, D., Rogers, S.F., 2007. The importance of intact rock bridges in the stability of high rock slopes - towards a quantitative investigation using an intergrated numerical modelling; discrete fracture network approach, in: Potvin, Y. (Ed.), Slope Stability 2007 : Proceedings of the 2007 International Sysmposium on Rock Slope Stability in Open Pit Mining and Civil Engineering. Australian centre for geomechanics, Perth, pp. 253–266.

Eppes, M.-C., Keanini, R., 2017. Mechanical Weathering and Rock Erosion by Climate-Dependent Subcritical Cracking. Rev. Geophys. 55, 1–39. https://doi.org/10.1002/2017RG000557

Eppes, M.C., Magi, B., Hallet, B., Delmelle, E., Mackenzie-Helnwein, P., Warren, K., Swami, S., 2016. Deciphering the role of solar-induced thermal stresses in rock weathering. Geol. Soc. Am. Bull. 128, 1315–1338. https://doi.org/10.1130/B31422.1

Espinosa-Marzal, R.M., Scherer, G.W., 2010. Mechanisms of damage by salt. Geol. Soc. London, Spec. Publ. 331, 61–77. https://doi.org/10.1144/SP331.5

Fabre, G., Pellet, F., 2006. Creep and time-dependent damage in argillaceous rocks. Int. J. Rock Mech. Min. Sci. 43, 950–960. https://doi.org/10.1016/j.ijrmms.2006.02.004

Fell, R., Corominas, J., Bonnard, C., Cascini, L., Leroi, E., Savage, W.Z., 2008. Guidelines for landslide susceptibility, hazard and risk zoning for land-use planning. Eng. Geol. 102, 99–111. https://doi.org/10.1016/j.enggeo.2008.03.014

Fookes, P.G., Gourley, C.S., Ohikere, C., 1988. Rock weathering in engineering time. Q. J. Eng. Geol. 21, 33–57.

Frayssines, M., Hantz, D., 2009. Modelling and back-analysing failures in steep limestone cliffs. Int. J. Rock Mech. Min. Sci. 46, 1115–1123. https://doi.org/10.1016/j.ijrmms.2009.06.003

Frayssines, M., Hantz, D., 2006. Failure mechanisms and triggering factors in calcareous cliffs of the Subalpine Ranges (French Alps). Eng. Geol. 86, 256–270. https://doi.org/10.1016/j.enggeo.2006.05.009

Freiman, S.W., 1984. Effect of chemical enviroments on slow crack growth in glasses and ceramics. J. Geophys. Res. 89, 4072–4076.

Gerber, E., Dorf, S., Schiedegger, A.E., 1973. Erosional and stress-induced features on steep slopes. Zeitschrift fur Geomorphol. 18, 38–49.

Gerber, E., Schiedegger, A.E., 1969. Stress induced weathering of rock masses. Eclogae geol. Helv. 62, 401–415.

Ghobadi, M., Babazadeh, R., 2015. Experimental studies on the effects of cyclic freezing – thawing , salt crystallization , and thermal shock on the physical and mechanical characteristics of selected sandstones. Rock Mech. Rock Eng. 48, 1001–1016. https://doi.org/10.1007/s00603-014-0609-6

Gischig, V., Amann, F., Moore, J.R., Loew, S., Eisenbeiss, H., Stempfhuber, W., 2011. Composite rock slope kinematics at the current Randa instability , Switzerland , based on remote sensing and numerical modeling. Eng. Geol. 118, 37–53. https://doi.org/10.1016/j.enggeo.2010.11.006

Gischig, V., Preisig, G., Eberhardt, E., 2016. Numerical Investigation of Seismically Induced Rock Mass Fatigue as a Mechanism Contributing to the Progressive Failure of Deep-Seated Landslides. Rock Mech. Rock Eng. 49, 2457–2478. https://doi.org/10.1007/s00603-015-0821-z

Gischig, V.S., Moore, J.R., Evans, K.., Amann, F., Loew, S., 2011. Thermomechanical forcing of deep rock slope deformation : 1 . Conceptual study of a simplified slope. J. Geophys. Res. 116, 1–18. https://doi.org/10.1029/2011JF002006

Goodman, R.E., Shi, G., 1985. Block Theory and its Application to Rock Engineering. Prentice-Hall Inc, New Jersey. https://doi.org/10.1016/0013-7952(88)90010-5

Griffith, A.A., 1924. The theory of rupture, in: Biezeno, C.B., Burgers, J.M. (Eds.), First International Congress of Applied Mechanics. Waltman, Delft, The Netherlands, pp. 55–63.

Griffith, A.A., 1921. The Phenomena of Rupture and Flow in Solid. Philos Trans R Soc L. A221 221, 163–198.

Grøneng, G., Nilsen, B., Sandven, R., 2009. Shear strength estimation for Aknes sliding area in western Norway. Int. J. Rock Mech. Min. Sci. 46, 479–488. https://doi.org/10.1016/j.ijrmms.2008.10.006

Gudmundsson, A., Simmenes, T.H., Larsen, B., Philipp, S.L., 2010. Effects of internal structure and local stresses on fracture propagation, deflection, and arrest in fault zones. J. Struct. Geol. 32, 1643–1655. https://doi.org/10.1016/j.jsg.2009.08.013

Gunzburger, Y., Merrien-Soukatchoff, V., Guglielmi, Y., 2005. Influence of daily surface temperature flucuations on rock slope stability: a case study of the Rochers de Valabres slope (France). Int. J. Rock Mech. Min. Sci. 42, 331–349.

Gupta, A.S., Seshagiri Rao, K., 2000. Weathering effects on the strength and deformational behaviour of crystalline rocks under uniaxial compression state. Eng. Geol. 56, 257–274. https://doi.org/10.1016/S0013-7952(99)00090-3

Guzzetti, F., Carrara, A., Cardinali, M., Reichenbach, P., 1999. Landslide hazard evaluation: A review of current techniques and their application in a multi-scale study, Central Italy. Geomorphology 31, 181–216. https://doi.org/10.1016/S0169-555X(99)00078-1

Guzzetti, F., Malamud, B.D., Turcotte, D.L., Reichenbach, P., 2002. Power-law correlations of landslide areas in central Italy. Earth Planet. Sci. Lett. 195, 169–183. https://doi.org/10.1016/S0012-821X(01)00589-1

Guzzetti, F., Reichenbach, P., Wieczorek, G.F., 2003. Rockfall hazard and risk assessment in the Yosemite Valley, California, USA. Nat. Hazards Earth Syst. Sci.

3, 491–503. https://doi.org/10.5194/nhess-3-491-2003

Hall, K., Thorn, C., Sumner, P., 2012. On the persistence of “weathering.” Geomorphology 149–150, 1–10. https://doi.org/10.1016/j.geomorph.2011.12.024

Havaej, M., Stead, D., 2016. Investigating the role of kinematics and damage in the failure of rock slopes. Comput. Geotech. 78, 181–193. https://doi.org/10.1016/j.compgeo.2016.05.014

Head, K.H.K., 2006. Manual of Soil Laboratory Testing, Volume 1: Soil Classification and Compaction Tests, 3rd ed. Whittles Publishing, Caithness.

Head, K.H.K., Epps, R.J., 2011. Manual of Soil Laboratory Testing, Volume 2: Permeability, Shear Strength and Compressibility Tests, 3rd ed. Whittles Publishing, Caithness.

Herterich, J.G., Cox, R., Dias, F., 2018. How does wave impact generate large boulders? Modelling hydraulic fracture of cliffs and shore platforms. Mar. Geol. https://doi.org/10.1016/j.margeo.2018.01.003

Hibbeler, R.C., 2010. Engineering Mechanics Statics, 12th ed. Pearson, Singapore.

Hoek, E., 1983. Strength of jointed rock masses. Geotechnique 23, 187–223. https://doi.org/10.1680/geot.1983.33.3.187

Hoek, E., Brown, E.., 1997. Practical estimates of rock mass strength. Int. J. Rock Mech. Min. Sci. 34, 1165–1186. https://doi.org/10.1016/S1365-1609(97)80069-X

Hollander, M., Wolfe, D.A., Chicken, E., 2015. Nonparametric Statistical Methods, 3rd ed. John Wiley & Sons. https://doi.org/10.1002/9781119196037

Huang, Q., Angelier, J., 1989. Fracture spacing and its relation to bed thickness. Geol. Mag. 126, 355–362. https://doi.org/10.1017/S0016756800006555

Huisman, M., Nieuwenhuis, J.D., Hack, H.R.G.K., 2011. Numerical modelling of combined erosion and weathering of slopes in weak rock. Earth Surf. Process. Landforms 36, 1705–1714. https://doi.org/10.1002/esp.2179

Hungr, O., Evans, S.G., Hazzard, J., 1999. Magnitude and frequency of rockfalls and rock slides along the main transportation corridors of southwestern British Columbia. Can. Geotech. J. 36, 224–238.

Irwin, G.R., 1957. Analysis of stresses and strains near the end of a crack traversing a plate. J. Appl. Mech. 24, 361–364.

Ishikawa, M., Kurashige, Y., Hirakawa, K., 2004. Analysis of crack movements observed in an alpine bedrock cliff. Earth Surf. Process. Landforms 29, 883–891. https://doi.org/10.1002/esp.1076

ISRM, 2015. The ISRM Suggested Methods for Rock Characterization, Testing and Monitoring:2007-2014, 1st ed. Springer International Publishing.

Iverson, R.M., 2000. Landslide triggering by rain infiltration. Water Resour. Res. 36, 1897–1910. https://doi.org/10.1029/2000WR900090

Jaboyedoff, M., Oppikofer, T., Abellán, A., Derron, M.H., Loye, A., Metzger, R., Pedrazzini, A., 2012. Use of LIDAR in landslide investigations: A review. Nat. Hazards 61, 5–28. https://doi.org/10.1007/s11069-010-9634-2

Jaeger, J.C., Cook, N.G.W., Zimmerman, R., 2007. Fundamentals of Rock Mechanics, 4th ed. Wiley-Blackwell.

Jennings, J.E., 1970. A mathematical theory for the calculation of the stability of open cast mines, in: Van Rensburg, P. (Ed.), Planning Open Pit Mines: Proceedings of

the Symposium on the Theoritical Background to the Planning of Open Pit Mines with Special Reference to Slope Stability. Balkema (A.A.), Johannesburg, pp. 87–102.

Karami, A., Greer, S., Beddoes, R., 2007. Numerical assessment of step-path failure of northwest wall of A154 Pit, Diavik Diamond Mines, in: Potvin, Y. (Ed.), Slope Stability 2007 : Proceedings of the 2007 International Symposium on Rock Slope Stability in Open Pit Mining and Civil Engineering. Australian centre for geomechanics, Perth, pp. 293–305.

Keefer, D., 1994. The importance of earthquake-induced landslides to long-term slope erosio and slope-failure hazards in seismically active regions, in: Proceedings of the 25th Binghamton Symposium in Geomorphology. Binghampton, USA, pp. 265–284. https://doi.org/10.1016/B978-0-444-82012-9.50022-0

Keefer, D.K., Keefer, 1994. The importance of earthquake-induced landslides to long-term slope erosion and slope-failue hazards in seismically active regions. Geomorphology 10, 265–284. https://doi.org/10.1109/TDEI.2009.5211872

Keefer, D.K., Wilson, R.C., Mark, R.K., Brabb, E.E., William, M., Ellen, S.D., Harp, E.L., Wieczorek, G.F., Alger, C.S., Robert, S., Iii, W.M.B., Zatkint, R.S., 1987. Real-Time During Warning Landslide Rainfall Heavy. Science (80-.). 238, 921–925.

Kemeny, J., 2005. Time-dependent drift degradation due to the progressive failure of rock bridges along discontinuities. Int. J. Rock Mech. Min. Sci. 42, 35–46. https://doi.org/10.1016/j.ijrmms.2004.07.001

Kemeny, J., 2003. The time-dependent reduction of sliding cohesion due to rock bridges along discontinuities: A fracture mechanics approach. Rock Mech. Rock Eng. 36, 27–38. https://doi.org/10.1007/s00603-002-0032-2

Kinakin, D., Stead, D., 2005. Analysis of the distributions of stress in natural ridge forms: implications for the deformation mechanisms of rock slopes and the formation of sackung. Geomorphology 65, 85–100. https://doi.org/10.1016/j.geomorph.2004.08.002

Kogure, T., Aoki, H., Maekado, A., Hirose, T., Matsukura, Y., 2006. Effect of the development of notches and tension cracks on instability of limestone coastal cliffs in the Ryukyus, Japan. Geomorphology 80, 236–244. https://doi.org/10.1016/j.geomorph.2006.02.012

Koons, P.O., Upton, P., Barker, A.D., 2012. The influence of mechanical properties on the link between tectonic and topographic evolution. Geomorphology 137, 168–180. https://doi.org/10.1016/j.geomorph.2010.11.012

Korup, O., Clague, J.J., Hermanns, R.L., Hewitt, K., Strom, A.L., Weidinger, J.T., 2007. Giant landslides, topography, and erosion. Earth Planet. Sci. Lett. 261, 578–589. https://doi.org/10.1016/j.epsl.2007.07.025

Kranz, R.., 1983. Microcracks in rocks: a review. Tectonophysics 100, 449–480.

Krautblatter, M., Dikau, R., 2007. Towards a uniform concept for the comparison and extrapolation of rockwall retreat and rockfall supply. Geogr. Ann. Ser. A, Phys. Geogr. 89, 21–40.

Krautblatter, M., Funk, D., Gunzel, F.K., 2013. Why permafrost rocks become unstable: A rock-ice-mechanical model in time and space. Earth Surf. Process. Landforms 38, 876–887. https://doi.org/10.1002/esp.3374

Kromer, R.A., Abellán, A., Hutchinson, D.J., Lato, M., Chanut, M., Dubois, L., Jaboyedoff, M., 2017. Automated terrestrial laser scanning with near-real-time change detection – monitoring of the Séchilienne landslide 293–310. https://doi.org/10.5194/esurf-5-

293-2017

Kromer, R.A., Hutchinson, D.J., Lato, M.J., Gauthier, D., Edwards, T., 2015. Identifying rock slope failure precursors using LiDAR for transportation corridor hazard management. Eng. Geol. 195, 93–103. https://doi.org/10.1016/j.enggeo.2015.05.012

Kromer, R.A., Rowe, E., Hutchinson, J., Lato, M., Abellán, A., 2017. Rockfall risk management using a pre-failure deformation database. Landslides. https://doi.org/10.1007/s10346-017-0921-9

Ladeira, F.L., Price, N.J., 1981. Relationship between fracture spacing and bed thickness. J. Struct. Geol. 3, 179–183. https://doi.org/10.1016/0191-8141(81)90013-4

Lajtai, E., Lajtai, V., 1974. The evolution of brittle fracture in rocks. J. Geol. Soc. London. 130, 1–16. https://doi.org/10.1144/gsjgs.130.1.0001

Lamp, J.L., Marchant, D.R., Mackay, S.L., Head, J.W., 2017. Thermal stress weathering and the spalling of Antarctic rocks. J. Geophys. Res. Earth Surf. 122, 3–24. https://doi.org/10.1002/2016JF003992

Leith, K., Moore, J.R., Amann, F., Loew, S., 2014a. In situ stress control on microcrack generation and macroscopic extensional fracture in exhuming bedrock. J. Geophys. Res. Solid Earth 119, 594–615. https://doi.org/10.1002/2012JB009801

Leith, K., Moore, J.R., Amann, F., Loew, S., 2014b. Subglacial extensional fracture development and implications for Alpine Valley evolution. J. Geophys. Res. Earth Surf. 119, 62–81. https://doi.org/10.1002/2012JF002691

Leroueil, S., 2001. Natural slopes and cuts: movement and failure mechanisms. Geotechnique 51, 197–243.

Lévy, C., Baillet, L., Jongmans, D., Mourot, P., Hantz, D., 2010. Dynamic response of the Chamousset rock column (Western Alps , France). J. Geophys. Res. 115, 1–13. https://doi.org/10.1029/2009JF001606

Li, Y., Onasch, C.M., Guo, Y., 2008. GIS-based detection of grain boundaries. J. Struct. Geol. 30, 431–443. https://doi.org/10.1016/j.jsg.2007.12.007

Lim, M., Petley, D.N., Rosser, N.J., Allison, R.J., Long, A.J., Pybus, D., 2005. Combined digital photogrammetry and time-of-flight laser scanning for monitoring cliff evolution. Photogramm. Rec. 20, 109–129.

Lim, M., Rosser, N.J., Allison, R.J., Petley, D.N., 2010. Erosional processes in the hard rock coastal cliffs at Staithes, North Yorkshire. Geomorphology 114, 12–21. https://doi.org/10.1016/j.geomorph.2009.02.011

Lim, M., Rosser, N.J., Petley, D.N., Keen, M., 2011. Quantifying the Controls and Influence of Tide and Wave Impacts on Coastal Rock Cliff Erosion. J. Coast. Res. 27, 46–56. https://doi.org/10.2112/JCOASTRES-D-09-00061.1

Liu, L., Zoback, M.D., 1992. The effect of topography on the state of stress in the crust: application to the site of the Cajon Pass Scientific Drilling Project. J. Geophys. Res. 97, 5095–5108. https://doi.org/10.1029/91JB01355

Loye, A., Jaboyedoff, M., Pedrazzini, A., 2009. Identification of potential rockfall source areas at a regional scale using a DEM-based geomorphometric analysis. Nat. Hazards Earth Syst. Sci. 9, 1643–1653.

Main, I.G., 2000. A damage mechanics model for power-law creep and earthquake aftershock and foreshock sequences. Geophys. J. Int. 142, 151–161. https://doi.org/10.1046/j.1365-246X.2000.00136.x

Main, I.G., Sammonds, P.R., Meredith, P.G., 1993. Damage During Compressional Rock Failure. Geophys. J. Int. 115, 367–380.

Malamud, B.D., Turcotte, D.L., Guzzetti, F., Reichenbach, P., 2004. Landslide inventories and their statistical properties. Earth Surf. Process. Landforms 29, 687–711. https://doi.org/10.1002/esp.1064

Martel, S.J., 2017. Progress in understanding sheeting joints over the past two centuries. J. Struct. Geol. 94, 68–86. https://doi.org/10.1016/j.jsg.2016.11.003

Martel, S.J., 2006. Effect of topographic curvature on near-surface stresses and application to sheeting joints. Geophys. Res. Lett. 33. https://doi.org/10.1029/2005GL024710

Martin, C.D., 1997. The effect of cohesion loss and stress path on brittle rock strength. Can. Geotech. J. 34, 698–725. https://doi.org/10.1139/cgj-34-5-698

Martin, C.D., Chandler, N.A., 1994. The progressive fracture of Lac du Bonnet granite. Int. J. Rock Mech. Min. Sci. 31, 643–659. https://doi.org/10.1016/0148-9062(94)90005-1

Matasci, B., Jaboyedoff, M., Loye, A., Pedrazzini, A., Derron, M.H., Pedrozzi, G., 2015. Impacts of fracturing patterns on the rockfall susceptibility and erosion rate of stratified limestone. Geomorphology 241, 83–97. https://doi.org/10.1016/j.geomorph.2015.03.037

Matsuoka, N., Sakai, H., 1999. Rockfall activity from an alpine cliff during thawing periods. Geomorphology 28, 309–328.

McConaughy, D.T., Engelder, T., 2001. Joint initiation in bedded clastic rocks. J. Struct. Geol. 23, 203–221. https://doi.org/10.1016/S0191-8141(00)00091-2

McTigue, D.F., Mei, C.C., 1981. Gravity-induced stresses near topography of small slope. J. Geophys. Res. 86, 9268–9278. https://doi.org/10.1029/JB086iB10p09268

Messenzehl, K., Meyer, H., Otto, J., Hoffmann, T., Dikau, R., 2017. Geomorphology Regional-scale controls on the spatial activity of rockfalls (Turtmann Valley , Swiss Alps) — A multivariate modeling approach. Geomorphology 287, 29–45. https://doi.org/10.1016/j.geomorph.2016.01.008

Migon, P., 2010. Mass movement and landscape evolution in weathered granite and gneiss terrains. Geol. Soc. London, Eng. Geol. Spec. Publ. 23, 33–45. https://doi.org/10.1144/EGSP23.4

Milledge, D.G., Bellugi, D., McKean, J., Densmore, A.L., Dietrich, W.E., 2014. A multidimensional stability model for predicting shallow landslide size and shape across landscapes. J. Geophys. Res. Earth Surf. 119, 2481–2504. https://doi.org/10.1002/2014JF003135.Received

Miller, D.J., Dunne, T., 1996. Topographic perturbations of regional stresses and consequent bedrock fracturing. J. Geophys. Res. 101, 25,523-25,536.

Mitchell, T.M., Faulkner, D.R., 2008. Experimental measurements of permeability evolution during triaxial compression of initially intact crystalline rocks and implications for fluid flow in fault zones. J. Geophys. Res. Solid Earth 113, 1–16. https://doi.org/10.1029/2008JB005588

Moffit, K., Rogers, S., Beddoes, R., 2007. Analysis of slope stability in strong, fractured rock at the Diavik Diamond Mine, NWT, in: Rock Mechanics: Meeting Society's Challenges and Demands, Proceedings of the 1st Canada-US Rock Mechanics Symposium. pp. 1245–1250.

Mol, L., Viles, H.A., 2012. The role of rock surface hardness and internal moisture in

tafoni development in sandstone. Earth Surf. Process. Landforms 37, 301–314. https://doi.org/10.1002/esp.2252

Molnar, P., 2004. Interactions among topographically induced elastic stress, static fatigue, and valley incision. J. Geophys. Res. 109, 1–9. https://doi.org/10.1029/2003JF000097

Moore, J.R., Gischig, V., Katterbach, M., Loew, S., 2011. Air circulation in deep fractures and the temperature field of an alpine rock slope. Earth Surf. Process. Landforms 36, 1985–1996. https://doi.org/10.1002/esp.2217

Moore, J.R., Sanders, J.W., Dietrich, W.E., Glaser, S.D., 2009. Influence of rock mass strength on the erosion rate of alpine cliffs. Earth Surf. Process. Landforms 34, 1339–1352. https://doi.org/10.1002/esp.1821

Moses, C., Robinson, D., Barlow, J., 2014. Methods for measuring rock surface weathering and erosion: A critical review. Earth-Science Rev. 135, 141–161. https://doi.org/10.1016/j.earscirev.2014.04.006

Mottershead, D., 2013. Coastal Weathering, in: Treatise on Geomorphology: Weathering and Soils Geomorphology. Elsevier, London, pp. 228–244.

Muller, J.R., Martel, S.J., 2000. Numerical Models of Translational Landslide Rupture Surface Growth. Pure Appl. Geophys. 157, 1009–1038. https://doi.org/10.1007/s000240050015

Mushkin, A., Sagy, A., Trabelci, E., Amit, R., Porat, N., 2014. Measuring the time and scale-dependency of subaerial rock weathering rates over geologic time scales with ground-based lidar. Geology. 42, 12, 1063-1066. https://doi.org/10.1130/G35866.1

Narr, W., Suppe, J., 1991. Joint spacing in sedimentary rocks. J. Struct. Geol. 13, 1037–1048. https://doi.org/10.1016/0191-8141(91)90055-N

Naylor, L.A., Coombes, M.A., Viles, H.A., 2012. Reconceptualising the role of organisms in the erosion of rock coasts: A new model. Geomorphology. 157-158, 17-30.

Nicholson, D.T., 2001. Pore properties as indicators of breakdown mechanisms in experimentally weathered limestones. Earth Surf. Process. Landforms 26, 819–838. https://doi.org/10.1002/esp.228

Nicholson, D.T., Nicholson, F.H., 2000. Physical deterioration of sedimentary rocks subjected to experimental freeze-thaw weathtering. Earth Surf. Process. Landforms 25, 1295–1307.

Norman, E.C., 2012. Microseismic monitoring of the controls on coastal rock cliff erosion.

Norman, E.C., Rosser, N.J., Brain, M.J., Petley, D.N., Lim, M., 2013. Coastal cliff-top ground motions as proxies for environmental processes. J. Geophys. Res. Ocean. 118, 6807–6823. https://doi.org/10.1002/2013JC008963

Oda, M., Takemura, T., Aoki, T., 2002. Damage growth and permeability change in triaxial compression tests of Inada granite. Mech. Mater. 34, 313–331. https://doi.org/10.1016/S0167-6636(02)00115-1

Otsu, N., 1979. A threshold selection method from gray-level histograms. IEEE transcations Syst. man, Cybern. SMC-9, 62–66.

Paronuzzi, P., Bolla, A., Rigo, E., 2016. 3D Stress – Strain Analysis of a Failed Limestone Wedge Influenced by an Intact Rock Bridge. Rock Mech. Rock Eng. 49, 3223–3242. https://doi.org/10.1007/s00603-016-0963-7

Paronuzzi, P., Sera, W., 2009. Stress state analysis of a collapsed overhanging rock

slab : A case study. Eng. Geol. 108, 65–75. https://doi.org/10.1016/j.enggeo.2009.06.019

Perras, M.A., Diederichs, M.S., 2014. A review of the tensile strength of rock: concepts and testing. Geotech. Geol. Eng. 32, 525–546. https://doi.org/10.1007/s10706-014-9732-0

Petley, D.N., Bulmer, M.H., Murphy, W., 2002. Patterns of movement in rotational and translational landslides. Geology 30, 719–722.

Petley, D.N.D.J., Higuchi, T., Petley, D.N.D.J., Bulmer, M.H., Carey, J., 2005. Development of progressive landslide failure in cohesive materials. Geology 33, 201–204. https://doi.org/10.1130/G21147.1

Phillips, J.D., 2003. Sources of nonlinearity and complexity in geomorphic systems. Prog. Phys. Geogr. 27, 1–23. https://doi.org/10.1191/0309133303pp340ra

Pollard, D.D., Aydin, A., 1988. Progress in understanding jointing over the past century. Geol. Soc. Am. Bull. 100, 1181–1204. https://doi.org/10.1130/0016-7606(1988)100<1181

Preisig, G., Eberhardt, E., Smithyman, M., 2016. Hydromechanical Rock Mass Fatigue in Deep-Seated Landslides Accompanying Seasonal Variations in Pore Pressures. Rock Mech. Rock Eng. 49, 2333–2351. https://doi.org/10.1007/s00603-016-0912-5

Priest, S.D., 1993. Discontinuity Analysis for Rock Engineering. Springer Netherlands. https://doi.org/10.1007/978-94-011-1498-1

Radbruch-Hall, D.H., Varnes, D.J., Savage, W.Z., 1976. Gravitational spreading of steep-sided ridges (“Sackung”) in Western United States. Bull. Int. Assoc. Eng. Geol. 14, 23–35.

Rawson, P.F., Wright, J.K., 2000. The Yorkshire Coast, 3rd ed, Geologists’ Association Guide. Geologists’Association, Burlington House, Piccadilly, London.

Rihosek, J., Bruthans, J., Masin, D., Filippi, M., Carling, G.T., Schweigstillova, J., 2016. Gravity-induced stress as a factor reducing decay of sandstone monuments in Petra, Jordan. J. Cult. Herit. 19, 415–425. https://doi.org/10.1016/j.culher.2015.10.004

Robinson, D.A., Williams, R.B.G., Williams, R.G.B., 1982. Salt weathering of rock specimens of varying shape. Area 14, 293–299.

RocScience, 2017. RS2: Rock and Soil 2-Dimensional analysis programme manual.

Rosser, N., Lim, M., Petley, D., Dunning, S., Allison, R., 2007. Patterns of precursory rockfall prior to slope failure. J. Geophys. Res. 112. https://doi.org/10.1029/2006JF000642

Rosser, N.J., Brain, M.J., Petley, D.N., Lim, M., Norman, E.C., 2013. Coastline retreat via progressive failure of rocky coastal cliffs. Geology 41, 939–942. https://doi.org/10.1130/G34371.1

Rosser, N.J., Petley, D.N., Lim, M., Dunning, S.A., Allison, R.J., 2005. Terrestrial laser scanning for monitoring the process of hard rock coastal cliff erosion. Q. J. Eng. Geol. Hydrogeol. 38, 363–375. https://doi.org/10.1144/1470-9236/05-008

Rowe, E., Hutchinson, D.J., Kromer, R.A., 2017. An analysis of failure mechanism constraints PNA70605on pre-failure rock block deformation using TLS and roto-translation methods. Landslides. https://doi.org/10.1007/s10346-017-0886-8

Royán, M.J., Abellán, A., Jaboyedoff, M., Vilaplana, J.M., Calvet, J., 2014. Spatio-temporal analysis of rockfall pre-failure deformation using Terrestrial LiDAR.

Landslides 11, 697–709. https://doi.org/10.1007/s10346-013-0442-0

Royan, M.J., Abellan, A., Vilaplana, J.M., 2015. Progressive failure leading to the 3 December 2013 rockfall at Puigcercos scarp (Catalonia, Spain). Landslides 12, 585–595. https://doi.org/10.1007/s10346-015-0573-6

Røyne, A., Jamtveit, B., Mathiesen, J., Malthe-Sørenssen, A., 2008. Controls on rock weathering rates by reaction-induced hierarchical fracturing. Earth Planet. Sci. Lett. 275, 364–369. https://doi.org/10.1016/j.epsl.2008.08.035

Saito, M., 1965. Forecasting the time of occurrence of a slope failure. Proc. 6th Int. Conf. Soil Mech. Found. Eng. 2, 573–541.

Sass, O., 2005. Spatial patterns of rockfall intensity in the northern Alps. Zeitschrift fur Geomorphol. 138, 51–65.

Savage, W.Z., 1993. Gravity-induced stresses near a vertical cliff. Int. J. Rock Mech. Min. Sci. Geomech. Abstr. 30, 325–330.

Savage, W.Z., Swolfs, S., 1986. Tectonic and Gravitational Stress in Long Symmetric Ridges and Valleys. J. Geophys. Res. 91, 3677–3685.

Savage, W.Z., Swolfs, S., Powers, P.S., Pan, E., Amadei, B., Savage, W.Z., 1994. Gravitational stresses in long symmetric ridges and valleys in anisotropic rock. Int. J. Rock Mech. Min. Sci. 22, 293–312. https://doi.org/10.1016/0148-9062(94)90899-0

Scavia, C., 1995. A method for the study of crack propagation in rock structures. Geotechnique 45, 447–463.

Scavia, C., 1990. Fracture mechanics approach to stability analysis of rock slopes. Eng. Fract. Mech. 35, 899–910.

Scavia, C., Castelli, M., 1996. Analysis of the propagation of natural discontinuities in rock bridges, in: Eurock. pp. 445–451.

Selby, M.J., 1993. Hillslope Materials and Processes, 2nd ed. Oxford University Press, Oxford.

Selby, M.J., 1982. Rock mass strength and the form of some inselbergs in the central Namib Desert. Earth Surf. Process. Landforms 7, 489–497.

Selby, M.J., 1980. A rock mass strength classification for geomorphic purposes: with tests from Antarctica and New Zealand. Zeitschrift für Geomorphol. 24, 31–51.

Senfaute, G., Duperret, a, Lawrence, J. a, 2009. Micro-seismic precursory cracks prior to rock-fall on coastal chalk cliffs: a case study at Mesnil-Val, Normandie, NW France. Nat. Hazards Earth Syst. Sci. 9, 1625–1641. https://doi.org/10.5194/nhess-9-1625-2009

Silverman, B.W., 1986. Density estimation for statistics and data analysis. Chapman and Hall, New York.

Slim, M., Perron, J.T., Martel, S.J., Singha, K., 2014. Topographic stress and rock fracture: a two-dimensional numerical model for arbitrary topography and preliminary comparison with borehole observations. Earth Surf. Process. Landforms 40, 512–529. https://doi.org/10.1002/esp.3646

St Clair, J., Moon, S., Holbrook, W.S., Perron, J.T., Riebe, C.S., Martel, S.J., Carr, B., Harman, C., Singha, K., Richter, D. deB, 2015. Geophysical imaging reveals topographic stress control of bedrock weathering. Science (80-.). 350, 534–8. https://doi.org/10.1126/science.aab2210

Stead, D., Eberhardt, E., Coggan, J.S., 2006. Developments in the characterization of complex rock slope deformation and failure using numerical modelling techniques. Eng. Geol. 83, 217–235. https://doi.org/10.1016/j.enggeo.2005.06.033

Stead, D., Wolter, A., 2015. A critical review of rock slope failure mechanisms : The importance of structural geology. J. Struct. Geol. 74, 1–23. https://doi.org/10.1016/j.jsg.2015.02.002

Stock, G.M., Bawden, G.W., Green, J.K., Hanson, E., Downing, G., Collins, B.D., Bond, S., Leslar, M., 2011. High-resolution three-dimensional imaging and analysis of rock falls in Yosemite Valley, California. Geosphere 7, 573–581.

Stock, G.M., Martel, S.J., Collins, B.D., Harp, E.L., 2012. Progressive failure of sheeted rock slopes: the 2009-2010 Rhombus Wall rock falls in Yosemite Valley, California, USA. Earth Surf. Process. Landforms 37, 546–561. https://doi.org/10.1002/esp.3192

Strunden, J., Ehlers, T.A., Brehm, D., Nettesheim, M., 2015. Spatial and temporal variations in rockfall determined from TLS measurements in a deglaciated valley, Switzerland. J. Geophys. Res. Earth Surf. 120, 1–23. https://doi.org/10.1002/2014JF003274.Received

Sturzenegger, M., Stead, D., 2012. The Palliser Rockslide , Canadian Rocky Mountains : Characterization and modeling of a stepped failure surface. Geomorphology 138, 145–161. https://doi.org/10.1016/j.geomorph.2011.09.001

Sturzenegger, M., Stead, D., 2009. Close-range terrestrial digital photogrammetry and terrestrial laser scanning for discontinuity characterization on rock cuts. Eng. Geol. 106, 163–182. https://doi.org/10.1016/j.enggeo.2009.03.004

Terzaghi, K., 1962. Stability of steep slopes on hard unweathered rock. Geotechnique 12, 251–270.

ThermoScientific, 2017. NITON XL3t 900 Analyzer with GOLDD Technology User ' s Guide (No. 6.5).

Thomson, B.J., Hurowitz, J.A., Baker, L.L., Bridges, N.T., Lennon, A.M., Paulsen, G., Zacny, K., 2014. The effects of weathering on the strength and chemistry of Columbia River Basalts and their implications for Mars Exploration Rover Rock Abrasion Tool (RAT) results. Earth Planet. Sci. Lett. 400, 130–144. https://doi.org/10.1016/j.epsl.2014.05.012

Tuckey, Z., Stead, D., 2016. Improvements to field and remote sensing methods for mapping discontinuity persistence and intact rock bridges in rock slopes. Eng. Geol. 208, 136–153. https://doi.org/10.1016/j.enggeo.2016.05.001

Twiss, R.J., Moore, E.M., 1992. Structural Geology. W.H.Freeman and Company, New York.

Vann Jones, E.C., Rosser, N.J., Brain, M.J., Petley, D.N., 2015. Quantifying the environmental controls on erosion of a hard rock cliff. Mar. Geol. 363, 230–242. https://doi.org/10.1016/j.margeo.2014.12.008

Varnes, D.J., 1978. Slope movement types and processes, in: Schuster, R.L., Krizek, R.J. (Eds.), Special Report 176: Landslides - Analysis and Control. Transportation and Road Research Board, National Academy of Science, Washington D.C., pp. 11–33.

Viles, H., 2013a. Linking weathering and rock slope instability: non-linear perspectives. Earth Surf. Process. Landforms 38, 62–70. https://doi.org/10.1002/esp.3294

Viles, H., 2013b. Synergistic weathering processes, in: Treatise on Geomorphology:

Weathering and Soils Geomorphology, Treatise on Geomorphology. Elsevier, London, pp. 12–26.

Viles, H., 2005. Self-organized or disorganized? Towards a general explanation of cavernous weathering. Earth Surf. Process. Landforms 30, 1471–1473. https://doi.org/10.1002/esp.1287

Viles, H., 2001. Scale issues in weathering studies. Geomorphology 41, 63–72.

Viles, H.A., 2005. Microclimate and weathering in the central Namib Desert, Namibia. Geomorphology 67, 189–209. https://doi.org/10.1016/j.geomorph.2004.04.006

Viles, H., Goudie, A., Grab, S., Lalley, J., 2011. The use of the Schmidt Hammer and Equotip for rock hardness assessment in geomorphology and heritage science: a comparative analysis. Earth Surf. Process. Landforms 36, 320–333. https://doi.org/10.1002/esp.2040

Viles, H., Messenzehl, K., Mayaud, J., Coombes, M., Bourke, M., 2018. Stress histories control rock-breakdown trajectories in arid environments. Geology 3–6.

Voight, B., 1989. A Relation to Describe Rate-Dependent Material Failure. Science (80-.). 243, 200–203. https://doi.org/10.1126/science.243.4888.200

Warke, P.A., 2007. Complex weathering in drylands: Implications of “stress” history for rock debris breakdown and sediment release. Geomorphology 85, 30–48. https://doi.org/10.1016/j.geomorph.2006.03.038

Whalley, W.B., 1984. Rockfalls, in: Brunsden, D., Prior, D.B. (Eds.), Slope Instability. Wiley, Chichester, pp. 217–256.

Wieczorek, G.F., Snyder, James, B., Alger, C.S., Isaacson, K.A., 1992. Rock falls in Yosemite Valley, California: U.S. Geological Survey Open-File report 93-387.

Wieczorek, G.F., Stefan, J., 1996. Triggering mechanisms and depositional rates of postglacial slope- movement processes in the Yosemite Valley, California. Geomorphology 15, 17–31.

Williams, J.G., Rosser, N.J., Hardy, R.J., Brain, M.J., Afana, A.A., 2018. Optimising 4-D surface change detection : an approach for capturing rockfall magnitude – frequency 101–119.

Wolters, G., Müller, G., 2008. Effect of cliff shape on internal stresses and rock slope stability. J. Coast. Res. 24, 43–50.

Wyllie, D.C., Mah, C.W., 2004. Rock Slope Engineering: Civil and Mining, 4th ed. Taylor and Francis Group, New York.

Yatsu, E., 1988. The Nature of Weathering: An Introduction. Sozosha, Tokyo, Japan.

Young, A., Ashford, S., 2008. Instability investigation of cantilevered seacliffs. Earth Surf. Process. Landforms 33, 1661–1677. https://doi.org/10.1002/esp

Zhang, B.Y., Zhang, J.H., Sun, G.L., 2015. Deformation and shear strength of rock fill materials composed of soft siltstones subjected to stress , cyclical drying/wetting and temperature variations. Eng. Geol. 190, 87–97. https://doi.org/10.1016/j.enggeo.2015.03.006

Zhang, B.Y., Zhang, J.H., Sun, G.L., 2012. Particle breakage of argillaceous siltstone subjected to stresses and weathering. Eng. Geol. 137–138, 21–28. https://doi.org/10.1016/j.enggeo.2012.03.009